



THE UNIVERSITY OF QUEENSLAND
AUSTRALIA

**Optimisation of Lead Inhibitors of the Imipenemase 1 (IMP-1) Metallo- β -
lactamase Enzyme**

Daniel Teoh Chuan Tan

Bachelor of Science with Education (Hons) (Universiti Sains Malaysia, USM)

Master of Science (Chemistry) (USM)

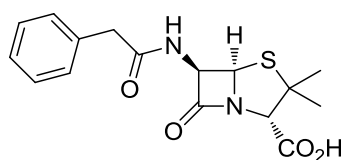
A thesis submitted for the degree of Doctor of Philosophy at

The University of Queensland in 2015

School of Chemistry and Molecular Biosciences

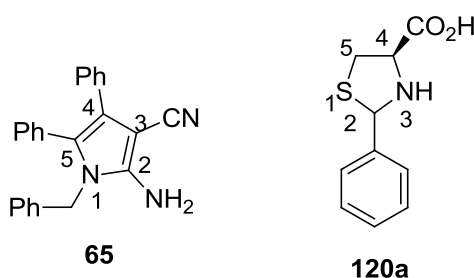
Abstract

β -Lactam antibiotics such as penicillin G (**1**) account for more than 50% of the world's antibiotics prescribed. These chemical agents work by disrupting bacterial cell wall synthesis. Over-prescription of β -lactam antibiotics has led to bacterial resistance in the form of β -lactamase expression. β -Lactamases, or β -lactam degrading enzymes, can be divided into four classes, A, B, C and D. The class B β -lactamases are the zinc-dependent enzymes, and are thus known as the metallo- β -lactamases (MBLs). Of particular concern are the MBLs, particularly the B1 MBLs, such as Imipenemase 1 (IMP-1), which can be spread by horizontal gene transfer. To date there are no known clinical inhibitors against MBLs.

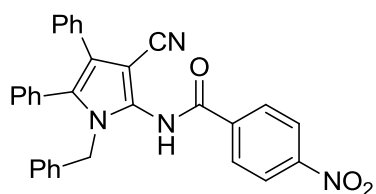


Penicillin G **1**

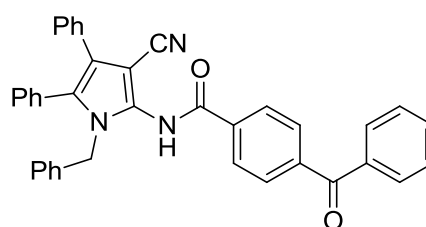
This thesis explores the optimisation of two classes of IMP-1 lead compounds, 2-amino-1-benzyl-4,5-diphenyl-1*H*-pyrrole-3-carbonitrile (**65**) and (2*RS*, 4*R*)-2-phenylthiazolidine-4-carboxylic acid (**120a**).



The structure-activity-relationship (SAR) study of pyrrole **65** led to the successful identification of two potent IMP-1 inhibitors, **93** and **99**, with a 14- to 17-fold increase in IMP-1 inhibitory potency as compared to pyrrole **65**. However, synthetic modification of the 3-carbonitrile group of **65**, or deletion of the *N*-benzyl chain resulted in a significant loss of IMP-1 inhibitory activity.

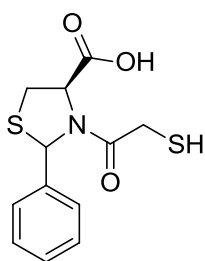


93

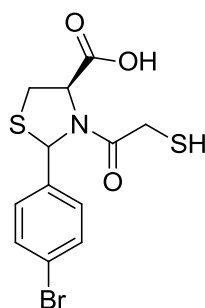


99

The SAR study of thiazolidine **120a** resulted in the discovery of the mercapto-amide-linked thiazolidine, **124a** with a 20-fold improvement in IMP-1 inhibitory activity as compared to **120a**. The extension of this study led to the identification of a highly potent thiazolidine derivative, **124g** with IMP-1 inhibitory potency in the sub-micromolar range.



124a



124g

Declaration by author

This thesis is composed of my original work, and contains no material previously published or written by another person except where due reference has been made in the text. I have clearly stated the contribution by others to jointly-authored works that I have included in my thesis.

I have clearly stated the contribution of others to my thesis as a whole, including statistical assistance, survey design, data analysis, significant technical procedures, professional editorial advice, and any other original research work used or reported in my thesis. The content of my thesis is the result of work I have carried out since the commencement of my research higher degree candidature and does not include a substantial part of work that has been submitted to qualify for the award of any other degree or diploma in any university or other tertiary institution. I have clearly stated which parts of my thesis, if any, have been submitted to qualify for another award.

I acknowledge that an electronic copy of my thesis must be lodged with the University Library and, subject to the policy and procedures of The University of Queensland, the thesis be made available for research and study in accordance with the Copyright Act 1968 unless a period of embargo has been approved by the Dean of the Graduate School.

I acknowledge that copyright of all material contained in my thesis resides with the copyright holder(s) of that material. Where appropriate I have obtained copyright permission from the copyright holder to reproduce material in this thesis.

Publications during candidature

No publications.

Publications included in this thesis

No publications included.

Contributions by others to the thesis

Ajit Kandale performed Glide computational modelling of compounds **91**, **93** and **99** for Chapter 2, **105** and **117** for Chapter 3, and **120a**, **124a**, **124b**, **124d**, **124e**, **124f**, **124g**, **124j**, **124k** and **124n** for Chapter 4. Ajit also drew the following figures: 1.32 (Chapter 1), 2.7, 2.8 and 2.9 (Chapter 2), 3.14 and 3.15 (Chapter 3), as well as 4.4, 4.5 and 4.6 (Chapter 4). Dr Sara Mustaddiq synthesised mercapto-amide-linked thiazolidines **124a-o**, as described in Chapter 4. Drs Peter Vella and Omid Khalili Arjomandi, as well as Yusralina Yusoff assisted in the synthesis of CENTA (**73**), the expression and purification of IMP-1. Graham MacFarlane and Dr Amanda Nouwens performed all the high resolution mass spectrometry measurements for all of the synthesised compounds.

Statement of parts of the thesis submitted to qualify for the award of another degree

None.

Acknowledgements

First and foremost, I'd like to thank my main supervisor, Assoc Prof Dr Ross McGeary for the privilege to be under his tutelage. Thank you, Ross for being so patient with me. I'd also like to thank my secondary supervisor, Assoc Prof Dr Gary Schenk for guiding me in the enzyme work. It was a great pleasure working with your research group, particularly, Manfredi Miraula, Chris Selleck, Dr Marcelo Pedroso and Charmaine Enculescu.

I'd also like to express my sincere thanks and gratitude to Assoc Profs Drs Luke Guddat, Joanne Blanchfield and Mark Riley for serving as my confirmation chair panel. Thank you, Joanne for giving me a thorough feedback on my confirmation document, and demonstrating the use of the freeze-dyer. I'd also like to thank Prof James De Voss for allowing me to work in his PC2 laboratory.

My sincere thanks and gratitude also go to Dr Tri Le for help with NMR experiments, Mr Graham MacFarlane and Dr Amanda Nouwens for all the HRMS data.

I also wish to thank Prof David Ollis, Ms Tracy Murray, Dr David Hou and the rest of the Ollis group for hosting me when I was in ANU, Canberra in 2013.

I'd also like to acknowledge Dr Peter Vella for demonstrating protein expression and purification, as well as enzyme kinetic assays. Thank you so much for your time and patience. Many thanks to Dr Waleed Hussein for his guidance during the early days of my PhD study.

I'd also like to take this opportunity to formally acknowledge Dr Sara Mustaddiq for her contribution to my PhD work and Mr Ajit Kandale for his help in the computational modelling work. Thank you, Sara and Ajit for your involvement, time, and hard work. A special thank you goes to Dr Kalimuthu Palraj for helping me with the Table of Contents and List of Figures and List of Tables.

I also wish to formally acknowledge the Australian Government and the University of Queensland for the IPRS and UQ Centennial scholarships, respectively.

I'd also like to thank present and past members of the McGeary group: Dr Omid Khalili Arjomandi, Dr Faridoon, Victoria Bullin, Dr Hajar Pahmi, Yusralina Yussoff and Jed Burns. Thank you all so much for your company and friendship in the laboratory.

I'd also like to thank my bible study and church friends: Adrian Tan, Chris Ho, Jennifer Nyanda, Hotnida Sinaga, Yoshie Samosir, James Brennan, Jonathan Ting, Tim Sparks, Kareen Tuyau, Chunyu, Abby Soo, Zhao Bing, Tim Ang, Henry Zhang, Eugene Chong, Damien Boulton, Dan Smartt, Dan Chan, Peter Nixon, Haney, Maren, Ling Chen,

Nickie Wescott, the Weatherheads, the Bidaris, the McKenzies, the van Vuurens, the Lews, the Youngs, the Leisters, the Ungureanus, the Elfes, the Gentles, the Savages, the Cookes, the Becks, the Foos, the Lims, the Mpofofus, the Lews, the Lees and everyone else at FOCUS and St Lucia Bible Church. Thank you all for your love, support, encouragement and prayers.

I'd also like to express my deepest, sincere thanks to both my parents, Mr and Mrs Tan Hong Kiet for their unwavering love, support and prayers.

Last but not least, I'd like to acknowledge God almighty, my creator and the author of my life. This thesis is dedicated to Him.

“For the foolishness of God is wiser than man’s wisdom, and the weakness of God is stronger than man’s strength.” (1 Corinthians 1: 25, NIV)

Daniel Tan
The University of Queensland
Australia
31st July 2015

Keywords

β -lactam, antibiotic resistance, metallo- β -lactamase, inhibitor, computational modelling, structure-activity-relationship, pyrrole, thiazolidine.

Australian and New Zealand Standard Research Classifications (ANZSRC)

ANZSRC code: 030503, Organic Chemistry, 80%

ANZSRC code: 030499, Medicinal and Biomolecular Chemistry, 20%

Fields of Research (FoR) Classification

FoR code: 0305, Organic Chemistry, 80%

FoR code: 0304, Medicinal and Biomolecular Chemistry, 20%

Table of Contents

Description	Page
Abstract	II
Declaration by author	IV
Publications during candidature	V
Publications included in this thesis	V
Contributions by others to the thesis	VI
Statement of parts of the thesis submitted to qualify for the award of another degree	VI
Acknowledgements	VII
Keywords	IX
Australian and New Zealand Standard Research Classifications (ANZSRC)	IX
Fields of Research (FoR) Classification	IX
List of Figures	XV
List of Tables	XXVIII
List of Abbreviations and Definitions	XXXI
CHAPTER 1 INTRODUCTION AND LITERATURE REVIEW	1
1.0 General introduction	1
1.1 The origins of β -lactam antibiotics	2
1.2 β -Lactam antibiotics: chemical structure and classification	3
1.3 Bacterial cell wall biosynthesis	7
1.4 Mechanism of action of β -lactam antibiotics	10
1.5 Bacterial resistance against β -lactam antibiotics and the development of β -lactam antibiotics	11
1.6 An overview and classification of β -lactamases	16
1.7 Mechanism of the SBLs with class A β -lactamase as an example	18
1.8 Overcoming the action of SBLs: SBL inhibitors and combination therapy	20
1.9 Classification and structural features of metallo- β -	24

	lactamases (MBLs)	
1.10	The Proposed Catalytic Mechanism for MBLs	30
1.11	General classification of inhibitors and reported reversible inhibitors of MBLs	36
1.11a	Generic metal chelators	38
1.11b	Trifluoromethyl alcohol and ketone inhibitors	39
1.11c	Biphenyl tetrazole inhibitors	41
1.11d	Mercaptocarboxylate inhibitors	44
1.11e	Mercaptophosphonate inhibitors	47
1.11f	Dicarboxylic acid and other MBL inhibitors	50
1.11g	Pyrrole-containing inhibitors	56
1.12	Research aims	60
	References	61
CHAPTER 2	SYNTHESIS AND EVALUATION OF <i>N</i>-ACYLPYRROLE-3-CARBONITRILE DERIVATIVES AS IMP-1 INHIBITORS	67
2.1	General introduction	67
2.2	Research plan	68
2.3	Results and discussion	75
2.3a	Synthetic work – first series	75
2.3b	Enzymatic kinetic studies – first series	84
2.3c	Synthetic work – second series	88
2.3d	Enzymatic kinetic study – second series	95
2.4	Conclusion	101
2.5	Experimental	103
2.5a	General synthetic, spectroscopic and spectrometric experimental	103
2.5b	Preparation of 2-Amino-1-benzyl-4,5-diphenyl-1 <i>H</i> -pyrrole-3-carbonitrile (65)	103
2.5c	General procedure for the derivatisation of acyl chlorides ³³	104
2.5d	General procedure for the condensation of pyrrole 65 with acyl chlorides	104
2.5e	General procedure for the partial deacylation of <i>N,N</i> -	105

	diacyl imides to <i>N</i> -acyl amides ²³	
2.5f	Experimental data of synthesised compounds	105
2.5g	Expression and purification of IMP-1	118
2.5h	Preparation of CENTA (73)	118
2.5i	IMP-1 screening assay of the derivatives ^{4,15,19,35}	118
2.5j	IMP-1 K _i assay of the inhibitors ^{4,15,19,35}	119
2.5k	Imide stability test	121
2.5l	Computational modelling	121
	References	121
CHAPTER 3	THE SAR STUDY OF THE 3-CYANO, 4,5-DIPHENYL AND <i>N</i>-BENZYL SIDE CHAINS OF 2-AMINO-1-BENZYL-4,5-DIPHENYL-1<i>H</i>-PYRROLE-3-CARBONITRILE	115
3.1	General introduction	124
3.2	Research plan	124
3.3	Results and discussion	133
3.3a	Synthetic work	133
3.3b	Enzymatic kinetic study	155
3.4	Conclusion	160
3.5	Experimental	161
3.5a	General synthetic, spectroscopic and spectrometric experimental	161
3.5b	Preparation of 2-Amino-1-benzyl-4,5-diphenyl-1 <i>H</i> -pyrrole-3-carbonitrile (65)	161
3.5c	General procedure for the syntheses of 2-aminopyrrole-3-carbonitrile derivatives 108a,b , 117 and 112b-d ^{21,37}	162
3.5d	Experimental data of synthesised compounds	162
3.5e	Expression and purification of IMP-1	170
3.5f	Preparation of CENTA (73)	170
3.5g	IMP-1 screening assay of the derivatives ⁴¹⁻⁴⁴	170
3.5h	Computational modelling	170
	References	170
CHAPTER 4	OPTIMISATION OF (2<i>RS</i>, 4<i>R</i>)-3-(2-	174

	MERCAPTOACETYL)-2-PHENYLTHIAZOLIDINE-4-CARBOXYLIC ACID AS POTENT INHIBITORS OF IMP-1	
4.1	General introduction	174
4.2	Research plan	180
4.3	Results and discussion	182
4.3a	Enzymatic kinetic studies	182
4.3b	Computational modelling study	189
4.4	Conclusion	192
4.5	Experimental	192
4.5a	IMP-1 screening assay of the inhibitors	192
4.5b	IMP-1 K _i assay of the inhibitors	193
	References	194
CHAPTER 5	CONCLUSIONS AND FUTURE STUDIES	196
5.1	Conclusions	196
5.2	Future studies	203
	References	205
APPENDIX 1	THE EXPRESSION AND PURIFICATION OF IMP-1	206
	Expression of IMP-1 ^{1,2}	206
	Extraction of IMP-1 from the cell pellet ^{1,2}	206
	Purification of crude IMP-1 ^{1,2}	206
	Enzymatic kinetic assay ²	207
	Enzyme quantification ^{1,2}	207
	Results and discussion	207
	References	212
APPENDIX 2	PREPARATION OF CENTA	213
a	General synthetic, spectroscopic and spectrometric experimental	213
b	5-Mercapto-2-nitrobenzoic acid (74b) ¹	213
c	CENTA (73) ^{2,3}	214
	Determination of kinetic parameters of IMP-1 with CENTA as the substrate	214
	References	216
APPENDIX 3	COMPUTATIONAL MODELLING	217

Docking program	217
Docking template	217
Docking validation	217
Ligand preparation	219
MVD docking with 1JJT as the docking template	219
Glide docking	220
References	220

List of Figures

Figure	Description	Page
1.1	The antibacterial effect of penicillin G (1) produced by <i>Penicillium notatum</i> (white colony) on a bacterial culture of <i>Staphylococcus</i> spp. (horizontal streaks) is shown as a clear semi-circle zone surrounding the <i>Penicillium</i> fungus (reproduced with permission from Christine L. Case of Skyline College, 25/11/15).	2
1.2	The molecular structures of cephalosporin C (3) and thienamycin (4).	3
1.3	Comparison between the molecular structures of penicillin and carbapenem. R, R ₁ and R ₂ are various side chains.	4
1.4	The classification of β -lactam antibiotics. ¹⁴	5
1.5	The general structures and specific examples of the most commonly prescribed β -lactam antibiotic subclasses, ampicillin (5), faropenem (6), imipenem (7), cephazolin (8) and aztreonam (9). ²⁰ R, R ₁ and R ₂ are variable chemical moieties.	6
1.6	Cartoon diagrams of a cross section of the cell wall of Gram-positive (left) and Gram-negative (right) bacteria containing the peptidoglycan or murein sacculus (reproduced with permission from Sigma-Aldrich, 24/11/15).	7
1.7	The chemical structure of a segment of the glycan strand of the <i>Streptococcus pneumonia</i> murein sacculus and DAP (10) which is the L-lysine analogue in <i>Escherichia coli</i> . ²³	8
1.8	Transpeptidation of two glycan strands with transpeptidase catalysis. The green structure represents the first glycan strand which forms the covalent acyl-enzyme complex with the enzyme (E) and the red structure is the second glycan strand which deacylates	9

	the acyl-enzyme complex <i>via</i> an activated DAP amino group (adapted from Lee <i>et al.</i>). ²⁴	
1.9	The structural resemblance of penicillin G (1) (highlighted in blue) with the D-Ala-D-Ala terminus of a bacterial glycan strand. R' is the remaining pentapeptide stem (adapted from Vella). ¹⁸	10
1.10	The development of semi-synthetic penams from the naturally isolated 6-APA (11). ³³	13
1.11	Newer-generation cephalosporins with antibacterial activity against MRSA. ⁵	14
1.12	The synthetic development of cephalosporins from 7-ACA (18) (adapted from Walsh and Wencewicz). ³⁰	15
1.13	The clinical serine β -lactamase inhibitors 23 , 24 and 25 together with the generic metal ion chelator, EDTA (26) used in the identification of β -lactamases.	16
1.14	The proposed mechanism for the hydrolysis of a generic β -lactam by a class A SBL. The dashed lines represent hydrogen bonds and also ionic interaction (adapted from Drawz and Bonomo). ⁶	19
1.15	Comparison between the molecular structure of penicillin G (1) and clavulanic acid (23).	21
1.16	The proposed products (expressed in Daltons) of the different possible pathways of class A SBL enzyme inhibition by clavulanic acid (23) as empirically observed by mass spectrometry (adapted from Drawz and Bonomo). ⁶ ' Δ ' refers to the molecular weight of the enzyme.	23
1.17	The cartoon diagrams of 3D structures of representative MBLs. The Zn ²⁺ ions are shown as cyan spheres. (a) The IMP-1 B1 MBL with the flexible loop in orange (PDB no.: 1JJT). ⁵⁷ (b) The CphA B2 MBL with the elongated α 3 helix in green (PDB no.: 1X8G). ⁵⁵ (c) The L1 B3 MBL with the mobile loop in green (PDB no.: 2AIO). ⁵⁴ Figures were drawn with Maestro. ⁹⁶	28

1.18	The amino acid residues and water molecules chelating the Zn ²⁺ ions in the active sites of (a) the B1 CcrA MBL (PDB no.: 1ZNB) ⁵⁸ and (b) the B3 MBL AIM-1 (PDB no.: 4AWY). ⁶⁰ Zn ²⁺ ions and water molecules are represented as cyan and red spheres, respectively. Dashed lines represent co-ordination bonds. Atom colours: carbon in gray, nitrogen in blue, oxygen in red and sulfur in gold. Figures were drawn with Maestro. ⁹⁶	29
1.19	The active site of (a) the monozinc form of Sfh-1 (PDB no.: 3SD9) ⁵⁶ and (b) the di-zinc form of CphA (PDB no.: 3F90). ⁶¹ Both of the enzymes belong to the B2 subclass. Zn ²⁺ ions and water molecules are represented as cyan and red spheres, respectively. Dashed lines represent co-ordination bonds. Atom colours: carbon in gray, nitrogen in blue, oxygen in red and sulfur in gold. Figures were drawn with Maestro. ⁹⁶	31
1.20	The mechanism of di-zinc MBLs as proposed by Herzberg and Fitzgerald ⁴⁰ , as well as Page and Badarau. ³² R represents the <i>N</i> -acyl moiety of penicillin.	33
1.21	The mechanism of moxalactam (28) hydrolysis by the B3 L1 MBL as proposed by Spencer <i>et al.</i> ⁵⁴ R represents the <i>N</i> -acyl side chain of moxalactam (28). The attacking nucleophile is suggested to be a terminally positioned, Zn1- bound hydroxide ion.	34
1.22	The mechanism of ampicillin (5) hydrolysis by the B1 NDM-1 MBL as proposed by Zhang and Hao. ⁵¹ R represents the <i>N</i> -acyl side chain of ampicillin (5).	34
1.23	The proposed mechanism of mono-zinc CphA catalysed hydrolysis of carbapenem. The carbapenem substrate is highlighted in red and the zinc centre is in green. Rotation about the C5-C6 bond of intermediate (b) gives intermediate (c) and reforms the hydrolytic water molecule (figure adapted from Garau <i>et al.</i>). ⁵⁵	35
1.24	Generic metal chelators and small molecular weight thiol	38

	inhibitors of MBLs used in biochemical assays to identify MBL-producing bacteria (^a IC ₅₀ values were taken from Roll <i>et al.</i> ⁶⁷ and Chen <i>et al.</i> ⁶⁸ , while ^b K _i values were taken from Goto <i>et al.</i>). ⁷⁰	
1.25	An Etest® MBL testing strip on a <i>Serratia marcescens</i> expressing IMP-1 culture plate. IP and IPI denotes “solely imipenem” and “imipenem plus EDTA”, respectively. The numbers on the strip represent the varying concentration of imipenem in µg mL ⁻¹ and the quantity of EDTA in the IPI portion of the strip is set at a constant, final concentration of 320 µg mL ⁻¹ . The MIC* of imipenem against the particular strain of <i>S. marcescens</i> decreased from 16 to ≤ 1.0 µg mL ⁻¹ when exposed to 320 µg mL ⁻¹ of EDTA (reproduced with permission from American Society for Microbiology, 27/11/15). ⁷¹	39
1.26	A selection of trifluoromethyl alcohol and ketone inhibitors from Walter <i>et al.</i> ⁷³	40
1.27	The X-ray structure of biphenyl tetrazole 38h (ball and stick diagram) co-crystallised with a variant of the B1 CcrA MBL (atom-atom distance: N1-Zn2, 2.36 Å) (PDB no. 1A8T). ³⁸ Atom colours: carbon on inhibitor 38h and enzyme is green and grey, respectively; nitrogen in dark blue; oxygen in red, sulfur in gold and the L3 loop is in orange. The Zn centres are depicted as cyan spheres (figure drawn with Maestro). ⁹⁶	43
1.28	A selection of mercaptocarboxylate inhibitors, together with an α-ketothiol 44 reported in the literature.	44
1.29	Active site view from the crystal structure of (a) BlaB-D-captopril complex (atom-atom distance: S-Zn1, 2.32 Å; S-Zn2, 2.30 Å) (PDB no.: 1M2X) ⁸² ; (b) CphA-D-captopril complex (O2-Zn distance is 2.1 Å) (PDB no.: 2QDS). ⁶⁴ Atom colours: carbon on D-captopril (41) and enzyme in green and gray, respectively; nitrogen in blue; oxygen in red and sulfur in gold. The Zn ²⁺ ion(s) are shown as	46

	cyan spheres (figures drawn with Maestro). ⁹⁶	
1.30	Mercaptophosphonate inhibitors studied by Lassaux <i>et al.</i> ⁶³	48
1.31	: Active site view from the crystal structure of (a) CphA in complex with 47a (S-Zn distance is 2.31 Å) (PDB no.: 3IOF); ⁶³ (b) CphA in complex with 51 (atom-atom distance: O11-Zn, 1.98 Å; O12-Zn, 3.38 Å) (PDB no.: 3IOG). ⁶³ Atom colours: carbon on inhibitor and enzyme in light green and grey, respectively; chlorine in dark green; nitrogen in blue; oxygen in red; phosphorus in magenta and sulfur in gold. Water molecules and the Zn ²⁺ ion are shown as red and cyan spheres, respectively. Protein-ligand interactions are depicted as dashed lines (figures drawn with Maestro). ⁹⁶	49
1.32	Dicarboxylic acid inhibitors, 56a-c , 57 and 58 , as reported by Toney <i>et al.</i> ⁵⁷ and Olsen <i>et al.</i> ⁸⁵	51
1.33	Active site view of the crystal structure of 56a co-crystallised with IMP-1 (atom-atom distance: 2S carboxylate O-Zn1, 2.06 Å; 2S carboxylate O-Zn2, 2.13 Å; 3S carboxylate O-Zn2, 2.43 Å) (PDB no: 1JJT). ⁵⁷ Atom colours: carbon on inhibitor in gray, carbon on IMP-1 in grey, nitrogen in blue, oxygen in red and the L3 loop is in orange. The Zn ²⁺ ions are represented as gray spheres (figure drawn with Maestro). ⁹⁶	52
1.34	Active site view of the crystal structure of 59 co-crystallised with IMP-1 (atom-atom distance: S-Zn1, 2.24 Å; S-Zn2, 2.40 Å) (PDB no: 1DD6). ⁸¹ Atom colours: carbon on inhibitor in green, carbon on IMP-1 in grey, nitrogen in blue, oxygen in red and sulfur in gold. The Zn ²⁺ ions are represented as gray spheres (figure drawn with Maestro). ⁹⁶	53
1.35	The inhibitors, 60a-c , 61a-b and 62a-b , which were studied by Feng <i>et al.</i> ⁸⁶	55
1.36	A selection of potent, competitive pyrrole-type inhibitors,	56

	63-65 as discovered by the McGeary and Schenk group. ^{88,89}	
1.37	Surface view of the active site of pyrrole 65 docked into IMP-1. Atom colours: carbon on inhibitor in green, carbon on IMP-1 in white, nitrogen in blue and oxygen in red. The Zn ²⁺ ions are depicted as magenta spheres (reproduced with permission from John Wiley and Sons, license number 3756770325531, 26/11/15). ⁸⁹	57
1.38	The world-wide dissemination of genetically-acquired MBLs (reproduced with permission from Elsevier, license number 3756880120346, 27/11/15). ³⁹	60
2.1	The computational model of pyrrole 65 docked into IMP-1 as predicted by MVD. Atom colours: carbon on ligand in olive green, carbon on IMP-1 in grey, nitrogen in blue, oxygen in red and hydrogen in white. The Zn ²⁺ ions are shown as red spheres. The dashed, green lines represent hydrogen bonds.	70
2.2	The <i>in silico</i> models of (a) <i>N</i> -acetamide 77 , (b) <i>N</i> -benzamide 79 and (c) <i>N</i> -butyramide 84 derivatives of pyrrole 65 docked into IMP-1 as predicted by MVD. Atom colours: carbon on ligand in blue for 77 , dark grey for 79 and lime green for 84 , carbon on IMP-1 in grey, nitrogen in blue, oxygen in red and hydrogen in white. The Zn ²⁺ ions are shown as red spheres. The dashed, green lines represent hydrogen bonds.	73
2.3	The IR spectrum of 82 (neat sample). The broad peak at 3236.6 cm ⁻¹ could probably be due to the hydroxyl, O-H stretch from moisture in the sample.	80
2.4	The ¹ H NMR (400 MHz, CDCl ₃) spectrum of 82 .	81
2.5	The ¹³ C NMR spectrum of 82 (100 MHz, CDCl ₃). The residual solvent peak is a triplet, resonating at δ 77.0 ppm.	83
2.6	The HSQC (500 MHz, CDCl ₃) spectrum of 82 .	84
2.7	The ESI-MS spectrum of 82 (10 μM) after overnight	88

	incubation with IMP-1 (5 nM). The peaks at m/z 301.1, 360.3, 413.2, 685.3, 827.5 and 902.3 correspond to the solvent or background noise of the analysis and can be safely ignored.	
2.8	The ^1H NMR (400 MHz, CDCl_3) spectrum of 101 . The singlet at δ 1.56 and 2.05 ppm is due to traces of water and ethyl acetate, respectively. The integration for the multiplet from δ 7.85-7.87 is 1.9284 (2H).	92
2.9	The ^{13}C NMR spectrum of 101 (100 MHz, CDCl_3). The triplet at δ 77.0 ppm is due to CDCl_3 .	93
2.10	The DEPT 135 spectrum of 101 (100 MHz, CDCl_3). The negatively-phased signal is at δ 49.049 ppm.	94
2.11	The molecular structure of 101 , showing the 11 non-equivalent CH carbons, labeled from a to n and the <i>N</i> -benzylic carbon, marked with an asterisk.	94
2.12	The <i>in silico</i> model of 93 bound to the active site of IMP-1 as predicted by Glide. Atom colours: carbon on ligand in green, carbon on IMP-1 in orange, nitrogen in blue, oxygen in red, sulfur in yellow and hydrogen in white. The Zn^{2+} ions are shown as cyan spheres. ZN 251 and ZN 252 denotes Zn1 and Zn2, respectively. The dashed orange and green lines represent the hydrogen bond and ionic interactions, respectively.	99
2.13	The <i>in silico</i> model of 91 bound to the active site of IMP-1 as predicted by Glide. Atom colours: carbon on ligand in magenta, carbon on IMP-1 in orange, nitrogen in blue, oxygen in red, sulfur in yellow and hydrogen in white. The Zn^{2+} ions are shown as cyan spheres. ZN 251 and ZN 252 denotes Zn1 and Zn2, respectively. The dashed orange and green lines represent the hydrogen bond and π -cation interactions, respectively.	100
2.14	The <i>in silico</i> model of 99 bound to the active site of IMP-1 as predicted by Glide. Atom colours: carbon on ligand in purple, carbon on IMP-1 in orange, nitrogen in blue,	101

	oxygen in red, sulfur in yellow and hydrogen in white. The Zn ²⁺ ions are shown as cyan spheres. The dashed orange and green line represents the hydrogen bond and the π - π stacking interaction, respectively. The surface of the enzyme is coloured electrostatically, with the blue and red region corresponding to the positively and negatively charged region, respectively.	
2.15	The two most potent IMP-1 inhibitors, 93 and 99 for this class of inhibitors.	102
2.16	The K _i plot of inhibitor 78 against IMP-1 ($r^2 = 0.97$).	120
2.17	The K _i plot of inhibitor 96 against IMP-1 ($r^2 = 0.97$)	120
3.1	The lead compound 65 and the optimised potent IMP-1 inhibitors, 93 and 99 .	124
3.2	The MVD computational model of 105 docked into the active site of IMP-1. Atom colours: carbon on ligand in yellow, carbon on IMP-1 in grey, nitrogen in blue, oxygen in red and hydrogen in white. The Zn ²⁺ ions are shown as red spheres. The dashed, green lines represent hydrogen bonds.	126
3.3	The <i>in silico</i> model of 108a complexed with IMP-1, as predicted by MVD. Atom colours: carbon on ligand in olive green, carbon on IMP-1 in grey, nitrogen in blue, oxygen in red and hydrogen in white. The Zn ²⁺ ions are shown as red spheres.	128
3.4	The MVD computational model of 112a bound in the active site of IMP-1. Atom colours: carbon on ligand in yellow, carbon on IMP-1 in grey, nitrogen in blue, oxygen in red and hydrogen in white. The Zn ²⁺ ions are shown as red spheres. The dashed, green line represents a hydrogen bond (N-N distance 3.10 Å).	130
3.5	The <i>in silico</i> model of 112d complexed with IMP-1, as proposed by MVD. Atom colours: carbon on ligand in magenta, carbon on IMP-1 in grey, nitrogen in blue, oxygen in red and hydrogen in white. The Zn ²⁺ ions are	131

	shown as red spheres. The dashed, green lines represent hydrogen bonds.	
3.6	The ^{13}C NMR (100 MHz, CDCl_3) spectrum of carboxamide 104 . The triplet at δ 77.0 ppm is due to CDCl_3 . The peaks at δ 15.2 and δ 65.8 ppm are due to a diethyl ether impurity in the sample.	137
3.7	The IR spectrum of carboxamide 104 .	137
3.8	The ^1H NMR (400 MHz, CDCl_3) spectrum of tetrazole 105 . A triplet, singlet and quartet at δ 1.24 ppm, 2.02 ppm and 4.10 ppm, respectively is due to trace amounts of ethyl acetate in the sample. The broad singlet at δ 5.09 corresponds to the amino, NH_2 protons of 105 , which was expected to give an integration of two protons.	138
3.9	The ^{13}C NMR (100 MHz, CDCl_3) spectrum of tetrazole 105 . The triplet at δ 77.0 ppm is due to CDCl_3 .	139
3.10	The ^{13}C NMR (100 MHz, CDCl_3) spectrum of 108a . The residual solvent peak is a triplet at δ 77.0.	141
3.11	The ^1H NMR (400 MHz, CDCl_3) spectrum of 108a .	142
3.12	The 5J homoallylic coupling between the protons of the two vicinal methyl groups of 108a .	142
3.13	The ^1H NMR (400 MHz, CDCl_3) spectrum of 117 . A singlet at δ 2.34 ppm and an excess of five protons in the aromatic region of δ 7.11-7.29 are due to a toluene impurity in the sample.	146
3.14	The ^{13}C NMR (100 MHz, CDCl_3) spectrum of 117 . ^{13}C signal at δ 21.4, 125.3, 128.2, 129.0 and 137.8 ppm are due to a toluene impurity in the sample, and the triplet at δ 77.0 ppm is due to CDCl_3 .	146
3.15	The ^1H NMR (400 MHz, $\text{DMSO}-d_6$) spectrum of 109 . A quintet at δ 2.49 is due to $\text{DMSO}-d_6$. An intense singlet at δ 3.35 ppm is due to water in the sample.	148
3.16	The ^{13}C NMR (100 MHz, $\text{DMSO}-d_6$) spectrum of 109 . A septet at 39.5 ppm is due to $\text{DMSO}-d_6$.	149

3.17	The IR spectrum of 109 (neat sample).	149
3.18	The negative mode HRMS spectrum of 109 .	150
3.19	The IR spectrum of pyrrole 112a (neat sample).	153
3.20	The IR spectrum of α -aminoketone 111a (neat sample).	153
3.21	The ^1H NMR spectrum (400 MHz, CDCl_3) of 112b . The protons of the <i>N</i> -phenethyl side chain of 112b (NCH_2CH_2) are shown to resonate as a pair of two-proton triplets at δ 2.72 and 3.90 ppm.	154
3.22	The ^{13}C NMR spectrum (100 MHz, CDCl_3) of 112b . The 3-carbonitrile carbon ($\text{C}\equiv\text{N}$) and the two carbon atoms of the <i>N</i> -phenethyl side chain of 112b (NCH_2CH_2) are shown to resonate at δ 117.7, 45.0 and 36.2 ppm, respectively. The triplet at δ 77.0 is due to CDCl_3 .	155
3.23	The Glide computational model of 105 complexed with IMP-1. Atom colours: carbon on ligand in green, carbon on IMP-1 in orange, nitrogen in blue, oxygen in red and hydrogen in white. The Zn^{2+} ions are shown as turquoise spheres, with Zn251 and Zn252 denoting Zn1 and Zn2, respectively. The dashed, orange, green and blue lines represent hydrogen bond, π -cation and π - π stacking interactions, respectively.	157
3.24	The Glide <i>in silico</i> model of 117 bound in the active site of IMP-1. Atom colours: carbon on ligand in green, carbon on IMP-1 in orange, nitrogen in blue, oxygen in red and hydrogen in white. The Zn^{2+} ions are shown as turquoise spheres, with Zn251 and Zn252 denoting Zn1 and Zn2, respectively.	158
4.1	The potent mercaptocarboxylate-type IMP-1 inhibitors, 59 and 119 , (left) which structurally resemble penicillins 1 and 5 (right). ²⁻⁴ Part of the structure of 59 which is similar to penicillin G (1) is highlighted in blue, whereas 119 has an open mercapto chain <i>in lieu</i> of a β -lactam ring.	174
4.2	The active site view of the crystal structure of 59 bound	175

	with IMP-1 (PDB No.: 1DD6). ² Atom colours: carbon on inhibitor in yellow, carbon on IMP-1 in grey, nitrogen in blue, oxygen in red and sulfur in gold. The red spheres represent the Zn ²⁺ ions and the green dotted lines represent ionic and hydrogen bonds (figure drawn with MVD). ¹⁷	
4.3	Reported MBL inhibitors, 60b and 120a bearing the thiazolidine ring, which is highlighted in blue.	176
4.4	The active site view of the <i>in silico</i> model of 2S, 4R- 120a bound with IMP-1, as predicted by Glide. Atom colours: carbon on ligand in green, carbon on IMP-1 in light blue, hydrogen in white, nitrogen in navy blue, oxygen in purple and sulfur in yellow. The zinc ions are represented as cyan spheres. The purple dotted lines represent ionic interactions between the ligand and zinc ions.	177
4.5	The active site view of the computational model of 2S, 4R- 124a in complex with IMP-1, as predicted by Glide. Atom colours: carbon on ligand in green, carbon on IMP-1 in light blue, hydrogen in white, nitrogen in navy blue, oxygen in purple and sulfur in yellow. The zinc ions are represented as cyan spheres. The dotted purple and green lines represent ionic and hydrogen bond interactions, respectively.	179
4.6	The active site view of the <i>in silico</i> model of 2R, 4R- 124a bound with IMP-1, as predicted by Glide. Atom colours: carbon on ligand in green, carbon on IMP-1 in light blue, hydrogen in white, nitrogen in navy blue, oxygen in purple and sulfur in yellow. The zinc ions are represented as cyan spheres. The dotted purple and green lines represent ionic and hydrogen bond interactions, respectively.	180
4.7	The various mercapto-amide-linked thiazolidines 124a-o , which were synthesised by Dr Sara Mustaddiq. ⁹	181

4.8	The K_i plot of thiazolidine 124f ($r^2 = 0.98$).	193
5.1	The first series of <i>N</i> -substituted derivatives of pyrrole 65 .	198
5.2	The second series of <i>N</i> -substituted derivatives of pyrrole 65 .	199
5.3	The two most potent <i>N</i> -arylamide derivatives of pyrrole 65 .	200
5.4	The synthetic derivatives which were used in the SAR study of the 3-cyano group, vicinal 4,5-diphenyl and <i>N</i> -benzyl side chains of pyrrole 65 .	200
5.5	The mercapto-amide-linked thiazolidines 124a-o , which were studied.	202
5.6	Suggestions for the future SAR study of pyrrole 65 .	204
5.7	Suggested examples for the future SAR study of thiazolidines	204
A.1.1	The chromatogram of the elution profile of IMP-1 from the SP-sepharose column, eluted with HEPES A over a gradient of 0–1.0 M NaCl, pH 7.0 at a flow rate of 4.0 ml min ⁻¹ .	208
A.1.2	The chromatogram of the elution profile of IMP-1 from the S-200 column, eluted with HEPES A, pH 7.0 at a flow rate of 0.5 ml min ⁻¹ .	210
A.1.3	The SDS-PAGE of purified IMP-1, stained with Bio-Safe Coomassie G-250. The band from two enzyme samples (in the black box) corresponds to 25kDa of the marker protein on the left.	211
A.2.1	The kinetic profile of IMP-1 (5 nM) with CENTA as the substrate at pH 7.0, 25 °C. The plot is typical of that of an enzyme obeying the Michaelis-Menten relationship.	215
A.3.1	The docking pose of 56a superimposed over the original position of the co-crystallised ligand in the 1JJT crystal structure, with the use of MVD as the docking program. The docked pose is in yellow, whereas the original co-crystallised ligand is in grey. Atom colours on amino acid residues: carbon in grey, hydrogen in white, nitrogen in	218

	blue, oxygen in red and sulfur in gold. The zinc ions are represented as red spheres.	
A.3.2	The docking pose of 56a superimposed over the original position of the co-crystallised ligand in the 1JJT crystal structure, with the use of Glide XP as the docking program. The docked pose is in green, whereas the original co-crystallised ligand is in orange. Atom colours on amino acid residues: carbon in teal, hydrogen in white, nitrogen in blue, oxygen in burgundy and sulfur in gold. The zinc ions are represented as cyan spheres.	219

List of Tables

Table	Description	Page
1.1	Classification of β -lactamases according to the Ambler and Bush-Jacoby schemes. ^{6,37}	17
1.2	Comparison between the catalytic mechanism of PBPs and SBLs in terms of substrate, the attacking nucleophile, acyl acceptor and reaction product.	20
1.3	Classification of MBLs based on substrate profile, amino acid residues chelating the Zn^{2+} ions and Zn^{2+} ion requirement for catalysis (adapted from Gupta, ⁴¹ Herzberg and Fitzgerald ⁴⁰).	25
1.4	Kinetic constants of representative MBLs in the hydrolytic reaction of common β -lactams.	26
1.5	Notable interatomic distances of Zn1, Zn2, the bridging hydroxide (W1) and the apical water (W2) in a selection of native, wild-type B1 and B3 MBLs.	30
1.6	Classification of reversible inhibitors on the basis of its kinetic effect and implication on enzyme inhibition.	37
1.7	The competitive inhibition constants, K_{ic} (μ M) of the trifluoromethyl alcohol and ketone inhibitors, 33-36 against the tested B1, B2 and B3 MBLs. ⁷³	40
1.8	The IC_{50} (μ M) data of a series of biphenyl tetrazoles, 38a-m against a variant of the B1 CcrA MBL. ³⁸	41
1.9	Collated inhibition data of the mercaptocarboxylate inhibitors, 40-43 and 45a-c , including α -ketothiol 44 against the tested B1, B2 and B3 MBLs. ^{64,75,77-80}	45
1.10	The K_{ic} data (μ M) of mercaptophosphonate inhibitors, 46a-55 against MBLs. ⁶³	48
1.11	The IC_{50} data (μ M) of dicarboxylic acid inhibitors, 56a-c , 57 and 58 against the B1 and B3 MBLs tested. ^{57,85}	52
1.12	The K_i data (μ M) of inhibitors, 60a-c , 61a-b and 62a-b , against the B1, B2 and B3 MBLs tested juxtaposed with the MIC data (μ gml ⁻¹) of the β -lactam in the	55

	inhibitor-antibiotic combinations against MBL- plasmid borne <i>E. coli</i> strains. ⁸⁶	
1.13	A list of MBLs from sub-classes B1, B2 and B3, covered in this chapter. ^{16,39}	58
2.1	Characteristic ¹³ C NMR peaks of known compounds 89a and b . ²⁶	82
2.2	The percentage inhibition of the first series of pyrrole derivatives (10 μM) against IMP-1 (5 nM, containing BSA at a final conc. of 20 μg mL ^{-1a}) at pH 7.0 and 25 °C, with CENTA (70 μM) as the substrate.	85
2.3	The competitive (K _{ic}) and uncompetitive (K _{iuc}) inhibition constants (μM) of inhibitors 78 and 79 against IMP-1 (5 nM, containing BSA at a final conc. of 20 μg mL ⁻¹) at pH 7.0 and 25 °C, with CENTA (5-70 μM) as the substrate.	86
2.4	The percentage inhibition of the second series of pyrrole derivatives (10 μM) against IMP-1 (5 nM, containing BSA at a final conc. of 20 μg mL ⁻¹) at pH 7.0 and 25 °C, with CENTA (70 μM) as the substrate.	95
2.5	The competitive (K _{ic}) and uncompetitive (K _{iuc}) inhibition constants (μM) of inhibitors 65 , 91 , 93 , 96 and 99 against IMP-1 (5 nM, containing BSA at a final conc. of 20 μg mL ⁻¹) at pH 7.0 and 25 °C, with CENTA (5-70 μM) as the substrate.	97
3.1	Notable atom-atom interactions and distances between ligand 105 and the active site of IMP-1, as predicted by MVD.	126
3.2	The MolDock scores (kcal mol ⁻¹) of pyrroles 65 , 104 , 105 , 108a , 108b , 109 and 112a-d bound with IMP-1, as predicted by MVD.	132
3.3	The percentage inhibition of pyrrole derivatives 104 , 105 , 108a , b , 109 and 117 against IMP-1 (10 nM, containing BSA at a final conc. of 20 μg mL ⁻¹), at pH 7.0 and 25 °C, with CENTA (20 μM) as the substrate.	156

3.4	The percentage inhibition of pyrrole derivatives 112a-d and 65 against IMP-1 (0.1 nM, containing BSA at a final conc. of 20 $\mu\text{g mL}^{-1}$), at pH 7.0 and 25 °C, with CENTA (70 μM) as the substrate.	159
4.1	The percentage inhibition of thiazolidine derivatives 124a-o screened against IMP-1 (5 nM, containing BSA at a final conc. of 20 $\mu\text{g mL}^{-1}$) at pH 7.0 and 25 °C, with penicillin G (1 mM) as the substrate.	183
4.2	The competitive (K_{ic}) and uncompetitive (K_{iuc}) inhibition constants (μM) of selected thiazolidine derivatives against IMP-1 (10 nM, containing BSA at a final conc. of 20 $\mu\text{g mL}^{-1}$) at pH 7.0 and 25 °C, with varying concentrations of the penicillin G substrate (0.4-1.2 mM).	187
4.3	The IC_{50} (μM) data of <i>N</i> -arylsulfonyl hydrazones 127-130, a-c against IMP-1 (4 nM, with a final BSA conc. of 1 $\mu\text{g mL}^{-1}$), with nitrocefin (20 μM) as the substrate at pH 7.3, and 30 °C. ¹³	189
4.4	The GlideScore values (kcal mol^{-1}) and binding affinities (μM) of selected thiazolidine derivatives, including 120a and the original co-crystallised ligand, 59 for comparison.	190
A.1.1	The IMP-1 enzyme activity ($\mu\text{mol min}^{-1}$) of fractions eluted from the SP-sepharose column with penicillin G (500 μM) as the substrate, at pH 7.0, 25 °C.	209
A.1.2	The IMP-1 specific activity ($\mu\text{mol min}^{-1}$), enzyme amount (mg), and turnover number, k_{cat} (s^{-1}) of fractions eluted from the S-200 column, with penicillin G (500 μM) as the substrate, at pH 7.0, 25 °C.	211
A.2.1	The experimental and literature kinetic parameters of IMP-1 with CENTA as the substrate.	216

List of abbreviations and Definitions

7-ACA	7-Aminocephalosporinic acid
6-APA	6-Aminopenicillanic acid
1D	One-dimensional
2D	Two-dimensional
3D	Three-dimensional
ACE	Angiotensin-converting enzyme
AEST	Australian Eastern Standard Time
AIM-1	Adelaide imipenemase 1
Ala	Alanine
Arg	Arginine
Asn	Asparagine
Asp	Aspartic acid
BBL	Class B β -lactamases
BcII	<i>Bacillus cereus</i> type II
BlaB	β -Lactamase class B
b.p.	Boiling point
br	broad
BSA	Bovine serum albumin
CcrA	Cefoxitin and carbapenem resistant
CDCl ₃	Deuterated chloroform
CENTA	(6 <i>R</i> ,7 <i>R</i>)-3-[(3-carboxy-4-nitrophenyl)sulfanylmethyl]-8-oxo-7-[(2-thiophen-2-ylacetyl)amino]-5-thia-1-azabicyclo[4.2.0]oct-2-ene-2-carboxylic acid
CHCl ₃	Chloroform
Conc.	Concentration
CphA	Carbapenem hydrolysing enzyme (from <i>Aeromonas hydrophila</i>)
Cys	Cysteine
d	doublet
DAP	<i>meso</i> -2,6-Diaminopimelic acid
dd	doublet of doublets
DEPT	Distortionless enhancement by polarisation transfer
DHP-1	Dehydropeptidase-1

DIPEA	<i>N,N</i> -Diisopropylethylamine
DTNB	5,5'-Dithiobis-(2-nitrobenzoic acid)
<i>E. coli</i>	<i>Escherichia coli</i>
EDTA	Ethylenediaminetetraacetic acid
eq.	equivalent
ESBL	Extended-spectrum β -lactamase
ESI-MS	Electrospray ionisation mass spectrometry
EtOAc	Ethyl acetate
EtOH	Ethanol
FEZ-1	<i>Legionella gormanii</i> endogenous zinc β -lactamase 1
FPLC	Fast protein liquid chromatography
Gln	Glutamine
Glu	Glutamic acid
h	hour(s)
HCl	Hydrochloric acid
HEPES	4-(2-Hydroxyethyl)-1-piperazineethanesulfonic acid
His	Histidine
HMBC	Heteronuclear multiple-quantum correlation
HMG-CoA	3-Hydroxy-3-methyl-glutaryl-coenzyme A
HRMS	High resolution mass spectrometry
HSQC	Heteronuclear single quantum correlation
Hz	Hertz
I	Inhibitor
IC ₅₀	The half-maximal inhibitory concentration
ImiS	Imipenemase (from <i>Aeromonas veronii</i> <i>bv. sobria</i>)
IMP-1	Imipenemase 1
IPTG	Isopropyl- β -D-1-thiogalactopyranoside
IR	Infrared
<i>J</i>	Coupling constant
k_{cat}	Turnover number
K_i	Inhibition constant
K_{ic}	Competitive inhibition constant
K_{iuc}	Uncompetitive inhibition constant
K_m	Michaelis constant
L1	Labile enzyme (from <i>Stenotrophomonas maltophilia</i>)

λ_{\max}	The wave length at maximum peak absorption for UV-Visible spectra
LB	Luria Bertani (a type of broth)
LCMS	Liquid chromatography-mass spectrometry
Lit.	Literature
Lys	Lysine
m	multiplet
<i>m</i>	meta
MBL	Metallo- β -lactamase
MeOH	Methanol
MES	2-(<i>N</i> -Morpholino)ethanesulfonic acid
MIC	Minimum inhibitory concentration
Milli-Q water	Ultrapure water of Type 1
min(s)	minute(s)
m.p.	Melting point
MRSA	Methicillin-resistant <i>Staphylococcus aureus</i>
MVD	Molegro Virtual Docker
MW	Molecular weight
NAG	<i>N</i> -acetylglucosamine
NAM	<i>N</i> -acetylmuramic acid
NDM-1	New Delhi metallo- β -lactamase 1
NMR	Nuclear magnetic resonance
OD ₆₀₀	Optical density at 600 nm
OMP	Outer membrane protein
P	Product
<i>p</i>	para
PBP	Penicillin binding protein
PDB	Protein data bank
PE	Petroleum ether
PFK	Perfluorokerosene
Ph	Phenyl ring
Phe	Phenylalanine
Py	Pyridine
QM/MM	Quantum meachanics/molecular mechanics
quin	quintet

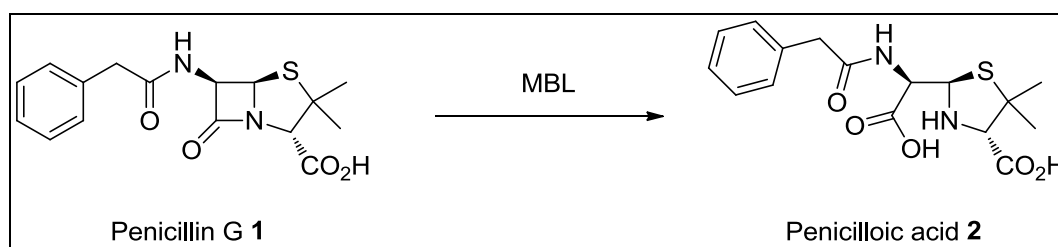
r^2	Coefficient of determination
R_f	Retention factor
RMSD	Root-mean-square deviation
rt	room temperature
s	singlet
S	Substrate
SAR	Structure-activity relationship
SBL	Serine β -lactamase
SDS-PAGE	Sodium dodecyl sulfate polyacrylamide gel electrophoresis
Ser	Serine
t	triplet
TCA	Trichloroacetic acid
TEA	Triethylamine
TEM-1	Temoneira 1(A β -lactamase isolated from a patient)
Thr	Threonine
TLC	Thin layer chromatography
TMS	Trimethylsilyl
Trp	Tryptophan
tt	triplet of triplets
UV	Ultraviolet
Val	Valine
VIM-4	Verona integron-encoded metallo- β -lactamase 4
ν_{max}	The wavenumber at maximum peak absorption for IR spectra
V_{max}	Limiting velocity

CHAPTER 1: INTRODUCTION AND LITERATURE REVIEW

1.0 General introduction

Metalloenzymes are biologically important enzymes which depend on metal ions (typically transition metal ions) as cofactors to facilitate catalytic activities.^{1,2} They make up about a third of the known enzymes.^{1,2} These enzymes are crucial for the existence and survival of organisms as they catalyse a vast array of physiological processes such as DNA, prostaglandin and collagen biosyntheses, steroid and neurotransmitter metabolism and the destruction of superoxide and hydrogen peroxide.^{1,2}

However, not all metalloenzymes are beneficial to human beings. Some of them even pose a serious health threat to humans. One such example is the group of zinc-dependent metallo- β -lactamases (MBLs) which degrade a plethora of β -lactam antibiotics (such as penicillins), a chemical class that selectively disrupt a key biochemical step essential to bacterial survival (bactericidal effect), without displaying any adverse effects on the eukaryotic host organism (Scheme 1).³⁻⁵

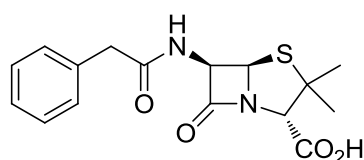


Scheme 1.1: The degradation reaction of penicillin G (1) by a metallo- β -lactamase (MBL). The product of the reaction is penicilloic acid (2) which has no antibacterial activity.

As previously mentioned, β -lactamases hydrolytically inactivate the β -lactam antibiotics.⁶ Due to unregulated, over-prescription of β -lactam antibiotics globally and the rapid transfer of β -lactamase-expressing genes among related and unrelated bacterial species *via* mobile genetic elements, the issue of antibiotic resistance is now a global concern.⁷ Thus far, there are no clinically available inhibitors for the chemotherapeutic treatment of MBL-mediated antibiotic resistance.²

1.1 The origins of β -lactam antibiotics

In 1928 Alexander Fleming first observed the antibacterial activity of the first chemotherapeutic β -lactam antibiotic, penicillin G (**1**), produced by the fungus *Penicillium notatum* on a bacterial culture contaminated with the fungus (Figure 1.1).⁸ It would take another 17 years for the structure of penicillin G (**1**) to be finally determined by X-ray crystallography.⁸ Within that time, mass-production of penicillin G (**1**) was being developed and made possible by fermentation technology.^{8,9}



Penicillin G **1**



Figure 1.1: The antibacterial effect of penicillin G (**1**) produced by *Penicillium notatum* (white colony) on a bacterial culture of *Staphylococcus* spp. (horizontal streaks) is shown as a clear semi-circle zone surrounding the *Penicillium* fungus (reproduced with permission from Christine L. Case of Skyline College, 25/11/15).

The seminal discovery by Fleming in 1928 would later pave the way for the discovery of other structurally diverse β -lactams from natural sources.^{8,10-12} The antibacterial activity of another notable β -lactam, cephalosporin C (**3**), which has its origin in the *Cephalosporium acremonium* fungus, was first observed in 1945 by Giuseppe Brotzu (Figure 1.2).^{8,10} And in 1976 yet another structurally distinctive β -lactam, thienamycin (**4**) was isolated from the non-pathogenic soil bacterium *Streptomyces cattleya* (Figure 1.2).^{11,12} Thienamycin (**4**) would subsequently become the precursor for all clinically prescribed carbapenems, which is the most potent and versatile β -lactam subclass until the emergence of carbapenem degrading enzymes, or carbapenemases.¹¹

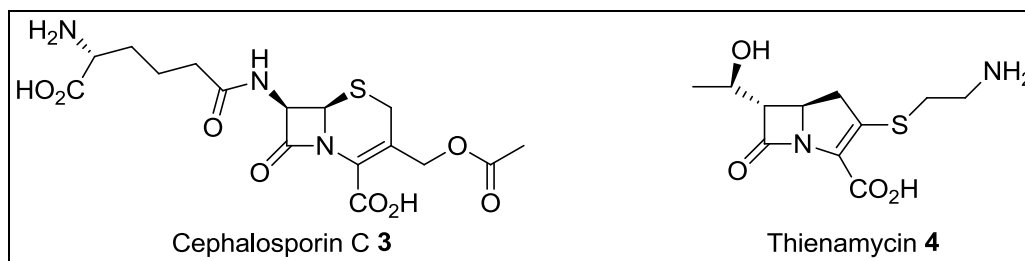
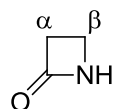


Figure 1.2: The molecular structures of cephalosporin C (**3**) and thienamycin (**4**).

1.2 β -Lactam antibiotics: chemical structure and classification

β -Lactam antibiotics function by interrupting bacterial cell wall biosynthesis.⁴ The four-membered β -lactam ring (**5**) is part of the pharmacophore or molecular features (both steric and electronic) which is crucial for the observed antibacterial activity of these drugs.^{4,13} A detailed description of the mode of mechanism of β -lactams is presented in the later part of this chapter (Section 1.4).



β -Lactam **5**

β -Lactam antibiotics can be classified into various sub-classes according to the following features:

- The absence or presence of a secondary ring fused to the β -lactam ring;
- The identity of the fused ring (if there is one) *i.e.* the type of atom occupying position 1 of the fused ring, the size of the fused ring and the absence or presence of a double bond in the fused ring (Figure 1.4).¹⁴

Currently the most extensively prescribed sub-classes of β -lactam antibiotics include the bicyclic penams (penicillins), penems, carbapenems and cepems (cephalosporins). In addition, the monocyclic monobactams are also clinically administered, but to a lesser extent (Figure 1.5).¹⁵

The only clinically administered monobactam is aztreonam (**9**).^{14,15} It has a unique sulfonic acid functional group directly attached to its β -lactam nitrogen.¹⁶ Aztreonam (**9**), however, exhibits a narrow-spectrum antibacterial activity and is specifically employed for the treatment of nosocomial infections (hospital-acquired infections) such as urinary and respiratory tract infections implicated with pathogenic Gram-negative bacteria.^{14,15,17}

All three penams, penems, and cepheids contain a sulfur atom at the 1-position while the carbapenems contain a carbon at the same position. Another structural distinction within the bicyclic β -lactams is the absence or presence of a double bond in the fused ring, with the former having an 'am' suffix in the name and the remaining β -lactams having an 'em' suffix in the name.¹⁸ Penems and carbapenems both contain a double bond at the C-2 and C-3 position of the fused ring. As for the 4:6 bicyclic cepheids, the double bond is located at the C-3 and C-4 position of the fused ring.

In addition, carbapenems have some unique structural characteristics which are not present in penams and cepheids (Figure 1.3).¹¹ Firstly, the spatial arrangement of the C-5 and C-6 hydrogen atoms are in the *trans* configuration and secondly, there is the presence of a hydroxyethyl side group at C-6.¹¹ These unusual structural features are essential for the observed antibacterial potency of carbapenems and are also found in penems, which are purely synthetic in origin.¹⁹ The idea behind the synthesis of faropenem (**6**) was first proposed by Robert Woodard as a hybrid between penams and cepheids.¹⁹

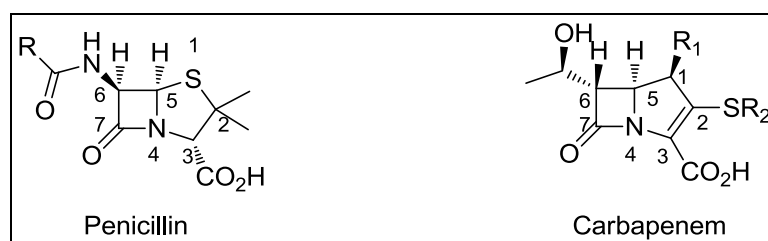


Figure 1.3: Comparison between the molecular structures of penicillin and carbapenem. R, R₁ and R₂ are various side chains.

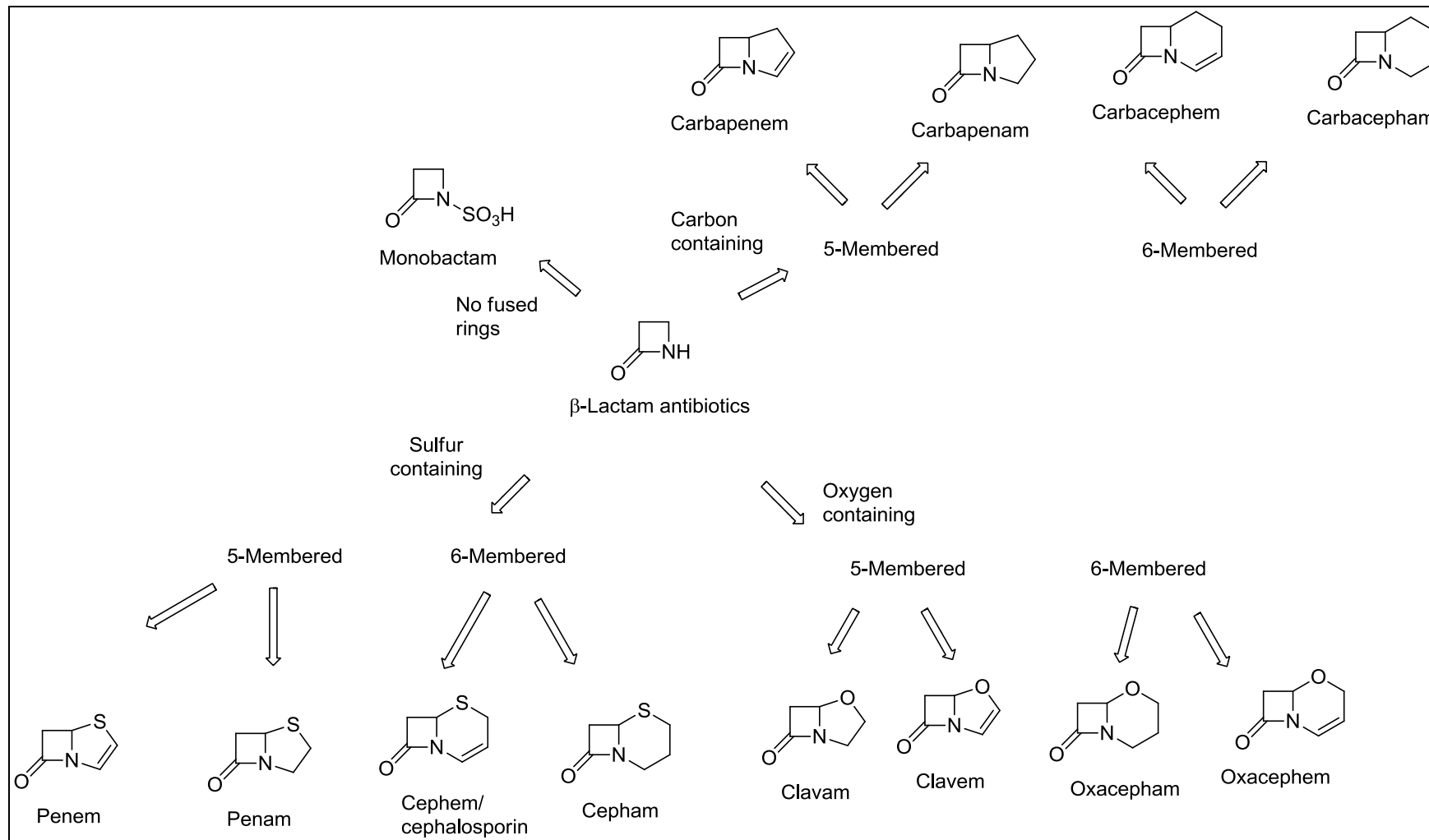


Figure 1.4 The classification of β-lactam antibiotics.¹⁴

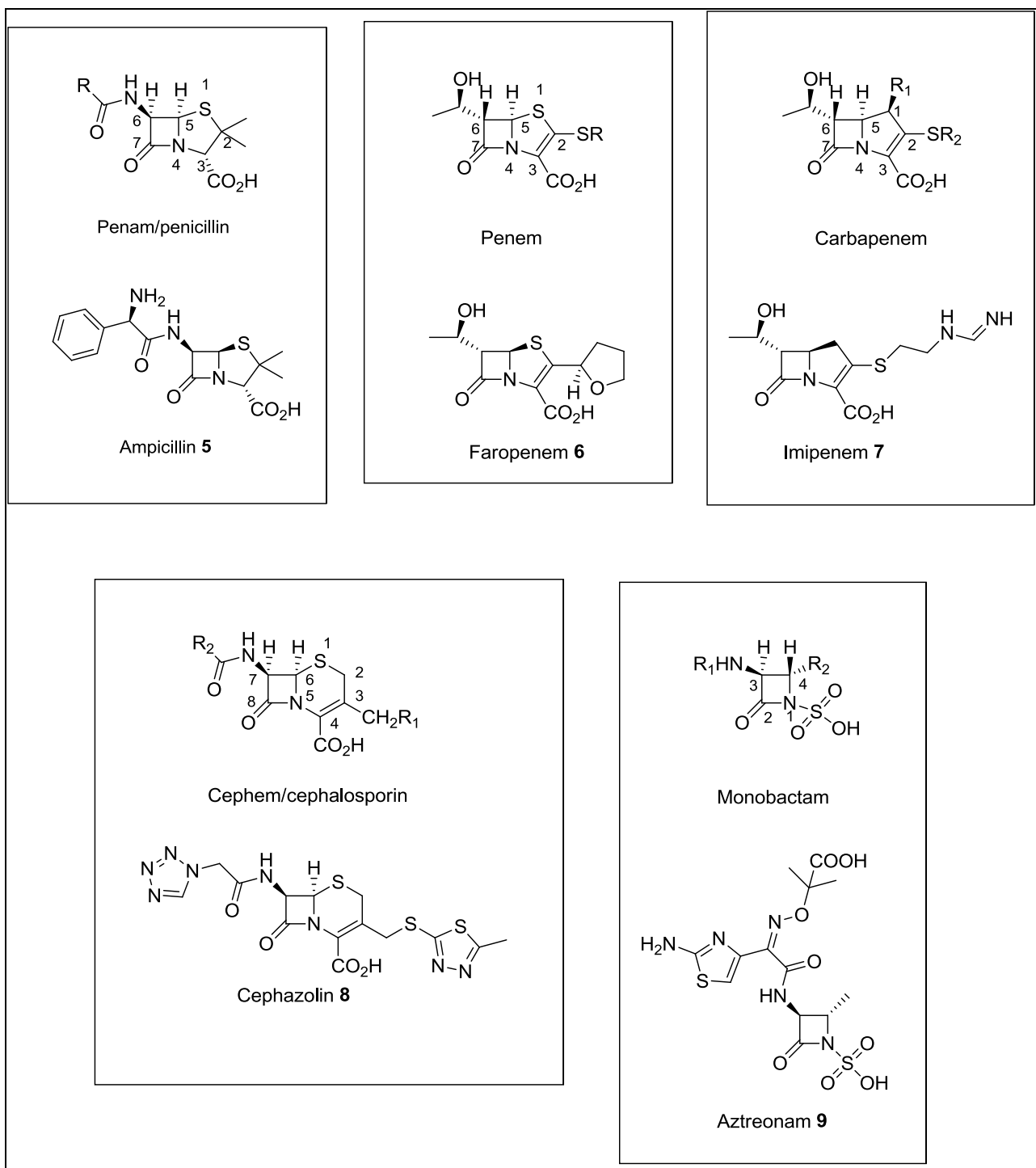


Figure 1.5: The general structures and specific examples of the most commonly prescribed β -lactam antibiotic sub-classes, ampicillin (**5**), faropenem (**6**), imipenem (**7**), cephazolin (**8**) and aztreonam (**9**).²⁰ R, R₁ and R₂ are variable chemical moieties.

1.3 Bacterial cell wall biosynthesis

The bacterial cell wall is not only rigid for structural maintenance, but also permeable to essential nutrients.^{4,21,22} The main structural backbone of the bacterial cell wall is a three-dimensional network of glycan strands cross-linked *via* peptide bonds.^{4,21-23} This structural composite is thus known as the peptidoglycan or 'murein sacculus'.^{4,21,22}

Bacteria can be classified into two separate classes: Gram-positive and Gram-negative bacteria, based on their affinity towards the Gram stain. Gram-positive bacteria have a much thicker murein sacculus (15-80 nm) than Gram-negative bacteria (2 nm) (Figure 1.6).²¹ Another distinction between Gram-positive and Gram-negative is the presence of an outer lipid membrane in the latter which is absent in the former. This unique outer membrane consists of porins and lipopolysaccharides.²¹ More details about porins will be discussed in Section 1.5.

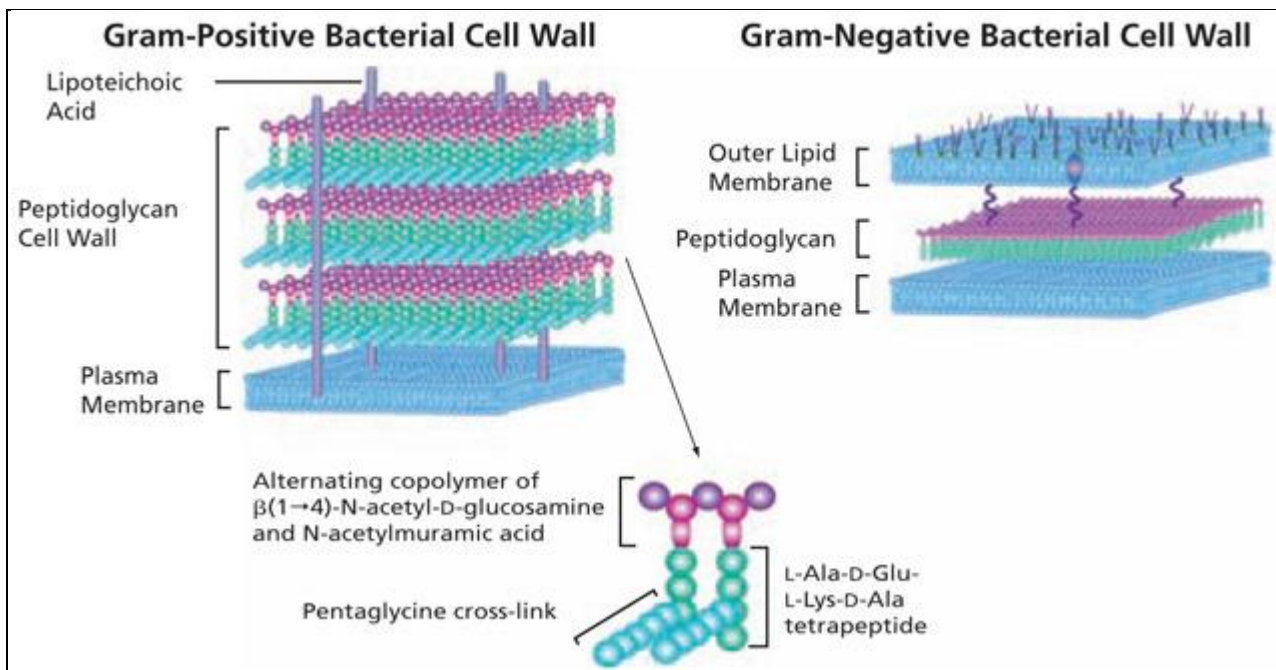


Figure 1.6: Cartoon diagrams of a cross section of the cell wall of Gram-positive (left) and Gram-negative (right) bacteria containing the peptidoglycan or murein sacculus (reproduced with permission from Sigma-Aldrich, 24/11/15).

Each glycan strand of the peptidoglycan structure consists of alternating *N*-acetylmuramic acid (NAM) and *N*-acetylglucosamine (NAG) units, with the former having a

pentapeptide stem (Figure 1.7).²¹⁻²³ The common pentapeptide motive is [L-Ala-D-γ-Glu-X-D-Ala-D-Ala], with X being L-lysine or *meso*-2,6-diaminopimelic acid, DAP (**10**) for *Streptococcus pneumonia* (Gram-positive bacteria) and *Escherichia coli* (Gram-negative bacteria), respectively.^{22,23} The amino group of the third residue, X is the attacking nucleophile for the peptidic cross-linking (Figure 1.8).

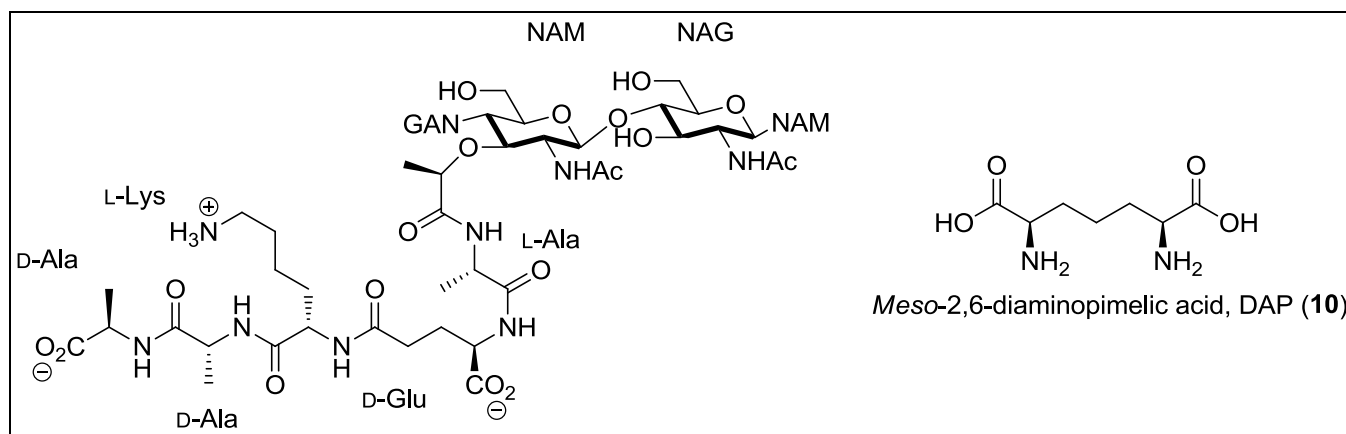


Figure 1.7: The chemical structure of a segment of the glycan strand of the *Streptococcus pneumonia* murein sacculus and DAP (**10**) which is the L-lysine analogue in *Escherichia coli*.²³

The final process in bacterial cell wall biosynthesis is the cross-linking of the glycan strands.^{22,24} This process is known as transpeptidation and is catalysed by the transpeptidase enzyme. Transpeptidation begins with an acylation step followed by a deacylation step. Initially, the D-Ala-D-Ala terminus of a glycan strand is acylated by an activated, nucleophilic serine residue to form an acyl-enzyme covalent complex and an expelled D-alanine unit.^{22,24} The acyl-enzyme complex is subsequently deacylated by an activated L-lysine or DAP amino group belonging to a second glycan strand, to form the cross-linked peptidoglycan strand and regenerated transpeptidase (Figure 1.8).^{22,24} It is this final, crucial process that is inhibited by β -lactam antibiotics.^{4,22,24}

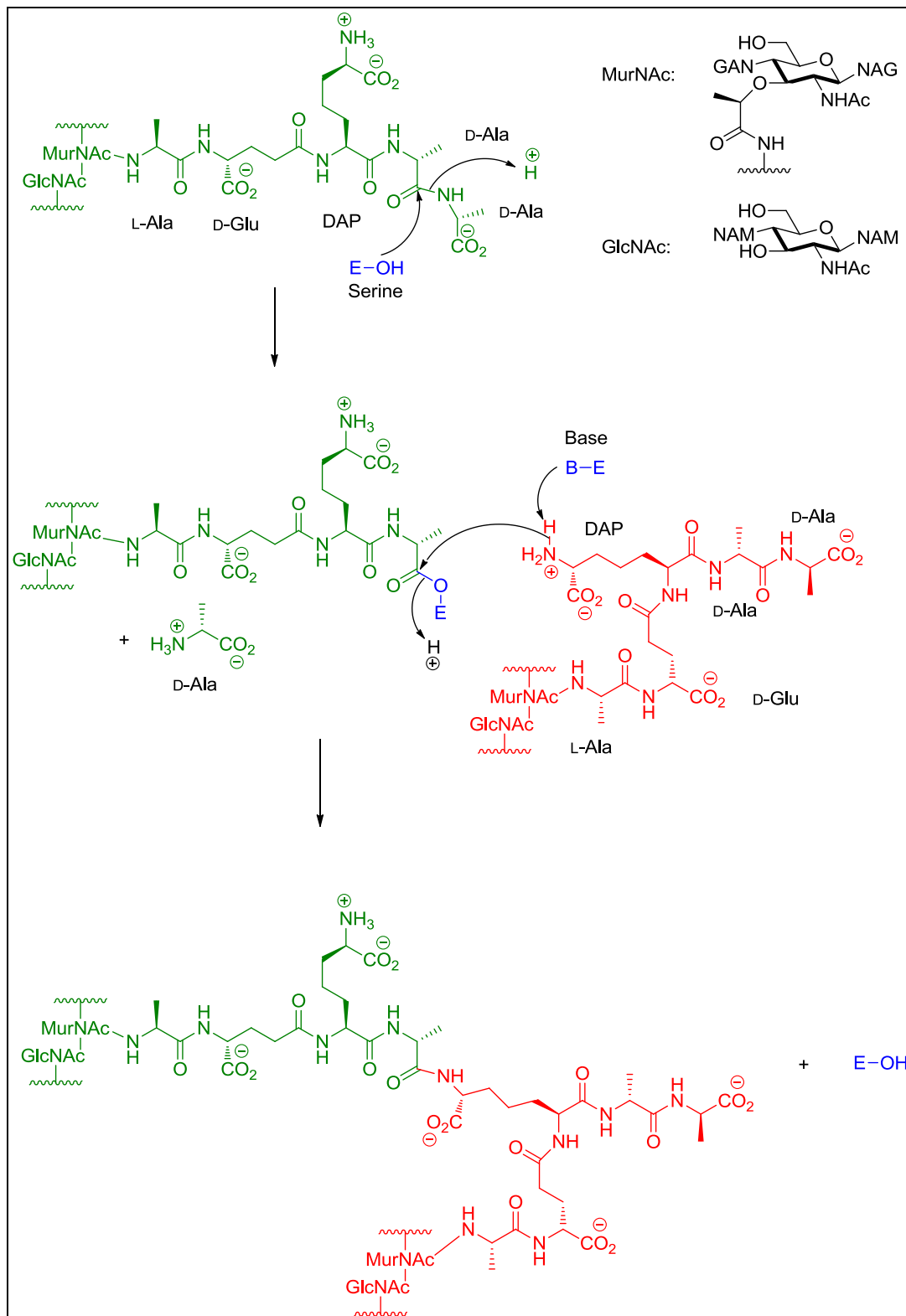


Figure 1.8: Transpeptidation of two glycan strands with transpeptidase catalysis. The green structure represents the first glycan strand which forms the covalent acyl-enzyme complex with the enzyme (E) and the red structure is the second glycan strand which deacylates the acyl-enzyme complex *via* an activated DAP amino group (adapted from Lee *et al.*).²⁴

1.4 Mechanism of action of β -lactam antibiotics

As previously mentioned, the β -lactam ring is part of the pharmacophore of β -lactam antibiotics. A closer inspection of the 3D structure of penicillin G (**1**) shows that the *N*-acylamino group at C-6, the lactam group (C-7 and N-4), C-3 and the carboxylic group at C-3 structurally resembles the D-Ala-D-Ala terminus of the bacterial glycan strand involved in transpeptidation.^{4,22,24,25} The four-membered β -lactam ring of penicillin G (**1**) functions to lock the pharmacophore in the right spatial arrangement similar to that of the D-Ala-D-Ala terminus (Figure 1.9).²⁵ This idea was first proposed by Tipper and Strominger in 1965 and it has since been accepted as the basis of β -lactam mechanism of action.^{4,22,24,26}

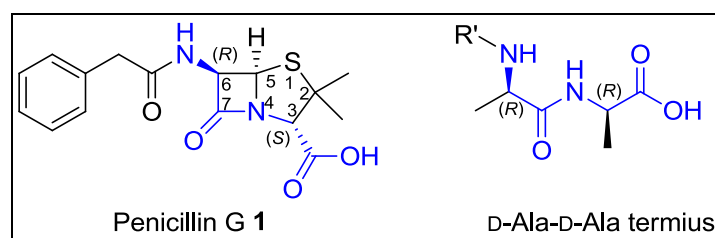
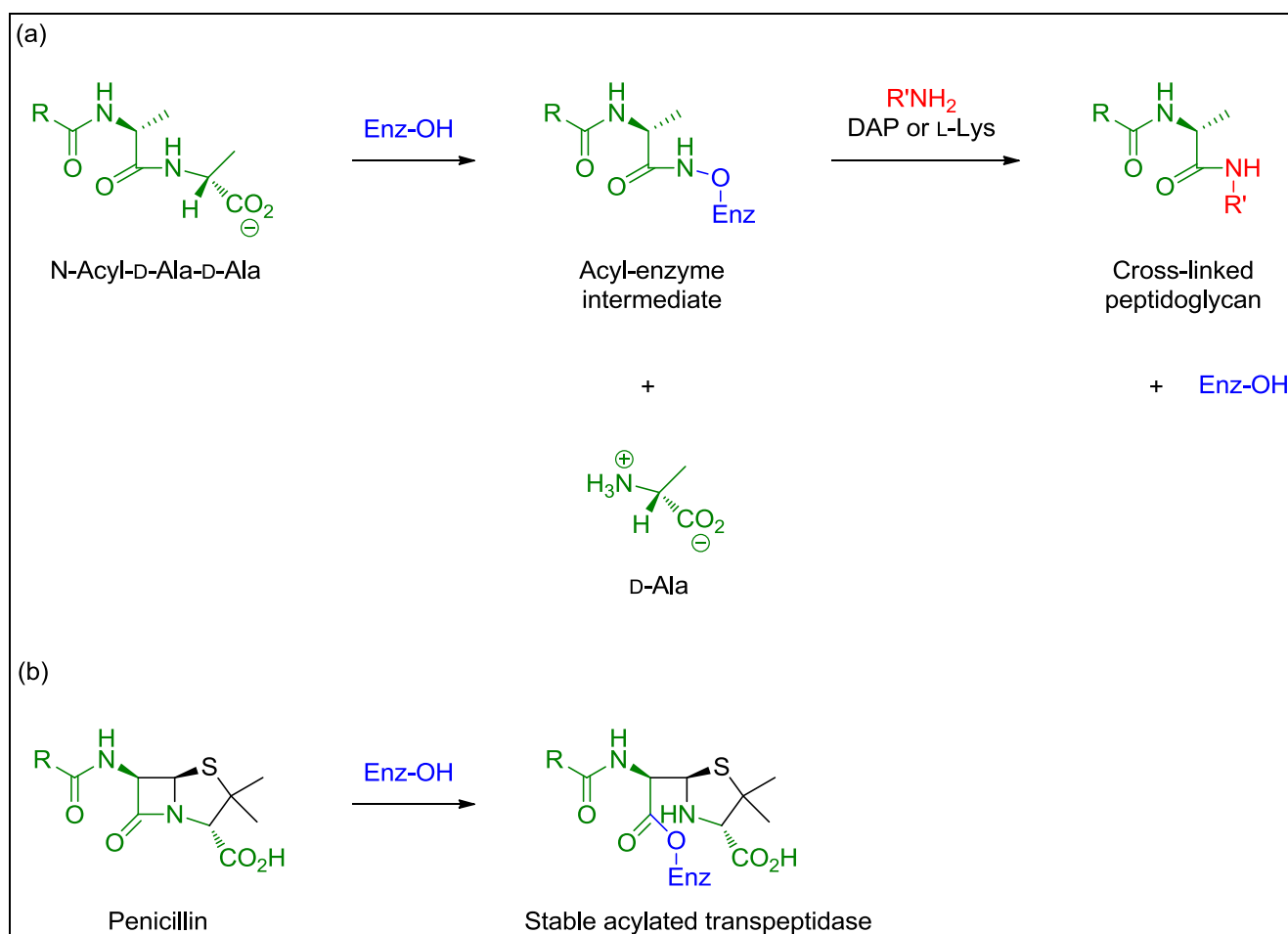


Figure 1.9: The structural resemblance of penicillin G (**1**) (highlighted in blue) with the D-Ala-D-Ala terminus of a bacterial glycan strand. R' is the remaining pentapeptide stem (adapted from Vella).¹⁸

Despite discrepancies between the above-mentioned structures, such as the absence of a methyl group at C-3 and a different absolute configuration at the same carbon atom, penicillin G (**1**) and β -lactams, collectively are still structurally recognised by bacterial transpeptidase.²⁵ Upon binding to the transpeptidase, β -lactams form a highly stable, irreversible acyl-enzyme covalent complex (Scheme 1.2).^{4,22,24,25,27} This is evident from x-ray crystallography structures of β -lactams covalently bound to transpeptidases in the literature.^{24,27} The acyl-bound enzyme is incapacitated to further catalyse the transpeptidation reaction and this subsequently results in loss of bacterial cell wall integrity and concomitant bacterial fatality (bactericidal effect).^{4,28} The transpeptidases have thus come to be known as the penicillin binding proteins (PBPs) with β -lactam antibiotics acting as pseudo-substrates to these enzymes.^{4,22,25}



Scheme 1.2: Comparison between the reactions of bacterial transpeptidase, Enz-OH with N-Acyl-D-Ala-D-Ala, the actual substrate, and penicillin, the pseudo-substrate, penicillin. R and R' refers to the first and second glycan strands, respectively (adapted from Buynak).²²

1.5 Bacterial resistance against β -lactam antibiotics and the development of β -lactam antibiotics

β -Lactam antibiotics account for approximately 50% of the world's prescribed antibiotics.^{2,4,29} As previously mentioned, the widespread administration of β -lactam antibiotics in both veterinary and human health has resulted in the spread of resistant genes which confer bacteria the ability to engage in a 'biochemical warfare' with the antibiotics.^{4,29,30}

Resistance against penicillin G (1) was first observed within 3 years of its introduction in 1943.³⁰ The cause of the resistance was found to be a penicillin degrading enzyme, or penicillinase, which is a member of the β -lactamase family of enzymes.⁶

In addition to β -lactamase expression, there are three other strategies by which bacteria circumvent the antibacterial activity of β -lactams:

- Structural alteration and or over-expression of PBPs (prevalent in pathogenic, Gram-positive bacteria, such as *Enterococcus faecium* and *Staphylococcus aureus*)^{4,5}
- Cell membrane impermeability towards β -lactams, specifically carbapenems, due to the omission or modification of Gram-negative bacteria porins or outer membrane proteins (OMPs) (Figure 1.6)^{4,5} (porins are hydrophilic, non-specific pores which are permeable to carbapenems with charged side groups)^{4,11,19,31}
- Expression of efflux pumps which expel β -lactams from the bacterial cells.⁴ This phenomenon is prevalent among the Gram-negative bacteria *Pseudomonas aeruginosa* and *Acinetobacter* spp.^{4,6,11,31}

The issue of β -lactamases, which is pervasive among pathogenic Gram-negative bacteria, is of a major concern as the genes responsible for the expression of these enzymes are being spread by mobile genetic elements among related and unrelated bacterial genera.^{4,5,32} The subject of β -lactamases will be covered in the next few sections of this chapter (Sections 1.7 and 1.8).

One of mankind's solutions towards β -lactam resistance is the development of existing and novel β -lactam antibiotics.^{4-6,30} Semi-synthetic penicillins with various *N*-acyl side groups were successfully derived from the naturally-sourced 6-aminopenicillanic acid, 6-APA (**11**) in the 1960s and 1970s (Figure 1.10).³³ One such important derivative is methicillin (**12**) which has activity against penicillin resistant strains of *S. aureus*.^{8,33-35} The bulky di-*ortho* methoxy groups play a role in diminishing the affinity of methicillin (**12**) towards penicillinase.³³⁻³⁵

Cloxacillin (**13**), which has improved antibacterial potency and oral bioavailability compared to methicillin (**12**), was developed later.^{33,34} In addition, carbenicillin (**14**), the first *P. aeruginosa*-susceptible penam was also developed within the same time frame.^{33,34}

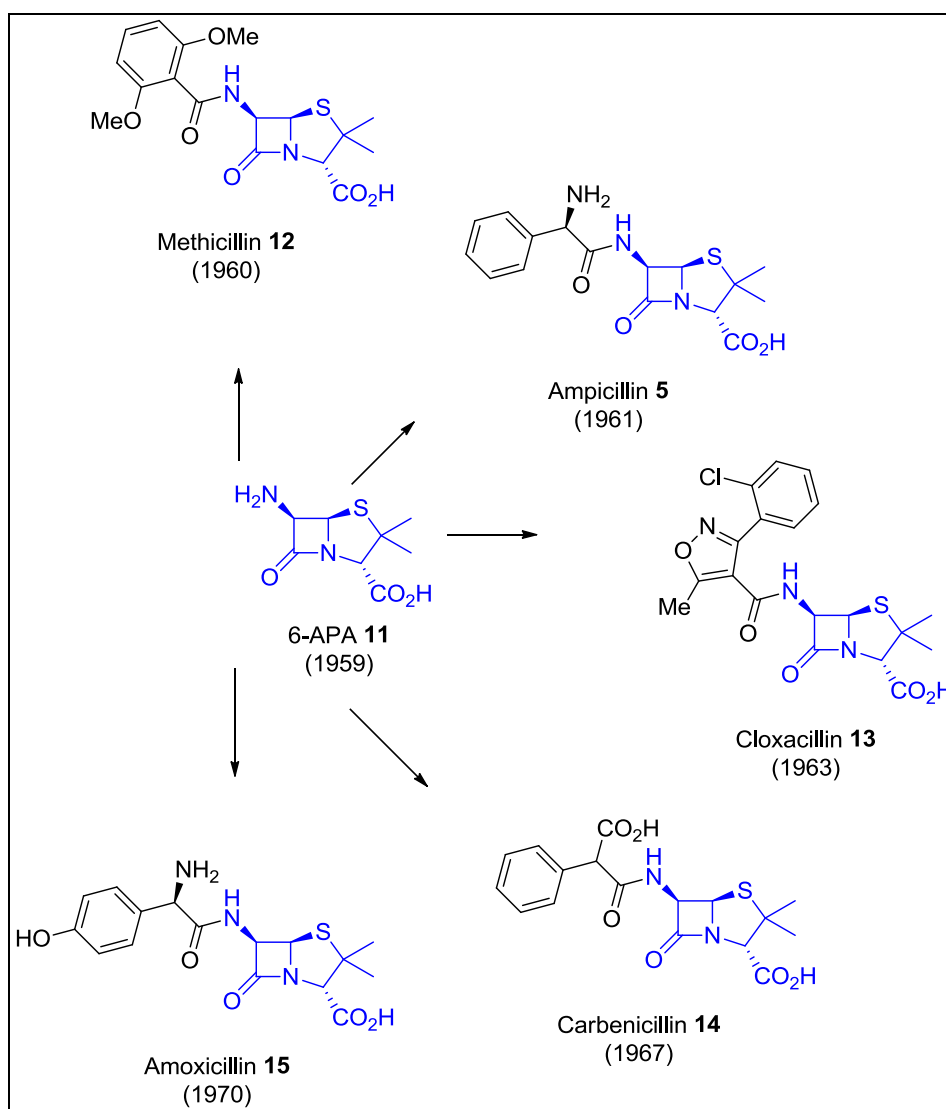


Figure 1.10: The development of semi-synthetic penams from the naturally isolated 6-APA (**11**).³³

However, within a year of its introduction, resistance against methicillin (**12**) was detected in a particular bacterial strain of *Staphylococcus aureus*. This resistant strain was later recognised as ‘methicillin-resistant *S. aureus*’ (MRSA).^{4,30} MRSA resistance was found to be implicated by a structurally-altered PBP with significantly decreased affinity towards methicillin (**12**).⁴ However, newer generation cephalosporins, such as ceftobiprole (**16**) and ceftatrolone (**17**), were developed in response to MRSA resistance (Figure 1.11).^{5,15}

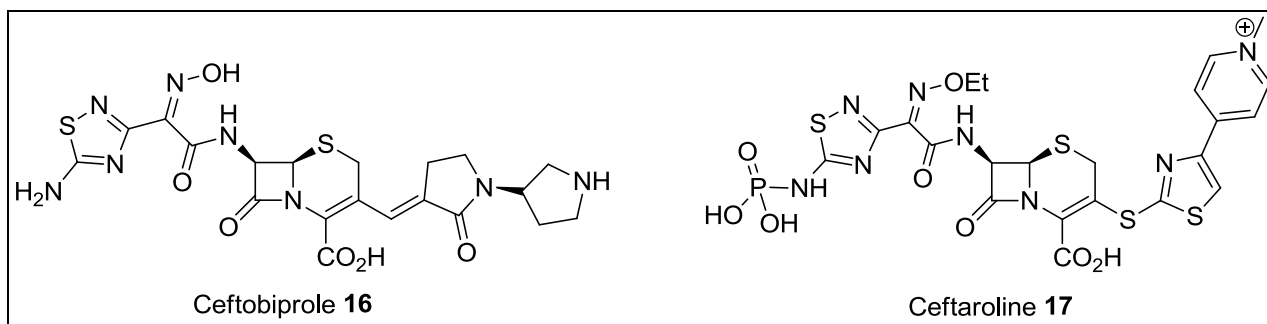


Figure 1.11: Newer-generation cephalosporins with antibacterial activity against MRSA.⁵

Parallel to the development of semi-synthetic penams, synthetic cephalosporins were developed from 7-aminocephalosporinic acid, 7-ACA (**18**) – first obtained from the mild acid hydrolysis of cephalosporin C (Figure 1.12).^{8,10,33} The development of cephalosporins has been spurred by three waves of innovation in response to bacterial resistance: the first is the narrow antibacterial spectrum of the first-generation cephalosporins; the second is the emergence of β -lactamases, particularly the extended-spectrum β -lactamases (ESBLs), which initially degraded the third-generation cephalosporins but have now also degraded the fifth-generation cephalosporins; and finally, the re-emergence of MRSA, as mentioned in the preceding text.^{6,10,15,34}

With the ever increasing onslaught of ESBLs, carbapenems were later administered as the next line of β -lactams after penicillins and cephalosporins, until the emergence of β -lactamases.^{7,11,36} The introduction of another novel β -lactam antibiotic is yet again met with bacterial resistance.^{30, 29} Therefore, there is not only a pressing need for novel β -lactam antibiotics, but also β -lactamase inhibitors to tackle the issue of antibiotic resistance.^{15,30}

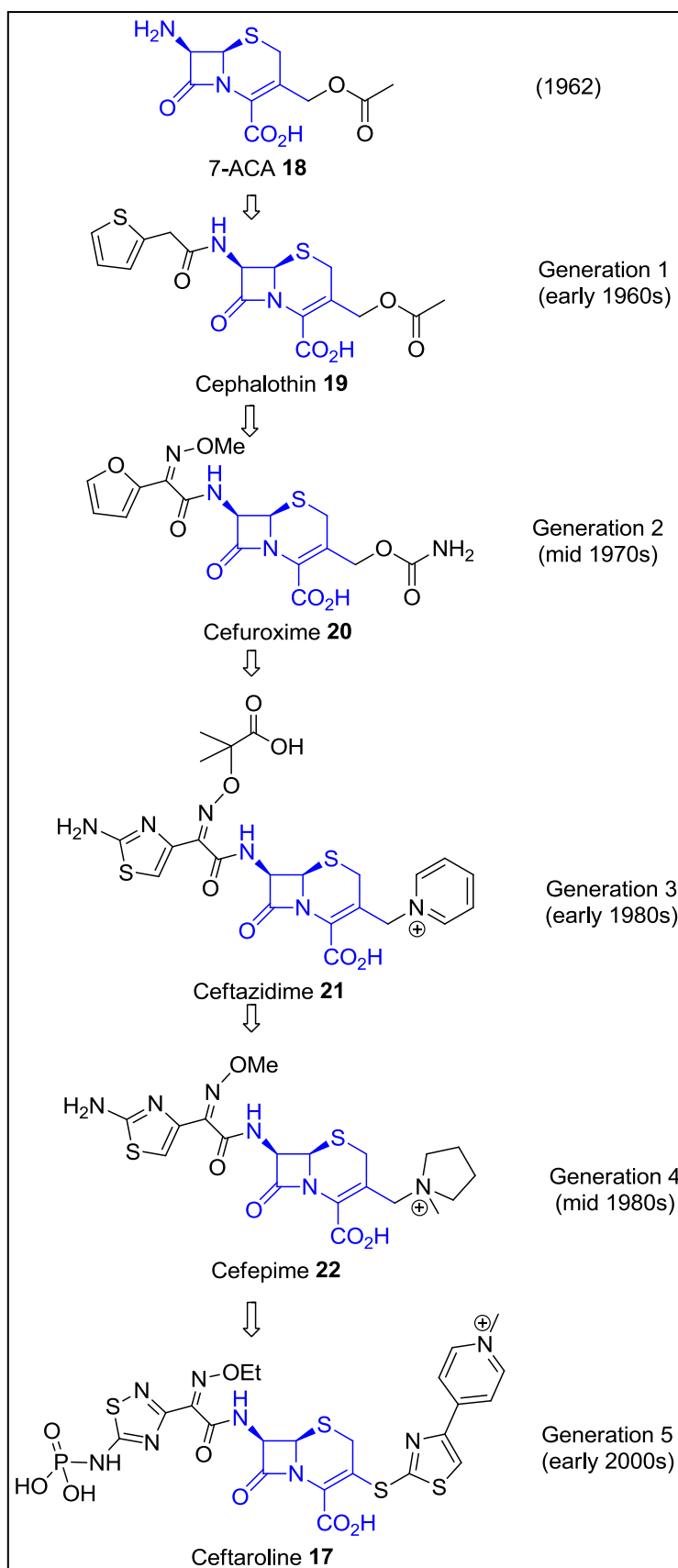


Figure 1.12: The synthetic development of cephalosporins from 7-ACA (**18**) (adapted from Walsh and Wenczewicz).³⁰

1.6 An overview and classification of β -lactamases

There are two ways to classify β -lactamases: the Ambler classification (classes A to D) which is based on amino acid sequence, specifically the conserved and distinct amino acid residues and the Bush-Jacoby classification which is based on substrate selectivity and inhibitor profile (Table 1.1).^{6,37} The broader and more commonly-used Ambler scheme will be employed in this thesis.

In the Ambler classification of β -lactamases, classes A, C and D are the serine β -lactamases (SBLs), which utilise a serine nucleophilic residue for hydrolytic activity, whereas class B are the zinc-dependent metallo- β -lactamases.^{4,6,32,37} Clavulanic acid (**23**), together with the penicillin sulfones sulbactam (**24**) and tazobactam (**25**) are known clinical inhibitors of the serine β -lactamases, whereas ethylenediaminetetraacetic acid, EDTA (**26**) is a known, generic metal ion chelator (Figure 1.13).^{4,37} These inhibitors are used as part of the identification process of β -lactamases.³⁷ The metallo- β -lactamases will be the main focus of this thesis.

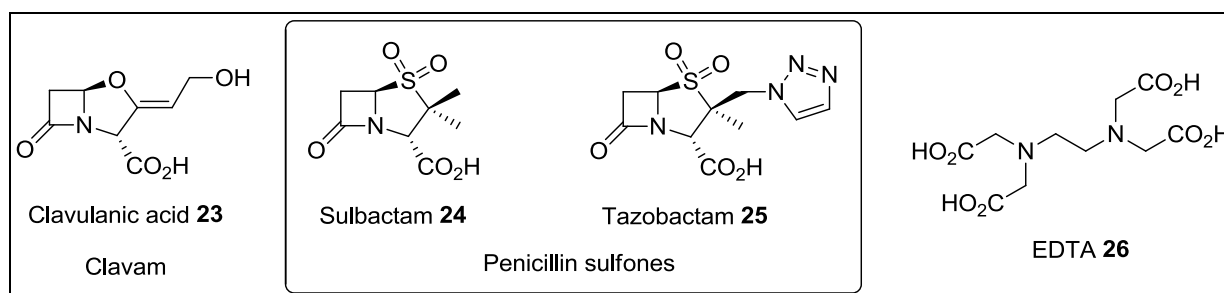


Figure 1.13: The clinical serine β -lactamase inhibitors **23**, **24** and **25** together with the generic metal ion chelator, EDTA (**26**) used in the identification of β -lactamases.

The class A SBLs constitute the largest class of the β -lactamases, and is growing due to the increasing identification of ESBLs.^{4,37} Members of this class of β -lactamase mostly hydrolyse penicillins (or penams) and are inhibited by clavulanic acid (**23**), tazobactam (**25**) and to a lesser extent sulbactam (**24**).^{6,37} The class C SBLs are the cephalosporin degrading enzymes, which are not inhibited by the usual SBL inhibitors.^{6,37} The class D SBLs preferably hydrolyse oxacillins such as cloxacillin. Most, but not all of the Class D SBLs are inhibited by clavulanic acid (**23**) or the penicillin sulfones.^{6,37}

Table 1.1: Classification of β -lactamases according to the Ambler and Bush-Jacoby schemes. ^{6,37}

Ambler class	Bush-Jacoby class	Preferred substrates	Inhibited by		Enzyme examples
			CA or TZB	EDTA	
A (serine penicillinases)	2a	Penicillins	Y	N	PC1
	2b	Penicillins and first-generation cephalosporins	Y	N	TEM-1, TEM-2, SHV-1
	2be (ESBLs)	Penicillins, first and newer-generation cephalosporins and aztreonam	Y	N	TEM-3, SHV-2, CTX-M-15
	2br	Same as 2b	N	N	TEM-30, SHV-10
	2c	Carbenicillin	Y	N	PSE-1
	2e	Newer-generation cephalosporins	Y	N	CepA
	2f	Penicillins, Carbapenems	V	N	KPC-2, SME-1
B (Metallo- β -lactamases)	3	Most β -lactams, especially carbapenems, excluding aztreonam	N	Y	IMP-1, VIM-1 (B1); CphA (B2); L1 (B3)
C (Cephalosporinases)	1	Cephalosporins	N	N	AmpC, GC1
D (Oxacillinases)	2d	Cloxacillin	V	N	OXA-1, OXA-10

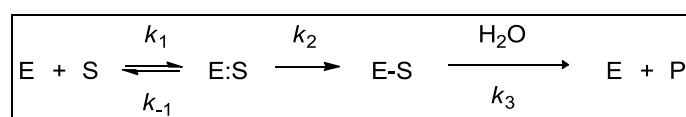
“Y”, “N” and “V” denotes inhibited, not inhibited and variably inhibited, respectively. CA and TZB denotes clavulanic acid and tazobactam, respectively.

1.7 Mechanism of the SBLs with class A β -lactamase as an example

SBLs hydrolyse β -lactams in two steps: an acylation step employing a serine nucleophile followed by a deacylation step with an activated water molecule (Figure 1.14).^{4,6} Before the acylation step, the enzyme forms a Michaelis complex with the β -lactam substrate *via* two types of interactions: an ionic interaction (salt bridge) between the carboxylate group of the substrate with Lys234; and hydrogen bond interactions between the β -lactam carbonyl oxygen with the backbone amide nitrogens of Ser70 and residue 237 (oxyanion hole).^{4,6,36} The purpose of the Michaelis complex is to activate the β -lactam carbonyl towards the nucleophilic attack.⁴ The amino acid residues Ser70 and Lys234 are highly conserved among Class A SBLs.^{4,6}

Upon formation of the Michaelis complex, the β -lactamase serine nucleophile (Ser70) attacks the carbonyl carbon of the β -lactam substrate to give a high-energy tetrahedral intermediate.⁶ The tetrahedral intermediate then collapses by scission of the C-N bond and protonation of the β -lactam nitrogen to give a covalent acyl-enzyme complex.^{4,6} Nucleophilic attack of the complex by an activated water molecule leads to a second tetrahedral intermediate which finally collapses to the deactivated β -lactam product and regenerated β -lactamase enzyme.⁶ Ser70 and the water molecule need to be activated by a general base (Glu166) prior to the acylation and deacylation steps, respectively.⁶ The activated water molecule required for the deacylation step is also known as the acyl acceptor.⁴

In short, the above-mentioned reaction can be summarised in the following scheme (Scheme 1.3).⁶ S, E, E:S, E-S and P denotes the substrate, the enzyme, the Michaelis complex, the acyl-enzyme complex and the deactivated β -lactam product, respectively. The association and dissociation rate constants for the Michaelis complex are k_1 and k_{-1} , respectively; and the acylation and deacylation rate constants is k_2 and k_3 , respectively.



Scheme 1.3: The summary of the hydrolysis of a β -lactam substrate, S catalysed by a class A SBL enzyme, E to give the deactivated β -lactam product, P.⁶

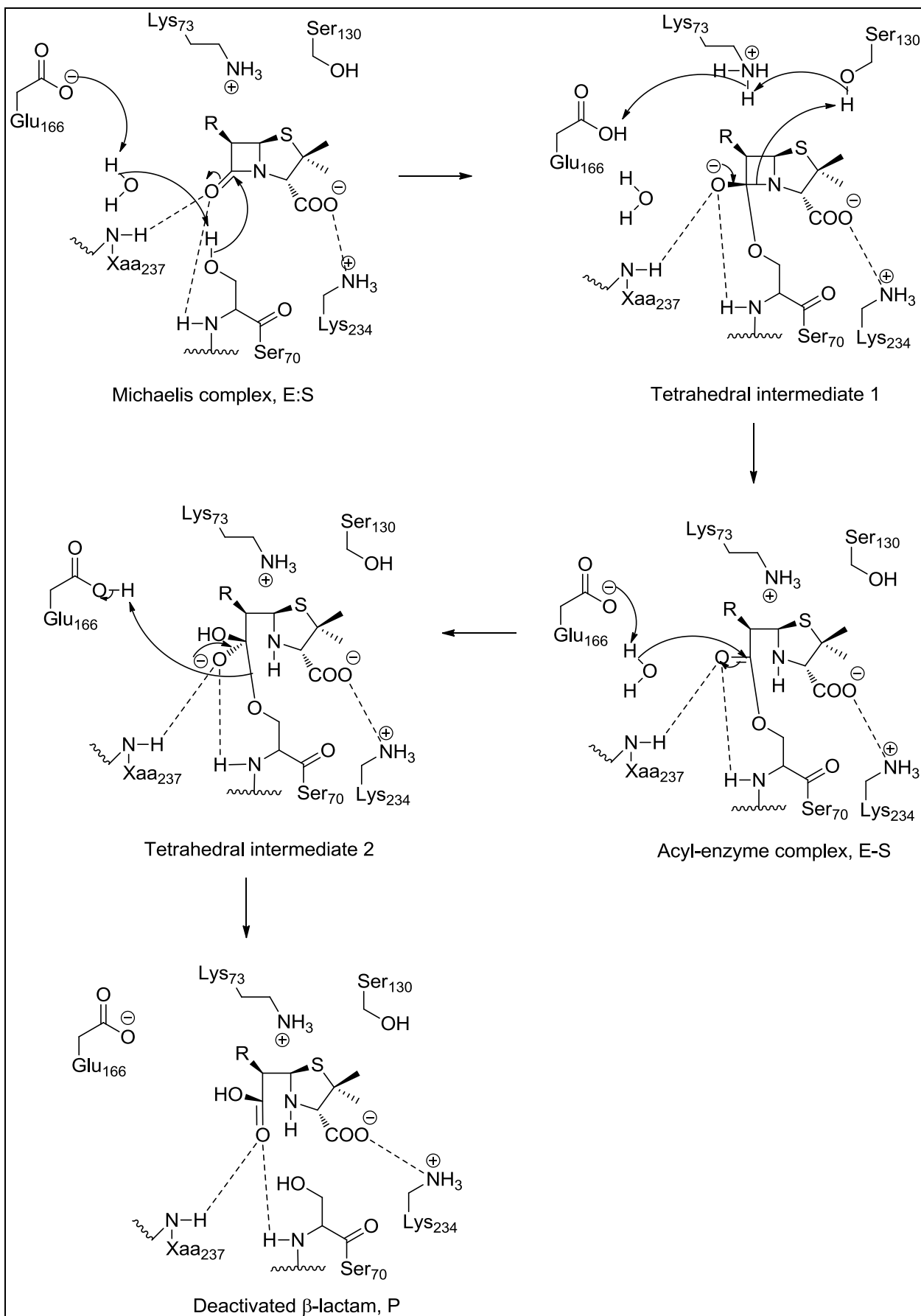


Figure 1.14: The proposed mechanism for the hydrolysis of a generic β -lactam by a class A SBL. The dashed lines represent hydrogen bonds and also ionic interaction (adapted from Drawz and Bonomo).⁶

Even though SBLs and PBPs are distinct classes of bacterial enzymes, yet there are some similarities between the two classes (Table 1.2).⁴ The mechanism machinery of SBLs and PBPs involve similar steps, *i.e.* the formation of an acyl-enzyme complex with the requirement of an activated serine residue, followed by a deacylation step.⁴ Principally, PBPs and SBLs share the same substrates which is β -lactam antibiotics.⁴ These similarities suggest the idea of SBLs having been evolved from PBPs.⁴

Table 1.2: Comparison between the catalytic mechanism of PBPs and SBLs in terms of substrate, the attacking nucleophile, acyl acceptor and reaction product.

Bacterial enzyme	Substrate	Nucleophile for the acylation step	Acyl acceptor for the deacylation step	Reaction product
PBP (transpeptidase)	Acetylmuramyl-pentapeptide and β -lactam antibiotics	Activated serine residue	Activated L-lysine (<i>S. pneumonia</i>), or DAP (<i>E. coli</i>)	Cross-linked peptidoglycan strands
SBL (<i>e.g.</i> class A β -lactamase)	β -lactam antibiotics	Activated serine residue	Activated water	Deactivated β -lactam

1.8 Overcoming the action of SBLs: SBL inhibitors and combination therapy.

Another approach undertaken by mankind in overcoming β -lactam resistance is the search and development of β -lactamase inhibitors.^{5,6} This approach has thus far proved successful as demonstrated by the development of clavulanic acid (**23**) as a clinical SBL inhibitor. Clavulanic acid (**23**) was first discovered from the non-pathogenic soil bacterium

Streptomyces clavuligerus in 1977.⁶ It does show any notable antibacterial activity on its own. However, when combined with amoxicillin (**15**), the inhibitor-drug combination shows enhanced antibacterial potency against pathogenic Gram-positive and negative bacteria.⁶ The synthetic development of other SBL inhibitors, such as the penicillin sulfones sulbactam (**24**) and tazobactam (**25**) subsequently followed suit (Figure 1.13).⁶

The molecular structures of all of the clinical SBL inhibitors **23**, **24** and **25** resemble that of penicillins, albeit with some differences, such as the absence of an amide side chain at C6 found in penicillins and the presence of a leaving group at C1 (Figure 1.15).^{6,36} This leaving group, which is an enol ether oxygen group for clavulanic acid (**23**) and a sulfone group for both sulbactam (**24**) and tazobactam (**25**) plays a critical role in the SBL inhibitory mechanism by allowing multiple branch reactions to take place after the formation of the acyl-enzyme complex (E-I) (Scheme 1.4).⁶ Some of these pathways could eventually lead to irreversible modification and inactivation of the enzyme (Figure 1.16).⁶ Results from several studies suggested that the clavulanic acid (**23**) acyl-enzyme complex (E-I) could undergo secondary ring opening to give a transient enzyme-imine intermediate (E-T). This transient intermediate could cross link with another serine residue to give a cross-linked enzyme complex or hydrolyse to an aldehyde complex, both of which are permanently deactivated enzyme species (E-I*). Additionally, tautomerisation of the imine intermediate could occur to give other transient intermediates, such as the *trans*-enamine intermediate which could then lead to a highly stable decarboxylated enzyme complex (Figure 1.16).^{6,36} Clavulanic acid (**23**), sulbactam (**24**) and tazobactam (**25**) are therefore known as mechanism-based, or suicide inhibitors.^{5,6}

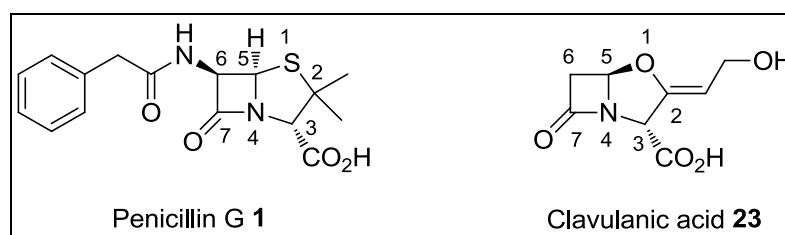
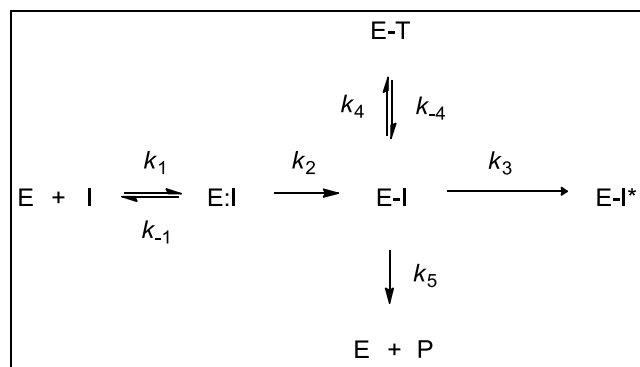


Figure 1.15: Comparison between the molecular structure of penicillin G (**1**) and clavulanic acid (**23**).



Scheme 1.4: The possible pathways of an SBL inhibitor, I reacting with an SBL enzyme, E; with E:I, E-I, E-I*, E-T and P denoting the Michaelis complex, the acyl-enzyme complex, the permanent acyl-enzyme complex, the acyl-enzyme tautomer and the hydrolysed product, respectively (adapted from Drawz and Bonomo).⁶

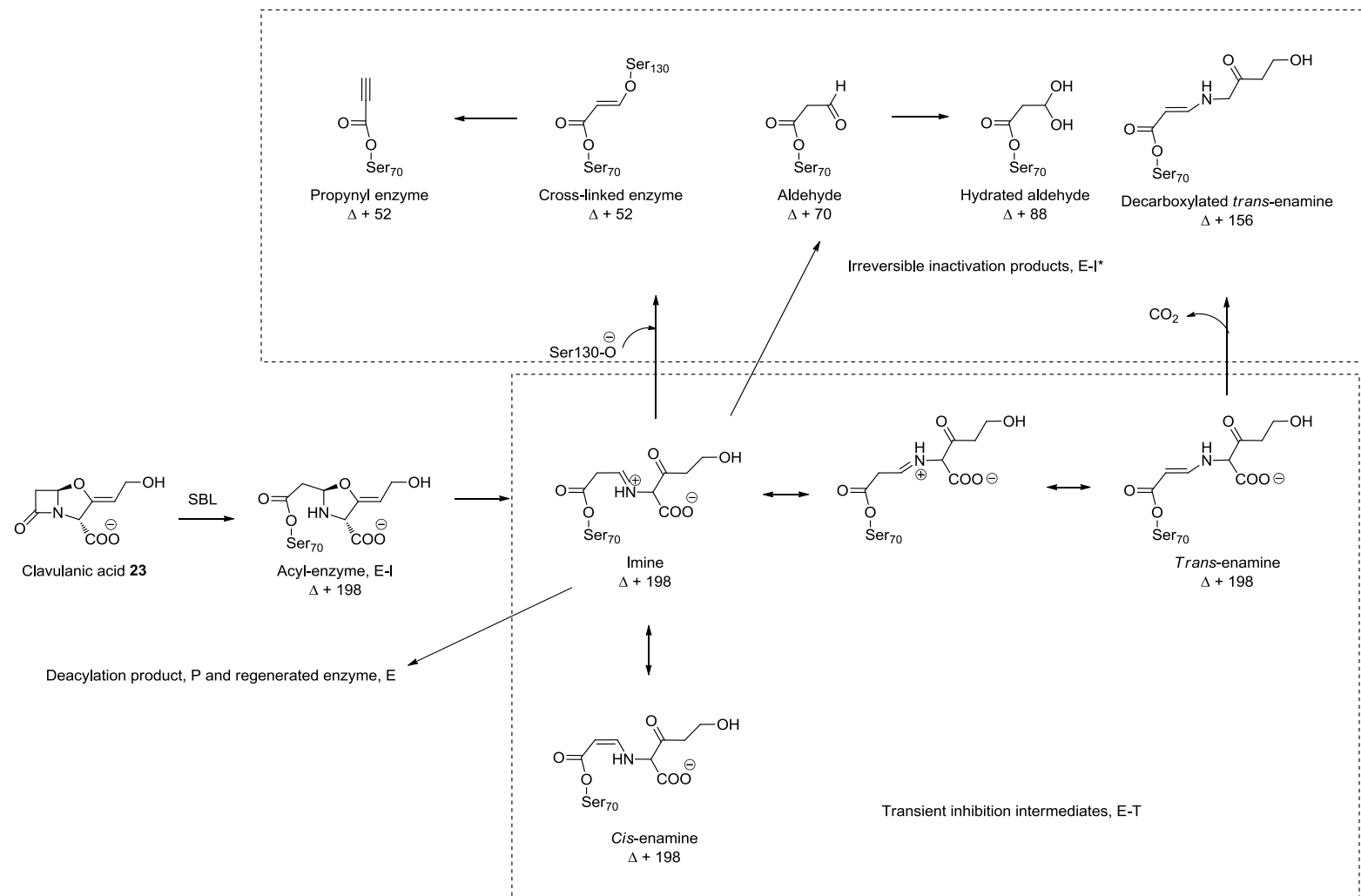


Figure 1.16: The proposed products (expressed in Daltons) of the different possible pathways of class A SBL enzyme inhibition by clavulanic acid (**23**) as empirically observed by mass spectrometry (adapted from Drawz and Bonomo).⁶ 'Δ' refers to the molecular weight of the enzyme.

The cornerstone of antibacterial chemotherapy, since the introduction of penicillin G (**1**) in the 1940s has been monotherapy, *i.e.* the administration of a single type of antibiotic.³⁰ This, however, changed with the co-administration of amoxicillin (**15**) and clavulanic acid (**23**) (tradename: Augmentin), in the early 1980s.^{6,36} The move from monotherapy to combination therapy was another revolution in antibiotic chemotherapy, since the discovery of penicillin G in 1928.^{3,30} The recent decline in the incidence of ESBLs among pathogenic Gram-negative bacteria in the UK has been credited to the co-administration of β -lactam antibiotics with SBL inhibitors.⁷ Combination therapy is therefore a viable option in preserving the lifetime of existing β -lactam antibiotics as mankind's chemotherapeutic armamentarium against bacteria.^{3,15,38}

1.9 Classification and structural features of metallo- β -lactamases (MBLs)

MBLs are divided into three subclasses, namely B1, B2 and B3. Division is based on substrate selectivity, amino acid sequence, particularly the amino acid residues that chelate the Zn^{2+} ions and Zn^{2+} ion requirement for catalysis (Table 1.3).^{16,32,39-41} All MBLs exist as monomers, except for the B3 MBL L1, which exists as a tetramer.^{32,39,41}

Both B1 and B3 MBLs hydrolyse a broad range of β -lactams: penicillins, early- and latter-generation cephalosporins and carbapenems; whereas B2 MBLs selectively hydrolyse carbapenems (Table 1.4).^{16,32,39,41} In general, MBLs are ineffective in hydrolysing the monobactam aztreonam (**9**). This may be due to unsuccessful binding interactions between the β -lactam and the enzymes.^{4,39}

As mentioned previously, the clinically-administered SBL inhibitors, such as clavulanic acid (**23**), sulbactam (**24**) or tazobactam (**25**) do not exhibit any inhibitory activity on MBLs. Instead, these β -lactams pose as poor substrates for the metalloenzymes.³⁹

Table 1.3: Classification of MBLs based on substrate profile, amino acid residues chelating the Zn²⁺ ions and Zn²⁺ ion requirement for catalysis (adapted from Gupta,⁴¹ Herzberg and Fitzgerald⁴⁰).

Sub-class	Examples	Substrate profile	Amino acid residues ^a		Involvement of Zn ²⁺ ions for catalytic activity
			Zn 1	Zn 2	
B1	BclI, IMP-1, CcrA, VIM, NDM-1	Broad spectrum, except aztreonam	His116, His118, His196	Asp120, Cys221, His263	Di-zinc (BclI is active with either one or two Zn ²⁺ ions)
B2	CphA, ImiS	Only carbapenems	Asn116, His118, His196	Asp120, Cys221, His263	Mono-zinc (Zn 2 site)
B3	L1 (tetramer), AIM-1	Broad spectrum, except aztreonam	His/Gln116, His118, His196	Asp120, His121, His263	Di-zinc

^aNumbering is based on a standard, consensual numbering scheme, known as the BBL numbering.³⁹⁻⁴¹

Table 1.4 presents the kinetic parameters of MBLs in the hydrolysis of common β -lactam substrates. The turnover number, k_{cat} is the number of moles of substrate molecules hydrolysed per mole enzyme per unit time; a bigger value of k_{cat} is indicative of faster product formation.^{18,42} The Michaelis constant, K_m of an enzyme-catalysed reaction is the substrate concentration at half the limiting rate of the reaction.⁴² It is a measure of an enzyme's affinity for a particular substrate; substrates with smaller K_m values are interpreted as possessing greater affinities for the enzyme.¹⁸ The k_{cat}/K_m ratio is a measure of the degree of selectivity of an enzyme for a particular substrate; a larger value of the ratio translates to a greater efficiency of the enzyme in catalysing the reaction of the said substrate.^{18,42}

Table 1.4 Kinetic constants of representative MBLs in the hydrolytic reaction of common β -lactams.

β-Lactam substrate	IMP-1 (B1)^a			CphA (B2)^b			AIM-1 (B3)^c		
	k_{cat} (s^{-1})	K_m (μM)	k_{cat}/K_m ($M^{-1}s^{-1}$)	k_{cat} (s^{-1})	K_m (μM)	k_{cat}/K_m ($M^{-1}s^{-1}$)	k_{cat} (s^{-1})	K_m (μM)	k_{cat}/K_m ($M^{-1}s^{-1}$)
Penicillin G	320 \pm 30	520 \pm 30	6.2 $\times 10^5$	0.03 \pm 0.003	870 \pm 70	35	778	31	2.6 $\times 10^7$
Ampicillin	950 \pm 50	200 \pm 25	4.8 $\times 10^6$	<0.01	2500*	<4	594	41	1.4 $\times 10^6$
Carbenicillin	ND	ND	2.0 $\times 10^4$	10	500	2.0 $\times 10^4$	NR	NR	NR
Cephalothin	48 \pm 4	21 \pm 2	2.4 $\times 10^6$	NR	NR	NR	529	38	1.4 $\times 10^7$
Nitrocefin (cephalothin analogue)	63 \pm 10	27 \pm 3	2.3 $\times 10^6$	0.0028 \pm 0.0001	1200 \pm 200	2.5	NR	NR	NR
Ceftazidime	8 \pm 1	44 \pm 3	1.8 $\times 10^5$	NR	NR	NR	7	148	4.9 $\times 10^4$
Imipenem	46 \pm 3	39 \pm 4	1.2 $\times 10^6$	1200 \pm 70	340 \pm 30	3.5 $\times 10^6$	1700	97	1.7 $\times 10^7$
Meropenem	50 \pm 5	10 \pm 2	1.2 $\times 10^5$	3100 \pm 200	1340 \pm 200	2.3 $\times 10^6$	1000	163	6.8 $\times 10^6$
Aztreonam	>0.01	>1000	<1.0 $\times 10^2$	NR	NR	NR	ND	ND	ND
Sulbactam	NR	NR	NR	0.12	37 \pm 4	3.24 $\times 10^3$	NR	NR	NR

ND and NR denotes not detectable and not reported, respectively. *Measured as an inhibition constant value.

^aValues taken from Laraki *et al.*⁴³

^bThe values for penicillin G, nitrocefin, imipenem and meropenem were taken from Vanhove *et al.*⁴⁴ The values for ampicillin, carbenicillin and sulbactam were taken from Bebrone *et al.*⁴⁵, Segatore *et al.*⁴⁶ and Felici *et al.*⁴⁷, respectively.

^cValues taken from Yong *et al.*⁴⁸ The standard deviation ranged from 3-8.5%

In 1995, the first X-ray crystallography structure of an MBL was reported to be that of the BclI enzyme, in its mono-zinc form, by Carfi and co-workers.⁴⁹ This structure, together with the X-ray crystallography structures of other MBLs revealed a distinct $\alpha\beta\alpha$ quaternary structural fold, with the central $\beta\beta$ -sheets flanked by five solvent-exposed α -helices; two α -helices on each side of the $\beta\beta$ -sheets and the fifth helix bridging the sheets (Figure 1.17).^{16,39,40,49-51} This characteristic structural fold, which is not present in other classes of β -lactamase, but is present in other metalloenzymes with various biochemical functions, suggests that MBLs are part of an ancient, superfamily of metalloenzymes.^{2,4,16,32,39-41,50}

Another structural insight obtained from the three dimensional (3D) structures of MBLs is the position of the Zn^{2+} ion(s) containing active site, which is located in a shallow channel at the interface of the two $\alpha\beta$ domains (Figure 1.17).^{16,39,50}

There are also other noteworthy structural features, such as a mobile β -hairpin loop in some MBLs that contributes towards substrate binding.^{16,39,50,52} The B1 MBLs contain a flexible β -hairpin loop (residues 60-66) in close proximity to the active site of the enzyme (Figure 1.17).^{39,50,53} Binding of a substrate or inhibitor to the enzyme's active site causes the loop to close and further interact with the hydrophobic pharmacophore of the substrate or inhibitor.^{16,39,51} The B3 L1 MBL has an analogous loop (residues 156-166) which functions in a similar way as that in the B1 MBLs (Figure 1.7).^{16,39,54} More details about the flexible loop of B1 MBLs interacting with inhibitors will be discussed in Section 1.11.

The B2 MBLs have an exceptionally elongated, kinked α -3 helix, which forms part of a hydrophobic wall that defines the active site pocket (Figure 1.17).^{39,55,56} This well-defined pocket is specific to the binding of carbapenems, which explains the narrow substrate profile of B2 MBLs.^{39,55}

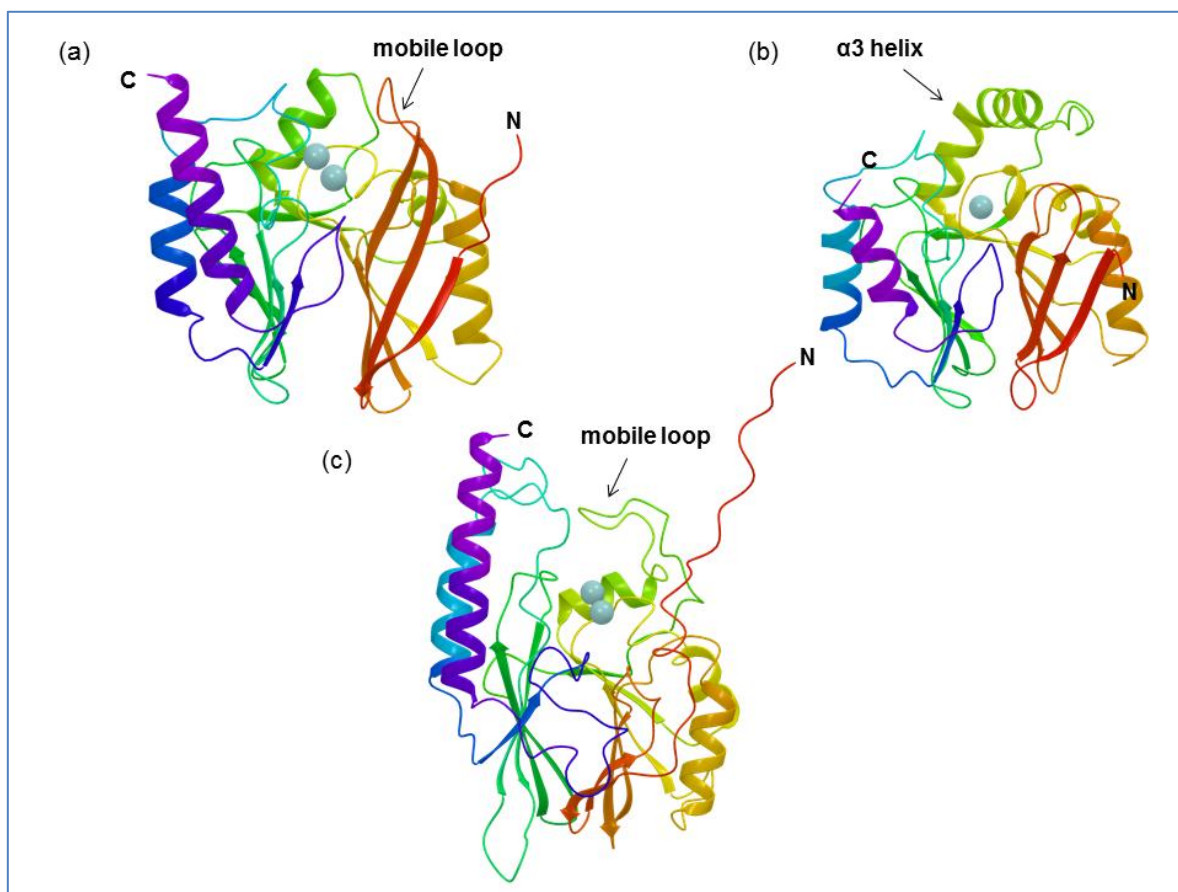


Figure 1.17: The cartoon diagrams of 3D structures of representative MBLs. The Zn^{2+} ions are shown as cyan spheres. (a) The IMP-1 B1 MBL with the flexible loop in orange (PDB no.: 1JJT).⁵⁷ (b) The CphA B2 MBL with the elongated $\alpha 3$ helix in green (PDB no.: 1X8G).⁵⁵ (c) The L1 B3 MBL with the mobile loop in green (PDB no.: 2AIO).⁵⁴ Figures were drawn with Maestro.⁹⁶

Within the MBL active site, there are two potential zinc binding sites, known as Zn1 and Zn2. In the di-zinc B1 and B3 MBLs, Zn1 and Zn2 are separated by a distance of 3.4-4.4 Å, with a bridging hydroxide ion (W1) asymmetrically positioned to the two metal centres; the bridging hydroxide ion is closer to the Zn1 site than the Zn 2 site (Figure 1.18 and Table 1.5).^{32,39,40,50,58-60} The Zn1 site of the B1 and B3 MBLs are co-ordinated by three histidine residues (His116, His118 and His196) and the bridging hydroxide ion in a tetrahedral geometry.^{39,40,58-61} It is also referred to as the histidine, or 3H site.^{16,32,39,61} In some B3 MBLs, His116 is found to be replaced with a glutamine residue (Gln116).^{16,32,40}

On the other hand, the Zn2 site of the B1 MBLs is co-ordinated by Asp120, Cys221, His263, the bridging hydroxide and another water molecule in a distorted trigonal

bipyramidal arrangement (Figure 1.18a).^{39,40,58-61} This metal centre is hence known as the cysteine, or DCH site.^{16,32,39,61} The Asp120 residue and a second water molecule (W2) are positioned at opposing, apical positions of the trigonal bipyramidal geometry.^{40,58-60} Besides the two metal centres, the bridging hydroxide also has an additional electrostatic contact with Asp120, through a shared proton.^{58,60} The cysteine residue Cys221, which is in direct contact with Zn2, exists in the thiolate form and has the propensity to be oxidised to a sulfonic group.^{50,53,58,61} As for the B3 MBLs, it is observed that another histidine residue (His121) is in lieu of Cys221 at the Zn2 site (Figure 1.18b).^{16,32,39,40,59,60} This difference causes the spatial arrangement of the ligands surrounding the Zn2 site of B3 MBLs to be shifted by 76° relative to that of the B1 MBLs.^{50,59} Moreover, the 221 position in B3 MBLs is instead replaced by a serine residue (Ser221), which is oriented towards the apical water (W2).^{40,59,60}

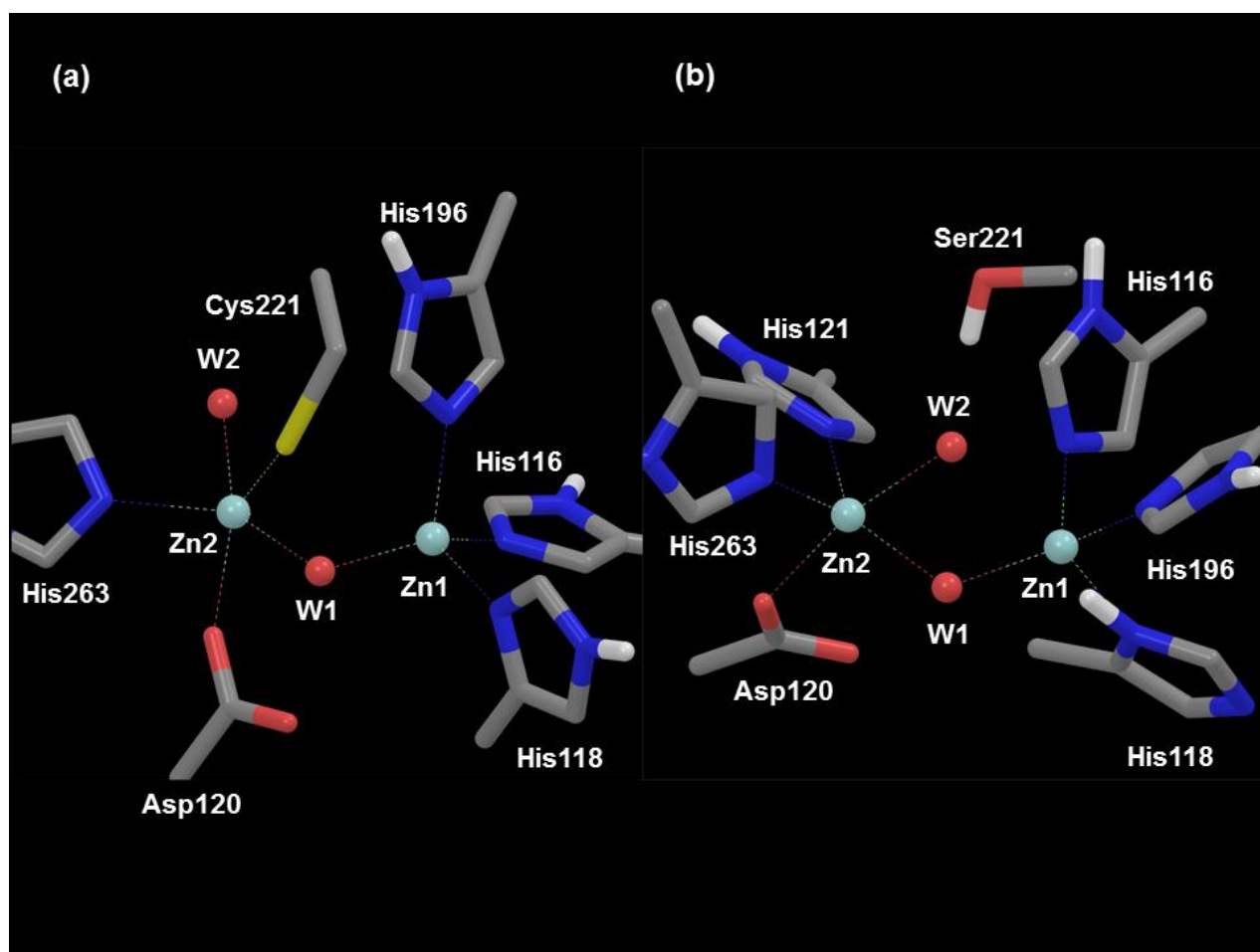


Figure 1.18: The amino acid residues and water molecules chelating the Zn²⁺ ions in the active sites of (a) the B1 CcrA MBL (PDB no.: 1ZNB)⁵⁸ and (b) the B3 MBL AIM-1 (PDB no.: 4AWY).⁶⁰ Zn²⁺ ions and water molecules are represented as cyan and red spheres,

respectively. Dashed lines represent co-ordination bonds. Atom colours: carbon in gray, nitrogen in blue, oxygen in red and sulfur in gold. Figures were drawn with Maestro.⁹⁶

Table 1.5: Notable interatomic distances of Zn1, Zn2, the bridging hydroxide (W1) and the apical water (W2) in a selection of native, wild-type B1 and B3 MBLs.

Enzyme	Sub-class	PDB no.	Distances to Zn1 (Å)		Distances to Zn2 (Å)	
			W1	Zn2	W1	W2
CcrA	B1	1ZNB ⁵⁸	1.88	3.47	2.06	2.27
VIM-2	B1	1KO3 ⁵³	2.10	4.20	2.52	2.93 (W2 replaced by a chloride ion)
L1	B3	1SML ⁵⁹	1.86	3.46	2.07	2.40
AIM-1	B3	4-AWY ⁶⁰	1.94	3.48	1.98	2.27

Positive cooperative binding, which is the increased zinc binding affinity for the second site upon zinc binding at the first site, is observed in most B1 MBLs, but isn't observed in the B2 MBLs.^{16,61} Instead, the B2 MBLs are functionally mono-zinc, in the sense that only one of the Zn²⁺ ions is utilised for catalytic activity- the Zn2 site.^{32,39,50,61} Binding of the other Zn²⁺ ion (Zn1 site) inhibits the enzyme.^{32,39,61}

In the mono-zinc form, the catalytic Zn2 site of B2 MBLs is co-ordinated by Asp120, Cys221, His263 and a water molecule (W1) in a tetrahedral co-ordination shell, whereas the Zn1 site is occupied by a second water molecule (W2), which has direct contacts with His118 and His196 (Figure 1.19a).⁵⁶ In some crystal structures of B2 MBLs, W1 is replaced by a carbonate or a sulfate ion.^{55,61} Asn116, which is the His116 equivalent in B1 and B3 MBLs, is indirectly bound to W2 through His196.^{55,56}

In 2009, the 3D structure of the di-zinc form of the CphA B2 MBL was published (Figure 1.19b).⁶¹ The structure reveals that the position of W2 is occupied by a Zn²⁺ ion (Zn1 site) which is directly co-ordinated by His118 and His196 residues, including a bridged sulfate ion and a water molecule in a tetrahedral geometry (Figure 1.19b).⁶¹ Again, Asn116 was shown to have no direct interaction with Zn1.⁶¹ This may possibly explain why binding of Zn1 inhibits the B2 MBLs, as W2 which is activated by His118, is the hydrolytic

nucleophile. Furthermore, His196 is suggested to play a role in the mechanism of B2 MBLs, by interacting with the carbonyl oxygen of the β -lactam. The binding of Zn1 hinders W2, His118 and His196 from carrying out their catalytic roles. More information about B2 MBL mechanism is presented in the next section.

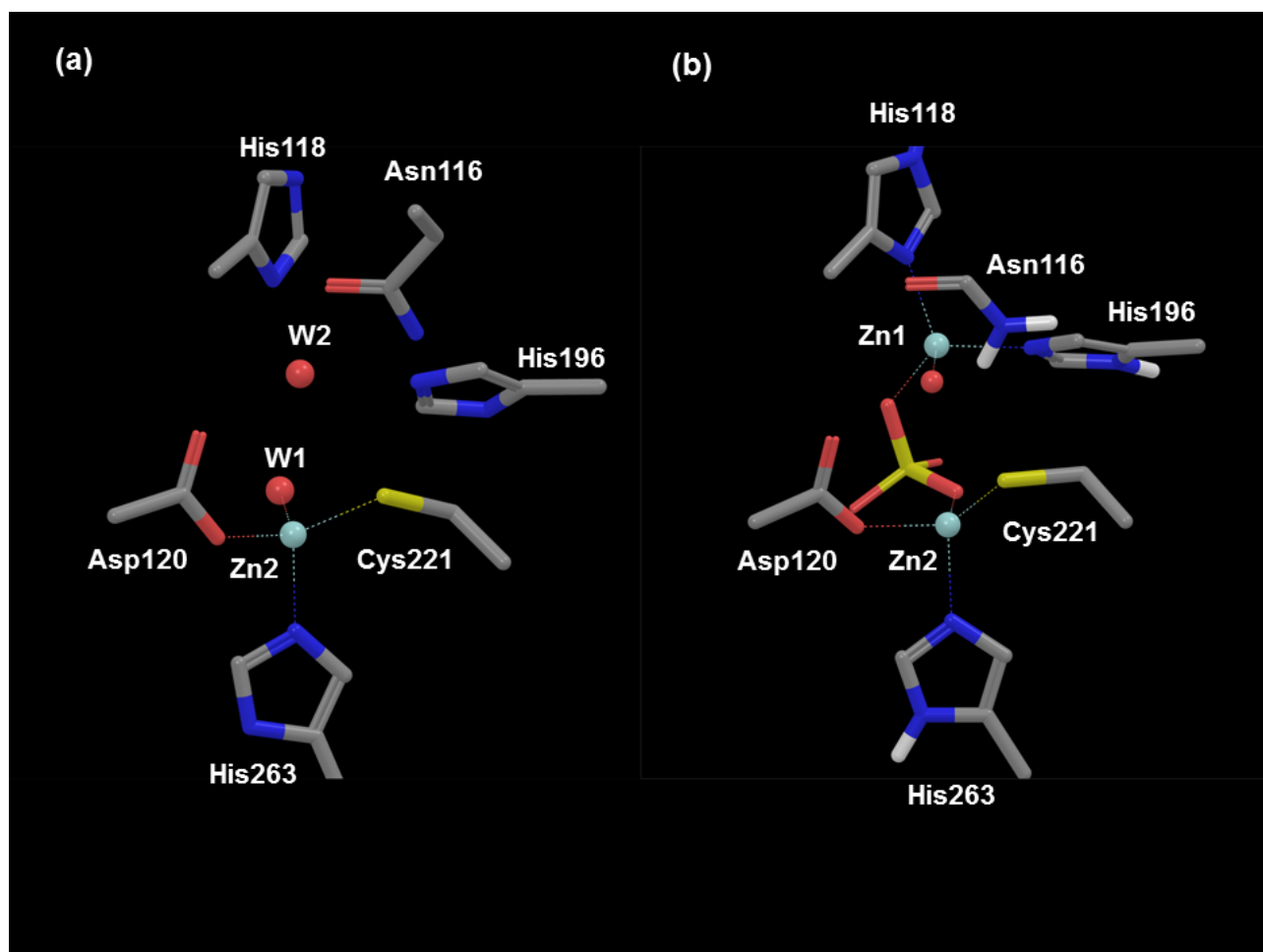


Figure 1.19: The active site of (a) the monozinc form of Sfh-1 (PDB no.: 3SD9)⁵⁶ and (b) the di-zinc form of CphA (PDB no.: 3F90).⁶¹ Both of the enzymes belong to the B2 subclass. Zn^{2+} ions and water molecules are represented as cyan and red spheres, respectively. Dashed lines represent co-ordination bonds. Atom colours: carbon in gray, nitrogen in blue, oxygen in red and sulfur in gold. Figures were drawn with Maestro.⁹⁶

1.10 The Proposed Catalytic Mechanism for MBLs

The mechanism of SBLs and MBLs follow the same order of events: initial formation of a Michaelis complex by the enzyme and β -lactam substrate, followed by

nucleophilic attack on the carbonyl carbon of the substrate, which leads to a short-lived tetrahedral intermediate that finally collapses to the deactivated, ring-opened product. However, there are a few differences between the two mechanisms. The SBL mechanism requires two attacking nucleophiles at separate stages: an activated serine residue, followed by an activated water molecule, whereas the MBLs only utilise a polarised water species for the same purpose. Consequently, a covalent acyl-enzyme complex, which is one of the key intermediates in the SBL mechanism, is not formed in the MBL mechanism. Furthermore, the Lewis acid disposition of Zn^{2+} ions allows the Zn centre(s) in MBLs to make interactions with the carbonyl oxygen and or the C-3 or C-4 carboxylate group of the β -lactam substrate.^{32,40,55} These interactions aid in the polarisation or positioning of the substrate carbonyl carbon towards nucleophilic attack.^{32,55}

Based on spectroscopic, kinetic and X-ray crystallography studies, several distinct mechanisms have been proposed for the di-zinc B1 and B3 MBLs as well as the mono-zinc B2 MBLs.^{16,32,50,51,55} The specific mechanistic details for each MBL varies and are dependent on the particular enzyme and substrate.^{16,51}

For the di-zinc MBLs, the nucleophile is thought to be the bridging hydroxide, which is specifically orientated by the metal ions and Asp120 for attack on the carbonyl carbon of the β -lactam substrate (Figure 1.20).^{16,32,40,50} The β -lactam carbonyl carbon is activated towards nucleophilic addition by direct interactions between the carbonyl oxygen and Zn1 as well as an oxyanion hole made up of Asn233 (B1 MBLs) or Tyr228 (B3 MBLs) (Figure 1.20).^{16,40,50} Ionic or hydrogen bond interaction(s) between the C-3 or C-4 carboxylate group of the substrate and Lys224 (B1 MBLs) or Ser221 and Ser223 (B3 MBLs) also contribute towards the formation of the Michaelis complex (Figures 1.20 and 1.21).^{16,50,51,54} It is also observed in some MBL-hydrolysed- β -lactam co-crystal structures that the C-3 or C-4 carboxylate group has direct interaction with Zn2; which results in the displacement of the apical water from Zn2.^{16,50,51,54}

After nucleophilic attack, the tetrahedral intermediate collapses by C-N bond scission, followed by protonation of the β -lactam nitrogen (Figure 1.20).^{32,40} The proton donor for the protonation step is proposed to be the apical water which is bound to Zn2 (Figure 1.20).^{32,40} However, there is another alternative proposal for di-zinc B1 and B3 MBLs, that C-N bond fission occurs without concerted protonation of the β -lactam nitrogen, which results in an accumulated anionic nitrogen intermediate that is stabilised by direct, ionic interaction with Zn2 (Figures 1.21 and 1.22). The latter proposed

mechanism is frequently observed with cepheids and oxacepheids that have a conjugated C-3 side chain, such as the non-therapeutic, chromogenic nitrocefin cepheid (**27**) and moxalactam (**28**).^{16,32,50} Recently, Zhang and Hao suggested that protonation of the anionic nitrogen intermediate formed from the hydrolysis of ampicillin (**5**) by the B1 NDM-1 MBL occurs through the participation of the newly formed C-7 carboxylate group which acts as the proton donor (Figure 1.22).^{16,51}

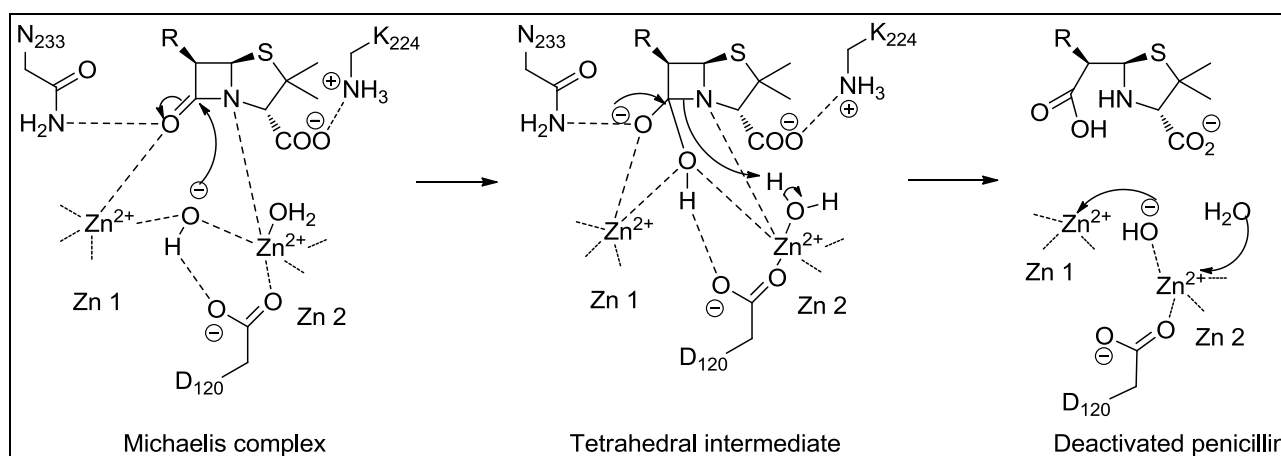
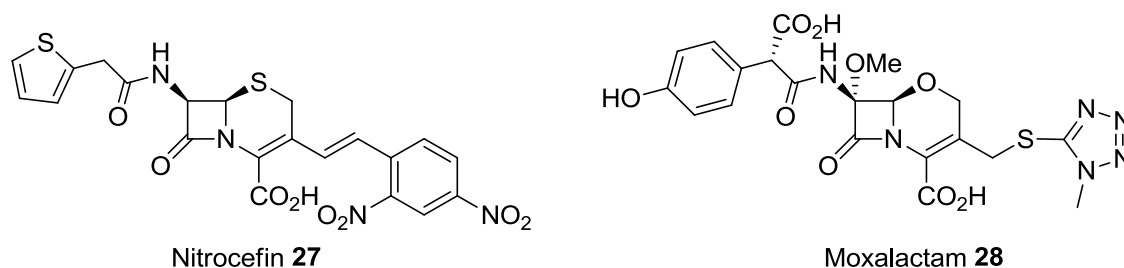


Figure 1.20: The mechanism of di-zinc MBLs as proposed by Herzberg and Fitzgerald⁴⁰, as well as Page and Badarau.³² R represents the *N*-acyl moiety of penicillin.

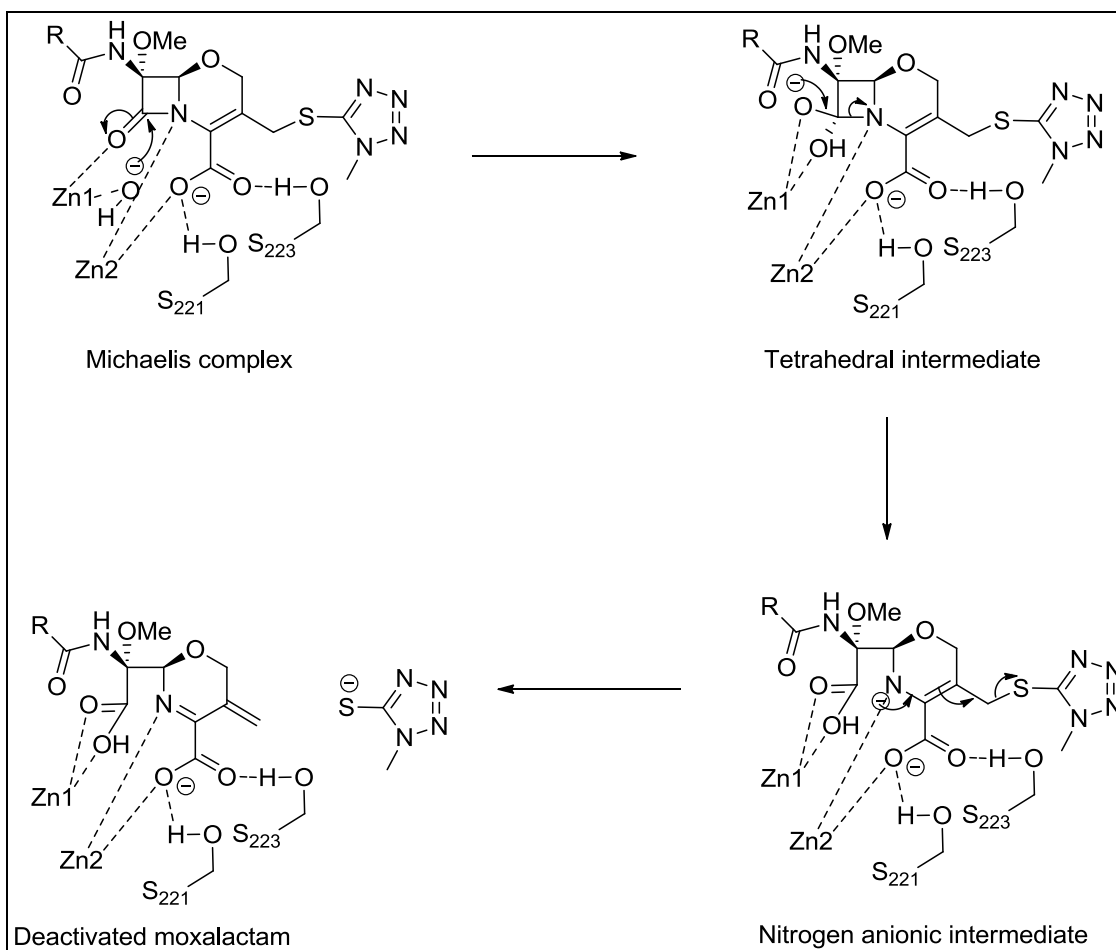


Figure 1.21: The mechanism of moxalactam (**28**) hydrolysis by the B3 L1 MBL as proposed by Spencer *et al.*⁵⁴ R represents the *N*-acyl side chain of moxalactam (**28**). The attacking nucleophile is suggested to be a terminally positioned, Zn1- bound hydroxide ion.

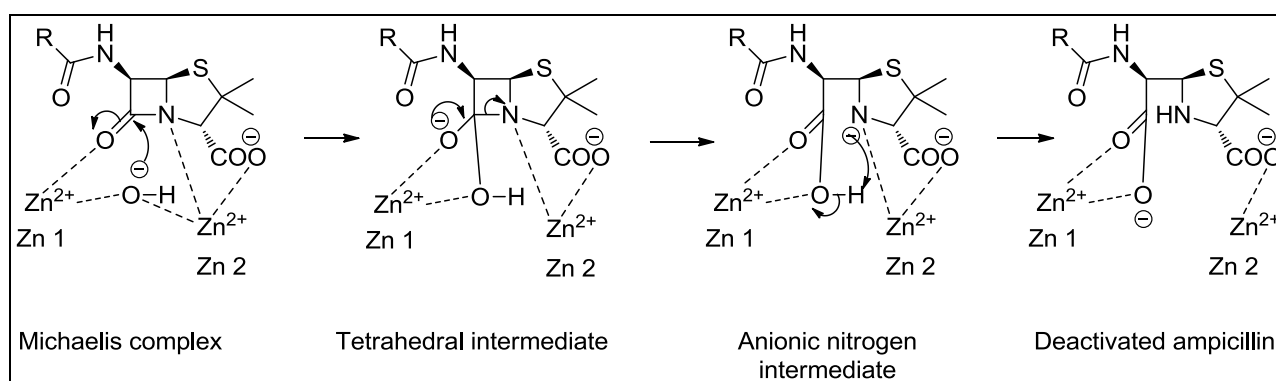


Figure 1.22: The mechanism of ampicillin (**5**) hydrolysis by the B1 NDM-1 MBL as proposed by Zhang and Hao.⁵¹ R represents the *N*-acyl side chain of ampicillin (**5**).

On the contrary, the attacking nucleophile involved in the hydrolysis of carbapenems by B2 MBLs is a water molecule activated by His118 and Asp120 (Figure 1.23).^{32,56} The Zn²⁺ ion plays a role in substrate binding of the C-3 carboxylate oxygen and stabilising the nitrogen anionic intermediate formed from the nucleophilic attack of the activated water molecule on the carbapenem carbonyl carbon.^{16,32,55,56} Additionally, the anionic intermediate is also stabilised by electron delocalisation into the C2=C3 double bond of the carbapenem five-membered ring.⁵⁶ Interestingly, this resonance effect allows an intramolecular arrangement involving the C-8 hydroxyethyl group as the nucleophile, to take place, resulting in a bicyclic intermediate.^{32,55,56} Lys224 and Asn233, which are both involved in substrate binding in B1 MBLs are also conserved among B2 MBLs.^{16,55,56,61}

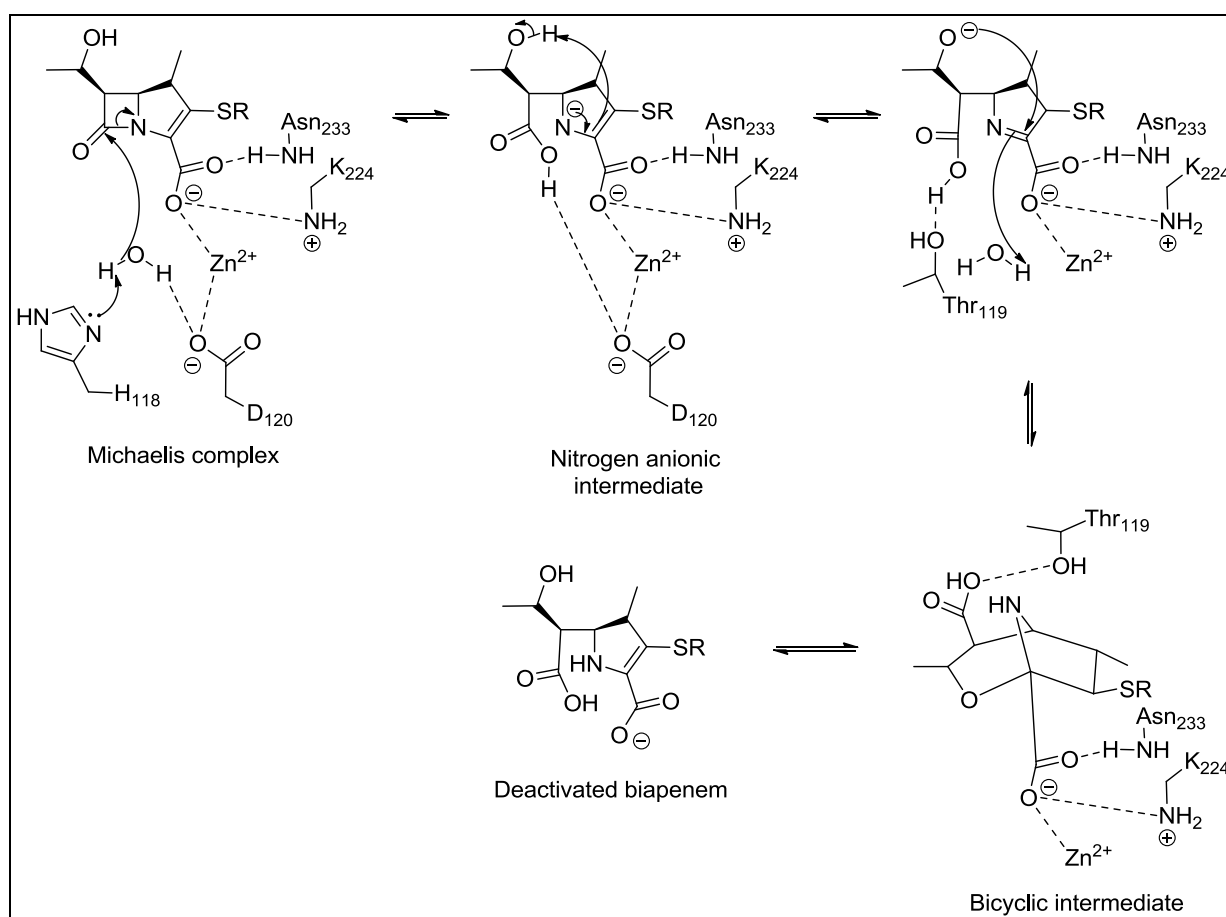
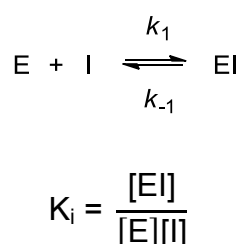


Figure 1.23: The proposed mechanism of mono-zinc CphA catalysed hydrolysis of carbapenem. The carbapenem substrate is highlighted in red and the zinc centre is in green. Rotation about the C5-C6 bond of intermediate (b) gives intermediate (c) and reforms the hydrolytic water molecule (figure adapted from Garau *et al.*).⁵⁵

1.11 General classification of inhibitors and reported reversible inhibitors of MBLs

The design of a clinically useful, versatile or broad-spectrum MBL inhibitor remains a formidable challenge due to differences in the amino acid sequence, particularly active site amino acid residues, requirement of Zn^{2+} ions in catalysis, hydrolytic mechanism and structural features close to the active site such as flexible loops or an elongated α -helix among MBLs.^{6,52,62-64} Despite these complexities, there have been numerous inhibitors of MBLs reported in the literature.^{2,52,62} These inhibitors can be classified according to their respective pharmacophores.⁵²

The potency of an inhibitor is expressed in terms of its IC_{50} or K_i value. The half maximal inhibitory concentration (IC_{50}) is the inhibitor concentration required to reduce the enzyme activity by half at a particular substrate concentration, whereas K_i is the inhibition constant for the equilibrium between the bound and unbound forms of the inhibitor with the enzyme (Scheme 1.5).^{65,66} The lower the IC_{50} or K_i value, the more potent the inhibitor is against the enzyme.



Scheme 1.5: The expression of inhibition constant, K_i in terms of enzyme-inhibitor complex concentration, $[EI]$; enzyme concentration, $[E]$ and inhibitor concentration, $[I]$.

Inhibitors can be generally divided into two categories - irreversible and reversible inhibitors, with the former forming stable covalent bonds with the enzyme and thus decreasing the active enzyme concentration, while the latter doesn't form any stable covalent bonds with the enzyme.⁴²

Reversible inhibitors can be further classified into three types: competitive, non-competitive or uncompetitive inhibitors, on the basis of the inhibitor's effect on the kinetic profile of the enzyme-catalysed reaction (Table 1.6).⁴² The rest of this section is a documentation of selected reversible MBL inhibitors found in the literature.

Table 1.6: Classification of reversible inhibitors on the basis of its kinetic effect and implication on enzyme inhibition.

Inhibitor type	Kinetic effect ^{a42}	Implication ⁴²	Equation ^{b66}
Competitive	K_m is increased but V_{max} is unaffected	The inhibitor competes with the substrate at the same binding site. Inhibition can be surmounted by increasing substrate concentration.	$ \begin{array}{c} \text{S} \\ \text{E} \rightleftharpoons \text{ES} \rightarrow \text{P} + \text{E} \\ \updownarrow \text{I} \\ \text{EI} \end{array} $
Non-competitive	V_{max} is decreased but K_m is unaffected	Inhibitor binds at a site which is distinct from that of the substrate binding site. Inhibitor binding and substrate binding are independent events. Therefore inhibition is not affected by substrate concentration.	$ \begin{array}{c} \text{S} \\ \text{E} \rightleftharpoons \text{ES} \rightarrow \text{P} + \text{E} \\ \updownarrow \text{I} \quad \updownarrow \text{I} \\ \text{EI} \rightleftharpoons \text{ESI} \end{array} $
Uncompetitive	Both K_m and V_{max} are decreased	Inhibitor binding can only take place upon binding of the substrate to the enzyme. The enzyme-substrate specificity ratio, k_{cat}/K_m is unchanged.	$ \begin{array}{c} \text{S} \\ \text{E} \rightleftharpoons \text{ES} \rightarrow \text{P} + \text{E} \\ \quad \quad \quad \updownarrow \text{I} \\ \quad \quad \quad \text{ESI} \end{array} $

^a V_{max} is the limiting reaction rate of the enzyme-catalysed reaction at a specific enzyme concentration, whereby all of the active sites of the enzyme molecules are occupied by the substrate molecules. ^bE, S, I and P denotes enzyme, substrate, inhibitor and product, respectively.

1.11 a) Generic metal chelators

As mentioned previously, MBLs are inhibited by common metal chelators such as EDTA (**26**) and dipicolinic acid (**29**) (Figure 1.24).^{67,68} EDTA (**26**) in tandem with other small molecular weight thiol compounds (**30-32**), are routinely used in biochemical assays in the identification of MBL-expressing bacteria (Figures 1.24 and 1.25).^{40,41,69} However, EDTA (**26**) and other non-specific metal chelators are not clinically useful inhibitors as there is a high probability that these chelators might interfere with the activity of existing, endogenous metalloenzymes in the human body.^{6,15,62,69}

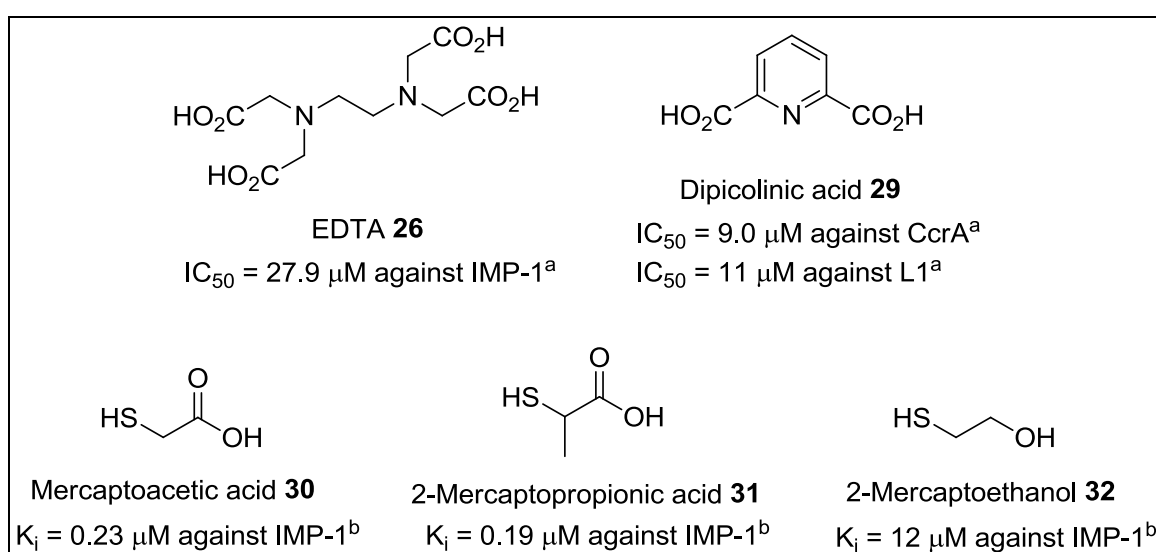


Figure 1.24: Generic metal chelators and small molecular weight thiol inhibitors of MBLs used in biochemical assays to identify MBL-producing bacteria (^a IC_{50} values were taken from Roll *et al.*⁶⁷ and Chen *et al.*⁶⁸, while ^b K_i values were taken from Goto *et al.*⁷⁰)

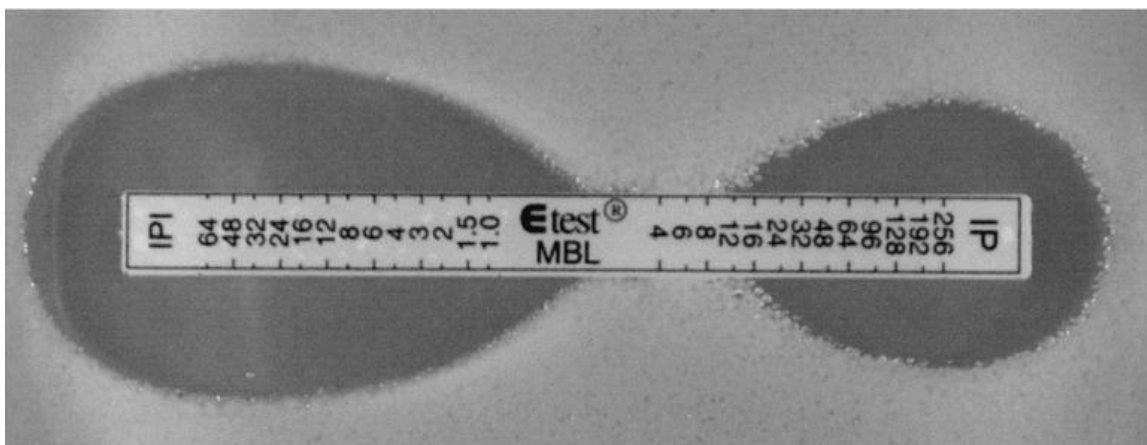


Figure 1.25: An Etest® MBL testing strip on a *Serratia marcescens* expressing IMP-1 culture plate. IP and IPI denotes “solely imipenem” and “imipenem plus EDTA”, respectively. The numbers on the strip represent the varying concentration of imipenem in $\mu\text{g mL}^{-1}$ and the quantity of EDTA in the IPI portion of the strip is set at a constant, final concentration of $320 \mu\text{g mL}^{-1}$. The MIC* of imipenem against the particular strain of *S. marcescens* decreased from 16 to $\leq 1.0 \mu\text{g mL}^{-1}$ when exposed to $320 \mu\text{g mL}^{-1}$ of EDTA (reproduced with permission from American Society for Microbiology, 27/11/15).⁷¹

*The minimum inhibitory concentration (MIC) is the lowest concentration of an antimicrobial agent that inhibits the visible growth of a microorganism after overnight incubation.⁷²

1.11 b) Trifluoromethyl alcohol and ketone inhibitors

Walter *et al.* was the first to report synthetic MBL inhibitors in 1996.^{2,73} They designed and assayed some α -amido trifluoromethyl alcohols and ketones against B1, B2 and B3 MBLs (Figure 1.26).⁷³ The idea behind the design of these compounds was that trifluoromethyl ketones are tetrahedral intermediate analogues of serine proteases and inhibitors of the mono-zinc carboxypeptidase A metalloenzyme.⁷³ The synthesis of the inhibitors was accomplished using Ruppert’s Reagent (TMS-CF_3) on corresponding oxazolidin-5-ones which were derived from L- and D-amino acids (Scheme 1.6).⁷³ The inhibitors are moderately potent against CphA and LI but not potent against the B1 MBLs tested (Table 1.7).⁷³

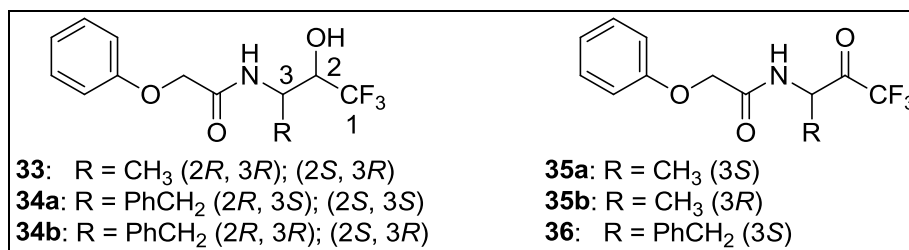
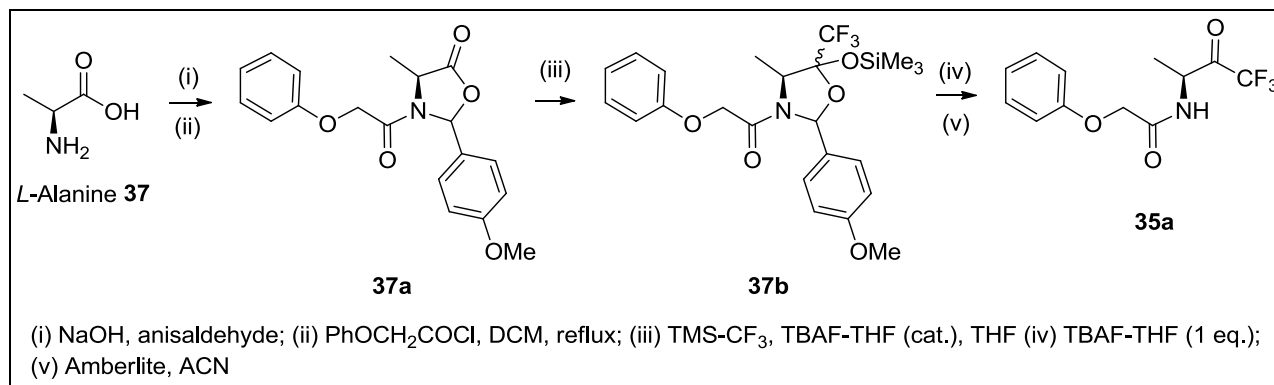


Figure 1.26: A selection of trifluoromethyl alcohol and ketone inhibitors from Walter *et al.*⁷³



Scheme 1.6: The synthesis of **35a** by addition of Rupert's reagent (TMS-CF₃) on the corresponding oxazolidin-5-one **37a**.⁷³

Table 1.7: The competitive inhibition constants, K_{ic} (μ M) of the trifluoromethyl alcohol and ketone inhibitors, **33-36** against the tested B1, B2 and B3 MBLs.⁷³

Inhibitor	K_{ic} (μ M)			
	B1*		B2	B3
	<i>IMP-1</i>	<i>BcII</i>	<i>CphA</i>	<i>L1</i>
33	400	700	217 \pm 2	35 \pm 2
34a	900	1000	19 \pm 1	> 5000
34b	60	30	20 \pm 1	>5000
35a	300	300	44 \pm 2	1.5 \pm 0.01
35b	500	700	11 \pm 0.5	3.0 \pm 0.4
36	530	500	6 \pm 0.4	15 \pm 1

*Errors were not reported.

1.11 c) Biphenyl tetrazole inhibitors

In 1998, Toney and colleagues identified a series of biphenyl tetrazoles as potent inhibitors of a mutant B1 CcrA MBL from a screening campaign of the Merck chemical collection and molecular docking study (Table 1.8).³⁸ The inhibitors were also shown to exhibit low activity (IC_{50} values of 120 μ M to >1 mM) against mammalian dehydropeptidase-1 (DHP-1), an endogenous renal metalloenzyme which hydrolyses imipenem (**7**).^{11,38} The results imply that the biphenyl tetrazole inhibitors are to a certain extent specific towards the tested MBL.⁶²

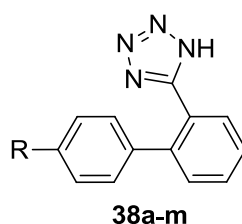
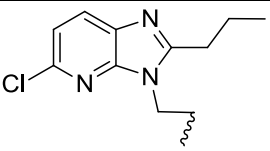
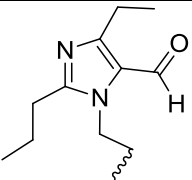
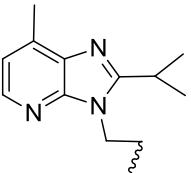


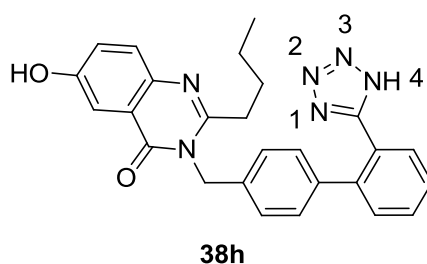
Table 1.8: The IC_{50} (μ M) data of a series of biphenyl tetrazoles, **38a-m** against a variant of the B1 CcrA MBL.³⁸

Inhibitor 38	Substituent R	IC_{50} (μ M)	Inhibitor 38	Substituent R	IC_{50} (μ M)
a	H	860 \pm 60	h		1.9 \pm 0.2
b	CH ₃	160 \pm 20	i		42 \pm 7
c		110 \pm 9	j		6 \pm 1
d		4 \pm 1	k		0.30 \pm 0.02
e		42 \pm 10	l		0.4 \pm 0.1

f		3.5±0.4	m		7±3
g		1.8±0.4			

The IC₅₀ data showed that biphenyl tetrazole **38k** was the most potent inhibitor against the MBL assayed.³⁸ However, **38k** was also the most active inhibitor against mammalian DHP-1.³⁸ Biphenyl tetrazoles **38f**, **h** and **l** were later found to be potent, competitive inhibitors against the same MBL tested, with K_i values ranging from 0.59-1.6 μM.³⁸

Biphenyl tetrazole **38h** was later selected for co-crystallisation with the same MBL (Figure 1.27).³⁸ The 3D structure shows that the tetrazole N-1 of **38h** binds to Zn²⁺ in a way that displaces the apical water bound to the said metal centre. In addition, the biphenyl moiety of **38h** has favourable hydrophobic interactions with the flexible loop that is positioned above the active site.³⁸ This flexible β-hairpin loop is common among most B1 MBLs, and is also known as the L3 loop (Section 1.9).^{51,62}



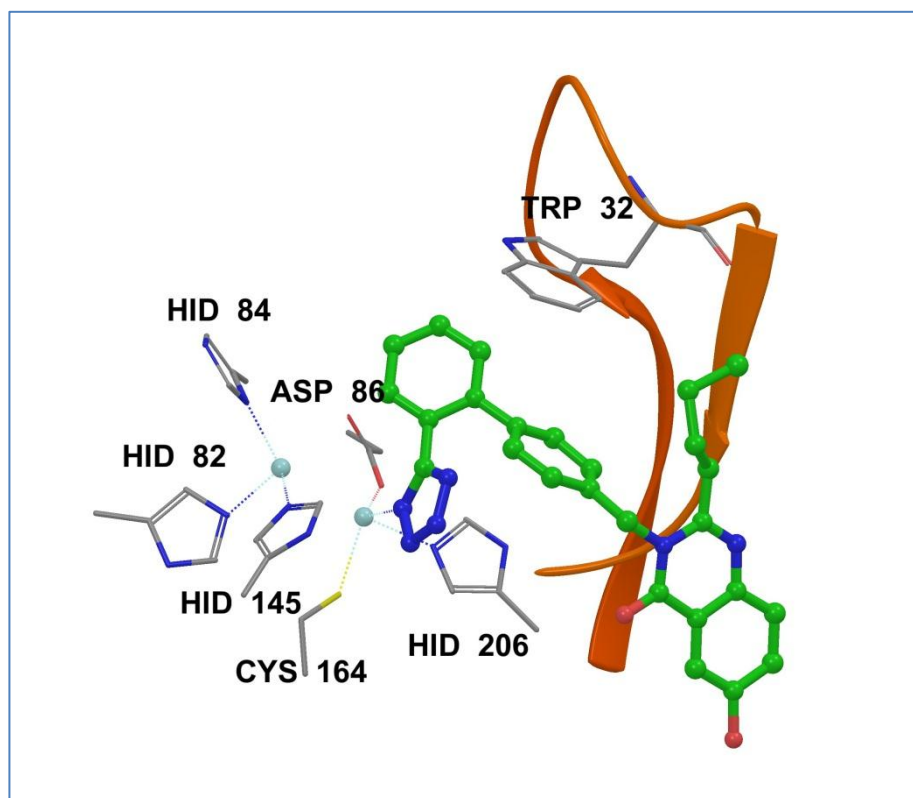
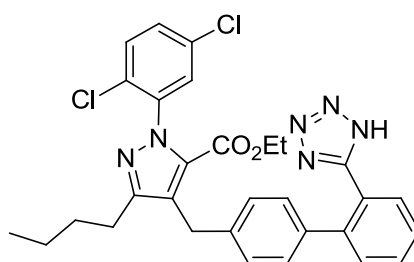


Figure 1.27: The X-ray structure of biphenyl tetrazole **38h** (ball and stick diagram) co-crystallised with a variant of the B1 CcrA MBL (atom-atom distance: N1-Zn2, 2.36 Å) (PDB no. 1A8T).³⁸ Atom colours: carbon on inhibitor **38h** and enzyme is green and grey, respectively; nitrogen in dark blue; oxygen in red, sulfur in gold and the L3 loop is in orange. The Zn centres are depicted as cyan spheres (figure drawn with Maestro).⁹⁶

Toney *et al.* later expanded the work by assaying a series of synthetic biphenyl tetrazoles on the CcrA and IMP-1 B1 MBLs.⁷⁴ Synthetic biphenyl tetrazole **39** was found to exhibit moderate inhibitory potency against both of the B1 MBLs tested.⁷⁴



39

IC₅₀ = 100 μM against CcrA
 IC₅₀ = 60 μM against IMP-1

1.11 d) Mercaptocarboxylate inhibitors

The high potency and broad spectrum inhibitory activity demonstrated by some mercaptocarboxylates against MBLs have made this class of inhibitors the most studied of all MBL inhibitors.^{2,64} As noted before, low-molecular-weight mercaptocarboxylate inhibitors are being employed in the identification of MBL-expressing bacteria (Section 1.11 a). Some representative mercaptocarboxylate inhibitors, together with the collated inhibition data of the inhibitors are shown in Figure 1.28 and Table 1.9, respectively.

Racemic thiomandelic acid (**40**) was the first reported mercaptocarboxylate-type broad spectrum MBL inhibitor in 2001.⁷⁵

L-Captopril (**42**) is a commercially available antihypertensive drug which functions by inhibiting the mono-zinc angiotensin-converting enzyme (ACE).^{76,77} Its diastereomer, D-captopril (**41**) is only accessible by synthesis from D-proline.⁷⁸ Both D- and L-captopril (**41** and **42**) have been studied as broad spectrum inhibitors of MBLs with the D-isomer exhibiting more potent inhibitory activity than the L-isomer against the MBLs tested.⁷⁷⁻⁸⁰

Thus far, the most potent broad spectrum mercaptocarboxylate inhibitors have been identified by Liénard *et al.* to be **43** and **45a-c**, including a simple α -ketothiol **44** (2008).⁶⁴ All five inhibitors are highly potent against all three MBL subclasses with some K_{ic} values in the nM range.⁶⁴

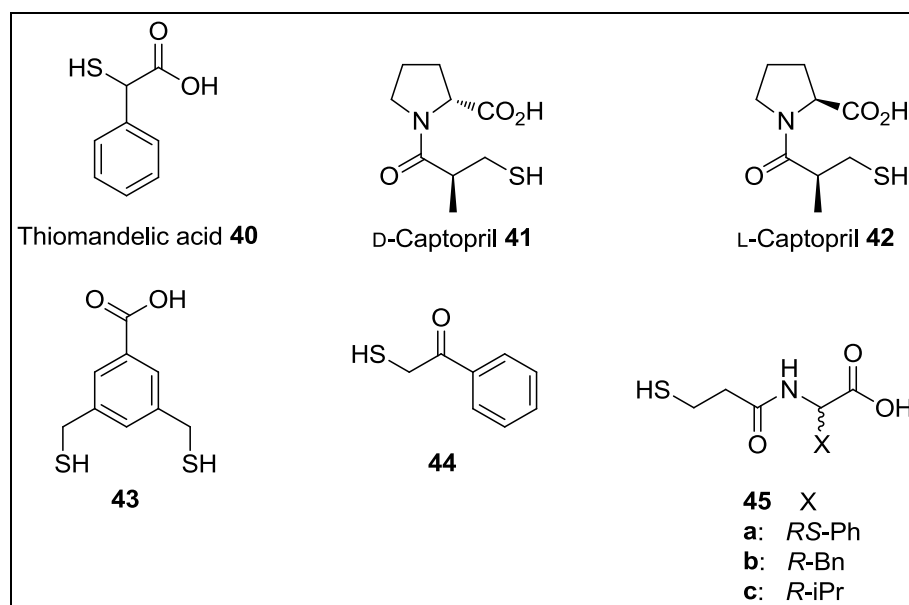


Figure 1.28: A selection of mercaptocarboxylate inhibitors, together with an α -ketothiol **44** reported in the literature.

Table 1.9: Collated inhibition data of the mercaptocarboxylate inhibitors, **40-43** and **45a-c**, including α -ketothiol **44** against the tested B1, B2 and B3 MBLs.^{64,75,77-80}

Inhibitor	B1			B2	B3	
	<i>IMP-1</i> ^a (μ M)	<i>BclI</i> ^a (μ M)	<i>NDM-1</i> ^b (μ M)	<i>CphA</i> ^a (μ M)	<i>L1</i> ^a (μ M)	<i>FEZ-1</i> ^a (μ M)
<i>Rac</i> -Thiomandelic acid (40)	0.029 ^c	0.34 ^c	-	144 ^c	0.081 ^c	0.27 ^c
D-Captopril (41)	-	45 \pm 5	7.9 ^b	72 \pm 6	20	-
L-Captopril (42)	12.5 \pm 2.4	63 \pm 5	202 ^b	950 \pm 80	-	-
43	0.36 \pm 0.01	0.97 \pm 0.2	-	0.09 \pm 0.004	0.21 \pm 0.01	0.3 ^b
44	0.67 \pm 0.09	2.7 \pm 0.2	-	0.05 \pm 0.02	0.24 \pm 0.01	1 ^b
45a	0.019 \pm 0.002	7.7 \pm 0.7	-	5.7 \pm 2.0	1.8 \pm 0.4	-
45b	0.088 \pm 0.010	0.85 \pm 0.08	-	15.0 \pm 5.0	0.96 \pm 0.08	-
45c	0.063 \pm 0.009	0.32 \pm 0.01	-	3.6 \pm 0.3	0.082 \pm 0.002	-

^a K_{ic} values. ^b IC_{50} values. ^c Standard deviation less than 20%. “-“ denotes not determined.

The noteworthy inhibitory properties of mercaptocarboxylates are attributed to two important types of interaction: the thiolate functional group which binds strongly to the Zn^{2+} ions and the carboxylate functional group which forms a salt bridge with the conserved Lys224 residue in B1 MBLs, or a hydrogen bond with the serine equivalent (Ser225) in B3 MBLs.^{52,62,64,77,81} Intercalation between the thiolate functional group and the Zn^{2+} ions in di-zinc MBLs results in the displacement of the bridging hydroxide ion, which is essentially

required for catalysis.^{6,52,64,77,81-83} This typical thiolate-Zn²⁺ binding mode is explicitly illustrated in the 3D structure of B1 BlaB MBL in complex with D-captopril (**41**) (Figure 1.29a).^{64,82}

The 3D structure of the mono-zinc CphA-D-captopril complex, however, shows that D-captopril (**41**) binds to the Zn²⁺ centre of CphA through its carboxylate functional group rather than the expected thiolate group (Figure 1.29b).⁶⁴ Unexpectedly, the thiol group of D-captopril was shown to interact with non-polar amino acid residues, such as Phe156, and Asn233.⁶⁴ This fascinating observation shows that the same mercaptocarboxylate inhibitor can adopt different binding modes to di-zinc and mono-zinc MBLs, while still retaining its inhibitory activity.⁶⁴

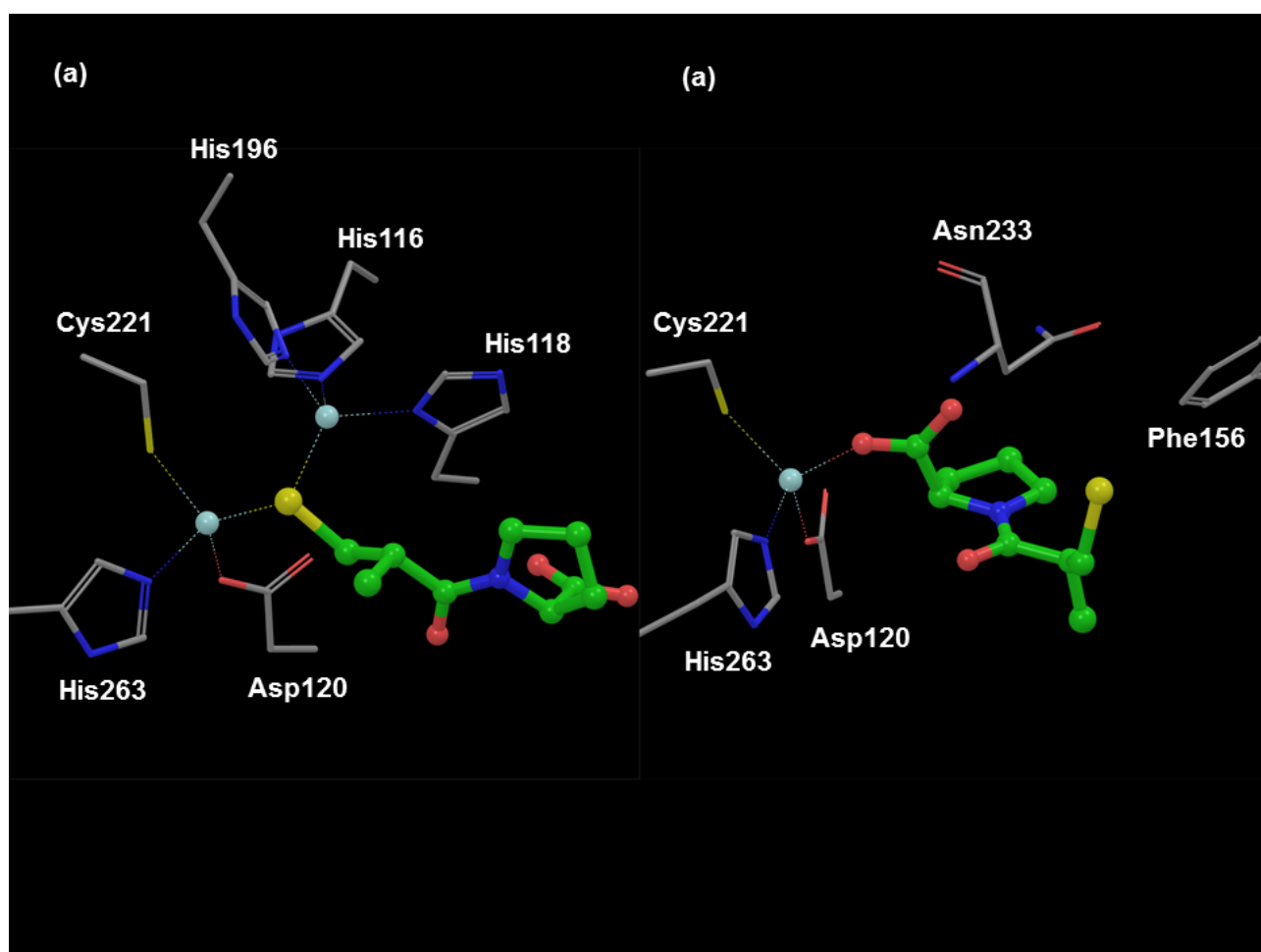
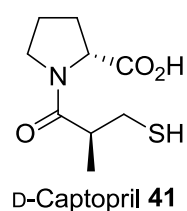


Figure 1.29: Active site view from the crystal structure of (a) BlaB-D-captopril complex (atom-atom distance: S-Zn1, 2.32 Å; S-Zn2, 2.30 Å) (PDB no.: 1M2X)⁸²; (b) CphA-D-captopril complex (O2-Zn distance is 2.1 Å) (PDB no.: 2QDS).⁶⁴ Atom colours: carbon on D-captopril (**41**) and enzyme in green and gray, respectively; nitrogen in blue; oxygen in red and sulfur in gold. The Zn²⁺ ion(s) are shown as cyan spheres (figures drawn with Maestro).⁹⁶

1.11 e) Mercaptophosphonate inhibitors

Lassaux *et al.* were the first group to design and test mercaptophosphonates as potent, broad-spectrum inhibitors of MBLs.⁶³ Based on the pharmacophore of thiomandelic acid (**40**), Lassaux and colleagues introduced the phosphonate group as a bioisostere of the carboxylate group.^{63,84} The molecular structure of the mercaptophosphonate inhibitors, including the competitive inhibition constant, K_{ic} data of the inhibitors are displayed in Figure 1.30 and Table 1.10, respectively.

In order to study the metal chelating strength of the mercaptophosphonate inhibitors, Lassaux *et al.* performed the inhibition assays of the di-zinc VIM-4 and L1 MBLs at two different concentrations of Zn²⁺ (0.4 μM and 50 μM).⁶³ An example of the results interpretation is as such: the substantial increase in K_{ic} values for **47b** in the presence of excess Zn²⁺ for both the di-zinc MBLs shows that **47b** is a significantly strong metal chelator. This is because, in the presence of a much higher concentration of Zn²⁺, **47b** binds to the excess zinc ions, leaving most of the enzyme unbound, which in turn increases the K_{ic} values significantly.⁶³

Inhibitors **46b**, **47a**, **49a** and **49b** were identified by Lassaux and colleagues as significantly potent MBL inhibitors, with K_{ic} values ranging from 0.25-32 μM. In addition, inhibitor **51**, which is the di-chloro analogue of **49b** showed improved potency against all the MBLs tested, in comparison to the non-substituted inhibitor, **49b**.⁶³

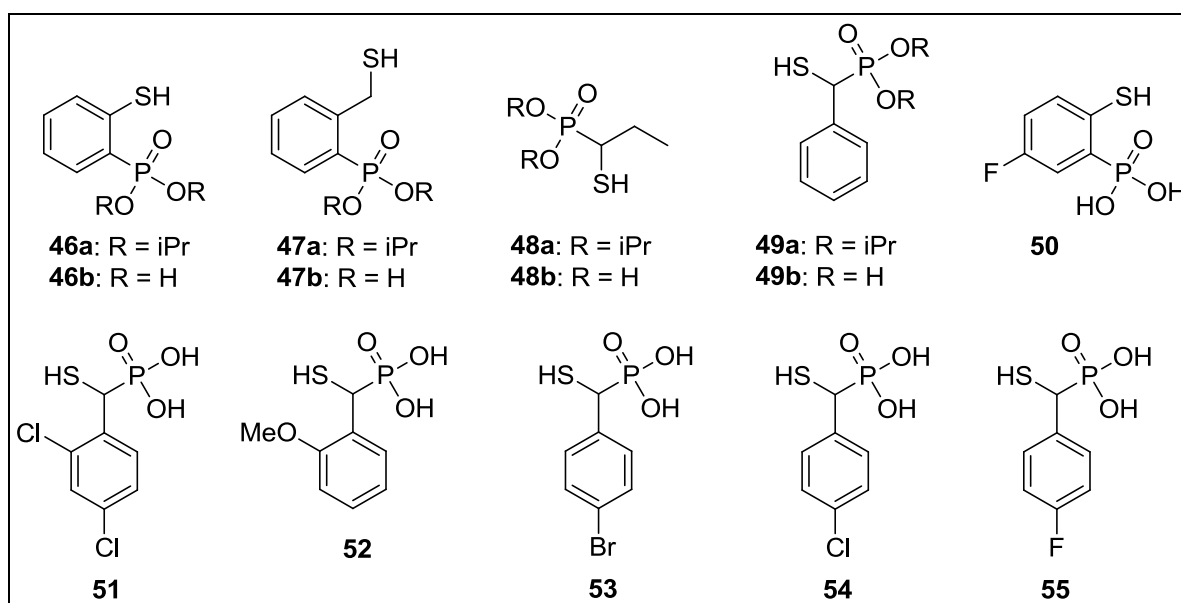


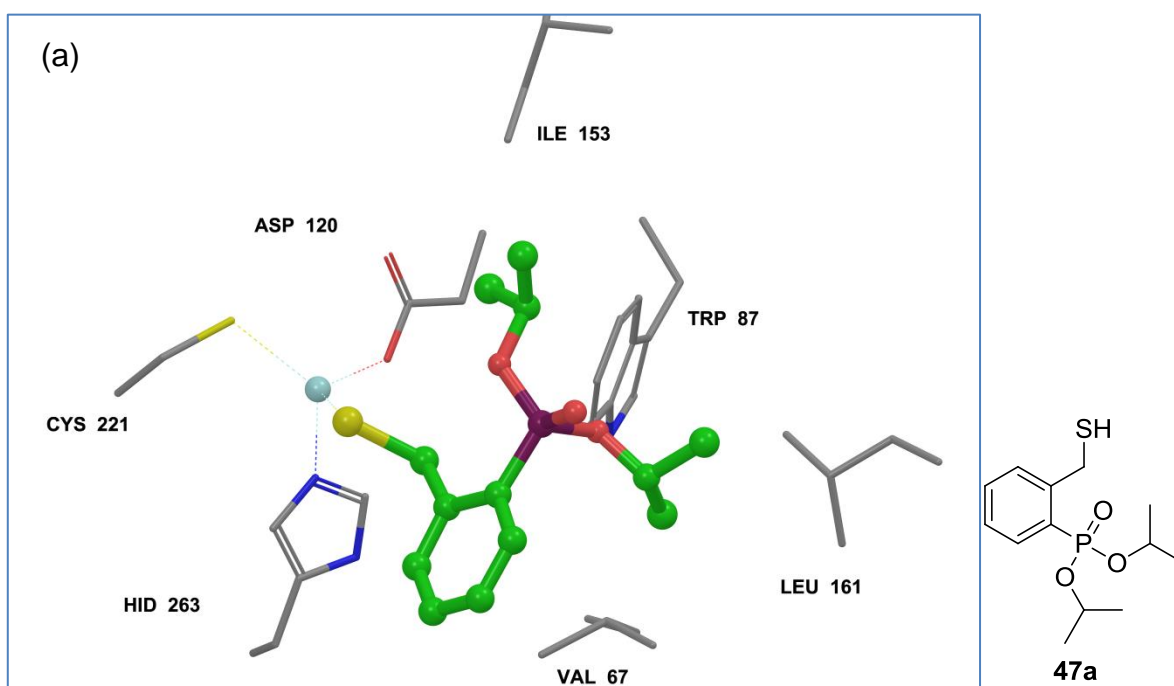
Figure 1.30: Mercaptophosphonate inhibitors studied by Lassaux *et al.*⁶³

Table 1.10: The K_{ic} data (μM) of mercaptophosphonate inhibitors, **46a-55** against MBLs.⁶³

Inhibitor	K_{ic} (μM)				
	VIM-4 (B1)		CphA (B2), >0.4 μM of Zn^{2+}	L1 (B3)	
	50 μM of Zn^{2+}	>0.4 μM of Zn^{2+}		50 μM of Zn^{2+}	>0.4 μM of Zn^{2+}
46a	>250	>250	>250	>250	>250
46b	4	2	7	12	9
47a	12	3	2	14	3
47b	>400	1	0.5	>50	2
48a	>20	>20	2	>40	>40
48b	6	11	15	>40	>80
49a	8	3	0.25	16	20
49b	3	2.5	11	32	>100
50	13	2.5	>40	4	40
51	4	1	5	0.40	0.40
52	4	2	15	4	9
53	13.5	5.5	13	1.7	8.4
54	10	6.7	24	0.7	3.8
55	11	16	1	18	>20

Interestingly, the 3D structures of **47a** and **51** co-crystallised with mono-zinc B2 CphA MBL illustrate that mercaptophosphonate ester and mercaptophosphonic acid exhibit distinct binding modes with the enzyme (Figure 1.31).⁶³ In the CphA-**47a** complex, the thiolate functional group is responsible for binding to the Zn²⁺ ion (Figure 1.31a).⁶³ Molecular docking suggested that the two bulky isopropyl groups of **47a** may have blocked the phosphonate oxygen of the inhibitor from binding to the Zn²⁺ ion.⁶³

On the other hand, inhibitor **51** binds to the Zn²⁺ ion *via* two of its phosphonate oxygen atoms (O11 and O12) (Figure 1.31b).⁶³ The thiol group of inhibitor **51** instead, interacts with a water molecule (W347, 3.06 Å) and the backbone nitrogen of Asn233 (3.45 Å), which is part of the Gly232-Asn233 loop that closes upon inhibitor binding.⁶³ In addition, O12 of inhibitor **51** also has an interaction with Lys224, *via* a hydrogen bond (2.72Å).⁶³



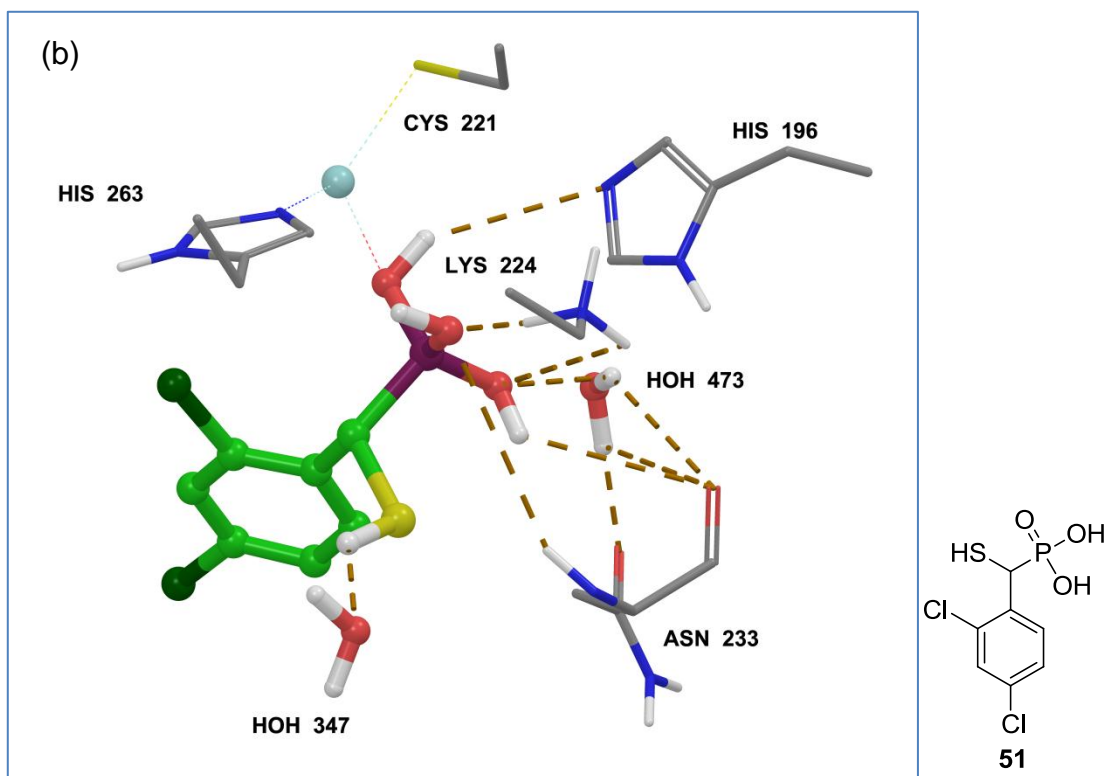


Figure 1.31: Active site view from the crystal structure of (a) CphA in complex with **47a** (S-Zn distance is 2.31 Å) (PDB no.: 3IOF);⁶³ (b) CphA in complex with **51** (atom-atom distance: O11-Zn, 1.98 Å; O12-Zn, 3.38 Å) (PDB no.: 3IOG).⁶³ Atom colours: carbon on inhibitor and enzyme in light green and grey, respectively; chlorine in dark green; nitrogen in blue; oxygen in red; phosphorus in magenta and sulfur in gold. Water molecules and the Zn²⁺ ion are shown as red and cyan spheres, respectively. Protein-ligand interactions are depicted as dashed lines (figures were drawn with Maestro).⁹⁶

In summary, the X-ray crystal structures of mercaptocarboxylate inhibitors and mercaptophosphonate inhibitors bound to MBLs reveal that in the di-zinc MBLs, the thiolate group binds to the zinc ions, whereas in the mono-zinc MBLs, the carboxylate or phosphonate group has the propensity to bind to the mono-zinc centre.^{63,64,77,81}

1.11 f) Dicarboxylic acid and other MBL inhibitors

Toney *et al.* made yet another fruitful discovery from the screening of the Merck compound library, when the authors successfully identified a few succinic acid derivatives, **56a-c** as highly potent inhibitors of the di-zinc IMP-1 MBL, with nanomolar potency (Figure

1.32 and Table 1.11).⁵⁷ The presence of the bulky, aromatic side chains in tandem with carboxylate groups at the 2S, 3S position are vital for the observed potency of inhibitors **56a-c**.⁵⁷

The X-ray crystal structure of **56a**-IMP-1 revealed that both of the carboxylate groups of **56a** bind to the Zn²⁺ ions, with one of the 2S carboxylate oxygens intercalating both of the Zn²⁺ centres and the 3S carboxylate oxygen in direct contact with Zn2 (Figure 1.33).⁸⁵ The result of these Zn-carboxylate oxygen interactions is the displacement of both the bridging hydroxide ion and apical water molecule, which were originally in the native enzyme.⁵⁷ The remaining 2S and 3S carboxylate oxygen atoms of **56a** have hydrogen bond interactions with the conserved Asn233 and Lys224 residues, respectively.⁵⁷ In addition, the aromatic side chains of **56a** are shown to make favourable hydrophobic interactions with the adjacent, flexible L3 loop, which is defined by Val61, Trp64 and Val67.⁵⁷ The L3 loop is stabilised and closes the active site upon binding to the inhibitor or β -lactam substrate.^{51,81}

In silico, or computational screening of the Available Chemicals Database (ACD) based on the 3D structures of inhibitors **56a** and **59** bound to IMP-1 (Figures 1.33 and 1.34, respectively), led to the identification of **57** and **58**, as the two most potent inhibitors out of thirteen hits assayed (Figure 1.32 and Table 1.11).⁸⁵ However, in comparison with other reported MBL inhibitors, dicarboxylic acids **57** and **58** are only moderately potent MBL inhibitors, with IC₅₀ values in the range of 10-100 μ M.⁸⁵

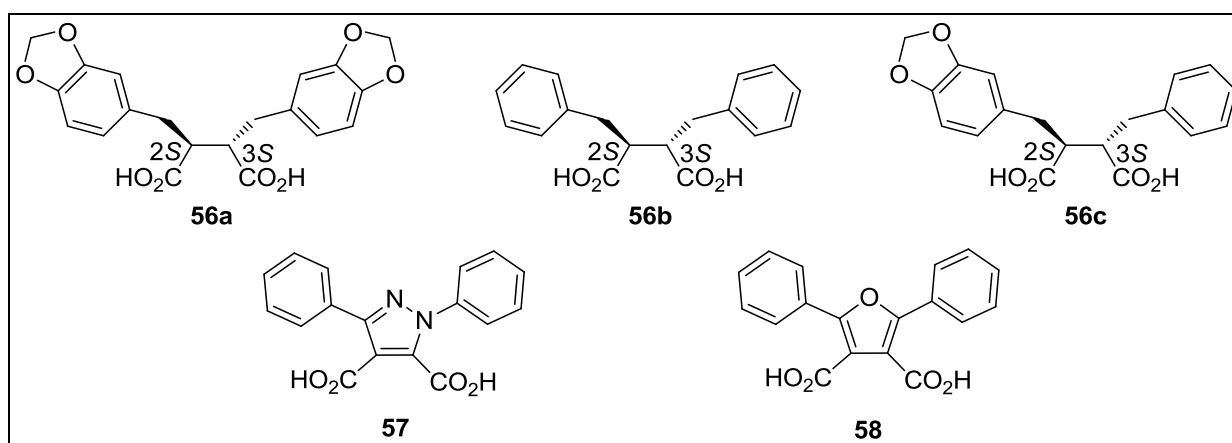


Figure 1.32: Dicarboxylic acid inhibitors, **56a-c**, **57** and **58**, as reported by Toney *et al.*⁵⁷ and Olsen *et al.*⁸⁵

Table 1.11: The IC₅₀ data (μM) of dicarboxylic acid inhibitors, **56a-c**, **57** and **58** against the B1 and B3 MBLs tested.^{57,85}

Inhibitor	IC ₅₀ (μM)*		
	B1		B3
	<i>IMP-1</i>	<i>BcII</i>	<i>L1</i>
56a	0.009	-	-
56b	0.0027	-	-
56c	0.0037	-	-
57	-	14	150
58	-	7	30

"-"denotes not determined. *Errors were not reported.

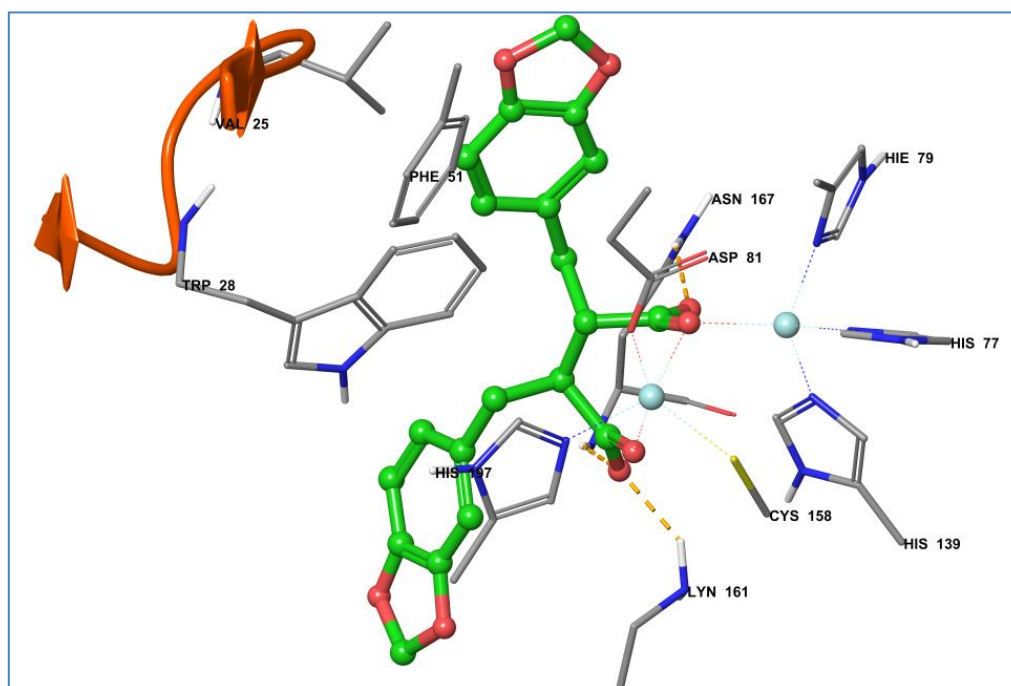
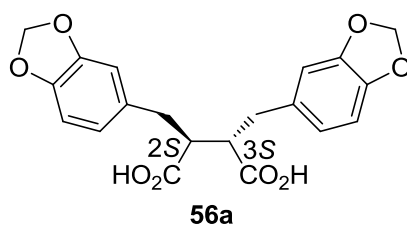
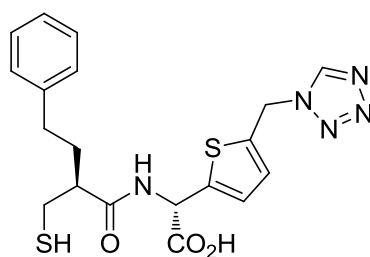


Figure 1.33: Active site view of the crystal structure of **56a** co-crystallized with IMP-1 (atom-atom distance: 2S carboxylate O-Zn1, 2.06 Å; 2S carboxylate O-Zn2, 2.13 Å; 3S

carboxylate O-Zn2, 2.43 Å) (PDB no: 1JJT).⁵⁷ Atom colours: carbon on inhibitor in gray, carbon on IMP-1 in grey, nitrogen in blue, oxygen in red and the L3 loop is in orange. The Zn²⁺ ions are represented as gray spheres (figure drawn with Maestro).⁹⁶



59

IC₅₀ = 0.09 μM against IMP-1

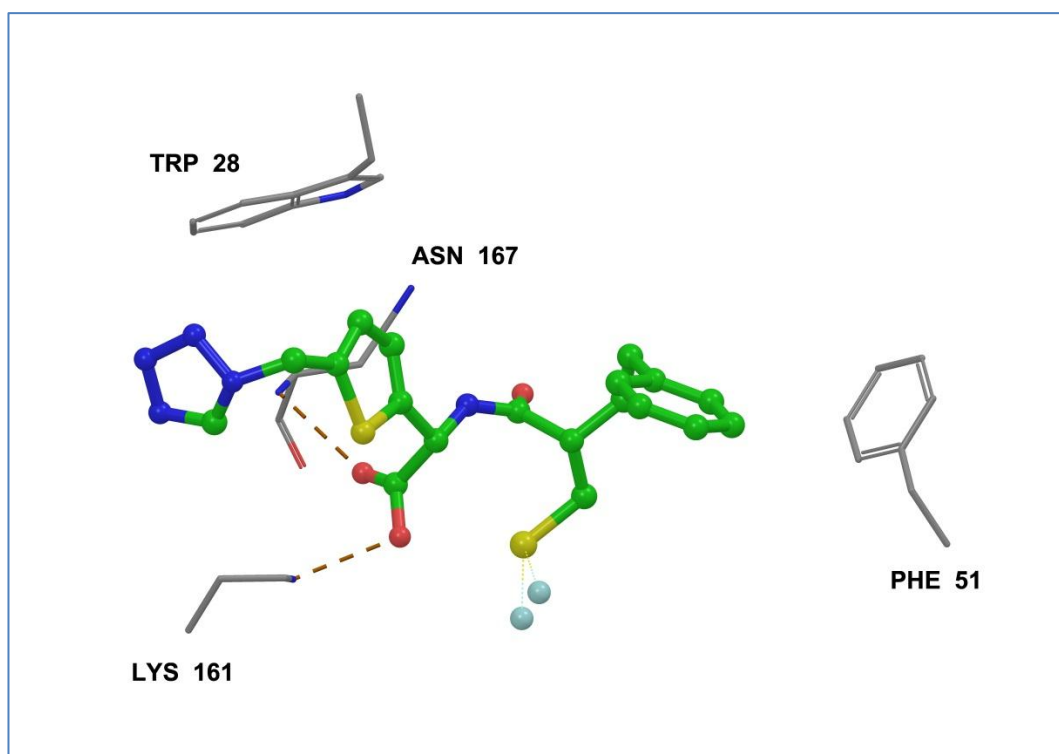
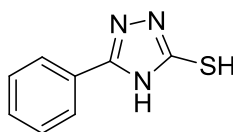


Figure 1.34: Active site view of the crystal structure of **59** co-crystallised with IMP-1 (atom-atom distance: S-Zn1, 2.24 Å; S-Zn2, 2.40 Å) (PDB no: 1DD6).⁸¹ Atom colours: carbon on inhibitor in green, carbon on IMP-1 in grey, nitrogen in blue, oxygen in red and sulfur in gold. The Zn²⁺ ions are represented as gray spheres (figure drawn with Maestro).⁹⁶

Recently, Feng and colleagues synthesised and assayed *N*-heterocyclic dicarboxylic acids **60a-c**, pyridylmercaptotriadiazoles, **61a-b** and pyridylmercaptotriazoles, **62a-b** against representative MBLs from all three subclasses (Figure 1.35, Table 1.12).⁸⁶ Part of their study was also to examine the MIC of β -lactam antibiotics against the MBL-plasmid borne *E. coli* strains in the presence of the inhibitors.⁸⁶

The authors concluded that dicarboxylic **60b** was the only broad-spectrum MBL inhibitor, out of the seven heterocyclic compounds assayed.⁸⁶ Pyridylmercaptotriadiazoles **61a-b**, were only active in inhibiting the B1 and B2 MBLs tested, in an uncompetitive mode.⁸⁶ The authors speculated that both the thiadiazoles may have reduced the sulfide bridge in the B3 L1 MBL and thus were unable to bind in the active site of the enzyme.⁸⁶ The sulfide bridge, which is made up of residues Cys256-Cys290, is conserved among B3 MBLs.^{60,87} On the other hand, pyridylmercaptotriazoles **62a-b**, didn't exhibit any inhibitory activity against the MBLs tested.⁸⁶ This similar observation was also observed by the McGeary and Schenk group, in which the authors found that mercaptotriazole **63** was inactive in inhibiting the B1 IMP-1 MBL, even at a concentration of 1 mM.²⁸



63

Overall, the MBL inhibitory potency of the inhibitors against the free, isolated enzyme is well correlated to the synergistic antibacterial activity of the inhibitor-antibiotic combination (Table 1.12).⁸⁶ An example of the interpretation of the two sets of data is as such: dicarboxylic acid **60b**, which is the only inhibitor that showed activity against the ImiS B2 MBL, recorded the lowest imipenem MIC against the ImiS-plasmid borne *E. coli* when assayed in tandem with the said antibiotic.

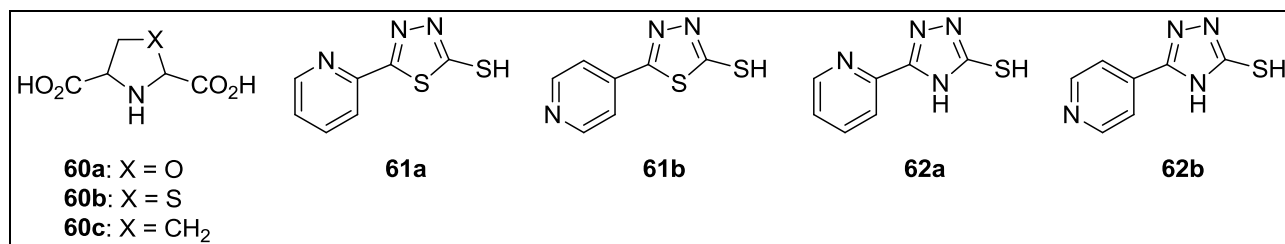


Figure 1.35: The inhibitors, **60a-c**, **61a-b** and **62a-b**, which were studied by Feng *et al.*⁸⁶

Table 1.12: The K_i data (μM) of inhibitors, **60a-c**, **61a-b** and **62a-b**, against the B1, B2 and B3 MBLs tested juxtaposed with the MIC data (μgml⁻¹) of the β-lactam in the inhibitor-antibiotic combinations against MBL- plasmid borne *E. coli* strains.⁸⁶

Inhibitor	K _{ic} (μM)			MIC (μgml ⁻¹)		
	<i>CcrA</i> (B1)	<i>ImiS</i> (B2)	<i>L1</i> (B3)	<i>E. coli-CcrA</i> ^a	<i>E. coli-ImiS</i> ^b	<i>E. coli-L1</i> ^a
No inhibitor	NA	NA	NA	2	4	2
60a	1.1 ± 0.1 ^C	NI	1.9 ± 0.2 ^C	1	4	1
60b	0.64 ± 0.09 ^C	7.1 ± 0.7 ^C	1.8 ± 0.2 ^C	1	0.5	1
60c	0.73 ± 0.06 ^C	NI	0.69 ± 0.03 ^C	0.25	4	0.125
61a	5.4 ± 0.3 ^{NC}	3.5 ± 0.2 ^{NC}	NI	1	2	2
61b	5.9 ± 0.3 ^{NC}	6.8 ± 0.4 ^{NC}	NI	1	2	2
62a	NI	NI	NI	2	4	2
62b	NI	NI	NI	2	4	2

NI denotes no inhibition. NA denotes not applicable. The antibiotic used was ^acefazolin and ^bimipenem, respectively. ^C and ^{NC} denotes competitive and non-competitive inhibition, respectively.

1.11 g) Pyrrole-containing inhibitors

The McGeary and Schenk group were the first group to report IMP-1 inhibitors with a pyrrole scaffold.^{88,89} A selection of the most potent, competitive pyrrole-type inhibitors, together with the K_{ic} data of the inhibitors are displayed in Figure 1.36 and Table 1.13, respectively.

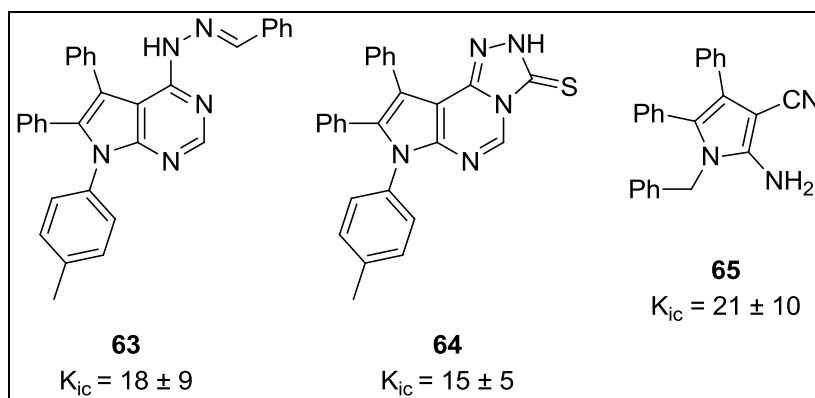


Figure 1.36: A selection of potent, competitive pyrrole-type inhibitors, **63-65** as discovered by the McGeary and Schenk group.^{88,89}

Computational modelling of inhibitor **65** bound into the active site of IMP-1 shows that the amino proton donor group of **65** interacts with the nitrogen atom on the imidazole ring of His197 (His263), which is one of the amino acid ligands of Zn²⁺ (Figure 1.37). In addition, hydrophobic interactions between the two phenyl side chains of **65** and the hydrophobic amino residues Val67 (Val31) and Phe87 (Phe51) of the flexible L3 loop are also observed in the *in silico* model.⁸⁹ In general, the computational model is inconclusive and a crystal structure of inhibitor **65** bound to IMP-1 is needed to ascertain the actual binding interactions between the inhibitor and enzyme.

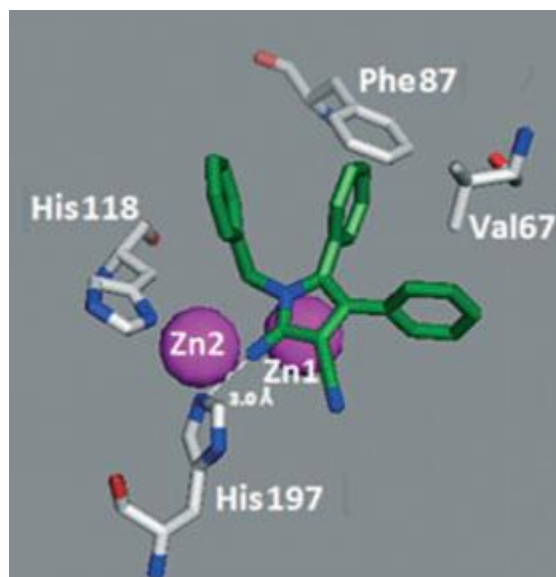


Figure 1.37: Surface view of the active site of pyrrole **65** docked into IMP-1. Atom colours: carbon on inhibitor in green, carbon on IMP-1 in white, nitrogen in blue and oxygen in red. The Zn^{2+} ions are depicted as magenta spheres (reproduced with permission from John Wiley and Sons, license number 3756770325531, 26/11/15).⁸⁹

A list of the MBLs mentioned in this chapter, including the bacterial strain in which the enzymes were isolated from, year of discovery and protein data bank (PDB) accession numbers of reported X-ray crystal structures of the enzymes are collated in Table 1.14.

Table 1.13: A list of MBLs from sub-classes B1, B2 and B3, covered in this chapter.^{16,39}

Subclass	MBL	Bacterial strain(s)	Discovery year	PDB number(s)	Description of crystal structure(s)
B1	BclI	<i>Bacillus cereus</i>	1966	1BMC, ⁴⁹ 1BME ⁹⁰	1BMC: Mono-zinc, native form 1BME: Di-zinc, native form
	CcrA	<i>Bacteroides fragilis</i>	1990	1ZNB, ⁵⁸ 1A8T, ³⁸ 1A7T ⁹¹	1ZNB: Native form 1A7T: CcrA bound with a sulfonic acid buffer (MES) 1A8T: CcrA mutant co-crystallised with biphenyl tetrazole inhibitor 38h
	IMP-1	<i>Serratia marcescens</i> , <i>Pseudomonas aeruginosa</i>	1994	1DDK, ⁸¹ 1DD6, ⁸¹ 1JJT ⁵⁷ , 3WXC ⁹²	1DDK: Native form 1DD6: IMP-1 co-crystallised with mercaptocarboxylate inhibitor 59 1JJT: IMP-1 co-crystallised with succinic acid derivative 56a 3WXC: IMP-1 co-crystallised with a phthalic acid-type inhibitor
	BlaB	<i>Chryseobacterium meningoseptica</i>	1998	1M2X ⁸²	1MX2: BlaB co-crystallised with <i>D</i> -captopril (41)
	VIM-2	<i>Pseudomonas aeruginosa</i> , <i>Acinetobacter baumannii</i>	2000	2YZ3, ⁹³ 1KO3 ⁵³	2YZ3: VIM-2 co-crystallised with a mercaptocarboxylate inhibitor 1KO3: Di-zinc, native form

	VIM-4	<i>Pseudomonas aeruginosa</i> , <i>Acinetobacter baumannii</i>	2003	2WHG ⁹⁴	2WHG: Native form
	NDM-1	<i>Klebsiella pneumonia</i> , <i>Escherichia coli</i>	2008	3Q6X, ⁵¹ 4EXS ⁹⁵	3Q6X: Hydrolysed ampicillin bound to NDM-1 4EXS: NDM-1 co-crystallised with <i>L</i> -captopril (42)
B2	CphA	<i>Aeromonas hydrophila</i>	1991	1X8G, ⁵⁵ 1X8I, ⁵⁵ 3F90, ⁶¹ 2QDS, ⁶⁴ 3IOF, ⁶³ 3IOG ⁶³	1X8G: Mono-zinc, native form 1X8I: Mono-zinc enzyme bound with hydrolysed biapenem 3F90: Di-zinc, native form 2QDS: Mono-zinc enzyme co-crystallised with <i>D</i> -captopril (41) 3IOF: Mono-zinc enzyme co-crystallised with mercaptophosphonate inhibitor 47a 3IOG: Mono-zinc enzyme co-crystallised with mercaptophosphonic acid inhibitor 51
	ImiS	<i>Aeromonas veronii</i>	1996	-	-
	Sfh-1	<i>Serratia fonticola</i>	2003	3SD9 ⁵⁶	3SD9: Mono-zinc, native form
B3	L1	<i>Stenotrophomonas maltophilia</i>	1991	1SML, ⁵⁹ 2AIO, ⁵⁴ 2FU8 ⁷⁷	1SML: Native form 2AIO: Hydrolysed moxalactam bound to L1 2FU8: L1 co-crystallised with <i>D</i> -captopril (41)
	FEZ-1	<i>Legionella gormanii</i>	2000	1K07, ⁸⁷ 1JT1 ⁸⁷	1K07: Native form 1JT1: FEZ-1 co-crystallised with <i>D</i> -captopril (41)
	AIM-1	<i>Pseudomonas aeruginosa</i>	2002	4AWY ⁶⁰	4AWY: Native form

1.12 Research aims

In view of all the literature available regarding MBL-mediated resistance, potent and specific inhibitors against this class of β -lactamase are urgently needed to resolve this global issue (Figure 1.38).^{39,51} Of immediate, particular concern is the B1 sub-class of MBLs. Members from this sub-class are clinically relevant, due to the fact that the genetic materials involved in the expression of the said enzymes are horizontally transferable on mobile genetic elements, like plasmids and integrons, between unrelated bacterial species. In addition, B1 MBLs display broad-spectrum β -lactam substrate profile and are uninhibited by clinically available serine- β -lactamase inhibitors, such as clavulanic acid (23).^{6,39,69}

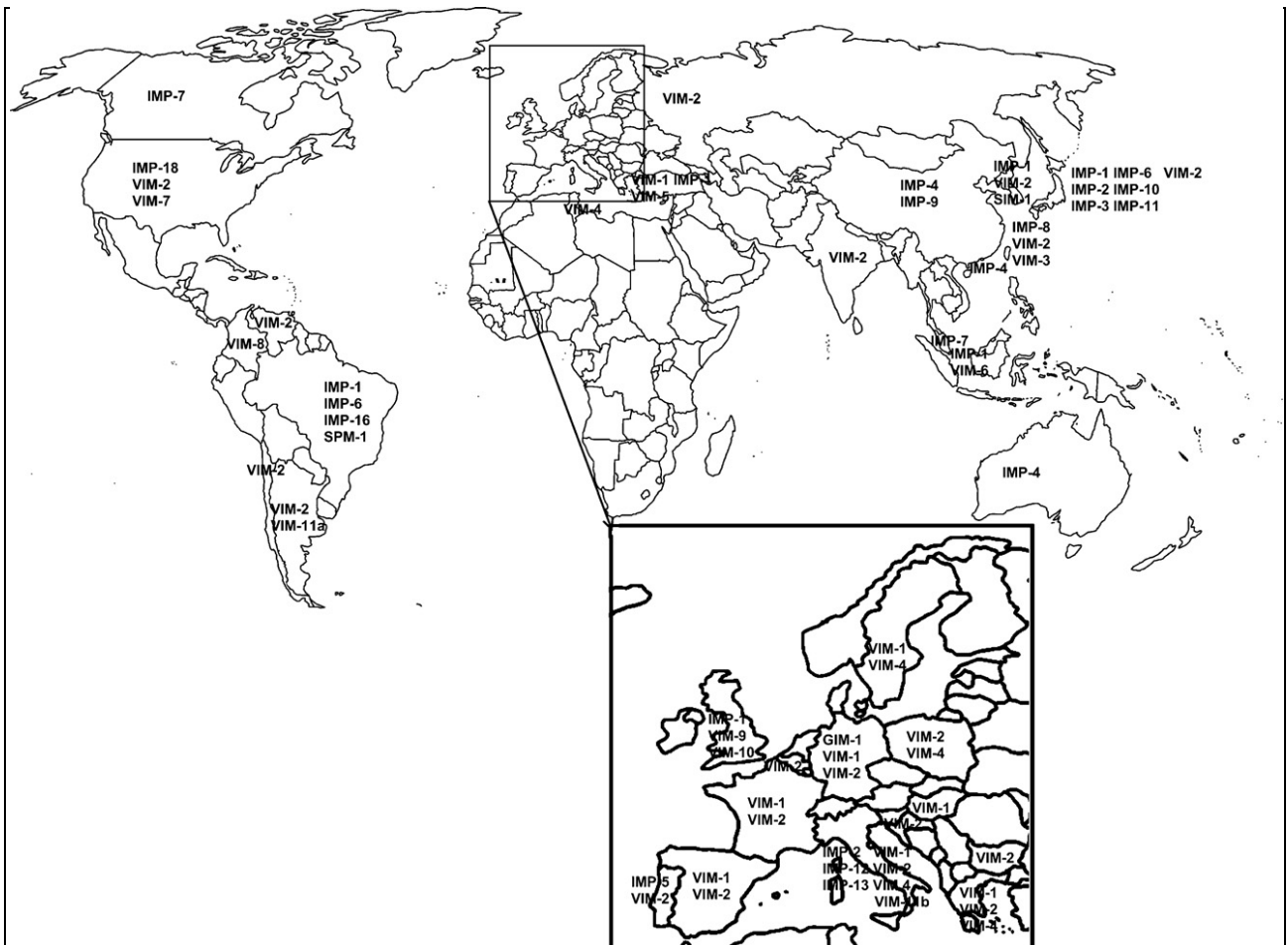


Figure 1.38: The world-wide dissemination of genetically-acquired MBLs (reproduced with permission from Elsevier, license number 3756880120346, 27/11/15).³⁹

Based on this premise, it was decided that new inhibitors of the imipenemase 1 (IMP-1) B1 MBL should be explored, so as to provide a starting point for the discovery and development of potent, broad-spectrum and specific inhibitors of MBLs. Thus far, there is sufficient kinetic, structural and inhibition information available in the literature for IMP-1.^{43,57,81} Furthermore, the enzyme is also well-studied in the McGeary and Schenk group.^{28,80,88,89}

Therefore, the specific aims of this research are as follows.

- To design and synthesis new inhibitors of IMP-1 based on existing inhibitor scaffolds of MBLs;
- To express and purify wild-type IMP-1 based on known protocol;
- To kinetically evaluate the IMP-1 inhibitory activities of the newly synthesised potential inhibitors;
- To predict the binding interaction of the new potential inhibitors with IMP-1 by computational modeling, based on available 3D structures of IMP-1 co-crystallised with known inhibitors;
- To co-crystallise the new inhibitors with MBL.

References

- (1) Ellis, W. R. In *Encyclopedia of Molecular Cell Biology and Molecular Medicine*; Wiley-VCH Verlag GmbH & Co. KGaA: 2006.
- (2) McGeary, R. P.; Schenk, G.; Guddat, L. W. *European Journal of Medicinal Chemistry* **2014**, *76*, 132.
- (3) Walsh, C. *Nature* **2000**, *406*, 775.
- (4) Fisher, J. F.; Meroueh, S. O.; Mobashery, S. *Chemical Reviews* **2005**, *105*, 395.
- (5) Babic, M.; Hujer, A. M.; Bonomo, R. A. *Drug Resistance Updates* **2006**, *9*, 142.
- (6) Drawz, S. M.; Bonomo, R. A. *Clinical Microbiology Reviews* **2010**, *23*, 160.
- (7) Livermore, D. M. *International Journal of Antimicrobial Agents* **2012**, *39*, 283.
- (8) Abraham, E. *Bioessays* **1990**, *12*, 601.
- (9) Bush, K. *Annals of the New York Academy of Sciences* **2010**, *1213*, 1.
- (10) Sader, H. S.; Jones, R. N. *Antimicrobial Newsletter* **1992**, *8*, 75.
- (11) Papp-Wallace, K. M.; Endimiani, A.; Taracila, M. A.; Bonomo, R. A. *Antimicrobial Agents and Chemotherapy* **2011**, *55*, 4943.

- (12) Kahan, J. S.; Kahan, F. M.; Goegelman, R.; Currie, S. A.; Jackson, M.; Stapley, E. O.; Miller, T. W.; Miller, A. K.; Hendlin, D.; Mochales, S.; Hernandez, S.; Woodruff, H. B.; Birnbaum, J. *The Journal of Antibiotics* **1979**, *32*, 1.
- (13) Yang, S.-Y. *Drug Discovery Today* **2010**, *15*, 444.
- (14) Dalhoff, A.; Thomson, C. J. *Chemotherapy* **2003**, *49*, 105.
- (15) Bush, K.; Macielag, M. J. *Expert Opinion on Therapeutic Patents* **2010**, *20*, 1277.
- (16) Palzkill, T. *Annals of the New York Academy of Sciences* **2013**, *1277*, 91.
- (17) Hollingsworth, J. A.; Donohoe, J. F.; Hone, R.; Keelan, P. J. *Current Medical Research and Opinion* **1984**, *9*, 316.
- (18) Vella, P., *The Development of New Drug Leads to Combat Bacterial Resistance towards Antibiotics*, PhD, The University of Queensland, 2012.
- (19) Dalhoff, A.; Janjic, N.; Echols, R. *Biochemical Pharmacology* **2006**, *71*, 1085.
- (20) "WHO Model List of Essential Medicines," World Health Organisation, 2015.
- (21) Fritz H. Kayser; Kurt A. Bienz; Johannes Eckert; Zinkernagel, R. M. *Medical Microbiology*; 10th ed.; Georg Thieme Verlag: Stuttgart, 2005.
- (22) Buynak, J. D. *ACS Chemical Biology* **2007**, *2*, 602.
- (23) Meroueh, S. O.; Bencze, K. Z.; Heseck, D.; Lee, M.; Fisher, J. F.; Stemmler, T. L.; Mobashery, S. *Proceedings of the National Academy of Sciences of the United States of America* **2006**, *103*, 4404.
- (24) Lee, W.; McDonough, M. A.; Kotra, L. P.; Li, Z.-H.; Silvaggi, N. R.; Takeda, Y.; Kelly, J. A.; Mobashery, S. *Proceedings of the National Academy of Sciences of the United States of America* **2001**, *98*, 1427.
- (25) Tipper, D. J.; Strominger, J. L. *Proceedings of the National Academy of Sciences of the United States of America* **1965**, *54*, 1133.
- (26) Shi, Q.; Meroueh, S. O.; Fisher, J. F.; Mobashery, S. *Journal of the American Chemical Society* **2011**, *133*, 5274.
- (27) Sauvage, E.; Kerff, F.; Terrak, M.; Ayala, J. A.; Charlier, P. *Federation of the European Microbiological Societies Microbiology Reviews*, 2008; Vol. 32.
- (28) Faridoun; Hussein, W. M.; Vella, P.; Islam, N. U.; Ollis, D. L.; Schenk, G.; McGeary, R. P. *Bioorganic & Medicinal Chemistry Letters* **2012**, *22*, 380.
- (29) Livermore, D. M. *Journal of Antimicrobial Chemotherapy* **1998**, *41*, 25.
- (30) Walsh, C. T.; Wencewicz, T. A. *Journal of Antibiotics* **2014**, *67*, 7.
- (31) Livermore, D. M. *Journal of Antimicrobial Chemotherapy* **2001**, *47*, 247.
- (32) Page, M. I.; Badarau, A. *Bioinorganic Chemistry and Applications* **2008**, 2008.
- (33) Rolinson, G. N. *Journal of Antimicrobial Chemotherapy* **1988**, *22*, 5.

- (34) Page, M. P. *Antibiotic Discovery and Development*; Dougherty, T. J., Pucci, M. J., Eds.; Springer US: New York, 2012, p 79.
- (35) Stapleton, P. D.; Taylor, P. W. *Science Progress* **2002**, *85*, 57.
- (36) Buynak, J. D. *Biochemical Pharmacology* **2006**, *71*, 930.
- (37) Bush, K.; Jacoby, G. A. *Antimicrobial Agents and Chemotherapy* **2010**, *54*, 969.
- (38) Toney, J. H.; Fitzgerald, P. M. D.; Grover-Sharma, N.; Olson, S. H.; May, W. J.; Sundelof, J. G.; Vanderwall, D. E.; Cleary, K. A.; Grant, S. K.; Wu, J. K.; Kozarich, J. W.; Pompliano, D. L.; Hammond, G. G. *Chemistry & Biology* **1998**, *5*, 185.
- (39) Bebrone, C. *Biochemical Pharmacology* **2007**, *74*, 1686.
- (40) Herzberg, O.; Fitzgerald, P. M. D. *Handbook of Metalloproteins*; Messerschmidt, A., Bode, W., Cygler, M., Eds.; John Wiley and Sons: Chichester, 2004; Vol. 3, p 217.
- (41) Gupta, V. *Expert Opinion on Investigational Drugs* **2008**, *17*, 131.
- (42) Nicholas C. Price; Raymond A. Dwek; R. George Ratcliffe; Wormald, M. R. *Principals and Problems in Physical Chemistry for Biochemists*; Oxford University Press: Oxford, 2008.
- (43) Laraki, N.; Franceschini, N.; Rossolini, G. M.; Santucci, P.; Meunier, C.; de Pauw, E.; Amicosante, G.; Frère, J. M.; Galleni, M. *Antimicrobial Agents and Chemotherapy* **1999**, *43*, 902.
- (44) Vanhove, M.; Zakhem, M.; Devreese, B.; Franceschini, N.; Anne, C.; Bebrone, C.; Amicosante, G.; Rossolini, G. M.; Van Beeumen, J.; Frère, J. M.; Galleni, M. *Cellular and Molecular Life Sciences* **2003**, *60*, 2501.
- (45) Bebrone, C.; Anne, C.; De Vriendt, K.; Devreese, B.; Rossolini, G. M.; Van Beeumen, J.; Frère, J.-M.; Galleni, M. *Journal of Biological Chemistry* **2005**, *280*, 28195.
- (46) Segatore, B.; Massidda, O.; Satta, G.; Setacci, D.; Amicosante, G. *Antimicrobial Agents and Chemotherapy* **1993**, *37*, 1324.
- (47) Felici, A.; Amicosante, G.; Oratore, A.; Strom, R.; Ledent, P.; Joris, B.; Fanuel, L.; Frère, J. M. *Biochemical Journal* **1993**, *291*, 151.
- (48) Yong, D.; Toleman, M. A.; Bell, J.; Ritchie, B.; Pratt, R.; Ryley, H.; Walsh, T. R. *Antimicrobial Agents and Chemotherapy* **2012**, *56*, 6154.
- (49) Carfi, A.; Pares, S.; Duée, E.; Galleni, M.; Duez, C.; Frère, J. M.; Dideberg, O. *The European Molecular Biology Organization Journal* **1995**, *14*, 4914.
- (50) Crowder, M. W.; Spencer, J.; Vila, A. J. *Accounts of Chemical Research* **2006**, *39*, 721.
- (51) Zhang, H.; Hao, Q. *The Federation of American Societies for Experimental Biology Journal* **2011**, *25*, 2574.

- (52) Fast, W.; Sutton, L. D. *Biochimica et Biophysica Acta (BBA) - Proteins and Proteomics* **2013**, 1834, 1648.
- (53) Garcia-Saez, I.; Docquier, J. D.; Rossolini, G. M.; Dideberg, O. *Journal of Molecular Biology* **2008**, 375, 604.
- (54) Spencer, J.; Read, J.; Sessions, R. B.; Howell, S.; Blackburn, G. M.; Gamblin, S. J. *Journal of the American Chemical Society* **2005**, 127, 14439.
- (55) Garau, G.; Bebrone, C.; Anne, C.; Galleni, M.; Frère, J.-M.; Dideberg, O. *Journal of Molecular Biology* **2005**, 345, 785.
- (56) Fonseca, F.; Bromley, E. H. C.; Saavedra, M. J.; Correia, A.; Spencer, J. *Journal of Molecular Biology* **2011**, 411, 951.
- (57) Toney, J. H.; Hammond, G. G.; Fitzgerald, P. M. D.; Sharma, N.; Balkovec, J. M.; Rouen, G. P.; Olson, S. H.; Hammond, M. L.; Greenlee, M. L.; Gao, Y.-D. *Journal of Biological Chemistry* **2001**, 276, 31913.
- (58) Concha, N. O.; Rasmussen, B. A.; Bush, K.; Herzberg, O. *Structure* **1996**, 4, 823.
- (59) Ullah, J. H.; Walsh, T. R.; Taylor, I. A.; Emery, D. C.; Verma, C. S.; Gamblin, S. J.; Spencer, J. *Journal of Molecular Biology* **1998**, 284, 125.
- (60) Leiros, H.-K. S.; Borra, P. S.; Brandsdal, B. O.; Edvardsen, K. S. W.; Spencer, J.; Walsh, T. R.; Samuelsen, Ø. *Antimicrobial Agents and Chemotherapy* **2012**, 56, 4341.
- (61) Bebrone, C.; Delbrück, H.; Kupper, M. B.; Schlömer, P.; Willmann, C.; Frère, J.-M.; Fischer, R.; Galleni, M.; Hoffmann, K. M. V. *Antimicrobial Agents and Chemotherapy* **2009**, 53, 4464.
- (62) King, D. T.; Strynadka, N. C. J. *Future Medicinal Chemistry* **2013**, 5, 1243.
- (63) Lassaux, P.; Hamel, M.; Gulea, M.; Delbrück, H.; Mercuri, P. S.; Horsfall, L.; Dehareng, D.; Kupper, M.; Frère, J.-M.; Hoffmann, K.; Galleni, M.; Bebrone, C. *Journal of Medicinal Chemistry* **2010**, 53, 4862.
- (64) Lienard, B. M. R.; Garau, G.; Horsfall, L.; Karsisiotis, A. I.; Damblon, C.; Lassaux, P.; Papamicael, C.; Roberts, G. C. K.; Galleni, M.; Dideberg, O.; Frere, J.-M.; Schofield, C. J. *Organic & Biomolecular Chemistry* **2008**, 6, 2282.
- (65) Patrick, G. L.; Spencer, J. *An Introduction to Medicinal Chemistry*, Oxford University Press Oxford, 2005; Vol. 2.
- (66) Yung-Chi, C.; Prusoff, W. H. *Biochemical Pharmacology* **1973**, 22, 3099.
- (67) Roll, D. M.; Yang, Y.; Wildey, M. J.; Bush, K.; Lee, M. D. *The Journal of Antibiotics* **2010**, 63, 255.
- (68) Chen, P.; Horton, L. B.; Mikulski, R. L.; Deng, L.; Sundriyal, S.; Palzkill, T.; Song, Y. *Bioorganic & Medicinal Chemistry Letters* **2012**, 22, 6229.

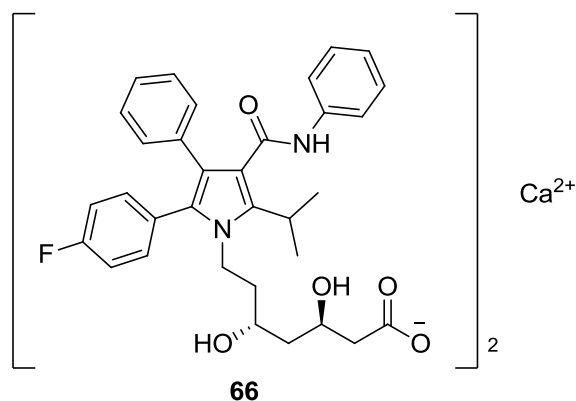
- (69) Walsh, T. R.; Toleman, M. A.; Poirel, L.; Nordmann, P. *Clinical Microbiology Reviews* **2005**, *18*, 306.
- (70) Goto, M.; Takahashi, T.; Yamashita, F.; Koreeda, A.; Mori, H.; Ohta, M.; Arakawa, Y. *Biological & Pharmaceutical Bulletin* **1997**, *20*, 1136.
- (71) Walsh, T. R.; Bolmström, A.; Qwörnström, A.; Gales, A. *Journal of Clinical Microbiology* **2002**, *40*, 2755.
- (72) Andrews, J. M. *Journal of Antimicrobial Chemotherapy* **2001**, *48*, 5.
- (73) Walter, M. W.; Felici, A.; Galleni, M.; Soto, R. P.; Adlington, R. M.; Baldwin, J. E.; Frère, J.-M.; Gololobov, M.; Schofield, C. J. *Bioorganic & Medicinal Chemistry Letters* **1996**, *6*, 2455.
- (74) Toney, J. H.; Cleary, K. A.; Hammond, G. G.; Yuan, X.; May, W. J.; Hutchins, S. M.; Ashton, W. T.; Vanderwall, D. E. *Bioorganic and Medicinal Chemistry Letters* **1999**, *9*, 2741.
- (75) Mollard, C.; Moali, C.; Papamicael, C.; Damblon, C.; Vessilier, S.; Amicosante, G.; Schofield, C. J.; Galleni, M.; Frère, J.-M.; Roberts, G. C. K. *Journal of Biological Chemistry* **2001**, *276*, 45015.
- (76) Kraatz, H.-B.; Metzler-Nolte, N. *Concepts and Models in Bioinorganic Chemistry*; Wiley-VCH Weinheim, 2006.
- (77) Nauton, L.; Kahn, R.; Garau, G.; Hernandez, J. F.; Dideberg, O. *Journal of Molecular Biology* **2008**, *375*, 257.
- (78) Heinz, U.; Bauer, R.; Wommer, S.; Meyer-Klaucke, W.; Papamichaels, C.; Bateson, J.; Adolph, H.-W. *Journal of Biological Chemistry* **2003**, *278*, 20659.
- (79) Guo, Y.; Wang, J.; Niu, G.; Shui, W.; Sun, Y.; Zhou, H.; Zhang, Y.; Yang, C.; Lou, Z.; Rao, Z. *Protein Cell* **2011**, *2*, 384.
- (80) Vella, P.; Hussein, W. M.; Leung, E. W. W.; Clayton, D.; Ollis, D. L.; Mitić, N.; Schenk, G.; McGeary, R. P. *Bioorganic and Medicinal Chemistry Letters* **2011**, *21*, 3282.
- (81) Concha, N. O.; Janson, C. A.; Rowling, P.; Pearson, S.; Cheever, C. A.; Clarke, B. P.; Lewis, C.; Galleni, M.; Frère, J.-M.; Payne, D. J.; Bateson, J. H.; Abdel-Meguid, S. S. *Biochemistry* **2000**, *39*, 4288.
- (82) García-Sáez, I.; Hopkins, J.; Papamicael, C.; Franceschini, N.; Amicosante, G.; Rossolini, G. M.; Galleni, M.; Frère, J.-M.; Dideberg, O. *Journal of Biological Chemistry* **2003**, *278*, 23868.
- (83) Fisher, J. F.; Meroueh, S. O.; Mobashery, S. *Chemical Reviews* **2005**, *105*, 395.
- (84) Meanwell, N. A. *Journal of Medicinal Chemistry* **2011**, *54*, 2529.

- (85) Olsen, L.; Jost, S.; Adolph, H.-W.; Pettersson, I.; Hemmingsen, L.; Jørgensen, F. S. *Bioorganic and Medicinal Chemistry* **2006**, *14*, 2627.
- (86) Feng, L.; Yang, K.-W.; Zhou, L.-S.; Xiao, J.-M.; Yang, X.; Zhai, L.; Zhang, Y.-L.; Crowder, M. W. *Bioorganic and Medicinal Chemistry Letters* **2012**, *22*, 5185.
- (87) García-Sáez, I.; Mercuri, P. S.; Papamicael, C.; Kahn, R.; Frère, J. M.; Galleni, M.; Rossolini, G. M.; Dideberg, O. *Journal of Molecular Biology* **2003**, *325*, 651.
- (88) Mohamed, M. S.; Hussein, W. M.; McGeary, R. P.; Vella, P.; Schenk, G.; Abd El-hameed, R. H. *European Journal of Medicinal Chemistry* **2011**, *46*, 6075.
- (89) Hussein, W. M.; Fatahala, S. S.; Mohamed, Z. M.; McGeary, R. P.; Schenk, G.; Ollis, D. L.; Mohamed, M. S. *Chemical Biology and Drug Design* **2012**, *80*, 500.
- (90) Carfi, A.; Duee, E.; Galleni, M.; Frere, J.-M.; Dideberg, O. *Acta Crystallographica Section D* **1998**, *54*, 313.
- (91) Fitzgerald, P. M. D.; Wu, J. K.; Toney, J. H. *Biochemistry* **1998**, *37*, 6791.
- (92) Hiraiwa, Y.; Saito, J.; Watanabe, T.; Yamada, M.; Morinaka, A.; Fukushima, T.; Kudo, T. *Bioorganic and Medicinal Chemistry Letters* **2014**, *24*, 4891.
- (93) Yamaguchi, Y.; Jin, W.; Matsunaga, K.; Ikemizu, S.; Yamagata, Y.; Wachino, J.-i.; Shibata, N.; Arakawa, Y.; Kurosaki, H. *Journal of Medicinal Chemistry* **2007**, *50*, 6647.
- (94) Lassaux, P.; Traoré, D. A. K.; Loisel, E.; Favier, A.; Docquier, J.-D.; Sohier, J. S.; Laurent, C.; Bebrone, C.; Frère, J.-M.; Ferrer, J.-L.; Galleni, M. *Antimicrobial Agents and Chemotherapy* **2011**, *55*, 1248.
- (95) King, D. T.; Worrall, L. J.; Gruninger, R.; Strynadka, N. C. J. *Journal of the American Chemical Society* **2012**, *134*, 11362.
- (96) Schrödinger Release 2015-4: Maestro, version 10.4, Schrödinger, LLC, New York, NY 2015.

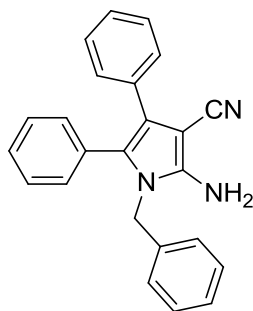
CHAPTER 2: SYNTHESIS AND EVALUATION OF *N*-ACYLPYRROLE-3-CARBONITRILE DERIVATIVES AS IMP-1 INHIBITORS

2.1 General introduction

Natural and synthetic vicinal diaryl-substituted pyrroles have been reported to display various significant biological properties, such as anti-tumour, anti-viral, anti-bacterial and anti-hyperlipidemic activities.¹ An example of such a pyrrole is atorvastatin calcium (**66**), a statin drug approved in 1996 by the Food and Drug Administration.² Atorvastatin (**66**) is a competitive inhibitor of 3-hydroxy-3-methyl-glutaryl-coenzyme A (HMG-CoA) reductase, a key enzyme involved in the biosynthesis of cholesterol.²



Since the discovery of MBL inhibitors, a lot of attention has been directed towards inhibitors with mercaptocarboxylate and dicarboxylate pharmacophores.³ This leaves room for the development of inhibitors with various molecular scaffolds and pharmacophores, such as pyrrole **65** - a solely competitive IMP-1 inhibitor to be developed as potent MBL inhibitors.⁴



2-Amino-1-benzyl-4,5-diphenyl-1*H*-pyrrole-3-carbonitrile **65**

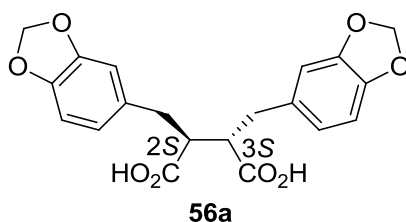
$K_{ic} = 21\mu\text{M}$ against IMP-1

Pyrrole **65** contains various functionalities, such as an amino group, a cyano group, vicinal diphenyl side chains and an *N*-benzyl group. The individual roles of each of these functional groups in contributing to the overall IMP-1 inhibitory activity of **65** could be further explored.⁴ This chapter will focus on the optimisation of pyrrole **65** as an IMP-1 inhibitor by the synthetic modification of the 2-amino group of the lead compound.

2.2 Research plan

Preliminary computational modelling based on a known 3D structure of an inhibitor co-crystallised with IMP-1 can be used as a predictive tool in the design of new IMP-1 inhibitors.⁵ The crystal structure of the succinic acid derivative **56a** co-crystallised with IMP-1 (PDB no.: 1JJT, Figure 1.32) was selected based on two reasons: 1) the inhibitor is the most potent IMP-1 inhibitor thus far, with an IC_{50} value of 9 nM, and 2) the 3D structure is one of the most well-resolved MBL crystal structure, with a resolution of 1.3 Å.⁶

Nevertheless, the amino acid residues of the 1JJT crystal structure are not numbered according to the standard BBL Ambler numbering system. In this chapter, the BBL numbering will be included in parenthesis next to the 1JJT numbering.⁷



$IC_{50} = 9 \text{ nM}$ against IMP-1

Computational programs such as Molegro Virtual Docker (MVD) can be used to model the binding modes of new inhibitors bound in the active site of IMP-1. MVD incorporates a cavity prediction algorithm that enables the efficient and accurate detection of possible inhibitor-enzyme binding modes.⁸ Furthermore, computational modelling results obtained from MVD can be compared with those obtained from other programs, such as Glide (Glide modelling was carried out by Ajit Kandale, a PhD student with the McGeary group).⁹

MVD computational modelling of pyrrole **65** bound in the active site of IMP-1 suggested that both of the phenyl rings of the inhibitor make favourable contacts with the mobile L3 loop *via* residues Val25 (61), Trp28 (64) and Val31 (67) (Figure 2.1). Binding of the mobile loop closes the active site of the enzyme.¹⁰ The *in silico* model also predicted that the 3-cyano group of **65** binds to the terminal amino group of Lys161 (224) through a hydrogen bond interaction (N-N distance 3.10 Å). Lys161 (224) is conserved among B1 MBLs and is known to form ionic interactions with the C3 or C-4 carboxylate group of β -lactam antibiotics.¹¹ In addition, one of the 2-amino hydrogen atoms of **65** was predicted by the model to have a hydrogen bond contact with the imidazole nitrogen of His139 (196), which is a Zn1 ligand (N-N distance 3.03 Å). This similar interaction was also suggested by Hussein *et al.*, although the histidine residue proposed by the authors was His197 (263), which is a Zn2 ligand (Section 1.11 g).⁴ Based on this computational prediction, it was proposed that the 2-amino group of pyrrole **65** may play a role in the binding of the inhibitor to the active site of IMP-1.

Nevertheless, the *in silico* model didn't predict any interactions between pyrrole **65** and the zinc centres in the active site of IMP-1 (Figure 2.1).

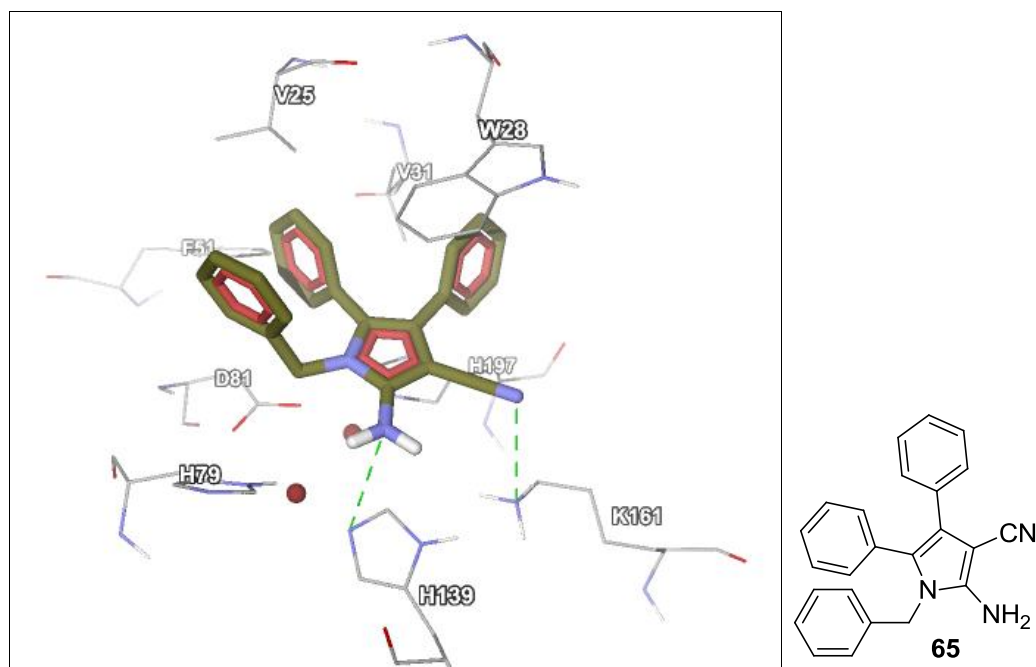
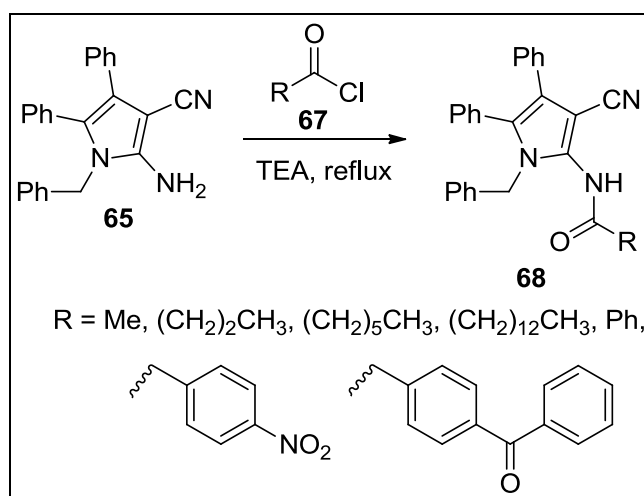


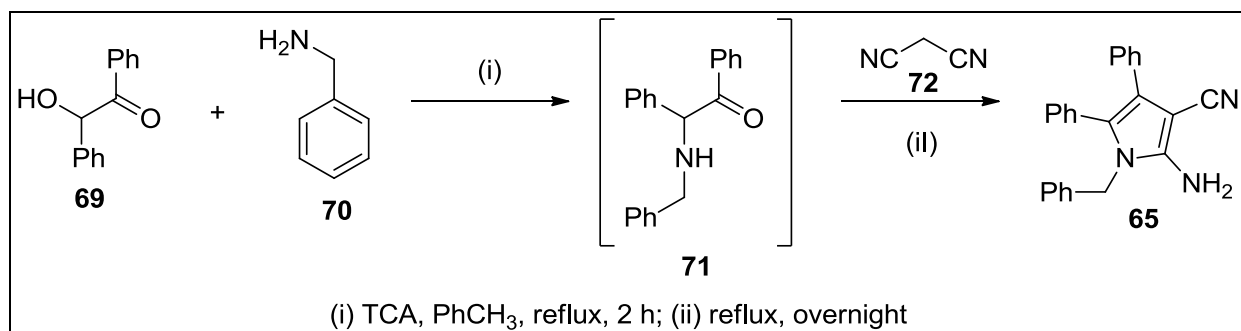
Figure 2.1: The computational model of pyrrole **65** docked into IMP-1 as predicted by MVD. Atom colours: carbon on ligand in olive green, carbon on IMP-1 in grey, nitrogen in blue, oxygen in red and hydrogen in white. The Zn^{2+} ions are shown as red spheres. The dashed, green lines represent hydrogen bonds.

Synthetic modification of the 2-amino group of pyrrole **65** can be achieved by acylation of the functional group with various aliphatic acyl chlorides **67** of various aliphatic chain lengths or aryl groups to yield *N*-acylated derivatives of pyrrole **65** (Scheme 2.1). Both *p*-nitro- and 4-benzoyl aryl-substituents have been reported to be potent IMP-1 inhibitor fragments.¹²

Pyrrole **65**, which is the starting material for this synthetic exercise, can be prepared from the condensation of benzoin (**69**), benzylamine (**70**) and malononitrile (**72**) in two synthetic steps according to known procedure (Scheme 2.2).^{13,14} Trichloroacetic acid, TCA can be used as the acid catalyst in the condensation reaction of benzoin (**69**) with benzylamine (**70**).¹³

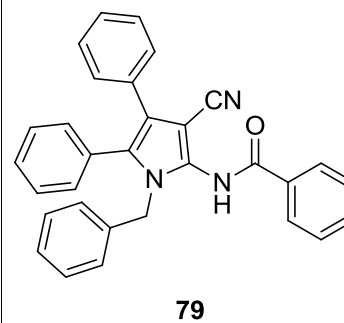
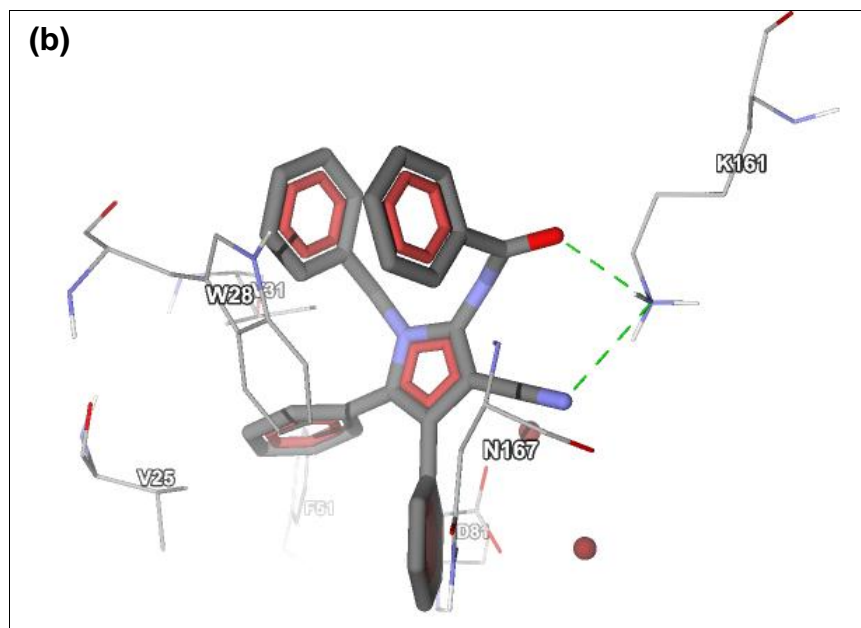
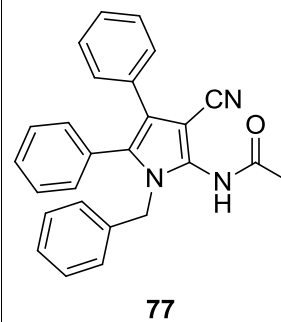
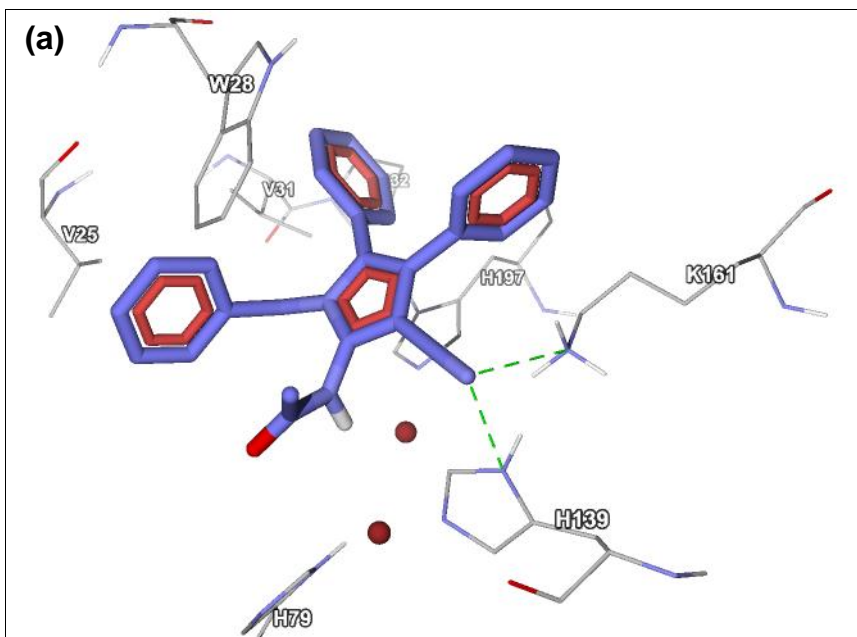


Scheme 2.1: The proposed synthetic modification of the 2-amino functional group of pyrrole **65**.



Scheme 2.2: The reported synthetic preparation of pyrrole **65**.^{13,14}

MVD molecular docking of a sample of *N*-acyl amide derivatives **77**, **79** and **84** bound to IMP-1 predicted considerably similar interactions with that of the lead compound **65** (Figure 2.2). All three *in silico* models suggested a hydrogen bond interaction between the nitrogen atom of the 3-cyano group of the derivatives and the terminal amino group of Lys161 (224), in addition to hydrophobic interactions between the vicinal diphenyl rings of the derivatives and the flexible loop, as previously described for that of pyrrole **65**.



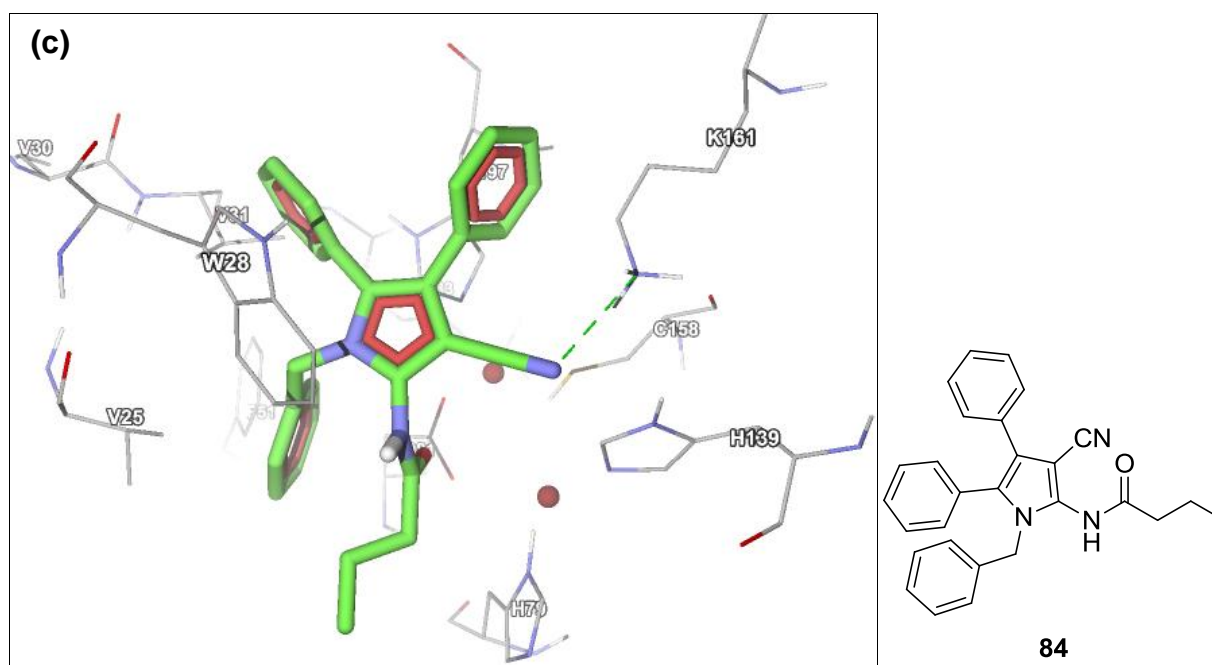
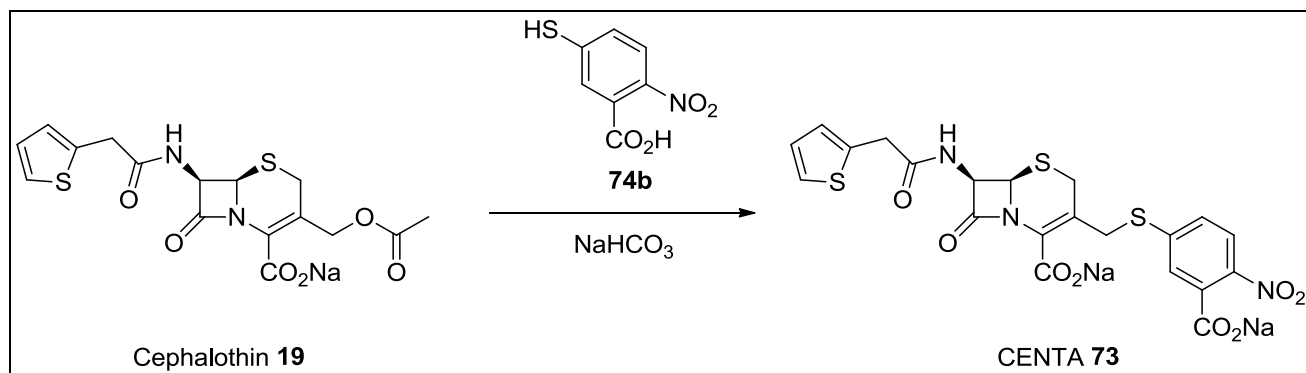


Figure 2.2: The *in silico* models of (a) *N*-acetamide **77**, (b) *N*-benzamide **79** and (c) *N*-butylamide **84** derivatives of pyrrole **65** docked into IMP-1 as predicted by MVD. Atom colours: carbon on ligand in blue for **77**, dark grey for **79** and lime green for **84**, carbon on IMP-1 in grey, nitrogen in blue, oxygen in red and hydrogen in white. The Zn²⁺ ions are shown as red spheres. The dashed, green lines represent hydrogen bonds.

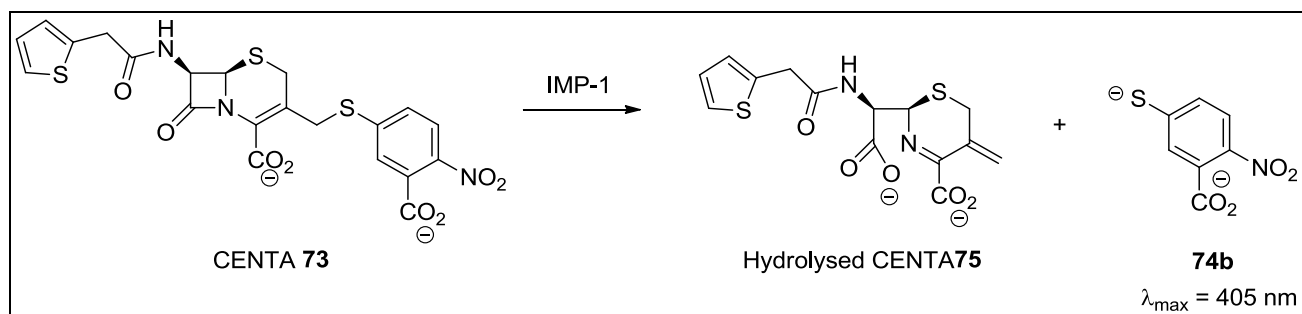
The IMP-1 inhibitory activity of the *N*-acylated pyrrole derivatives can be evaluated by a kinetic assay which measures the residual activity of IMP-1 in the presence of an inhibitor.¹⁵ The difference between the residual activity and the activity of the uninhibited enzyme is taken as the percentage inhibition of the particular inhibitor.^{15,16} The percentage inhibition of the lead compound, pyrrole **65** can be used as a reference for comparing the inhibitory potency of the synthetic derivatives. Derivatives that show greater percentage inhibition than the reference compound **65** can be further evaluated to determine the inhibition constant and mode of inhibition of the particular derivative.

The substrate used in the kinetic assay is CENTA (**73**), a chromogenic derivative of cephalothin (**19**) (Scheme 2.3).^{17,18} CENTA (**73**) has been successfully used by the McGearry and Schenk group in the screening and kinetic inhibition studies of various types of IMP-1 inhibitors.^{4,12,15,19}



Scheme 2.3: The derivatisation of CENTA (**73**) from cephalothin (**19**).^{17,18}

The activity of IMP-1 in the presence or absence of an inhibitor can be measured as the hydrolytic rate of CENTA (**73**), which is determined spectrophotometrically by monitoring the rate of formation of 2-nitro-5-sulfidobenzoate (**74b**) at 405 nm ($\epsilon = 6400 \text{ M}^{-1} \text{ cm}^{-1}$) (Scheme 2.4).^{4,19} The K_m and k_{cat} parameter for the hydrolysis of CENTA by IMP-1 is $200 \mu\text{M}$ and 400 s^{-1} , respectively.¹⁷

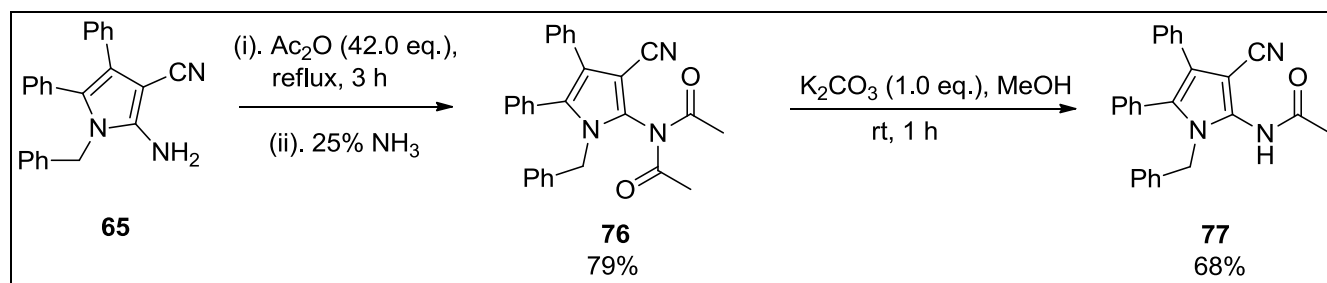


Scheme 2.4: Hydrolysis of CENTA (**73**) by IMP-1 as a measurement of IMP-1 activity.

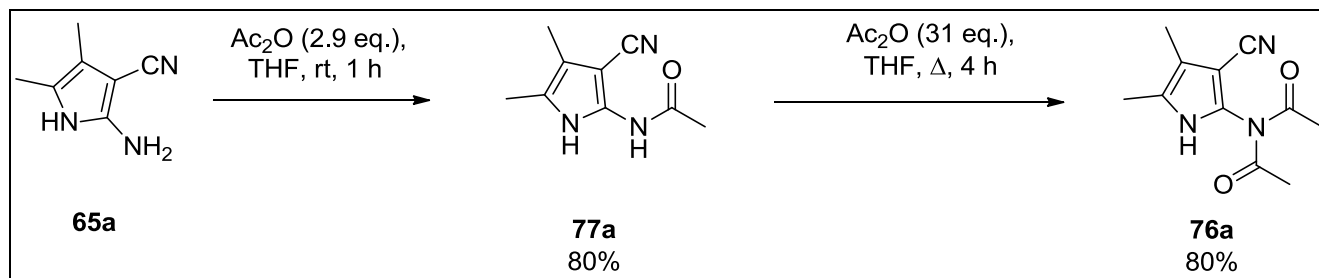
2.3 Results and discussion

2.3 a) Synthetic work – first series

It was anticipated that the acylation of 2-aminopyrrole-3-carbonitrile **65** would require relatively harsh conditions, as the 2-amino group of the pyrrole is not a reactive nucleophile due to the delocalisation of the non-bonding electrons of the nitrogen into the aromatic pyrrole ring.²⁰ However, acetylation of pyrrole **65** with excess acetic anhydride (42.0 eq.) under refluxing condition afforded *N,N*-diacetyl imide **76** as the sole product and not the *N*-acetamide **77** product as reported by Fathallah.²¹ This observation was also recorded by Bayomi *et al.* in the acetylation of 2-amino-3-carbonitrilepyrrole **65a** which gave imide **76a** with excess equivalents of acetic anhydride at refluxing condition (Scheme 2.6).²² Amide **77** was later obtained from the partial deacylation of imide **76** with slightly basic methanol (Scheme 2.5).²³

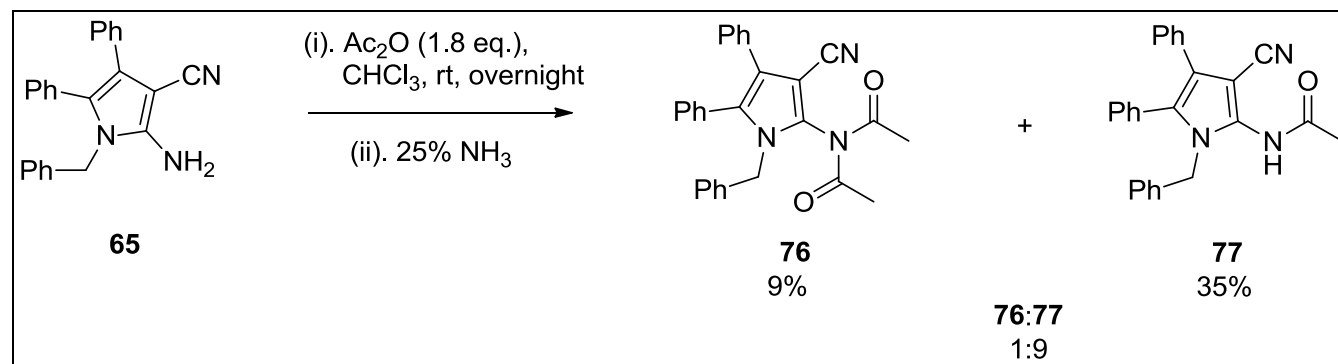


Scheme 2.5: The acetylation of pyrrole **65** with excess acetic anhydride and partial deacylation of *N,N*-diacetyl imide **73** with potassium carbonate.^{21,23}



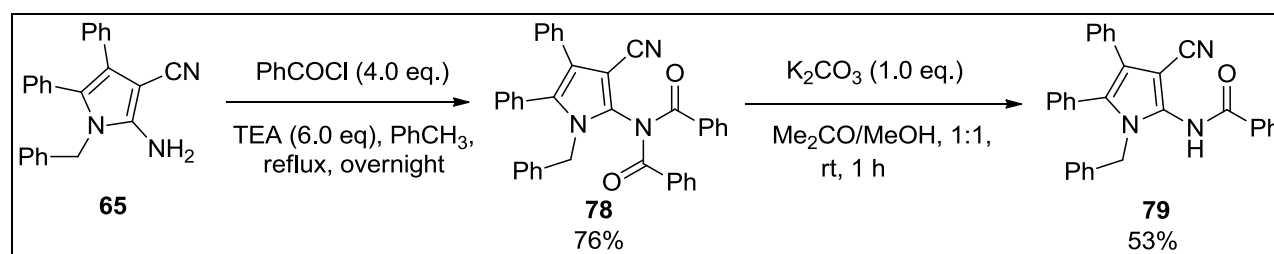
Scheme 2.6: The acetylation of pyrrole **65a** with both 2.9 equivalents and excess acetic anhydride which gave amide **77a** and imide **76a**, respectively.²²

A second attempt of the acetylation reaction was carried out with fewer molar equivalents of acetic anhydride (1.8 eq.) at room temperature. Interestingly, the reaction afforded amide **77** and imide **76** as the major and minor product, respectively (Scheme 2.7).



Scheme 2.7: The mild acetylation of pyrrole **65** which results in a mixture of imide **76** and amide **77** products.

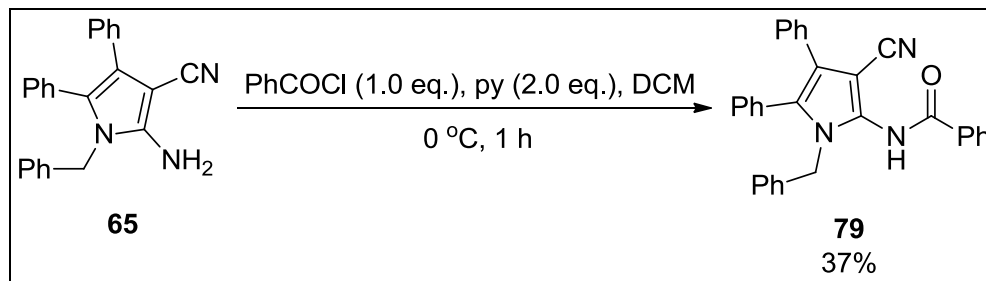
Similarly *N,N*-dibenzoyl imide **78** was obtained as the only product from the reaction of pyrrole **65** with benzoyl chloride (4.0 eq.) under refluxing condition. Triethylamine (6.0 eq.) was employed as the base in the reaction. Again, partial deacylation of imide **78** with potassium carbonate afforded *N*-benzamide **79** as the final product (Scheme 2.8).



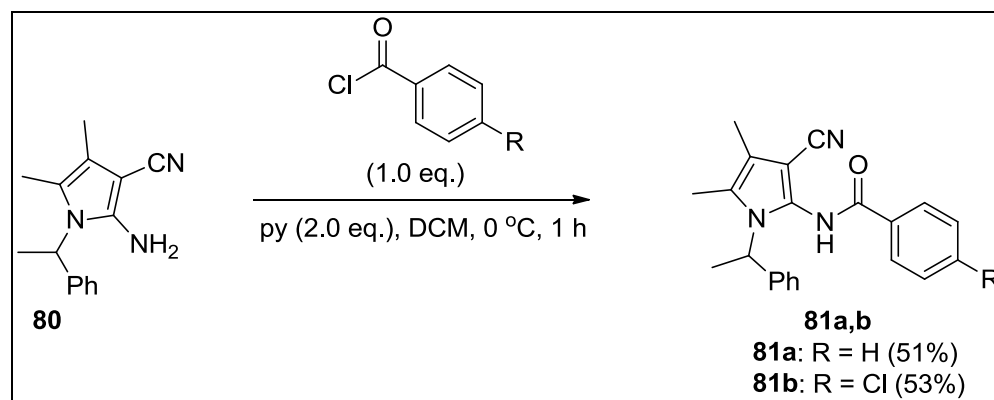
Scheme 2.8: The benzoylation of pyrrole **65** with benzoyl chloride and the partial deacylation of imide **78** with potassium carbonate.

A second attempt at the benzoylation reaction was carried out at 0 °C for 1 h with 1.0 eq. of benzoyl chloride and 2.0 eq. of pyridine, according to Müller *et al.*²⁴ The reaction

afforded the expected amide **79** as the sole product, albeit in low yield (37%). Moreover, 52% of the pyrrole **65** starting material was recovered from the reaction mixture (Scheme 2.9). In contrast, Müller and colleagues reported yields of 51% or 53% for the mild benzoylation of a similar 2-aminopyrrole-3-carbonitrile **80** which primarily gave *N*-benzamides **81a** or **81b** as the sole reaction product with no report of un-reacted starting material (Scheme 2.10).



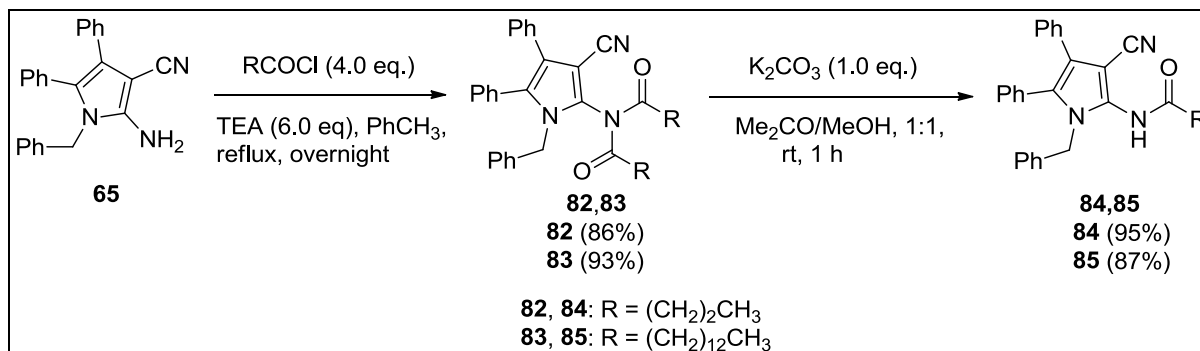
Scheme 2.9: The mild benzoylation of pyrrole **65** according to the procedure by Müller *et al.*²⁴



Scheme 2.10: The mild benzoylation of pyrrole **80** according to the procedure by Müller *et al.*²⁴

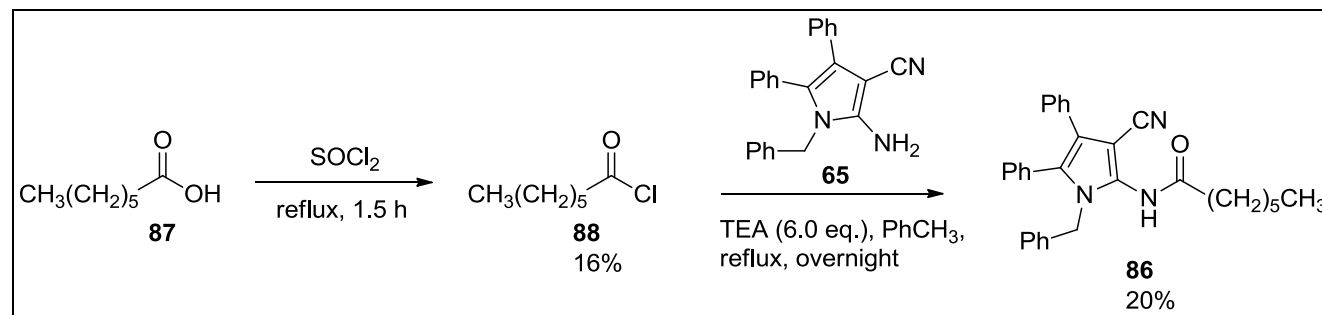
It was subsequently decided that the acylation of pyrrole **65** with other aliphatic acyl chloride derivatives would proceed by initial conversion of pyrrole **65** to the *N,N*-diacyl imide intermediate followed by partial deacylation of the corresponding imide with slightly basic methanol to the desired amide. This method is not only synthetically more efficient but is also advantageous to the aim of the research, as it provides additional imide derivatives for IMP-1

inhibition study. Scheme 2.11 shows two other *N,N*-diacyl imide derivatives (**82**, **83**) and the desired amide derivatives (**84**, **85**) synthesised in this manner.



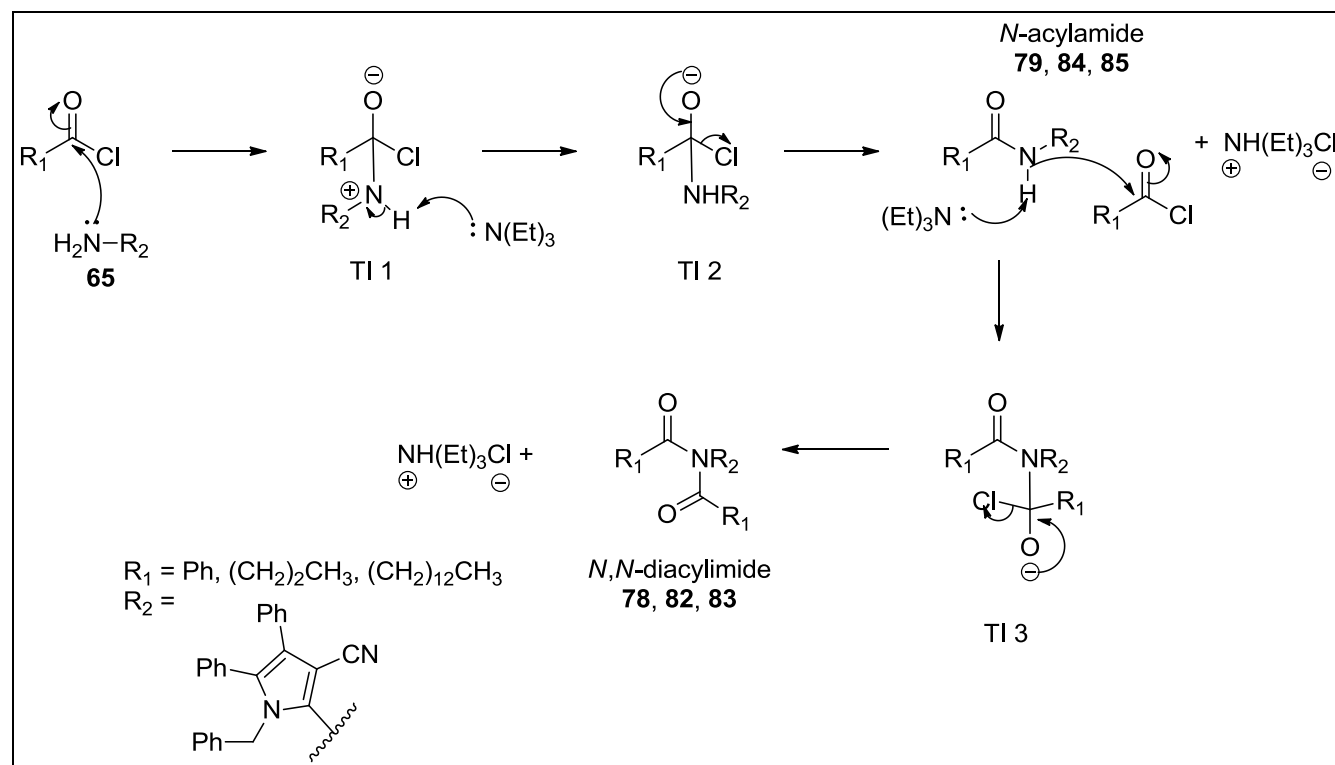
Scheme 2.11: The syntheses of imides (**82**, **83**) and amides (**84**, **85**) from pyrrole **65**.

However, the observed low yield of *N*-heptanamide **86** was due to heptanoyl chloride (**88**), which was lost during high-vacuum drying before the amide coupling step with pyrrole **65** (Scheme 2.12). The drying step was introduced to remove trace amounts of thionyl chloride from the acyl chloride reagent. As a result, most of the pyrrole starting material **65** was recovered from the reaction mixture (80%). Nevertheless, *N*-heptanamide **86** was obtained as the sole reaction product. Therefore, this observation demonstrates that even at refluxing condition, the *N*-amide is the only product obtained when limiting amounts of the acyl chloride reagent is used. Moreover, the amount of **86** obtained was sufficient for the inhibition assay and there was no need for the coupling reaction to be repeated.



Scheme 2.12: Synthesis of *N*-heptanamide **86** from pyrrole **65** and heptanoyl chloride (**88**).

The proposed mechanism for the formation of imide **78**, **82** and **83** is illustrated in Scheme 2.13. It starts with the nucleophilic acyl substitution of one molecule of acyl chloride ($R_1C=O$) with 2-aminocyanopyrrole **65** to give amide **79**, **84** or **85** via tetrahedral intermediates 1 and 2 (TI 1 and 2).²⁵ The triethylamine base facilitates the substitution reaction by deprotonating the positively charged ammonium end of TI 1. This then leads to TI 2, with the expulsion of the chloride ion in TI 2 to form the amide intermediate.²⁵ Next, another molecule of triethylamine is required to deprotonate the amide intermediate for the acyl substitution of a second molecule of acyl chloride to furnish the imide product **78**, **82** or **83**, via TI 3.



Scheme 2.13: The proposed mechanism for the formation of imides **78**, **82** and **83** by the coupling of pyrrole **65** with 4.0 equivalents of the appropriate acyl chloride reagent and 6.0 equivalents of TEA, under refluxing condition. TI stands for tetrahedral intermediate.

The synthesised *N*-acyl amide and *N,N*-diacyl imide derivatives of pyrrole **65** were characterised by infrared (IR), ^1H and ^{13}C nuclear magnetic resonance (NMR) spectroscopy, in addition to low- and high-resolution mass spectrometry (LRMS and HRMS).^{14,26,27} The IR, ^1H and ^{13}C NMR spectra of derivative **82** are presented as a representative of the spectral data of the synthetic derivatives of pyrrole **65** (Figures 2.3, 2.4 and 2.5).

The 3-cyano functional group of the starting material **65** and derivative **82** can be identified by the presence of a medium-intensity peak at around 2220 cm^{-1} , which corresponds to the nitrile, $\text{C}\equiv\text{N}$ stretch in the IR spectra (Figure 2.3).²⁶⁻²⁸ Pyrrole **65** and derivative **82** can be further distinguished by the presence of a strong peak at 1683.3 cm^{-1} in the IR spectrum of the latter, which corresponds to the carbonyl, $\text{C}=\text{O}$ stretch.²⁸

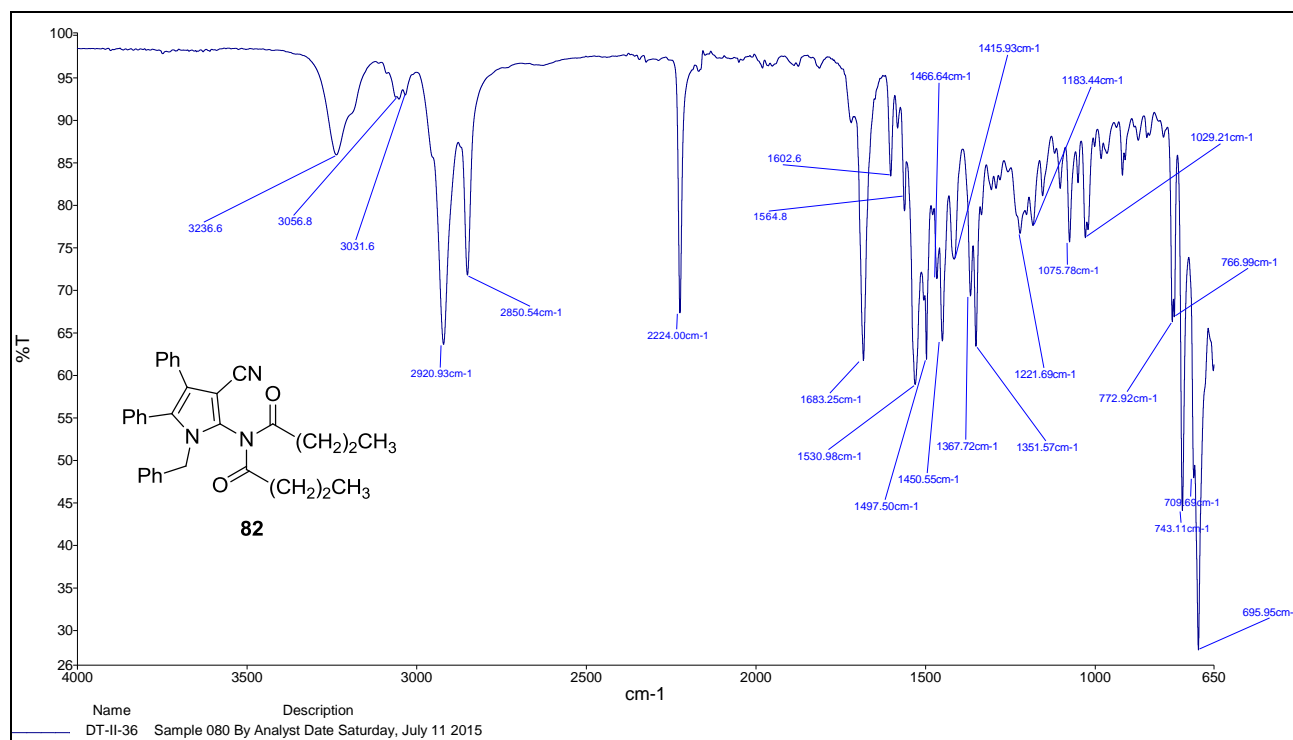


Figure 2.3: The IR spectrum of **82** (neat sample). The broad peak at 3236.6 cm^{-1} could probably be due to the hydroxyl, O-H stretch from moisture in the sample.

The ^1H NMR spectrum of derivative **82** shows a characteristic singlet (2H) at δ 4.88 ppm, which corresponds to the *N*-benzyl protons of **82** (NCH_2Ph) (Figure 2.4).²⁸ This

characteristic resonance signal is used in the ^1H NMR spectral identification of pyrrole **65** and its synthetic derivatives which contain the *N*-benzyl side chain.

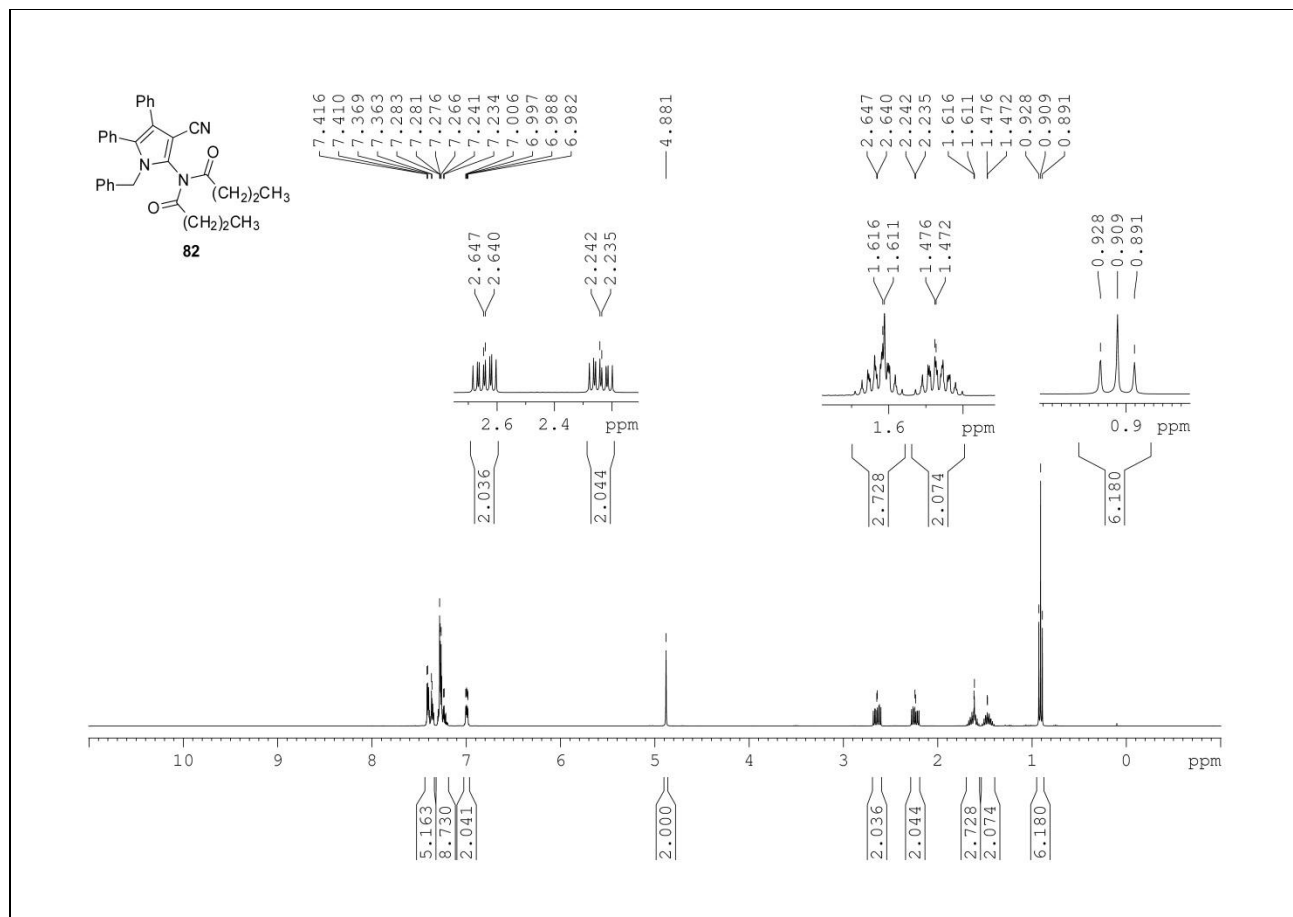
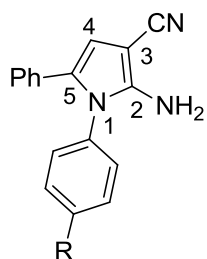


Figure 2.4: The ^1H NMR (400 MHz, CDCl_3) spectrum of **82**.

Characteristic ^{13}C NMR signals of pyrrole **65** and its synthetic derivatives were assigned with the aid of distortionless enhancement by polarisation transfer (DEPT) spectroscopy and 2D NMR spectroscopic techniques, such as heteronuclear single quantum correlation (HSQC) and heteronuclear multiple-quantum correlation (HMBC) (only the HSQC spectrum is shown, Figure 2.6).²⁸ In addition, the ^{13}C NMR data and assignment of two closely related, known 2-amino-3-pyrrocarbonitriles **89a** and **b** were also employed to confirm the assignment of the characteristic signals (Table 2.1).²⁶



89a,b

a: R = H
b: R = Cl

Table 2.1: Characteristic ^{13}C NMR peaks of known compounds **89a** and **b**.²⁶

Compound 89	Chemical shift, δ (ppm)		
	C-3	C\equivN	C-2
a	70.9	117.6	148.9
b	70.9	117.5	149.1

The ^{13}C NMR spectrum of **82** shows characteristic signals at δ 48.4 (**CH₂**), 92.6 (**C**), 114.6 (**C**), and 135.2 (**C**), which correspond to the *N*-benzylic carbon (**NCH₂Ph**), the carbon adjacent to the 3-cyano group (**C-CN**), the cyano carbon (**C \equiv N**), and the carbon adjacent to the 2-amino group (**C-NH₂**), respectively (Figure 2.5).²⁶ The identity of the *N*-benzylic carbon was confirmed with HSQC which shows a direct correlation between the benzylic proton signal and benzylic carbon signal (6-**CH₂** and **C-6**, Figure 2.6). These characteristic ^{13}C NMR signals, in conjunction with the aforementioned ^1H NMR characteristic signal are utilised in the NMR spectroscopic identification of pyrrole **65** and its synthetic derivatives. In addition, the appearance of a downfield signal at δ 175.1 (**C**) in the ^{13}C NMR spectrum of **82** is due to the resonance from the carbonyl carbon (**C=O**).²⁸ This downfield ^{13}C NMR signal is used to further distinguish pyrrole **65** from its *N*-acyl and *N,N*-diacyl synthetic derivatives.

Furthermore, positive mode HRMS analysis of **82** had detected a molecular ion peak with a *m/z* ratio of 512.2309, corresponding to the $[\text{M} + \text{Na}]^+$ ion of the imide (spectrum not shown). The observed *m/z* value corresponds to a chemical formula of $\text{C}_{32}\text{H}_{31}\text{N}_3\text{NaO}_2$ and has a mass error measurement of 0.10 mDa or 0.20 ppm from its calculated *m/z* value of 512.2308.²⁹

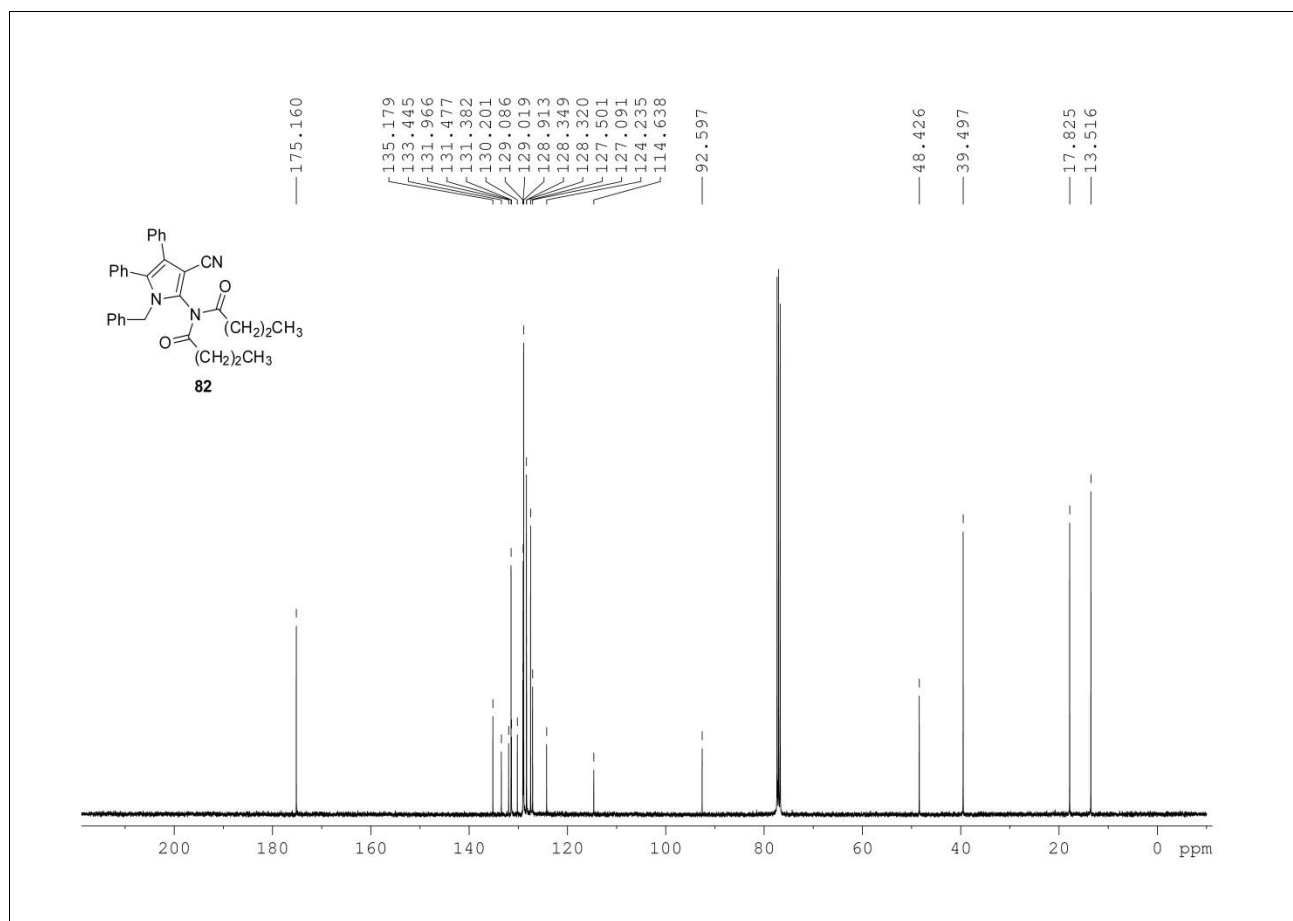


Figure 2.5: The ^{13}C NMR spectrum of **82** (100 MHz, CDCl_3). The residual solvent peak is a triplet, resonating at δ 77.0 ppm.

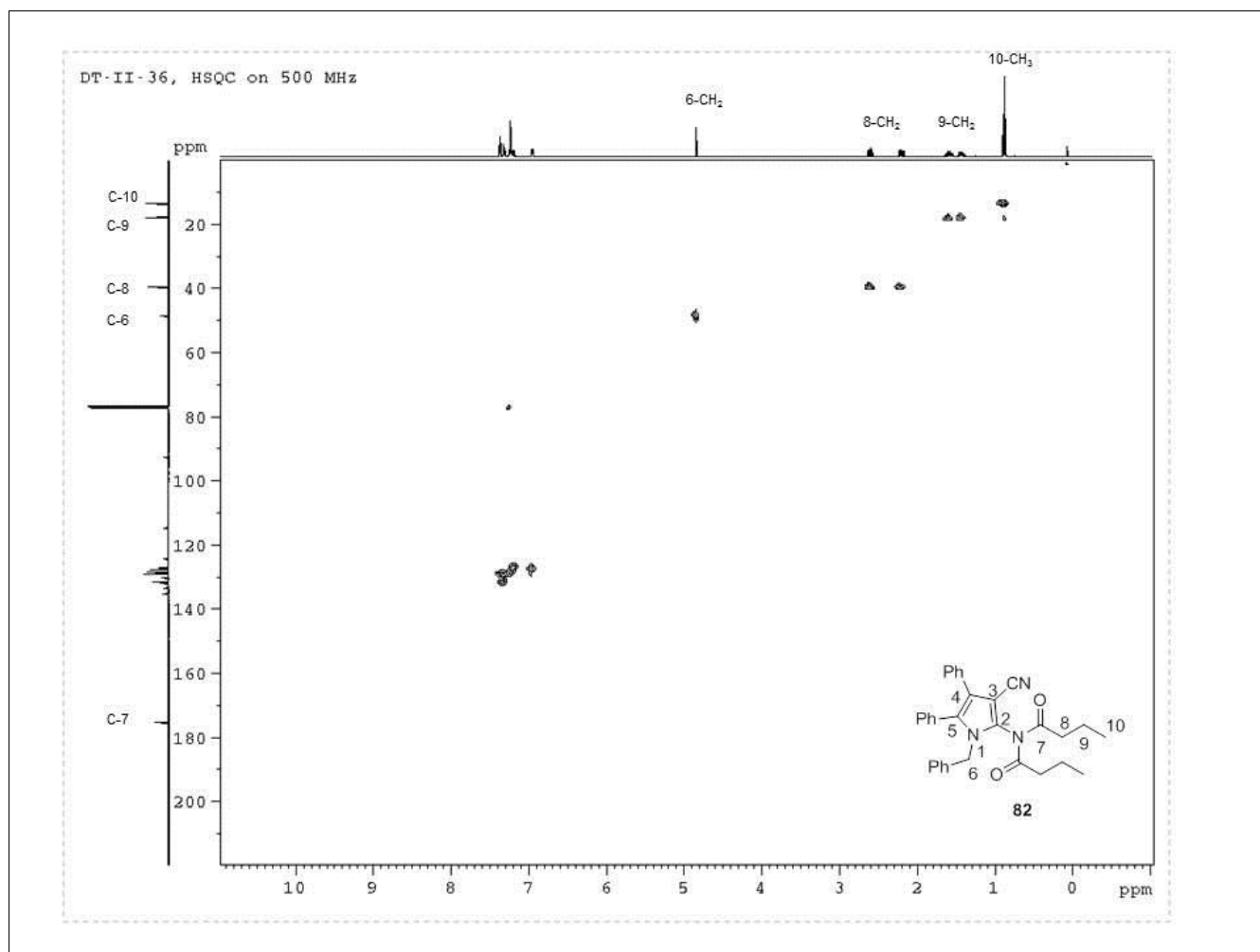
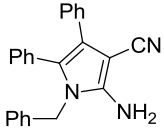
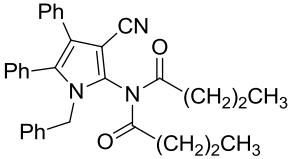
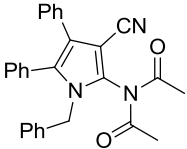
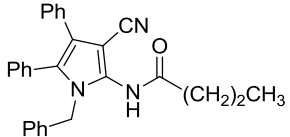
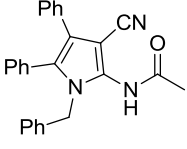
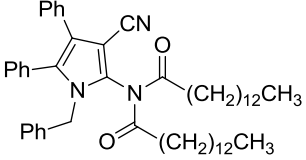
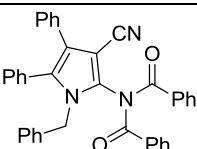
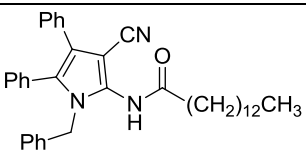
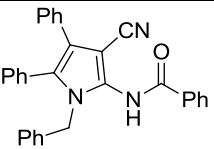
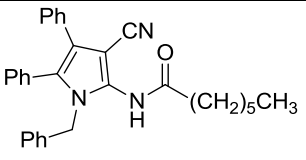


Figure 2.6: The HSQC (500 MHz, CDCl₃) spectrum of **82**.

2.3 b) Enzymatic kinetic studies – first series

The percentage inhibitions of the compounds in the first series of synthetic pyrrole derivatives against IMP-1 are presented in Table 2.2. According to the results shown, imide **78** and the corresponding *N*-benzamide **79** are the only two inhibitors which are more potent than the lead compound **65**. The rest of the imide and amide inhibitors exhibit lower or comparable inhibition percentages with inhibitor **65**. Thus, regardless of the chain length, aliphatic amide or imide derivatives of **65** are less potent IMP-1 inhibitors than aromatic amide **79** or aromatic imide **78**.

Table 2.2: The percentage inhibition of the first series of pyrrole derivatives (10 μM) against IMP-1 (5 nM, containing BSA at a final conc. of 20 $\mu\text{g mL}^{-1\text{a}}$) at pH 7.0 and 25 $^{\circ}\text{C}$, with CENTA (70 μM) as the substrate.

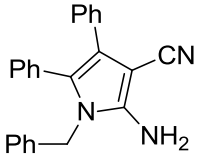
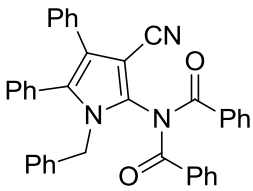
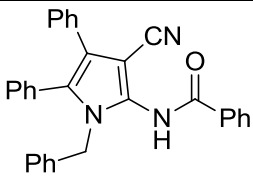
Inhibitor	Structure	Percentage Inhibition (%)	Inhibitor	Structure	Percentage Inhibition (%)
65^b		26.3 \pm 4.2	82		17.1 \pm 3.4
76		18.6 \pm 4.8	84		21.0 \pm 2.5
77		16.1 \pm 6.6	83		14.3 \pm 2.4
78		48.0 \pm 5.9	85		8.2 \pm 4.5
79		50.9 \pm 2.5	86		23.2 \pm 5.9

^aBovine serum albumin (BSA) was added to IMP-1 for enzyme stability. ^bPyrrole **65** is shown for comparison. Inhibition percentages of derivatives which are higher than that of pyrrole **65** are highlighted in red.

The competitive (K_{ic}) and uncompetitive (K_{iuc}) inhibition data obtained for inhibitors **78** and **79** (Table 2.3) suggests that the inhibitors exhibit a mixed-inhibition mode against IMP-1, *i.e.* the inhibitor may possibly bind to the enzyme at the same binding site as the substrate,

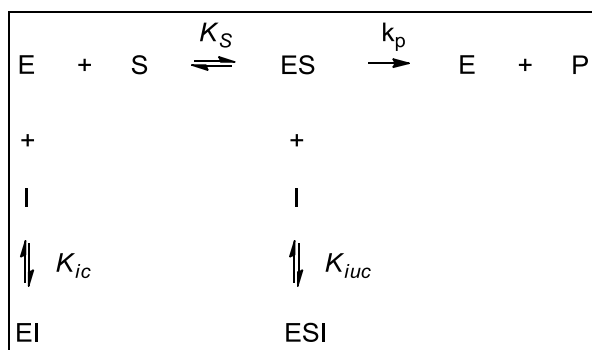
resulting in an enzyme-inhibitor (EI) complex or to the substrate bound enzyme, forming a ternary enzyme-substrate-inhibitor (ESI) complex (Scheme 2.14).^{19,30} In either mode, the EI or ESI complex does not result in turnover of substrate to product.^{19,30} This is in contrast to **65** which is a purely competitive inhibitor,⁴ in which case the inhibitor only competes with the substrate for the same binding site (Table 2.3).³⁰

Table 2.3: The competitive (K_{ic}) and uncompetitive (K_{iuc}) inhibition constants (μM) of inhibitors **78** and **79** against IMP-1 (5 nM, containing BSA at a final conc. of $20 \mu\text{g mL}^{-1}$) at pH 7.0 and 25 °C, with CENTA (5-70 μM) as the substrate.

Inhibitor	Structure	K_{ic} (μM)	K_{iuc} (μM)
65*		21 ± 10	-
78		468 ± 6	55.2 ± 19.0
79		10.7 ± 9.3	4.31 ± 1.82

*Pyrrole **65** is shown for comparison.⁴

Further analysis of the kinetic data of inhibitor **78** suggests that its uncompetitive mode is more dominant than its competitive mode as the K_{iuc} value of **78** is a magnitude lower than its corresponding K_{ic} value^{4,19} (in general, for either competitive or uncompetitive inhibition mode, a smaller inhibition constant implies that a smaller concentration of the inhibitor is required to inhibit the enzyme by 50%, on condition that the substrate concentration is close to the K_m value).³⁰



Scheme 2.14: The reaction pathway of a mixed-inhibition mode inhibitor, I with the enzyme, E, substrate, S and product, P. K_{ic} and K_{iuc} is the competitive and uncompetitive inhibition constants, respectively. K_S and k_p is the K_m and k_{cat} equivalent of the uninhibited enzyme, respectively.³⁰

In addition, among the three inhibitors presented, **79** is the most potent IMP-1 inhibitor, exhibiting the lowest inhibition constant (uncompetitive) of 4.31 μ M (Table 2.3). Therefore, the derivatisation of the 2-amino group of **65** to an *N*-benzamide group in **79** has the propensity to increase the IMP-1 inhibitory potency of the lead compound. This important observation was used as the basis for the design and synthesis of another series of synthetic *N*-benzamide pyrrole derivatives having various moieties such as *p*-nitro and 4-benzoyl (Section 2.2).

In order to determine whether the apparent IMP-1 inhibition of the imide derivatives were due to the corresponding hydrolysed amides or the imides themselves, a study on the stability of a few imide derivatives in the presence of IMP-1 was carried out. The study involved overnight incubation of DMSO solution of imides **76**, **78** and **82** with the enzyme, followed by sample analysis with low resolution electrospray ionisation mass spectrometry (ESI-MS).

The results of the MS analysis only showed the m/z ratio of the imides tested and no detectable m/z ratio of the corresponding hydrolysed amides. A representative result of the test is presented in Figure 2.7, showing a major peak at m/z 512.1 that corresponds to the $[M + Na]^+$ ion of imide **82**. However, no m/z peaks corresponding to the hydrolysed amide **84** (MW 419.5 $g\ mol^{-1}$) was detected in the analysis. As ESI-MS is a qualitative analysis, the result does not necessarily imply that imide **82** is unchanged, but that some of it may have

remained in the sample. Nevertheless, the absence of any of the m/z peaks of **84** in the spectrum suggests that the imide is stable against IMP-1 even after overnight incubation with the enzyme.

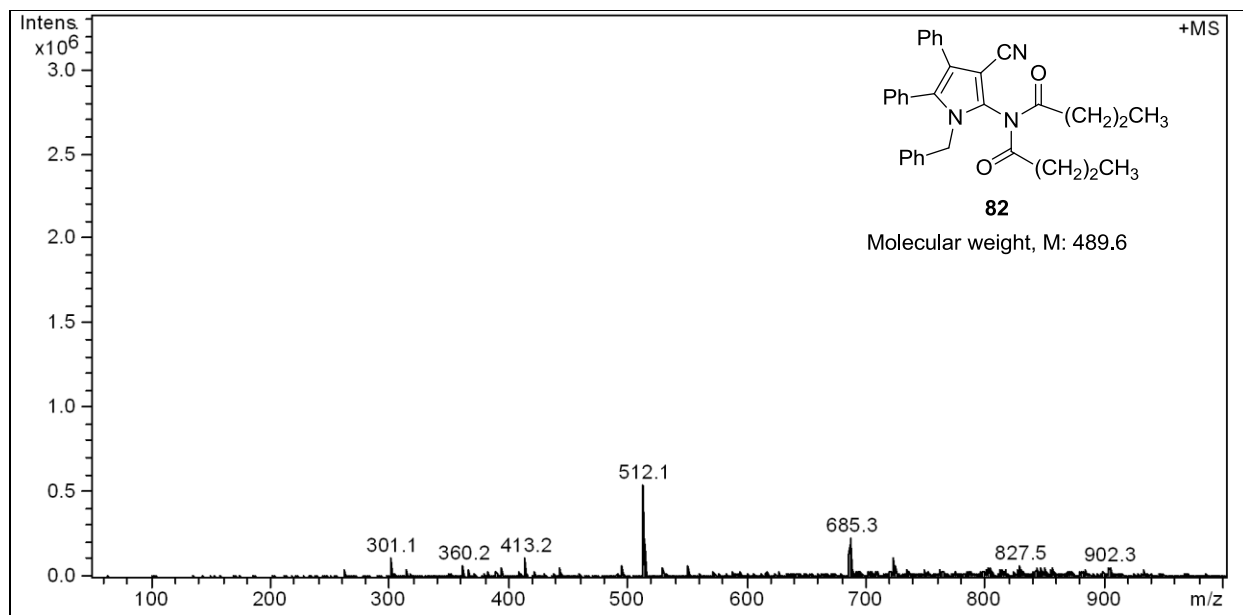


Figure 2.7: The ESI-MS spectrum of **82** (10 μ M) after overnight incubation with IMP-1 (5 nM). The peaks at m/z 301.1, 360.3, 413.2, 685.3, 827.5 and 902.3 correspond to the solvent or background noise of the analysis and can be safely ignored.

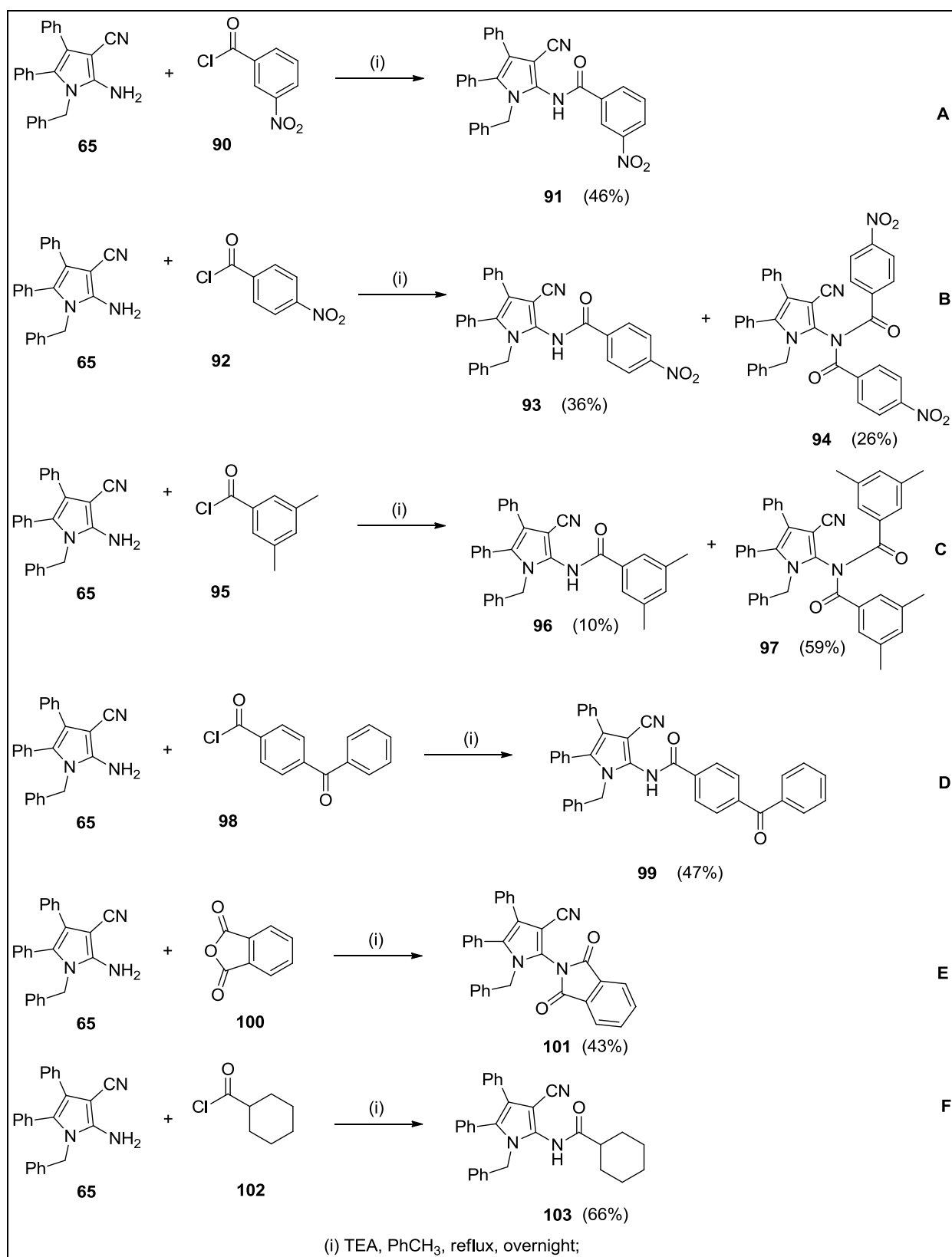
2.3 c) Synthetic work – second series

Scheme 2.15 presents the synthetic work, including the reaction yields of another series of pyrrole derivatives. Interestingly, none of the entries involving substituted benzoyl chlorides **90**, **92**, **95** and **98** (entries **A-D**) afforded *N,N*-diacyl imide as the sole reaction product. Entries **A** and **D** afforded *N*-acyl amide as the only reaction product, whereas entries **B** and **C** afforded a mixture of imide and amide products. Overall, the reaction yields of the imide and/or amide products were modest. This observation is in contrast to the acylation of pyrrole **65** with benzoyl chloride, affording imide **78** as the sole reaction product in a good yield of 76%, under the same experimental conditions and with the same amount of acyl chloride and TEA used (Scheme 2.8). Therefore, this indicates that derivatising the benzoyl

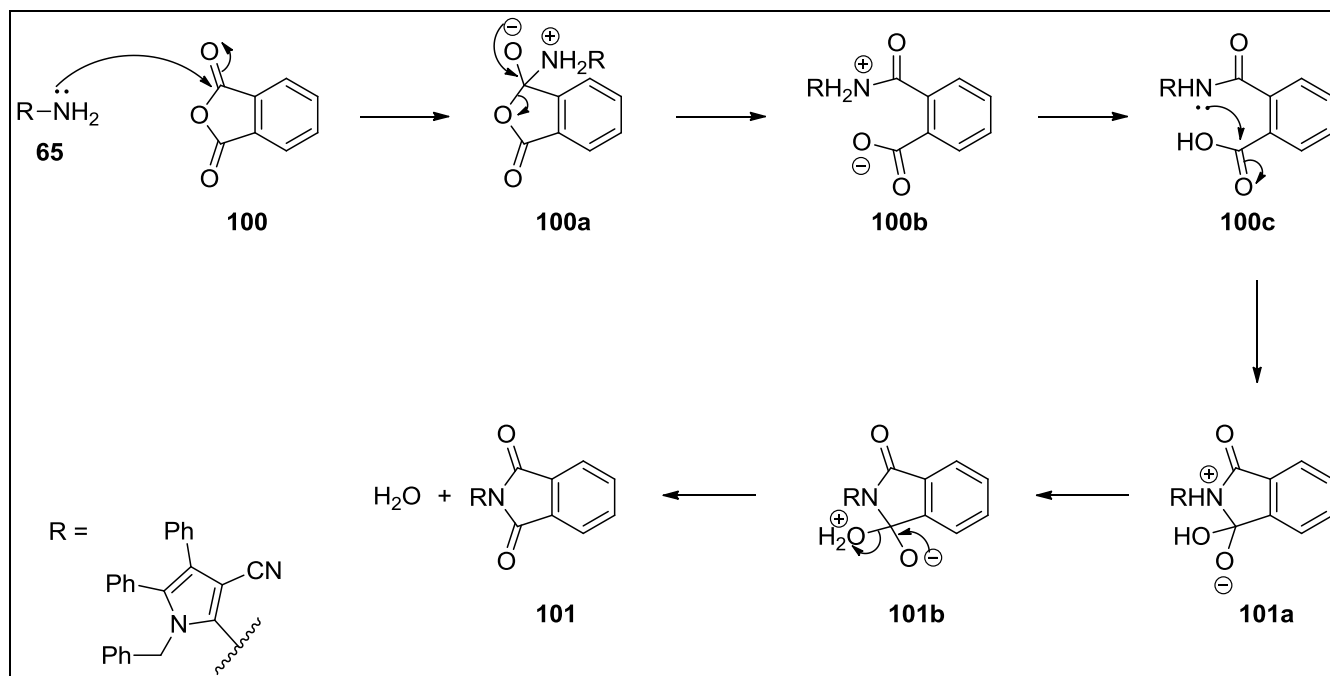
chloride with various substituents, such as 3-nitro, 4-nitro, 3,5-dimethyl or 4-benzoyl results in a less reactive acyl chloride towards nucleophilic acyl substitution with 2-amino-3-cyanopyrrole **65**.

In addition, The *N*-cyclohexanoyl pyrrole derivative **103** was introduced in the study as the unsaturated ring analogue of the *N*-benzamide derivative **79**. Amide **103** was also obtained as the only reaction product from the acylation of pyrrole **65** with cyclohexanoyl chloride (**102**) (entry **F**). One possible explanation for this could be due to the steric hindrance of the cyclohexyl ring of the acyl chloride, thus rendering it less accessible for a second round of nucleophilic acyl substitution by amide **103**. This explanation could also be applied to entry **D**, whereby the 4-benzoyl moiety of **98** could be deemed as too bulky a group for further imide formation.

The *N*-phthalimide pyrrole derivative **101** was also another molecule of interest, as it structurally resembles *N,N*-dibenzoyl imide **78** (entry **E**). The proposed mechanism for the synthesis of **101**, *via* the condensation of pyrrole **65** with two equivalents of phthalic anhydride (**100**), under refluxing condition is illustrated in Scheme 2.16.³¹ The condensation reaction was neither catalysed by acid nor base. As shown by the proposed mechanism, the only driving force for the formation of phthalimide **101** is the expulsion of water from the condensation reaction, as phthalic anhydride (**100**) undergoes nucleophilic acyl substitution with 2-amino-3-cyanopyrrole **65**.



Scheme 2.15: The syntheses of the second series of *N*-acyl and *N,N*-diacyl derivatives of pyrrole **65**.



Scheme 2.16: The proposed mechanism for the formation of phthalimide **101** (adapted from Thale et al.)³¹

The structural identities of the second series were identified based on key diagnostic IR and NMR spectral signals, as previously identified for that of the first series (Section 2.3 a). For example, the presence of bands around $2225\text{-}2230\text{ cm}^{-1}$ and $1655\text{-}1700\text{ cm}^{-1}$, found in the IR spectra of the compounds correspond to the nitrile and amide carbonyl stretching bands, respectively (spectra not shown). Interestingly, the carbonyl stretching bands for phthalimide **101** were observed to appear as two strong peaks at 1750.0 and 1732.6 cm^{-1} in its IR spectrum (spectrum not shown). These stretching frequencies are characteristic of that of a cyclic imide.²⁸

Moreover, the *N*-benzylic protons (NCH_2Ph) of the compounds could be identified as a two proton-singlet at around δ 5.0 ppm in their respective ^1H NMR spectra. On the other hand, the *N*-benzylic (NCH_2Ph), 3-carbonitrile ($\text{C}\equiv\text{N}$) and carbonyl ($\text{C}=\text{O}$) carbon of the compounds could be each identified as a ^{13}C signal, resonating at around δ 47-49, 114-116 and 165-176 ppm, respectively in their ^{13}C NMR spectra. The ^1H and ^{13}C NMR spectra of

phthalimide **101** are shown in Figure 2.8 and 2.9, respectively as a representative spectral data for this series of compounds.

As mentioned earlier, DEPT analysis was also instrumental in ^{13}C NMR signal assignment for the compounds. The DEPT 135 spectrum of phthalimide **101** revealed a negatively-phased signal at δ 49.0, that corresponds to the *N*-benzylic (NCH_2Ph) carbon, as well as 11 aromatic CH signals from δ 124.2 to 134.9 ppm, all of which could be seen pointing upwards (Figure 2.10). This result is consistent with the expected number of methylene and non-equivalent methine carbons for phthalimide **101** (Figure 2.11).

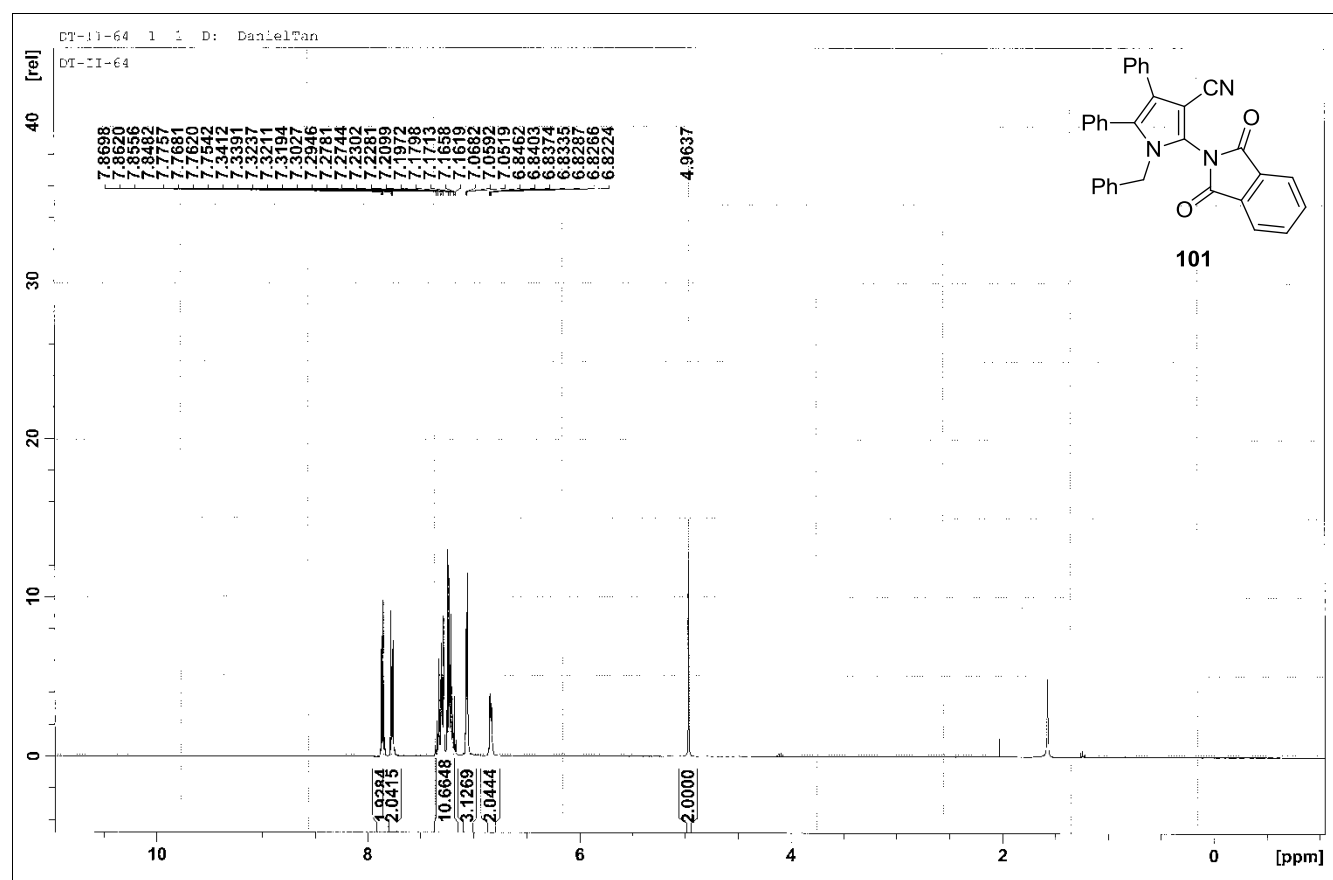


Figure 2.8: The ^1H NMR (400 MHz, CDCl_3) spectrum of **101**. The singlet at δ 1.56 and 2.05 ppm is due to traces of water and ethyl acetate, respectively. The integration for the multiplet from δ 7.85-7.87 is 1.9284 (2H).

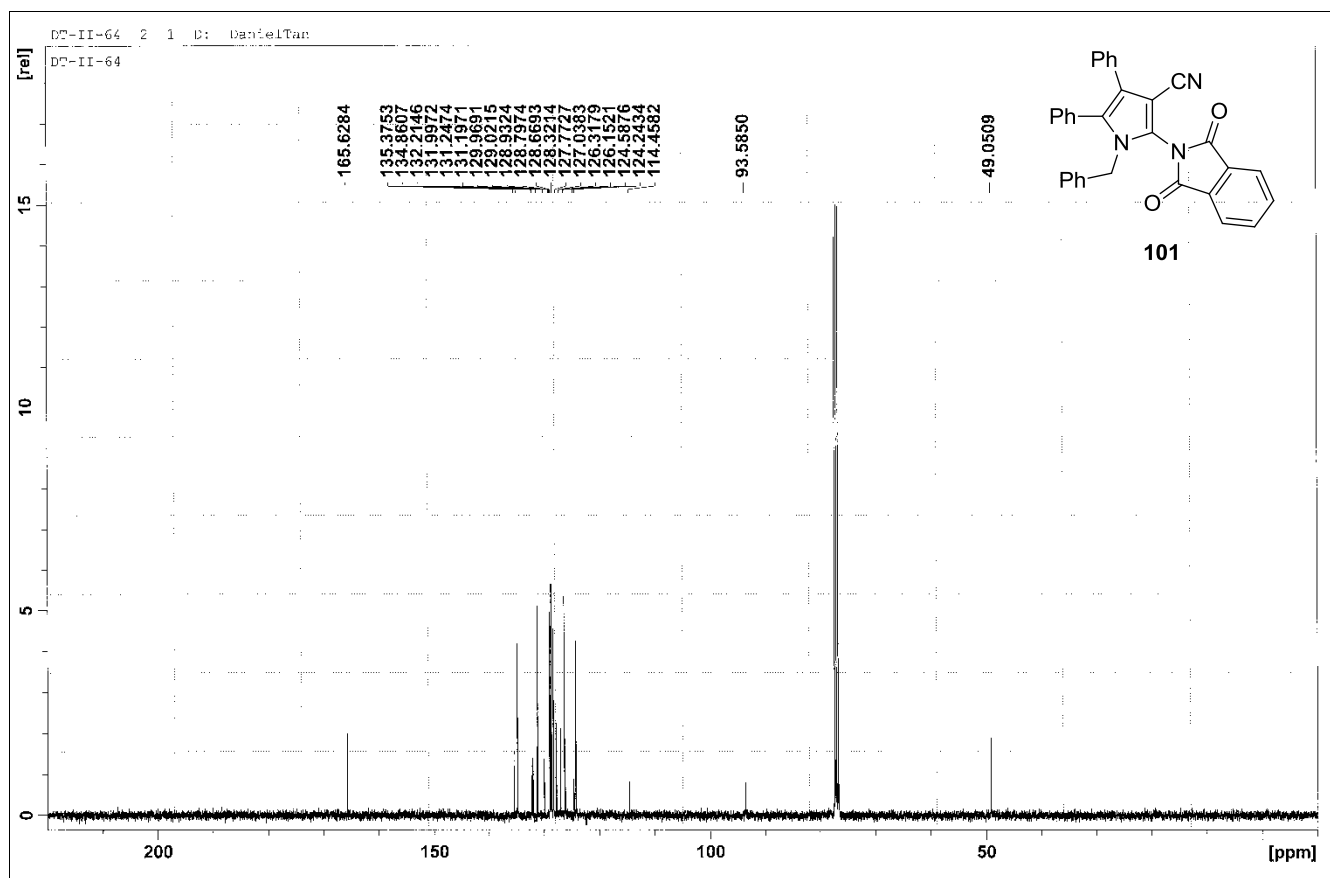


Figure 2.9: The ^{13}C NMR spectrum of **101** (100 MHz, CDCl_3). The triplet at δ 77.0 ppm is due to CDCl_3 .

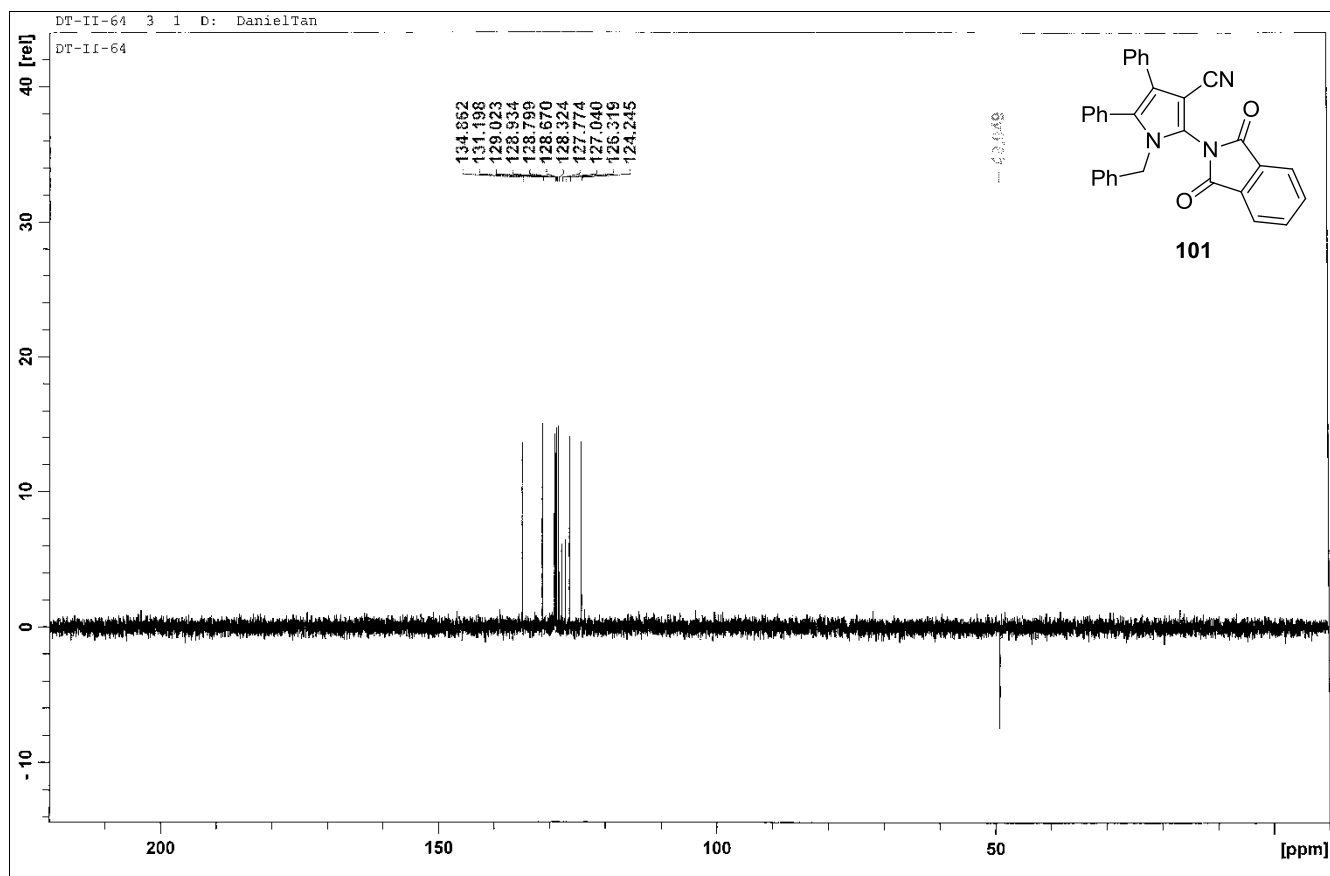


Figure 2.10: The DEPT 135 spectrum of **101** (100 MHz, CDCl₃). The negatively-phased signal resonates at δ 49.049 ppm.

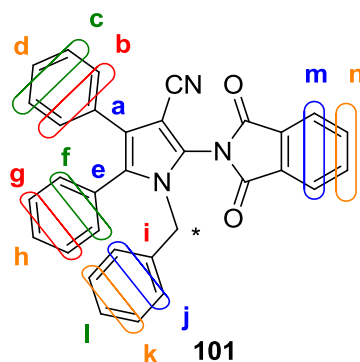


Figure 2.11: The molecular structure of **101**, showing the 11 non-equivalent **CH** carbons, labeled from **a** to **n** and the *N*-benzylic carbon, marked with an asterisk.

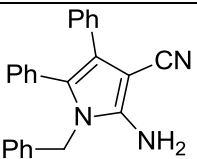
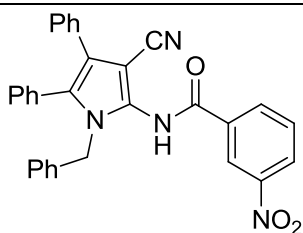
Lastly, the molecular weight and chemical formula of phthalimide **101** was confirmed by HRMS analysis. The HRMS spectrum of the phthalimide showed a molecular ion peak with

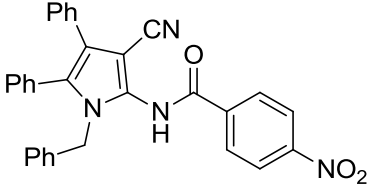
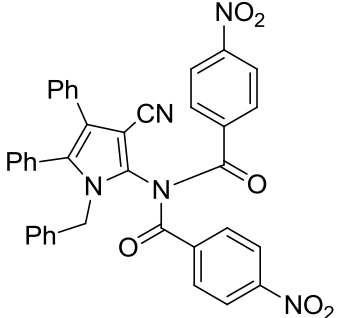
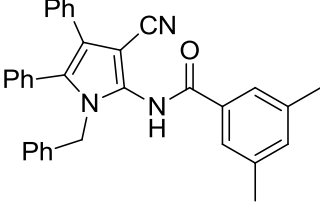
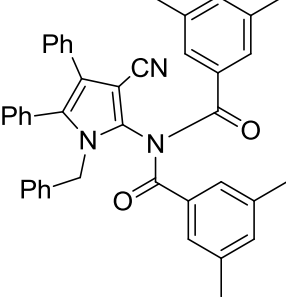
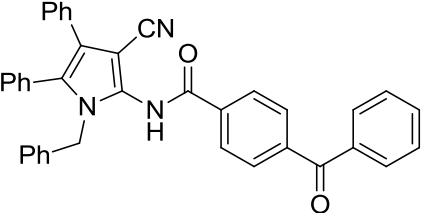
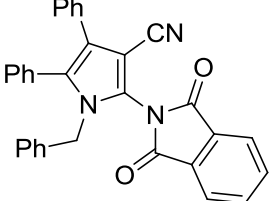
a m/z ratio of 502.1527, corresponding to the $[M + Na]^+$ ion of the compound. The observed m/z ratio corresponds to a chemical formula of $C_{32}H_{21}N_3NaO_2$ and has a mass error measurement of 0.10 mDa or 0.20 ppm from its calculated m/z value of 502.1526.

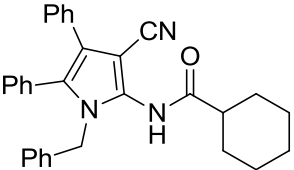
2.3 d) Enzymatic kinetic study – second series

Derivatives **91**, **93**, **96** and **99** were identified as significantly potent inhibitors against IMP-1 as they showed improved IMP-1 inhibitory potencies compared to the pyrrole lead compound **65** (Table 2.4). However, the *N,N*-diaromatic imides, **94** and **97** together with the *N*-phthalimide derivative **101** exhibit lower inhibitory activities than **65**. This result taken together with the previous kinetic result (Section 2.2 b) implies that the imide derivatives are less potent inhibitors than the corresponding amide derivatives. In addition, example **103** substantiates an earlier claim that the *N*-aromatic amide derivatives are more potent IMP-1 inhibitors than the *N*-aliphatic or non-aromatic amide derivatives (Section 2.2 b).

Table 2.4: The percentage inhibition of the second series of pyrrole derivatives (10 μ M) against IMP-1 (5 nM, containing BSA at a final conc. of 20 μ g mL⁻¹) at pH 7.0 and 25 °C, with CENTA (70 μ M) as the substrate.

Inhibitor	Structure	Percentage Inhibition (%)
65*		26.3 ± 4.2
91		48.7 ± 1.9

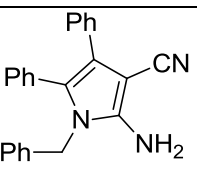
93		36.9 ± 2.4
94		20.2 ± 3.4
96		32.3 ± 4.7
97		13.3 ± 2.4
99		44.3 ± 3.3
101		20.3 ± 3.7

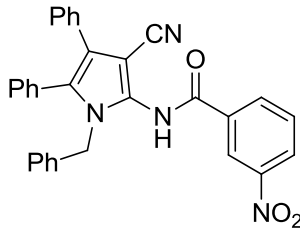
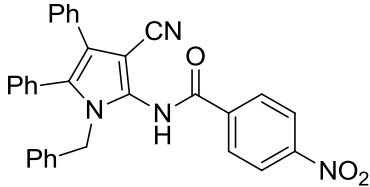
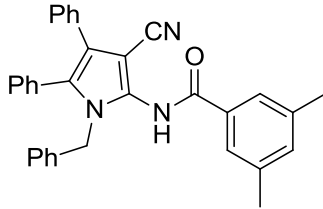
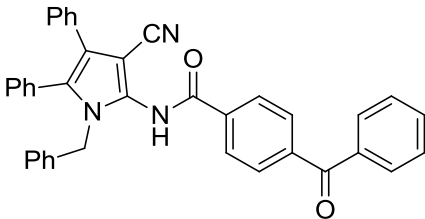
103		23.3 ± 3.7
------------	---	----------------

*Pyrrole **65** is shown for comparison. Inhibition percentages of derivatives which are higher than that of pyrrole **65** are highlighted in red.

Inhibitors **91**, **93**, **96** and **99** were then selected for further kinetic study (Table 2.5). The results revealed that inhibitor **91** and **96** exhibit a mixed-inhibition mode against IMP-1, whereas the *N-p*-nitrobenzamide derivative **93** is a purely competitive IMP-1 inhibitor with a K_{ic} value of $1.24 \mu\text{M}$ (Table 2.5). Inhibitor **93** is thus far the most potent IMP-1 inhibitor for this class of inhibitors. The low K_{ic} value of inhibitor **93** in comparison to the K_m value of the CENTA substrate ($200 \mu\text{M}$) implies that binding of the inhibitor to the enzyme prevents the substrate from entering the active site of the enzyme, as a competitive inhibitor competes with the substrate for the same binding site in the enzyme molecule and the K_{ic} and K_m is a measure of affinity for the inhibitor and substrate to bind to the enzyme, respectively.⁶ The second most potent IMP-1 inhibitor for this series is inhibitor **99**, which is a solely uncompetitive inhibitor with a K_{iuc} magnitude of $1.52 \mu\text{M}$.

Table 2.5: The competitive (K_{ic}) and uncompetitive (K_{iuc}) inhibition constants (μM) of inhibitors **65**, **91**, **93**, **96** and **99** against IMP-1 (5 nM, containing BSA at a final conc. of $20 \mu\text{g mL}^{-1}$) at pH 7.0 and $25 \text{ }^\circ\text{C}$, with CENTA (5-70 μM) as the substrate.

Inhibitor	Structure	K_{ic} (μM)	K_{iuc} (μM)
65*		21 ± 10	-

91		23.7 ± 25.2	3.33 ± 0.81
93		1.24 ± 0.59	-
96		20.2 ± 10.9	7.78 ± 2.54
99		-	1.52 ± 0.36

*Pyrrole **65** is shown for comparison.⁴ “-” Denotes a large value (10^2 - 10^5 mM range).

The difference in the mode of inhibition between *N*-nitrobenzamides **91** and **93** could be explained by molecular modelling with the Glide program. The modelling results suggested that the nitro group of **93** binds in the vicinity of the metal centres, whereas the nitro group of **91** doesn't make any significant interactions within the active site of the enzyme (Figures 2.8 and 2.9, respectively).

Further analysis of the *in silico* model of **93** bound with IMP-1 suggested that one of the oxygen ions of the *p*-nitro group of the inhibitor binds electrostatically to both of the Zn²⁺ ions (O-Zn1 distance 2.08 Å and O-Zn2 distance 2.52 Å), thereby displacing the bridging hydroxide ion which is required for catalysis (Figure 2.12). The same oxygen ion is also predicted to make a hydrogen bond interaction with a nitrogen atom on the imidazole ring of His79 (118) (O-N distance 3.19 Å). Other possible interactions predicted by the model are a salt-bridge interaction between the nitrogen cation of the nitro group of **93** and the terminal

carboxylate ion of Asp81 (120) (N-O distance 3.44 Å), and a π - π stacking interaction between the *p*-nitrophenyl ring of **93** and the imidazole ring of His197 (263) (C-C distance 4.27 Å). The modelling therefore suggested that inhibitor **93** may possibly compete with the same binding site as the substrate CENTA in binding with IMP-1.

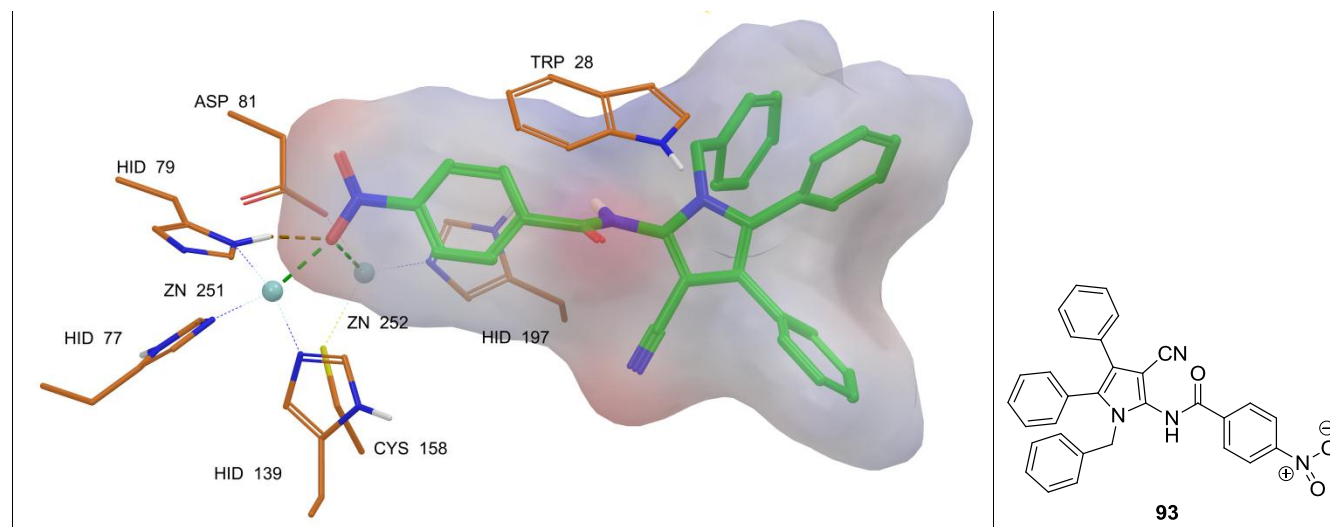


Figure 2.12: The *in silico* model of **93** bound to the active site of IMP-1 as predicted by Glide. Atom colours: carbon on ligand in green, carbon on IMP-1 in orange, nitrogen in blue, oxygen in red, sulfur in yellow and hydrogen in white. The Zn^{2+} ions are shown as cyan spheres. ZN 251 and ZN 252 denotes Zn1 and Zn2, respectively. The dashed orange and green lines represent the hydrogen bond and ionic interactions, respectively.

On the other hand, the computational model of inhibitor **91** docked into IMP-1 predicted that the 3-nitro group of the inhibitor is orientated away from the Zn^{2+} ions, with the nitrogen atom of the nitro group forming π -cation interactions with the imidazole ring of His197 (263) (N-C distance 4.92 Å) and the indole ring of Trp28 (64) (N-C distance 4.37 Å) (Figure 2.13). Unexpectedly, none of the oxygen atoms of the 3-nitro group of **91** were shown by the model to have any interactions with the hydrogen bond donor region of the active site. Instead, the model predicted that the carbonyl oxygen of **91** is hydrogen bonded to a nitrogen atom on the imidazole ring of His79 (118) (O-N distance 3.13 Å).

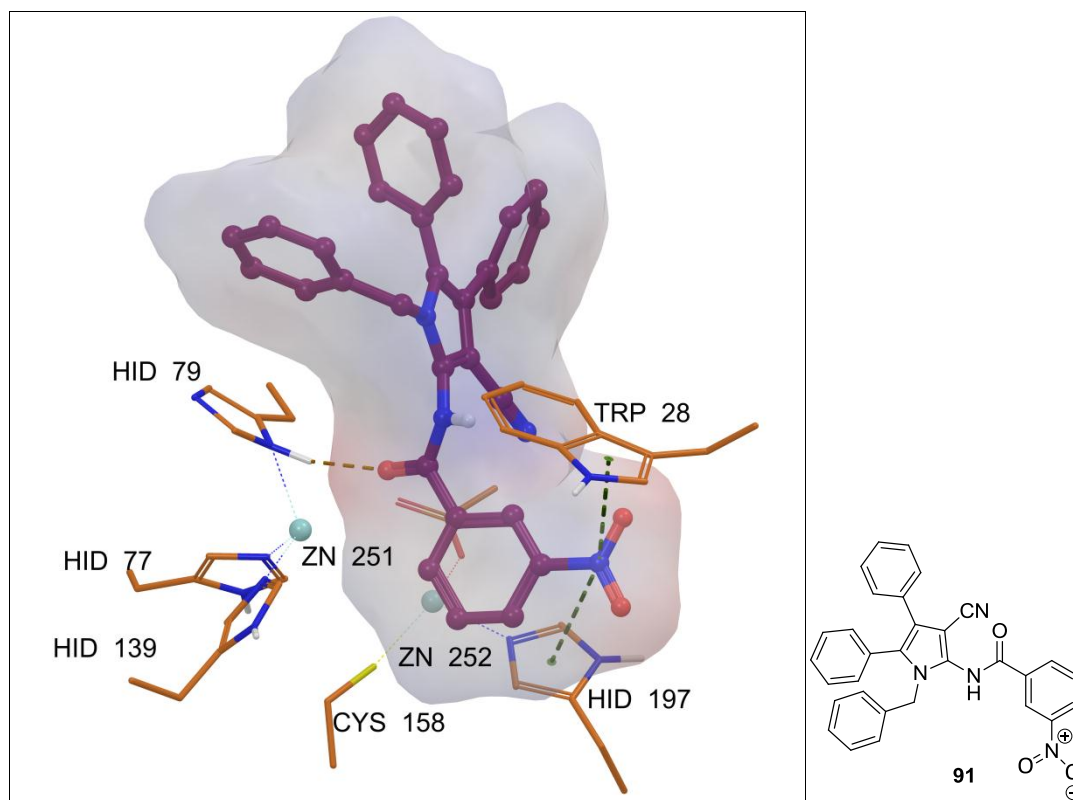


Figure 2.13: The *in silico* model of **91** bound to the active site of IMP-1 as predicted by Glide. Atom colours: carbon on ligand in magenta, carbon on IMP-1 in orange, nitrogen in blue, oxygen in red, sulfur in yellow and hydrogen in white. The Zn^{2+} ions are shown as cyan spheres. ZN 251 and ZN 252 denotes Zn1 and Zn2, respectively. The dashed orange and green lines represent the hydrogen bond and π -cation interactions, respectively.

The uncompetitive inhibition mode displayed by inhibitor **99** could also be rationalised by molecular docking study of the inhibitor with IMP-1, which showed that only a segment of the inhibitor is bound to the enzyme active site (Figure 2.14). According to the docking result, inhibitor **99** is predicted to have two significant interactions with the enzyme: a hydrogen bond between the carbonyl oxygen of **99** and a nitrogen atom of His79 (118) (O-N distance 2.86 Å), as previously described for the **91**-IMP-1 model, and a π - π stacking interaction between the *N*-benzamide ring and the imidazole ring of His197 (263) (C-C distance 4.27 Å). The rest of the inhibitor, such as the pyrrole ring together with the *N*-benzyl ring, vicinal diphenyl side chains and 4-benzoyl ring are exposed to the surface of the enzyme. This implies that the active site of the enzyme isn't large enough to accommodate the inhibitor. The preferred

binding site of inhibitor **99** and IMP-1 may therefore possibly be an induced binding site formed from the binding of the CENTA substrate to the enzyme.

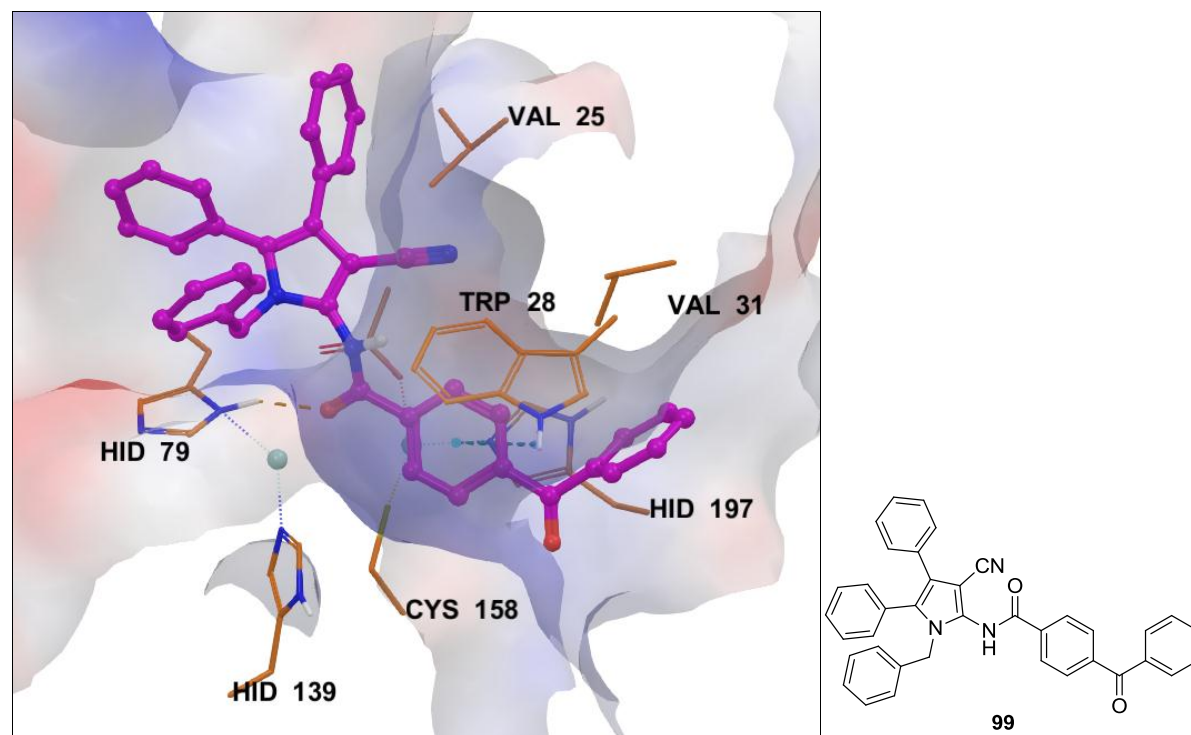


Figure 2.14: The *in silico* model of **99** bound to the active site of IMP-1 as predicted by Glide. Atom colours: carbon on ligand in purple, carbon on IMP-1 in orange, nitrogen in blue, oxygen in red, sulfur in yellow and hydrogen in white. The Zn^{2+} ions are shown as cyan spheres. The dashed orange and green line represents the hydrogen bond and the π - π stacking interaction, respectively. The surface of the enzyme is coloured electrostatically, with the blue and red region corresponding to the positively and negatively charged region, respectively.

2.4 Conclusion

First and foremost, the IMP-1 structure-activity relationship (SAR) of a series of *N*-acyl amide and *N,N*-diacyl imide derivatives of pyrrole **65** showed that the imide derivatives are less potent than the corresponding amide derivatives. A stability test of the imide derivatives in the presence of the enzyme revealed that the apparent inhibitory activity of the imides were due to the imides themselves, and not by the corresponding amides.

In addition, the SAR study also showed that the aromatic *N*-acyl amide derivatives are more potent than the aliphatic or non-aromatic *N*-acyl amide derivatives. In line with this observation, a series of aromatic *N*-aryl amide derivatives of pyrrole **65** were explored, which resulted in the discovery of two potent IMP-1 inhibitors, **93** and **99** for this class of inhibitors (Figure 2.15).

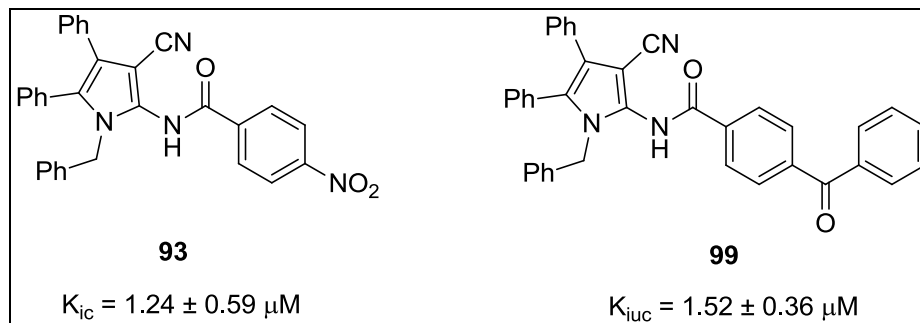
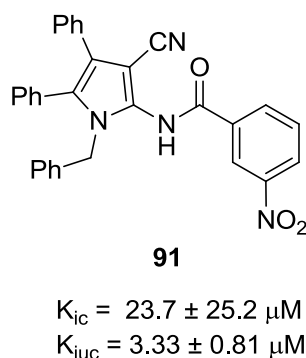


Figure 2.15: The two most potent IMP-1 inhibitors, **93** and **99** for this class of inhibitors.

Finally, the position of the nitro group in the *N*-nitrobenzamide ring of inhibitors **91** and **93** dictates the mode of IMP-1 inhibition, with the *N*-3-nitrobenzamide **91** exhibiting a mixed-mode inhibition and the *N*-4-nitrobenzamide **93** being a purely competitive inhibitor against the enzyme. Computational modelling of isomers **91** and **93** predicted that the former doesn't bind in the vicinity of the metal centres, whereas the latter binds directly with the Zn^{2+} ions *via* the 4-nitro group, thus displacing the bridging hydroxide which is involved in β -lactam hydrolysis.

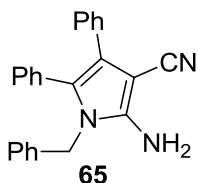


2.5 Experimental

2.5 a) General synthetic, spectroscopic and spectrometric experimental

Thionyl chloride (b.p. 74.6 °C) and petroleum ether, PE (b.p. 40-60 °C) were distilled before use. The rest of the chemicals and reagents were used without prior purification. Flash column chromatography was carried out with Merck Kieselgel 60. Melting points were recorded on a SMP11 (Stuart) and DigiMelt MPA161 (Stanford Research Systems) equipment, and are uncorrected. NMR spectra were recorded on Bruker AVANCE 500 or 400 MHz spectrometers. Chemical shifts are reported in parts per million (ppm) on a scale relative to the solvent peak CDCl_3 (^1H , 7.24 ppm; ^{13}C , 77.0 ppm) and $\text{DMSO-}d_6$ (^1H , 2.49 ppm; ^{13}C , 39.5 ppm). Coupling constants (J) are reported in Hz and peak multiplicities described as singlet (s), doublet (d), triplet (t), doublet of doublets (dd), quintet (quin), triplet of triplets (tt), multiplet (m), or broad (br). Low-resolution ESI-MS measurements were carried out on a Bruker Esquire HCT (High Capacity 3D ion trap) instrument with a Bruker ESI source. High-resolution electrospray ionisation accurate mass measurements (HRMS) were recorded on a Bruker MicrOTOF-Q (quadrupole–Time of Flight) instrument with a Bruker ESI source. Accurate mass measurements were carried out with external calibration using sodium formate as reference calibrant. Infrared (IR) spectroscopy samples were analysed as neat on a Perkin Elmer FT-IR/NIR Spectrometer Frontier.

2.5 b) Preparation of 2-Amino-1-benzyl-4,5-diphenyl-1H-pyrrole-3-carbonitrile (65)^{13,14,21}



A mixture of benzoin (2.1 g, 10 mmol), benzylamine (1.1 ml, 1.1 g, 10 mmol) and trichloroacetic acid, TCA (0.17 g, 1.0 mmol) in dry toluene (20 ml) was refluxed using a Dean-Stark apparatus for 2 h. A yellow solution was obtained. Malononitrile (0.66 g, 10 mmol) was then added to the reaction mixture, followed by 3 drops of pyridine. The mixture was further refluxed under Ar for 17 h. A colour change from yellow to olive green and finally dark brown was observed. The excess solvent was removed *in vacuo* to give a brown semi solid residue

(7.33 g). The residue was purified by silica gel column chromatography [EtOAc/PE (2:23) → EtOAc/PE (7:43)], followed by recrystallisation from diethyl ether to afford the title compound as a light brown solid (4.67 g, 67%), m.p.:173.5-175.9 °C (literature m.p.: 173-175 °C).³² R_f : 0.42 (30% EtOAc in PE, visible as a blue spot under UV). ^1H NMR (500 MHz, CDCl_3) δ (ppm): 3.85 (br s, 2H, NH_2 , D_2O exchangeable), 4.90 (s, 2H, NCH_2Ph), 7.06-7.08 (m, 2H, Ar-H), 7.13-7.15 (m, 3H, Ar-H), 7.18-7.32 (m, 8H, Ar-H), 7.35-7.38 (m, 2H, Ar-H). ^{13}C NMR (125 MHz, CDCl_3) δ (ppm): 47.0 (NCH_2Ph), 75.9 (C-CN), 117.5 ($\text{C}\equiv\text{N}$), 121.0 (Ar-C), 125.65 (Ar-C), 125.63 (Ar-C), 126.4 (Ar-CH), 128.0 (Ar-CH), 128.1 (Ar-CH), 128.2 (Ar-CH), 128.67 (Ar-CH), 128.72 (Ar-CH), 129.3 (Ar-CH), 130.8 (Ar-CH), 131.0 (Ar-CH), 133.2 (Ar-C), 136.1 (Ar-C), 145.9 (C-NH_2). ESI-MS: m/z 350.1 [$\text{M} + \text{H}$] $^+$. IR ν_{max} (cm^{-1}): 3406.0 (N-H stretch), 3333.0 (N-H stretch), 2199.7 ($\text{C}\equiv\text{N}$ stretch), 1624.5, 1601.7, 1541.8, 1496.8, 1470.9, 1438.1, 1365.4, 1339.3. ^1H NMR and ESI-MS data are in agreement with the literature.¹⁴

2.5 c) General procedure for the derivatisation of acyl chlorides³³

A mixture of thionyl chloride (2.0 ml, 3.6 g, 30 mmol) and the corresponding carboxylic acid (3 mmol) was refluxed for 1.5 h. Excess thionyl chloride was removed by distillation (74-76 °C, 1 atm). The residue obtained was co-evaporated with toluene (3 x 5 ml) *in vacuo* to ensure the complete removal of thionyl chloride. The acyl chloride product was used without further purification in the next step.

2.5 d) General procedure for the condensation of pyrrole 65 with acyl chlorides

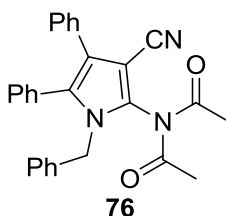
A solution of the appropriate acyl chloride (2.4 mmol) in toluene (2.0 ml) was added dropwise to a stirred mixture of pyrrole **65** (0.21 g, 0.60 mmol) and triethylamine, TEA (0.50 ml, 0.36 g, 3.6 mmol) in dry toluene (8 ml). The reaction mixture was refluxed overnight under Ar. The excess solvent was removed *in vacuo* and the residue obtained was dissolved in EtOAc (20 ml) and washed successively with 5% HCl (10 ml), saturated NaHCO_3 (10 ml) and brine (10 ml). The organic layer was dried over Na_2SO_4 and concentrated *in vacuo*. The crude product was purified by silica gel column chromatography.

2.5 e) General procedure for the partial deacylation of *N,N*-diacyl imides to *N*-acyl amides²³

Equimolar quantities of potassium carbonate (28 mg, 0.20 mmol) and the appropriate *N,N*-diacyl imide (0.20 mmol) was stirred at rt for 1 h in MeOH or AcMe/MeOH (1:1) (2.5 ml). The excess solvent was removed *in vacuo* and the residue obtained was dissolved in CHCl₃ (15 ml) and partitioned with water (15 ml). The aqueous layer was extracted with CHCl₃ (2 x 5 ml). The organic layers were combined, washed with brine (20 ml), dried over Na₂SO₄ and concentrated *in vacuo*. The crude product was purified by recrystallisation or silica gel column chromatography.

2.5 f) Experimental data of synthesised compounds

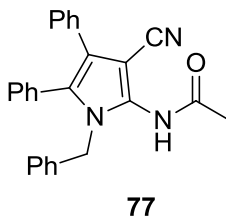
N-acetyl-*N*-(1-benzyl-3-cyano-4,5-diphenyl-1*H*-pyrrol-2-yl)acetamide (**76**)²¹



A mixture of pyrrole **65** (0.20 g, 0.58 mmol) and acetic anhydride (2.3 ml, 2.5 g, 24 mmol) was refluxed for 3 h under Ar. The reaction mixture was cooled and poured into a mixture of ice and water. A 25% solution of ammonia (10 ml) was added to the mixture until a red precipitate was formed. The precipitate was vacuum filtered and recrystallised from diethyl ether to afford the title compound as a brown solid (0.20 g, 79%), m.p.: 170.2-171.1 °C. *R*_f: 0.45 (30% EtOAc in PE). ¹H NMR (300 MHz, CDCl₃) δ (ppm): 2.15 (s, 6H, 2 x COCH₃), 4.85 (s, 2H, NCH₂Ph), 6.95-6.99 (m, 2H, Ar-H), 7.22-7.38 (m, 13H, Ar-H). ¹³C NMR (75 MHz, CDCl₃) δ (ppm): 25.6 (COCH₃), 48.6 (NCH₂Ph), 92.5 (C-CN), 114.4 (C≡N), 124.2 (Ar-C), 127.1 (Ar-CH), 127.5 (Ar-CH), 128.3 (Ar-CH), 128.4 (Ar-CH), 128.8 (Ar-CH), 128.95 (Ar-CH), 129.01 (Ar-CH), 129.1 (Ar-CH), 130.0 (Ar-C), 131.4 (Ar-CH), 131.8 (Ar-C), 133.6 (Ar-C), 135.2 (C-NH₂), 172.1 (C=O). ESI-MS: *m/z* 456.2 [M + Na]⁺. HRMS, found: *m/z* 456.1683, C₂₈H₂₃N₃NaO₂ requires 456.1682. IR ν_{max} (cm⁻¹): 3033.8, 2223.8 (C≡N stretch), 1743.3 (C=O stretch), 1705.0 (C=O

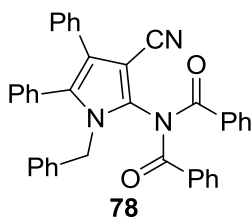
stretch), 1605.2, 1533.7, 1497.2, 1479.3, 1455.9, 1446.4, 1429.1, 1364.1, 1349.7, 1255.8, 1202.2, 1016.6.

N-(1-benzyl-3-cyano-4,5-diphenyl-1*H*-pyrrol-2-yl)acetamide (**77**)



Potassium carbonate (21 mg, 0.15 mmol) and imide **76** (65 mg, 0.15 mmol) were used. MeOH (6 ml) was used as the solvent. The crude product was recrystallised from diethyl ether to afford the title compound as a peach coloured solid (40 mg, 68%), m.p.: 130.2-132.6 °C. *R_f*: 0.14 (30% EtOAc in PE). ¹H NMR (400 MHz, CDCl₃) δ (ppm): 2.05 (s, 3H, COCH₃), 4.97 (s, 2H, NCH₂Ph), 6.84-6.86 (m, 2H, Ar-H), 7.14-7.27 (m, 13H, Ar-H), 7.67 (br s, 1H NH). ¹³C NMR (100 MHz, CDCl₃) δ (ppm): 29.7 (COCH₃), 48.5 (NCH₂Ph), 89.8 (C-CN), 115.7 (C≡N), 123.4 (Ar-C), 126.0 (Ar-CH), 126.8 (Ar-CH), 127.7 (Ar-CH), 128.3 (Ar-CH), 128.7 (Ar-CH), 128.9 (Ar-CH), 130.2 (Ar-C), 130.4 (Ar-C), 131.2 (Ar-CH), 132.4 (Ar-C), 132.7 (Ar-C), 136.8 (C-NH₂), 170.1 (C=O). ESI-MS: *m/z* 414.2 [M + Na]⁺. HRMS, found: *m/z* 414.1573, C₂₆H₂₁N₃NaO requires 414.1577. IR *v*_{max} (cm⁻¹): 3236.6 (N-H stretch), 3063.1, 3031.6, 2222.2 (C≡N stretch), 1675.2 (C=O stretch), 1583.2, 1564.1, 1541.8, 1497.3, 1452.7, 1423.7, 1366.9, 1355.2, 1332.4, 1296.3, 1260.5, 1075.4, 1020.1, 1003.7.

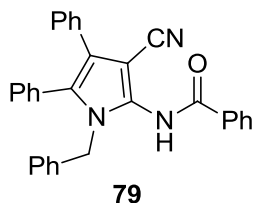
N-benzoyl-*N*-(1-benzyl-3-cyano-4,5-diphenyl-1*H*-pyrrol-2-yl)benzamide (**78**)



Benzoyl chloride (0.28 ml, 0.34 g, 2.4 mmol) was used as the acyl chloride. The crude product was purified by silica gel chromatography [EtOAc/PE (3:97) → EtOAc/PE (3:22)] to

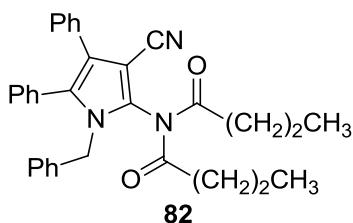
afford the title compound as a light brown solid (0.25 g, 76%), m.p.: 181.9-184.4 °C. R_f : 0.56 (30% EtOAc in PE). ^1H NMR (300 MHz, CDCl_3) δ (ppm): 5.05 (s, 2H, NCH_2Ph), 6.84-6.87 (m, 2H, Ar-H), 7.00-7.03 (m, 2H, Ar-H), 7.09-7.26 (m, 15H, Ar-H), 7.37 (tt, 2H, $J_1 = 7.5$ Hz, $J_2 = 1.5$ Hz, Ar-H), 7.58-7.61 (m, 4H, Ar-H). ^{13}C NMR (75 MHz, CDCl_3) δ (ppm): 48.5 (NCH_2Ph), 93.0 (C-CN), 115.2 ($\text{C}\equiv\text{N}$), 124.5, 126.4, 127.0, 127.5, 128.3, 128.5, 128.6, 128.7, 128.9, 129.1, 130.1, 131.0, 131.5, 132.0, 132.8, 133.6, 133.8, 134.0, 135.4 (C-NH_2), 172.10 (C=O). ESI-MS: m/z 580.2 [$\text{M} + \text{Na}$] $^+$. HRMS, found: m/z 580.1979, $\text{C}_{38}\text{H}_{27}\text{N}_3\text{NaO}_2$ requires 580.1995. IR ν_{max} (cm^{-1}): 3063.1, 3031.6, 2222.8 ($\text{C}\equiv\text{N}$ stretch), 1713.0 (C=O stretch), 1677.5 (C=O stretch), 1596.3, 1580.6, 1564.8, 1532.9, 1497.3, 1476.5, 1463.8, 1448.9, 1424.5, 1316.1, 1223.1, 1120.4, 1073.3, 1065.1, 1073.3.

N-(1-benzyl-3-cyano-4,5-diphenyl-1*H*-pyrrol-2-yl)benzamide (**79**)



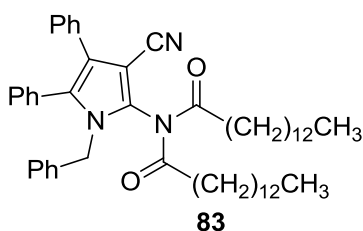
Potassium carbonate (28 mg, 0.20 mmol) and imide **78** (0.11 g, 0.20 mmol) were used. A 1:1 mixture of acetone/MeOH (12 ml) was used as the solvent. The title compound was obtained as a white solid by recrystallisation of the crude product from MeOH (48 mg, 53%), m.p.: 198.2-200.2 °C. R_f : 0.51 (30% EtOAc in PE). ^1H NMR (400 MHz, CDCl_3) δ (ppm): 5.05 (s, 2H, Ar- CH_2), 6.86-6.88 (m, 2H, Ar-H), 7.16-7.40 (m, 15H, Ar-H), 7.51 (tt, 1H, $J_1 = 7.5$ Hz, $J_2 = 1.4$ Hz, Ar-H), 7.61-7.64 (m, 2H, Ar-H), 7.81 (br s, 1H, NH). ^{13}C NMR (100 MHz, CDCl_3) δ (ppm): 48.7 (NCH_2Ph), 89.9 (C-CN), 115.8 ($\text{C}\equiv\text{N}$), 123.5, 126.1, 126.8, 127.5, 127.7, 128.3, 128.69, 128.74, 128.95, 128.96, 130.3, 130.6, 131.2, 132.4, 132.6, 132.77, 136.8 (C-NH_2), 166.9 (C=O). ESI-MS: m/z 452.1 [$\text{M} - \text{H}$] $^-$. HRMS, found: m/z 452.1762, $\text{C}_{31}\text{H}_{22}\text{N}_3\text{O}$ requires 452.1768. IR ν_{max} (cm^{-1}): 3249.2 (N-H stretch), 3063.1, 3031.6, 2221.9 ($\text{C}\equiv\text{N}$ stretch), 1678.0 (C=O stretch), 1581.0, 1555.6, 1532.7, 1498.1, 1479.2, 1448.5, 1422.9, 1353.4, 1314.4, 1275.4, 1222.9, 1180.3, 1120.1, 1073.9, 1022.1.

N-(1-benzyl-3-cyano-4,5-diphenyl-1*H*-pyrrol-2-yl)-*N*-butyrylbutyramide (**82**)



Butyryl chloride (0.25 ml, 0.26 g, 2.4 mmol) was used as the acyl chloride. The crude product was purified by silica gel chromatography [EtOAc/PE (1:49) → EtOAc/PE (1:19)] to afford the title compound as a light brown solid (0.25 g, 86%), m.p.: 114.6-115.2 °C. R_f : 0.73 (30% EtOAc in PE). ^1H NMR (400 MHz, CDCl_3) δ (ppm): 0.91 (t, 6H, $J = 7.4$ Hz, 2 x CH_3), 1.40-1.53 (m, 2H, CH_2CH_3), 1.56-1.69 (m, 2H, CH_2CH_3), 2.20-2.28 (m, 2H, COCH_2), 2.60-2.68 (m, 2H, COCH_2), 4.88 (s, 2H, NCH_2Ph), 6.98-7.01 (m, 2H, Ar-H), 7.22-7.28 (m, 8H, Ar-H), 7.34-7.42 (m, 5H, Ar-H). ^{13}C NMR (100 MHz, CDCl_3) δ (ppm): 13.5 (CH_3), 17.8 (CH_2CH_3), 39.5 (COCH_2), 48.4 (NCH_2Ph), 92.6 (C-CN), 114.6 ($\text{C}\equiv\text{N}$), 124.2 (Ar-C), 127.1 (Ar-CH), 127.5 (Ar-CH), 128.29 (Ar-CH), 128.32 (Ar-CH), 128.9 (Ar-CH), 129.0 (Ar-CH), 129.1 (Ar-CH), 130.2 (Ar-C), 131.4 (Ar-C), 131.5 (Ar-CH), 131.9 (Ar-C), 133.4 (Ar-C), 135.2 (C-NH_2), 175.1 (C=O). ESI-MS: m/z 512.2 [$\text{M} + \text{Na}$] $^+$. HRMS, found: m/z 512.2309, $\text{C}_{32}\text{H}_{31}\text{N}_3\text{NaO}_2$ requires 512.2308. IR ν_{max} (cm^{-1}): 3056.8, 3031.6, 2920.9 (sp^3 C-H stretch), 2850.5 (sp^3 C-H stretch), 2224.0 ($\text{C}\equiv\text{N}$ stretch), 1683.3 (C=O stretch), 1602.6, 1564.8, 1531.0, 1497.5, 1466.6, 1450.6, 1415.9, 1367.7, 1351.6, 1221.7, 1183.4, 1075.8, 1029.2, 709.7.

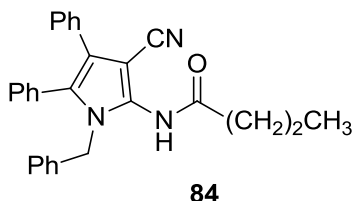
N-(1-benzyl-3-cyano-4,5-diphenyl-1*H*-pyrrol-2-yl)-*N*-tetradecanoyltetradecanamide (**83**)



Myristoyl chloride (0.61 g, 2.5 mmol) was used as the acyl chloride. The crude product was purified by silica gel chromatography [EtOAc/PE (1:49) → EtOAc/PE (1:19)] to afford the title compound as a golden oil (0.43 g, 93%). R_f : 0.90 (30% EtOAc in PE). ^1H NMR (400 MHz,

CDCl₃) δ (ppm): 0.86 (t, 6H, J = 6.0 Hz, 2 x CH₃), 1.24 (br s, 44H, CH₂CH₃ x 22), 2.16-2.24 (m, 2H, COCH₂), 2.56-2.64 (m, 2H, COCH₂), 4.83 (s, 2H, NCH₂Ph), 6.93-6.95 (m, 2H, Ar-H), 7.19-7.37 (m, 13H, Ar-H). ¹³C NMR (100 MHz, CDCl₃) δ (ppm): 14.1 (CH₃), 22.7 (CH₂), 25.4 (CH₂), 29.1 (CH₂), 29.28 (CH₂), 29.33 (CH₂), 29.4 (CH₂), 29.59 (CH₂), 29.63 (CH₂), 29.7 (CH₂), 31.9 (CH₂), 36.2 (COCH₂), 48.4 (NCH₂Ph), 89.6 (C-CN), 115.7 (C \equiv N), 123.4 (Ar-C), 125.9 (Ar-CH), 126.8 (Ar-CH), 127.6 (Ar-CH), 128.2 (Ar-CH), 128.6 (Ar-CH), 128.7 (Ar-CH), 128.86 (Ar-CH), 128.91(Ar-CH), 130.29 (Ar-C), 130.34(Ar-C), 131.1 (Ar-CH), 132.4 (Ar-C), 132.9 (Ar-C), 136.8 (C-NH₂), 173.2 (C=O). ESI-MS: m/z 792.5 [M + Na]⁺. HRMS, found: m/z 792.5449, C₅₂H₇₁N₃NaO₂ requires 792.5438. IR ν_{\max} (cm⁻¹): 3066.0, 3028.0, 2918.0 (sp³ C-H stretch), 2849.9 (sp³ C-H stretch), 2221.9 (C \equiv N stretch), 1677.6 (C=O stretch), 1603.0, 1562.7, 1497.6, 1465.3, 1453.7, 1422.5, 1354.0, 1301.0, 1275.3, 1223.8, 1180.5, 1074.4, 1022.4, 727.5.

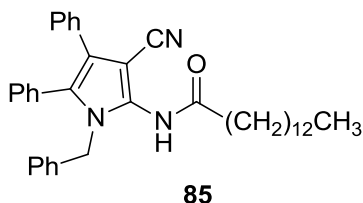
N-(1-benzyl-3-cyano-4,5-diphenyl-1*H*-pyrrol-2-yl)butyramide (**84**)



Potassium carbonate (28 mg, 0.20 mmol) and imide **82** (0.10 g, 0.20 mmol) were used. MeOH (12 ml) was used as the solvent. The crude product was purified by recrystallisation from MeOH to afford the title compound as a light yellow solid (80 mg, 95%), m.p.: 201.0-203.0 °C. R_f : 0.50 (30% EtOAc in PE). ¹H NMR (400 MHz, CDCl₃) δ (ppm): 0.94 (t, 3H, J = 7.4 Hz, CH₃), 1.63-1.68 (m, 2H, CH₂CH₃), 2.25 (t, 2H, J = 7.4 Hz, COCH₂), 4.98 (s, 2H, NCH₂Ph), 6.84-6.86 (m, 2H, Ar-H), 7.10-7.27 (m, 13H, Ar-H). ¹³C NMR (100 MHz, CDCl₃) δ (ppm): 13.6 (CH₃), 18.9 (CH₂CH₃), 38.0 (COCH₂), 48.4 (NCH₂Ph), 89.7 (C-CN), 115.7 (C \equiv N), 123.4 (Ar-C), 125.9 (Ar-CH), 126.8 (Ar-CH), 127.6 (Ar-CH), 128.2 (Ar-CH), 128.6 (Ar-CH), 128.7 (Ar-CH), 128.85 (Ar-CH), 128.91 (Ar-CH), 130.29 (Ar-C), 130.34 (Ar-C), 131.1 (Ar-CH), 132.4 (Ar-C), 132.9 (Ar-C), 136.8 (C-NH₂), 173.1 (C=O). ESI-MS: m/z 418.1 [M - H]⁻. HRMS, found: m/z 418.1923, C₂₈H₂₄N₃O requires 418.1925. IR ν_{\max} (cm⁻¹): 3236.6 (N-H stretch), 3053.7, 3034.7, 2920.8 (sp³ C-H stretch), 2850.5 (sp³ C-H stretch), 2224.1 (C \equiv N stretch),

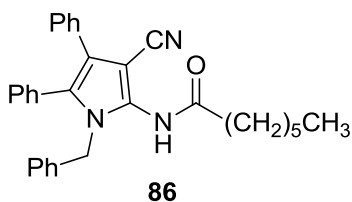
1683.1 (C=O stretch), 1605.8, 1561.6, 1530.6, 1497.5, 1466.7, 1450.3, 1415.4, 1367.9, 1351.6, 1221.1, 1076.0, 1029.2, 709.9.

N-(1-benzyl-3-cyano-4,5-diphenyl-1*H*-pyrrol-2-yl)tetradecanamide (**85**)



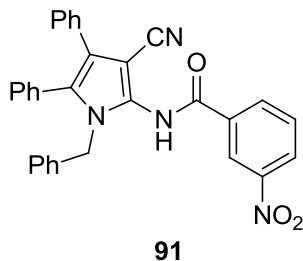
Potassium carbonate (37 mg, 0.27 mmol) and imide **83** (0.21 g, 0.27 mmol) were used. A 1:1 mixture of AcMe/MeOH (12 ml) was used as the solvent. Silica gel column chromatography [EtOAc/PE (1:49) → EtOAc/PE (7:93)] of the crude product afforded the title compound as a light yellow solid (0.13 g, 87%), m.p.: 125.4-126.6 °C. *R*_f: 0.80 (30% EtOAc in PE). ¹H NMR (400 MHz, CDCl₃) δ (ppm): 0.86 (t, 3H, *J* = 6.9 Hz, CH₃), 1.24 (s, 20H, 10 x CH₂CH₃), 1.56-1.59 (m, 2H, COCH₂CH₂), 2.26 (t, 2H, *J* = 7.5 Hz, COCH₂), 4.98 (s, 2H, NCH₂Ph), 6.84-6.86 (m, 2H, Ar-H), 6.97 (br s, 1H, NH), 7.14-7.28 (m, 13H, Ar-H). ¹³C NMR (100 MHz, CDCl₃) δ (ppm): 14.1 (CH₃), 22.7 (CH₂), 25.4 (CH₂), 29.1 (CH₂), 29.28(CH₂), 29.33 (CH₂), 29.4 (CH₂), 29.59 (CH₂), 29.63 (CH₂), 29.7 (CH₂), 31.9 (CH₂), 36.2 (COCH₂), 48.4 (NCH₂Ph), 89.7 (C-CN), 115.7 (C≡N), 123.4 (Ar-C), 125.9 (Ar-CH), 126.8 (Ar-CH), 127.6 (Ar-CH), 128.2 (Ar-CH), 128.6 (Ar-CH), 128.7 (Ar-CH), 128.86 (Ar-CH), 128.91 (Ar-CH), 130.29 (Ar-C), 130.34 (Ar-C), 131.1 (Ar-CH), 132.4 (Ar-C), 132.9 (Ar-C), 136.8 (C-NH₂), 173.2 (C=O). ESI-MS: *m/z* 582.4 [M + Na]⁺. HRMS, found: *m/z* 582.3460, C₃₈H₄₅N₃NaO requires 582.3455. IR ν_{max} (cm⁻¹): 3239.8 (N-H stretch), 3053.7, 3034.7, 2920.5 (sp³ C-H stretch), 2850.4 (sp³ C-H stretch), 2224.2 (C≡N stretch), 1683.4 (C=O stretch), 1602.6, 1561.8, 1529.7, 1497.4, 1467.0, 1450.3, 1415.9, 1367.9, 1351.7, 1221.5, 1076.1, 1029.3, 709.9.

N-(1-Benzyl-3-cyano-4,5-diphenyl-1*H*-pyrrol-2-yl)heptanamide (**86**)



Heptanoyl chloride (61 mg, 0.41 mmol) was used as the acyl chloride. The title compound was obtained as a white solid from silica gel column chromatography [EtOAc/PE (1:49) → EtOAc/PE (1:6)] of the crude product (0.04 g, 20%) m.p.: 155.8-158.8 °C. *R*_f: 0.64 (30% EtOAc in PE). ¹H NMR (400 MHz, CDCl₃) δ (ppm): 0.86 (t, 3H, *J* = 6.8 Hz, CH₃), 1.24-1.32 (m, 6H, CH₂CH₃ x 3), 1.58-1.62 (m, 2H, COCH₂CH₂), 2.26 (t, 2H, *J* = 7.6 Hz, COCH₂), 4.98 (br s, 2H, NCH₂Ph), 6.84-6.86 (m, 2H, Ar-H), 7.00 (br s, 1H, NHCO), 7.14-7.30 (m, 13H, Ar-H). ¹³C NMR (100 MHz, CDCl₃) δ (ppm): 14.0 (CH₃), 22.4 (CH₂), 25.3 (CH₂), 28.8 (CH₂), 31.4 (CH₂), 36.2 (CH₂), 48.4 (NCH₂Ph), 89.9 (C-CN), 115.5 (C≡N), 123.4 (C-Ar), 125.8 (CH-Ar), 126.8 (CH-Ar), 127.7 (CH-Ar), 128.3 (CH-Ar), 128.67 (CH-Ar), 128.71 (CH-Ar), 128.9 (CH-Ar), 130.3 (C-Ar), 130.4 (C-Ar), 131.1 (CH-Ar), 132.4 (C-Ar), 132.6 (C-Ar), 136.9 (C-NH₂), 173.0 (C=O). ESI-MS: *m/z* 460.3 [M - H]⁻. HRMS, found: *m/z* 484.2353, C₃₁H₃₁N₃NaO requires 484.2359. IR *v*_{max} (cm⁻¹): 3239.8 (N-H stretch), 3056.8, 3034.7, 2920.9 (sp³ C-H stretch), 2850.6 (sp³ C-H stretch), 2224.2 (C≡N stretch), 1683.1 (C=O stretch), 1602.6, 1561.8, 1530.5, 1497.6, 1466.9, 1450.3, 1415.9, 1368.1, 1351.8, 1221.6, 1076.1, 1029.4, 711.0.

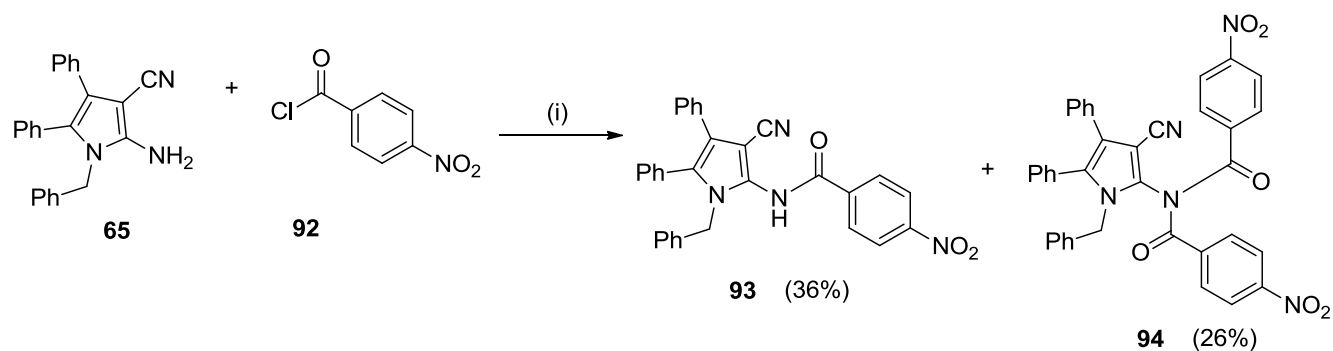
N-(1-Benzyl-3-cyano-4,5-diphenyl-1*H*-pyrrol-2-yl)-3-nitrobenzamide (**91**)



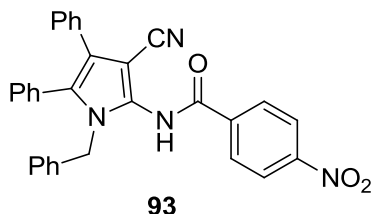
The acyl chloride used was 3-nitrobenzoyl chloride (0.45 g, 2.4 mmol). The title compound was obtained as a white solid from silica gel column chromatography [EtOAc/PE (1:24) → EtOAc/PE (1:6)] of the crude product (0.14 g, 46%), m.p.: 219.0-220.0 °C. *R*_f: 0.51 (30%

EtOAc in PE). ^1H NMR (400 MHz, CDCl_3) δ (ppm): 5.08 (s, 2H, NCH_2Ph), 6.91-6.93 (m, 2H, Ar-H), 7.25-7.36 (m, 13H, Ar-H), 7.56 (t, 1H, $J = 7.8$ Hz, Ar-H), 7.99 (d, 1H, $J = 7.2$ Hz, Ar-H), 8.34-8.36 (m, 2H, Ar-H), 8.41 (br s, 1H, NHCO). ^{13}C NMR (100 MHz, CDCl_3) δ (ppm): 48.9 (NCH_2Ph), 89.9 (C-CN), 115.8 ($\text{C}\equiv\text{N}$), 122.7, 123.6, 126.0, 126.9, 127.0, 127.94, 128.3, 128.8, 128.9, 129.0, 129.1, 129.9, 130.0, 131.0, 131.2, 132.2, 132.3, 133.6, 134.1, 136.4, 148.1 (C-NH_2), 164.6 (C=O). ESI-MS: m/z 521.2 $[\text{M} + \text{Na}]^+$. HRMS, found: m/z 521.1570, $\text{C}_{31}\text{H}_{22}\text{N}_4\text{NaO}_3$ requires 521.1584. IR ν_{max} (cm^{-1}): 3243.0 (N-H stretch), 3053.7, 3031.6, 2225.4 ($\text{C}\equiv\text{N}$ stretch), 1684.3 (C=O stretch), 1602.6, 1531.3, 1505.4, 1498.1 (N-O asymmetric stretch), 1467.2, 1449.3, 1426.6, 1343.8 (N-O symmetric stretch), 1298.3, 1258.8, 1223.4, 1075.5.

Synthesis of amide **93** and imide **94**



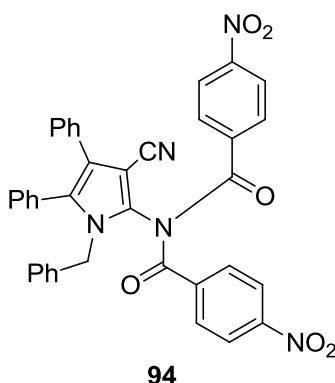
N-(1-Benzyl-3-cyano-4,5-diphenyl-1*H*-pyrrol-2-yl)-4-nitrobenzamide (**93**)



The acyl chloride used was 4-nitrobenzoyl chloride (0.46 g, 2.4 mmol). The title compound was obtained as a light yellow solid from silica gel column chromatography [EtOAc/PE (1:49) \rightarrow EtOAc/PE (1:12)] of the crude product (0.11 g, 36%), m.p.: 214.3-215.4 $^\circ\text{C}$. R_f : 0.51 (30%

EtOAc in PE). ^1H NMR (400 MHz, CDCl_3) δ (ppm): 5.02 (br s, 2H, NCH_2Ph), 6.85-6.87 (m, 2H, Ar-H), 7.17-7.33 (m, 13H, Ar-H), 7.70 (d, 2H, $J = 8.7$ Hz, Ar-H), 8.12 (d, 2H, $J = 8.8$ Hz, Ar-H), 8.46 (br s, 1H, NHCO). ^{13}C NMR (100 MHz, CDCl_3) δ (ppm): 49.0 (NCH_2Ph), 89.6 (C-CN), 116.1 ($\text{C}\equiv\text{N}$), 123.68, 123.72, 126.0, 127.1, 127.9, 128.3, 128.8, 128.90, 128.9, 129.1, 130.0, 131.1, 131.2, 132.2, 132.3, 136.4, 137.8, 150.0 (C-NH_2), 165.0 (C=O). ESI-MS: m/z 497.2 [$\text{M} - \text{H}$]. HRMS, found: m/z 521.1589, $\text{C}_{31}\text{H}_{22}\text{N}_4\text{NaO}_3$ requires 521.1584. IR ν_{max} (cm^{-1}): 3293.4 (N-H stretch), 3113.6, 3060.0, 3034.7, 2224.7 ($\text{C}\equiv\text{N}$ stretch), 1699.6 (C=O stretch), 1605.8, 1574.2, 1518.5 (N-O asymmetric stretch), 1495.6, 1463.9, 1455.9, 1410.2, 1342.1 (N-O symmetric stretch), 1272.3, 1256.0, 1206.3, 1076.1, 1009.3.

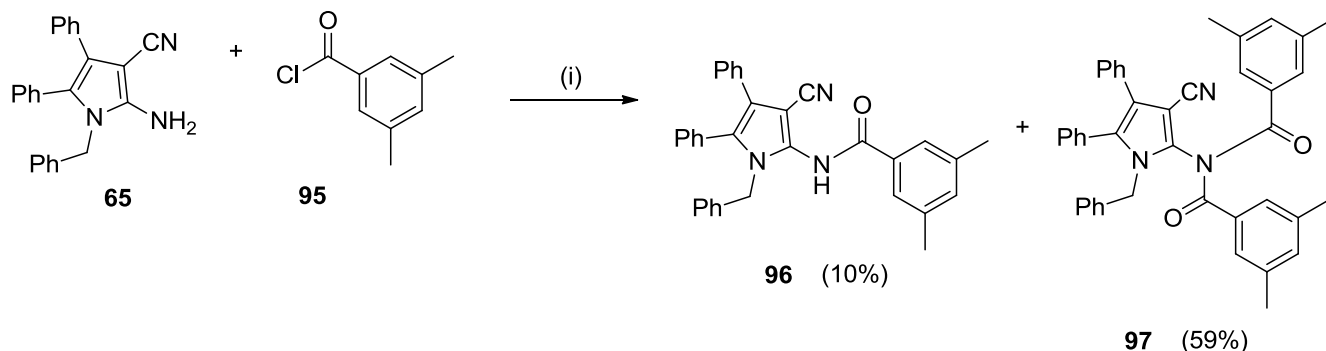
N-(1-Benzyl-3-cyano-4,5-diphenyl-1*H*-pyrrol-2-yl)-4-nitro-*N*-(4-nitrobenzoyl)benzamide (**94**)



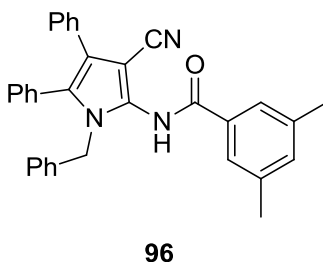
The title compound was obtained as an orange solid from silica gel column chromatography [EtOAc/PE (1:49) \rightarrow EtOAc/PE (1:24)] of the crude product (0.12 g, 26%), m.p.: 243.5-245.4 $^\circ\text{C}$. R_f : 0.75 (30% EtOAc in PE). ^1H NMR (400 MHz, CDCl_3) δ (ppm): 5.43 (br s, 2H, NCH_2Ph), 6.94-6.96 (m, 2H, Ar-H), 7.10-7.13 (m, 2H, Ar-H), 7.23-7.36 (m, 11H, Ar-H), 8.08 (d, 2H, $J = 9.0$ Hz, Ar-H), 8.15 (d, 2H, $J = 9.0$ Hz, Ar-H), 8.33 (d, 2H, $J = 9.1$ Hz, Ar-H), 8.49 (d, 2H, $J = 9.0$ Hz, Ar-H). ESI-MS: m/z 648.3 [$\text{M} + \text{H}$] $^+$. ^{13}C NMR (100 MHz, CDCl_3) δ (ppm): 46.9 (NCH_2Ph), 102.0 (C-CN), 120.7 ($\text{C}\equiv\text{N}$), 123.2 (CH-Ar), 124.1 (CH-Ar), 127.0 (CH-Ar), 127.5 (CH-Ar), 127.9 (CH-Ar), 128.6 (CH-Ar), 128.8 (CH-Ar), 129.0 (CH-Ar), 129.1 (CH-Ar), 129.4 (C-Ar), 130.8 (CH-Ar), 131.0 (CH-Ar), 131.2 (CH-Ar), 132.1 (C-Ar), 135.5 (C-Ar), 136.5 (C-Ar), 136.9 (C-Ar), 141.8 (C-Ar), 144.7 (C-Ar), 149.9 (C-Ar), 152.0 (C-Ar), 155.1 (C-NH_2), 172.3 (C=O). ESI-MS: m/z 648.3 [$\text{M} + \text{H}$] $^+$. HRMS, found: m/z 648.1883, $\text{C}_{38}\text{H}_{26}\text{N}_5\text{O}_6$ requires 648.1878. IR ν_{max} (cm^{-1}): 3113.6, 3060.0, 3034.7, 2224.9 ($\text{C}\equiv\text{N}$ stretch), 1699.7 (C=O stretch),

1605.8, 1518.6 (N-O asymmetric stretch), 1496.1, 1445.9, 1342.0 (N-O symmetric stretch), 1272.3, 1255.7, 1206.7, 1076.4, 1009.7.

Synthesis of amide **96** and imide **97**



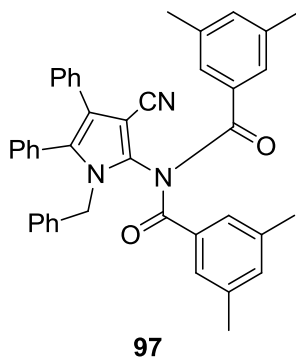
N-(1-Benzyl-3-cyano-4,5-diphenyl-1*H*-pyrrol-2-yl)-3,5-dimethylbenzamide (**96**)



The acyl chloride used was 3,5-dimethylbenzoyl chloride (0.47 g, 2.8 mmol). The title compound was obtained as a white solid from silica gel column chromatography [EtOAc/PE (1:49) → EtOAc/PE (1:16)] of the crude product (0.03 g, 10%), m.p.: 79.9-82.5 °C. *R_f*: 0.60 (30% EtOAc in PE). ¹H NMR (300 MHz, CDCl₃) δ (ppm): 2.30 (s, 6H, 2 x CH₃), 5.04 (br s, 2H, NCH₂Ph), 6.88-6.92 (m, 2H, Ar-H), 7.15-7.31 (m, 16H, Ar-H), 7.48 (s, 1H, NHCO). ¹³C NMR (100 MHz, CDCl₃) δ (ppm): 19.3 (CH₃), 47.5 (NCH₂Ph), 90.0 (C-CN), 115.6 (C≡N), 123.5, 125.1, 125.3, 125.9, 126.2, 127.7, 128.6, 128.8, 129.0, 129.2, 130.5, 131.2, 132.4, 132.5, 132.7, 134.2, 136.9, 138.5 (C-NH₂), 167.1 (C=O). ESI-MS: *m/z* 480.2 [M - H]⁻. HRMS, found: *m/z* 504.2044, C₃₃H₂₇N₃NaO requires 504.2046. IR *v*_{max} (cm⁻¹): 3523.7 (N-H stretch), 3391.2,

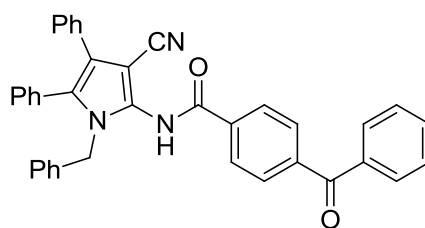
3280.9, 3189.3, 2971.7, 2918.0, 2848.6, 2760.3, 2722.5, 2485.9, 2227.2 (C≡N stretch), 1682.0 (C=O stretch), 1605.4, 1586.9, 1497.1, 1447.4, 1396.9, 1345.5, 1324.7, 1260.6, 1153.4, 1100.3, 1079.1, 1045.5, 1012.4.

N-(1-Benzyl-3-cyano-4,5-diphenyl-1*H*-pyrrol-2-yl)-*N*-(3,5-dimethylbenzoyl)-3,5-dimethylbenzamide (**97**)



The title compound was obtained as an off white solid from silica gel column chromatography [EtOAc/PE (1:49) → EtOAc/PE (1:25)] of the crude product (0.22 g, 59%), m.p.: 188.4-190.2 °C. R_f : 0.71 (30% EtOAc in PE). ^1H NMR (400 MHz, CDCl_3) δ (ppm): 2.19 (s, 12H, 4 x CH_3), 5.04 (br s, 2H, NCH_2Ph), 6.86-6.89 (m, 2H, Ar-H), 6.95 (br s, 2H, Ar-H), 7.05-7.07 (m, 2H, Ar-H) 7.11-7.25 (m, 15H, Ar-H). ^{13}C NMR (100 MHz, CDCl_3) δ (ppm): 21.0 (CH_3), 48.4 (NCH_2Ph), 93.0 (C-CN), 115.2 ($\text{C}\equiv\text{N}$), 124.5, 126.4, 126.8, 126.9, 127.4, 128.3, 128.4, 128.57, 128.65, 129.0, 130.3, 131.0, 131.3, 132.2, 134.0, 134.1, 134.2, 135.7, 138.0 (C-NH_2), 172.5 (C=O). ESI-MS: m/z 636.2 [$\text{M} + \text{Na}$] $^+$. HRMS, found: m/z 636.2637, $\text{C}_{42}\text{H}_{35}\text{N}_3\text{NaO}_2$ requires 636.2621. IR ν_{max} (cm^{-1}): 3284.4, 3116.6, 3078.6, 3062.8, 3040.6, 3012.0, 2971.0, 2945.6, 2917.1, 2866.4, 2227.2 (C≡N stretch), 1678.0 (C=O stretch), 1606.2, 1533.4, 1495.4, 1476.4, 1453.8, 1333.5, 1297.0, 1251.8, 1180.1, 1168.0, 1129.7, 1077.6, 1027.7.

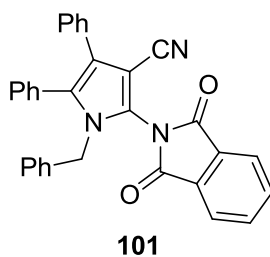
4-Benzoyl-*N*-(1-benzyl-3-cyano-4,5-diphenyl-1*H*-pyrrol-2-yl)benzamide (**99**)



99

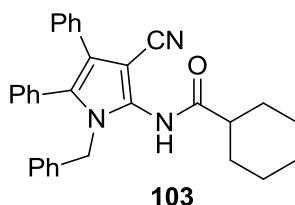
The acyl chloride used was 4-benzoylbenzoyl chloride (0.72 g, 3.0 mmol). The title compound was obtained as a light yellow solid from silica gel column chromatography [EtOAc/PE (1:24) → EtOAc/PE (1:6)] of the crude product and recrystallisation from dichloromethane (0.16 g, 47%), m.p.: 240.3-242.3 °C. R_f : 0.47 (30% EtOAc in PE). ^1H NMR (400 MHz, CDCl_3) δ (ppm): 5.06 (br s, 2H, NCH_2Ph), 6.88-6.91 (m, 2H, Ar-H), 7.15-7.32 (m, 13H, Ar-H), 7.48 (tt, 2H, $J_1 = 7.6$ Hz, $J_2 = 1.5$ Hz, Ar-H), 7.61 (tt, 1H, $J_1 = 7.4$ Hz, $J_2 = 1.5$ Hz, Ar-H), 7.70-7.77 (m, 6H, Ar-H), 8.01 (br s, 1H, NHCO). ^{13}C NMR (100 MHz, CDCl_3) δ (ppm): 48.8 (NCH_2Ph), 90.1 (C-CN), 115.7 ($\text{C}\equiv\text{N}$), 123.6 (C-Ar), 126.1 (CH-Ar), 126.9 (CH-Ar), 127.6 (CH-Ar), 127.8 (CH-Ar), 128.3 (CH-Ar), 128.5 (CH-Ar), 128.8 (CH-Ar), 128.95 (CH-Ar), 129.04 (CH-Ar), 130.1 (CH-Ar), 130.8 (C-Ar), 131.2 (CH-Ar), 132.3 (C-Ar), 132.4 (C-Ar), 133.0 (CH-Ar), 135.6 (C-Ar), 136.7 (C-Ar), 136.8 (C-Ar), 141.0 (C-NH_2), 166.1 (C=O), 195.8 (C=O). ESI-MS: m/z 556.2 [$\text{M} - \text{H}$] $^-$. HRMS, found: m/z 580.1981, $\text{C}_{38}\text{H}_{27}\text{N}_3\text{NaO}_2$ requires 580.1995. IR ν_{max} (cm^{-1}): 3284.4 (N-H stretch), 3176.7, 3113.4, 3094.4, 3075.4, 3062.8, 3040.6, 3012.0, 2230.0 ($\text{C}\equiv\text{N}$ stretch), 1655.2 (C=O stretch), 1596.7, 1565.0, 1529.5, 1497.5, 1455.4, 1445.5, 1429.7, 1319.2, 1276.5, 1182.0, 1153.4, 1077.2, 1015.9.

1-Benzyl-2-(1,3-dioxoisindolin-2-yl)-4,5-diphenyl-1H-pyrrole-3-carbonitrile (**101**)³⁴



A mixture of phthalic anhydride (0.18 g, 1.2 mmol) and pyrrole **65** (0.21 g, 0.60 mmol) in dry toluene (10 ml) was refluxed overnight under Ar. The reaction mixture was then cooled and the excess solvent was removed by evaporation *in vacuo*. This gave a dark brown solid which was recrystallised from diethyl ether to afford the title compound as a light brown solid (0.12 g, 43%), m.p.: 207.6-209.7 °C. R_f : 0.48 (30% EtOAc in PE). ^1H NMR (300 MHz, CDCl_3) δ (ppm): 4.96 (br s, 2H, NCH_2Ph), 6.82-6.85 (m, 2H, Ar-H), 7.05-7.07 (m, 3H, Ar-H), 7.18-7.32 (m, 10H, Ar-H), 7.77 (dd, 2H, $J_1 = 3.0$ Hz, $J_2 = 5.7$ Hz, Ar-H), 7.86 (dd, 2H, $J_1 = 3.0$ Hz, $J_2 = 5.6$ Hz, Ar-H). ^{13}C NMR (75 MHz, CDCl_3) δ (ppm): 49.1 (NCH_2Ph), 93.6 (C-CN), 114.5 ($\text{C}\equiv\text{N}$), 124.3 (Ar-CH), 124.6 (Ar-C), 126.2 (Ar-C), 126.3 (Ar-CH), 127.0 (Ar-CH), 127.8 (Ar-CH), 128.3 (Ar-CH), 128.7 (Ar-CH), 128.8 (Ar-CH), 128.9 (Ar-CH), 129.0 (Ar-CH), 130.0 (Ar-C), 131.2 (Ar-CH), 131.3 (Ar-C), 132.0 (Ar-C), 132.2 (Ar-C), 134.9 (Ar-CH), 135.4 (C-NH_2), 165.6 (C=O). ESI-MS: m/z 480.2 [$\text{M} + \text{H}$] $^+$. HRMS, found: m/z 502.1527, $\text{C}_{32}\text{H}_{21}\text{N}_3\text{NaO}_2$ requires 502.1526. IR ν_{max} (cm^{-1}): 3113.6, 3060.0, 2226.3 ($\text{C}\equiv\text{N}$ stretch), 1750.0 (C=O stretch), 1732.6 (C=O stretch), 1605.8, 1533.2, 1505.0, 1480.7, 1457.3, 1345.1, 1325.0, 1260.3, 1077.8, 1017.0.

N-(1-Benzyl-3-cyano-4,5-diphenyl-1H-pyrrol-2-yl)cyclohexanecarboxamide (**103**)



The title compound was obtained as light pink solid from silica gel column chromatography [EtOAc/PE (1:49) → EtOAc/PE (1:12)] of the crude product (0.07 g, 66 %), m.p.: 227.5-229.5 °C. *R_f*: 0.63 (30% EtOAc in PE). ¹H NMR (400 MHz, CDCl₃) δ (ppm): 1.19-1.83 (m, 10H, 5 x CH₂), 2.16-2.23 (m, 1H, CHCO), 4.97 (br s, 2H, NCH₂Ph), 6.83-6.85 (m, 2H, Ar-H), 7.06 (br s, 1H, CONH), 7.13-7.30 (m, 13H, Ar-H). ¹³C NMR (100 MHz, CDCl₃) δ (ppm): 25.4 (CH₂), 25.5 (CH₂), 29.4 (CH₂), 45.0 (COCH), 48.4 (NCH₂Ph), 89.7 (C-CN), 115.6 (C≡N), 123.3 (C-Ar), 125.8 (CH-Ar), 126.8 (CH-Ar), 127.6 (CH-Ar), 128.3 (CH-Ar), 128.6 (CH-Ar), 128.7 (CH-Ar), 128.86 (CH-Ar), 128.91 (CH-Ar), 130.3 (C-Ar), 130.4 (C-Ar), 131.1 (CH-Ar), 132.4 (C-Ar), 132.9 (C-Ar), 136.9 (C-NH₂), 176.0 (C=O). ESI-MS: *m/z* 482.2 [M + Na]⁺. HRMS, found: *m/z* 482.2209, C₃₁H₂₉N₃NaO requires 482.2203. IR *v*_{max} (cm⁻¹): 3274.5 (N-H stretch), 2931.5 (sp³ C-H stretch), 2855.0 (sp³ C-H stretch), 2227.7 (C≡N stretch), 1673.3 (C=O stretch), 1602.6, 1583.7, 1567.5, 1535.3, 1496.4, 1446.9, 1350.2, 1300.8, 1249.8, 1229.8, 1173.9, 1132.6, 1105.9, 1078.5, 1029.4, 723.0.

2.5 g) Expression and purification of IMP-1

Refer to Appendix 1.

2.5 h) Preparation of CENTA (73)

Refer to Appendix 2.

2.5 i) IMP-1 screening assay of the derivatives^{4,15,19,35}

The screening assays were performed in triplicates, with CENTA as the substrate and HEPES X (50 mM HEPES, 0.1 M NaCl, 100 μM ZnCl₂, pH 7.0) as the buffer at 25 °C. The final concentration of IMP-1 and CENTA was 5 nM and 70 μM, respectively. Bovine serum albumin (final concentration of 20 μg ml⁻¹) was added to the enzyme solution for enzyme stability. The imide and amide derivatives of pyrrole **65** were assayed at a final concentration of 10 μM. The rate of CENTA hydrolysis was monitored at 405 nm ($\epsilon = 6400 \text{ M}^{-1} \text{ cm}^{-1}$)

(Scheme 2.4). The percentage inhibition of a compound was calculated based on the residual activity of the enzyme in the presence of the inhibitor (Equation 2.1).

Percentage inhibition

$$= \frac{(\text{Enzyme activity without inhibitor}) - (\text{Enzyme activity with inhibitor})}{\text{Enzyme activity without inhibitor}} \times 100\%$$

Equation 2.1: The percentage inhibition of a compound.

2.5 j) IMP-1 K_i assay of the inhibitors^{4,15,19,35}

The K_i assay conditions are the same as the screening assay conditions, except that various inhibitor concentrations were assayed against different substrate concentrations. The final inhibitor concentrations assayed were: 5, 10 and 25 μM , while the final substrate concentrations used were: 5, 10, 20, 30, 40, 50, 60 and 70 μM . The raw kinetic data were analysed by non-linear regression method, based on Equation 2.1, with the aid of WinCurveFit program (Kevin Raner Software). The substrate hydrolysis rate, v is the dependent variable, whereas the substrate concentration, $[S]$ and inhibitor concentration, $[I]$ are the independent variables. K_{ic} and K_{iuc} is the competitive and uncompetitive inhibition constant, respectively. V_{\max} is the limiting rate and K_m is the Michaelis constant.

$$v = \frac{V_{\max}[S]}{[S] \left(1 + \frac{[I]}{K_{iuc}}\right) + K_m \left(1 + \frac{[I]}{K_{ic}}\right)}$$

Equation 2.2: The relationship between substrate hydrolysis rate, v and substrate concentration, $[S]$ and inhibitor concentration, $[I]$.

According to the Equation 2.2, it is assumed that the inhibitor is either competitive, uncompetitive or a mixed-mode inhibitor. A selection of experimental K_i plots for inhibitors **78** and **96** are shown in Figures 2.16 and 2.17, respectively.

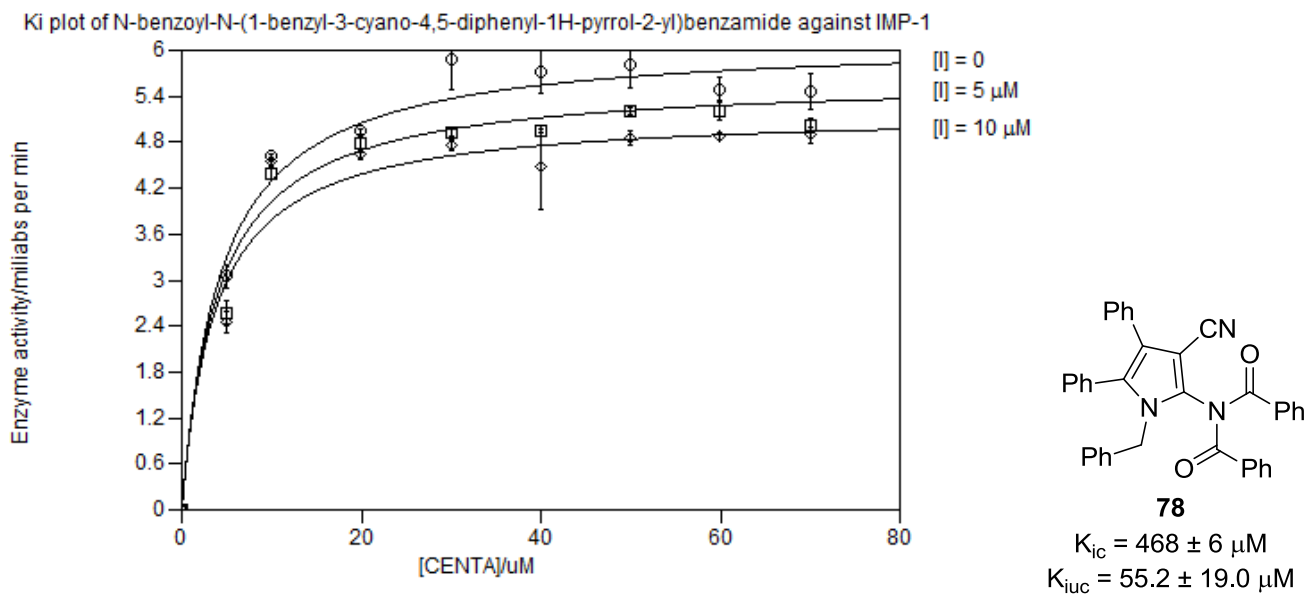


Figure 2.16: The K_i plot of inhibitor **78** against IMP-1 ($r^2 = 0.97$).

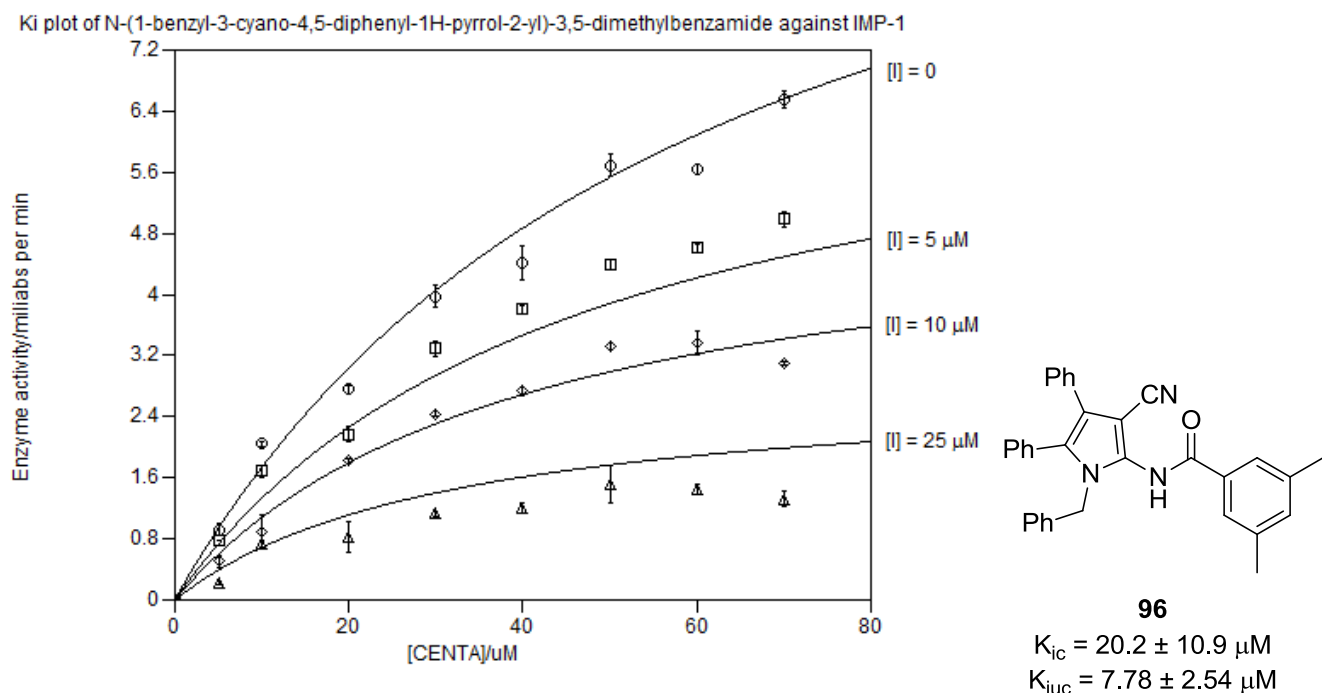


Figure 2.17: The K_i plot of inhibitor **96** against IMP-1 ($r^2 = 0.97$).

2.5 k) Imide stability test

A mixture of the imide (1 mM, 10 μ l) in DMSO and IMP-1 (10 nM, 490 μ l) in HEPES X buffer were kept at 25 °C for 30 mins and then at 4 °C overnight. The mixture was then extracted with EtOAc (2 x 500 μ l). The organic layers were combined and evaporated under a steady stream of nitrogen. The dried samples were diluted in LCMS grade MeOH (1 ml) and analysed by low resolution ESI-MS.

2.5 l) Computational modelling

Refer to Appendix 3.

References

- (1) Bellina, F.; Rossi, R. *Tetrahedron* **2006**, *62*, 7213.
- (2) Chong, P. H.; Seeger, J. D. *Pharmacotherapy: The Journal of Human Pharmacology and Drug Therapy* **1997**, *17*, 1157.
- (3) Fast, W.; Sutton, L. D. *Biochimica et Biophysica Acta (BBA) - Proteins and Proteomics* **2013**, *1834*, 1648.
- (4) Hussein, W. M.; Fatahala, S. S.; Mohamed, Z. M.; McGeary, R. P.; Schenk, G.; Ollis, D. L.; Mohamed, M. S. *Chemical Biology and Drug Design* **2012**, *80*, 500.
- (5) Olsen, L.; Pettersson, I.; Hemmingsen, L.; Adolph, H.-W.; Jørgensen, F. *Journal of Computational Aided Molecular Design* **2004**, *18*, 287.
- (6) Toney, J. H.; Hammond, G. G.; Fitzgerald, P. M. D.; Sharma, N.; Balkovec, J. M.; Rouen, G. P.; Olson, S. H.; Hammond, M. L.; Greenlee, M. L.; Gao, Y.-D. *Journal of Biological Chemistry* **2001**, *276*, 31913.
- (7) Hiraiwa, Y.; Saito, J.; Watanabe, T.; Yamada, M.; Morinaka, A.; Fukushima, T.; Kudo, T. *Bioorganic and Medicinal Chemistry Letters* **2014**, *24*, 4891.
- (8) Thomsen, R.; Christensen, M. H. *Journal of Medicinal Chemistry* **2006**, *49*, 3315.

- (9) Friesner, R. A.; Murphy, R. B.; Repasky, M. P.; Frye, L. L.; Greenwood, J. R.; Halgren, T. A.; Sanschagrin, P. C.; Mainz, D. T. *Journal of Medicinal Chemistry* **2006**, *49*, 6177.
- (10) Concha, N. O.; Rasmussen, B. A.; Bush, K.; Herzberg, O. *Structure* **1996**, *4*, 823.
- (11) Spencer, J.; Read, J.; Sessions, R. B.; Howell, S.; Blackburn, G. M.; Gamblin, S. J. *Journal of the American Chemical Society* **2005**, *127*, 14439.
- (12) Faridoo; Hussein, W. M.; Vella, P.; Islam, N. U.; Ollis, D. L.; Schenk, G.; McGeary, R. P. *Bioorganic and Medicinal Chemistry Letters* **2012**, *22*, 380.
- (13) Vorob'ev E.V.; Kurbatov E.S.; Krasnikov V.V.; Mezheritskii, V. V.; Usova, E. V. *Russian Chemical Bulletin, International Edition* **2006**, *55*, 1492.
- (14) Coumar, M. S.; Tsai, M.-T.; Chu, C.-Y.; Uang, B.-J.; Lin, W.-H.; Chang, C.-Y.; Chang, T.-Y.; Leou, J.-S.; Teng, C.-H.; Wu, J.-S.; Fang, M.-Y.; Chen, C.-H.; Hsu, J. T. A.; Wu, S.-Y.; Chao, Y.-S.; Hsieh, H.-P. *ChemMedChem* **2010**, *5*, 255.
- (15) Mohamed, M. S.; Hussein, W. M.; McGeary, R. P.; Vella, P.; Schenk, G.; Abd El-hameed, R. H. *European Journal of Medicinal Chemistry* **2011**, *46*, 6075.
- (16) Mollard, C.; Moali, C.; Papamicael, C.; Damblon, C.; Vessilier, S.; Amicosante, G.; Schofield, C. J.; Galleni, M.; Frère, J.-M.; Roberts, G. C. K. *Journal of Biological Chemistry* **2001**, *276*, 45015.
- (17) Bebrone, C.; Moali, C.; Mahy, F.; Rival, S.; Docquier, J. D.; Rossolini, G. M.; Fastrez, J.; Pratt, R. F.; Frère, J. M.; Galleni, M. *Antimicrobial agents and chemotherapy* **2001**, *45*, 1868.
- (18) van Berkel, S. S.; Brem, J.; Rydzik, A. M.; Salimraj, R.; Cain, R.; Verma, A.; Owens, R. J.; Fishwick, C. W. G.; Spencer, J.; Schofield, C. J. *Journal of Medicinal Chemistry* **2013**, *56*, 6945.
- (19) Vella, P.; Hussein, W. M.; Leung, E. W. W.; Clayton, D.; Ollis, D. L.; Mitić, N.; Schenk, G.; McGeary, R. P. *Bioorganic and Medicinal Chemistry Letters* **2011**, *21*, 3282.
- (20) Wie, C. T.; Sunder, S.; DeWitt Blanton Jr, C. *Tetrahedron Letters* **1968**, *9*, 4605.
- (21) Fathallah, S. S., Helwan University, 2007.
- (22) Bayomi, S. M.; Al-Khamees, H. A.; Ismail, A.-K. M.; Eissa, H. M.; El-Kerdawy, M. *Journal of the Chinese Chemical Society* **1989**, *36*, 159.
- (23) Zhou Yuanxi; Bourque Elyse; Zhu Yongbao; Langille Jonathan; Metz Markus; Yang Wen; McEachern Ernest J.; Harwig Curtis; Baird Ian R.; Li Tong-shuang; T., S. R.; Organization, W. I. P., Ed. USA, 2006, p 200.

- (24) Müller, C. E.; Geis, U.; Grahner, B.; Lanzner, W.; Eger, K. *Journal of Medicinal Chemistry* **1996**, 39, 2482.
- (25) Clayden, J.; Greeves, N.; Warren, S. *Organic Chemistry*, second ed.; Oxford University Press: Oxford, 2012.
- (26) Hilmy, K. M. H.; Pedersen, E. B. *Liebigs Annalen der Chemie* **1989**, 1989, 1145.
- (27) Abdelhamid, A. O.; Negm, A. M.; Abbas, I. M. *Journal für Praktische Chemie* **1989**, 331, 31.
- (28) Dudley Williams; Fleming, I. *Spectroscopic Methods in Organic Chemistry*, sixth ed.; McGraw-Hill Education: Berkshire, UK, 2008.
- (29) Brenton, A. G.; Godfrey, A. R. *Journal of the American Society for Mass Spectrometry* **2010**, 21, 1821.
- (30) Segel, I. H. *Enzyme kinetics: Behavior and Analysis of Rapid Equilibrium and Steady State Enzyme Systems*; John Wiley and Sons, 1993.
- (31) Thale, P. B.; Borase, P. N.; Shankarling, G. S. *RSC Advances* **2014**, 4, 59454.
- (32) Roth, H. J.; Eger, K. *Archiv der Pharmazie* **1975**, 308, 179.
- (33) Hussein, W. M.; Ross, B. P.; Landsberg, M. J.; Lévy, D.; Hankamer, B.; McGeary, R. P. *The Journal of Organic Chemistry* **2009**, 74, 1473.
- (34) Vora, M. M.; Yi, C. S.; Blanton, C. D. *Journal of Heterocyclic Chemistry* **1981**, 18, 507.
- (35) Vella, P., *The Development of New Drug Leads to Combat Bacterial Resistance towards Antibiotics*, PhD, The University of Queensland, 2012.

CHAPTER 3: THE SAR STUDY OF THE 3-CYANO, 4,5-DIPHENYL AND *N*-BENZYL SIDE CHAINS OF 2-AMINO-1-BENZYL-4,5-DIPHENYL-1*H*-PYRROLE-3-CARBONITRILE

3.1 General introduction

The previous structure-activity relationship (SAR) study of the 2-amino functional group of the pyrrole lead compound **65** has successfully led to the identification of two potent IMP-1 inhibitors, **93** and **99** for this class of inhibitors, with a 14- to 17-fold increase in IMP-1 inhibitory potency (Figure 3.1).

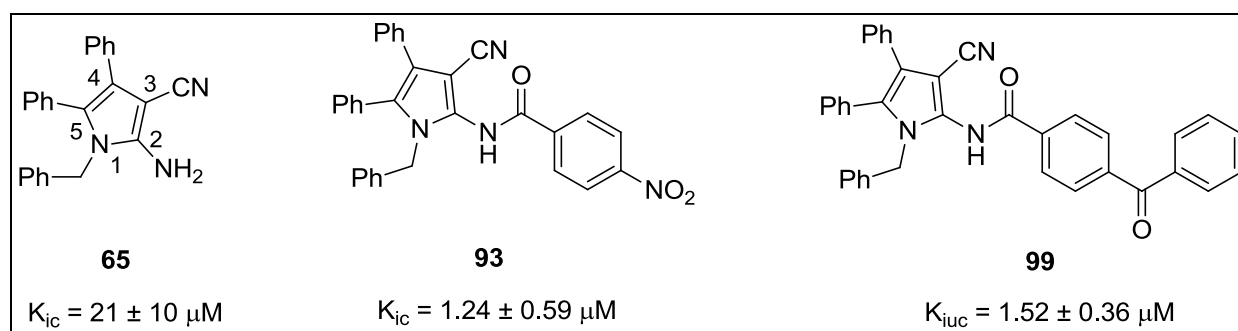


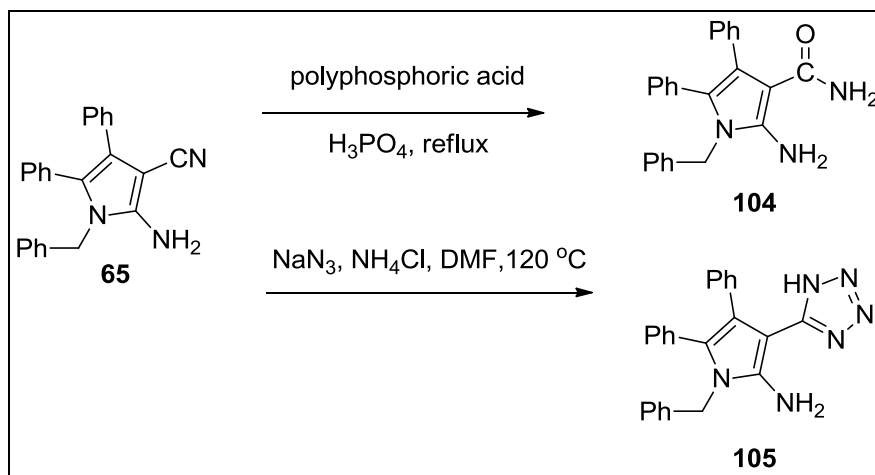
Figure 3.1: The lead compound **65** and the optimised potent IMP-1 inhibitors, **93** and **99**.

This chapter will focus on the SAR of the 3-cyano group, vicinal 4,5-diphenyl and *N*-benzyl side chains of pyrrole **65**.

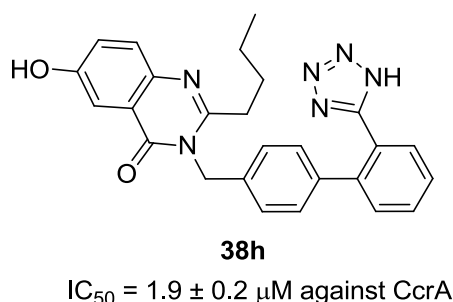
3.2 Research plan

Previous MVD computational study of pyrrole **65** bound with IMP-1 suggested that the 3-cyano group of pyrrole **65** is involved in hydrogen bonding with the terminal amino group of Lys161 (224) (Section 2.2). The same *in silico* model however, did not predict any interactions between the inhibitor and the zinc ions. Therefore, it is envisioned that derivatisation of the 3-cyano group to a tetrazole ring, **105** may possibly form additional contacts between the inhibitor and the zinc ions, as previous 3D structure of biphenyl tetrazole **38h** bound with the B1 CcrA MBL showed an ionic interaction between one of the

negatively charged tetrazole ring nitrogens and the Zn² site (Section 1.11 c).¹ In addition, the 3-cyano group of pyrrole **65** can also be hydrolysed into an amide group, **104** to further evaluate the role of the 3-cyano group in IMP-1-binding (Scheme 3.1).



Scheme 3.1: The proposed synthetic derivitisation of the 3-cyano group of pyrrole **65**.



Molecular modelling of **105** with a deprotonated tetrazole ring bound in the active site of IMP-1 with MVD predicted that N-4 and N-5 of the tetrazole ring is close to the metal centres, with N-Zn distances of 2.03-2.26 Å (Figure 3.2 and Table 3.1). Based on the 3D structure of **38h** co-crystallised with a variant of the B1 CcrA MBL, a N-Zn distance of ≤ 2.36 Å is indicative of an ionic tetrazolyl N-Zn interaction (Section 1.11 c).¹ In addition, the *in silico* model also predicted plausible hydrogen bond interactions between the tetrazole nitrogen atoms of the ligand with the carboxamide terminal group of Asn167 (233) and the N-H of the imidazole ring of His79 (118). Asn167 (233), that is conserved among two-thirds of all sequenced MBLs, is part of the oxyanion hole that activates the

carbonyl carbon of the β -lactam substrate for nucleophilic attack by the bridging hydroxide (Section 1.10).^{2,3}

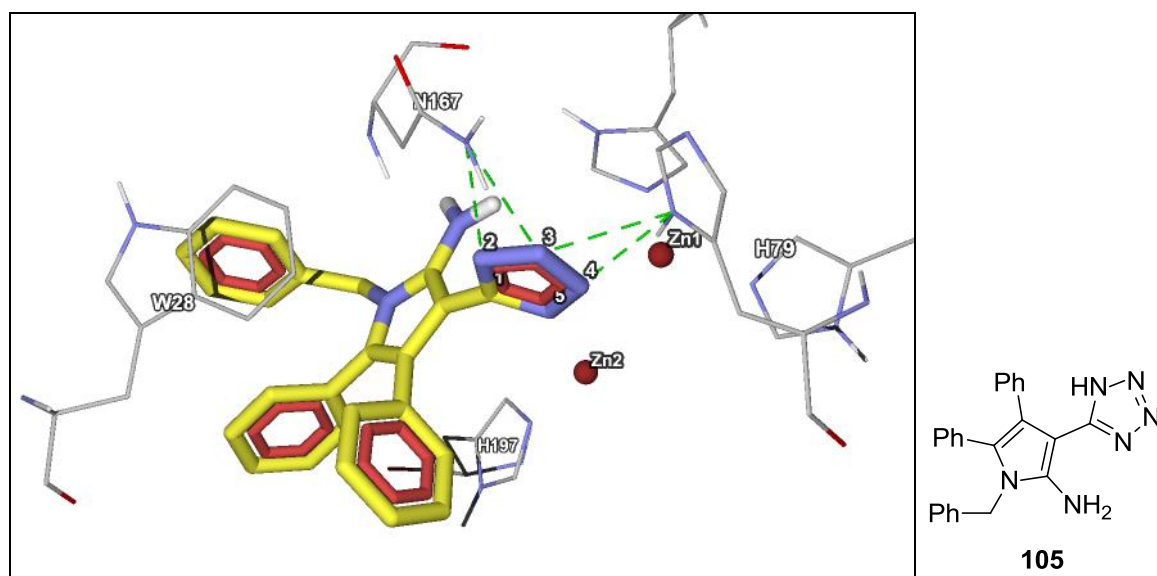
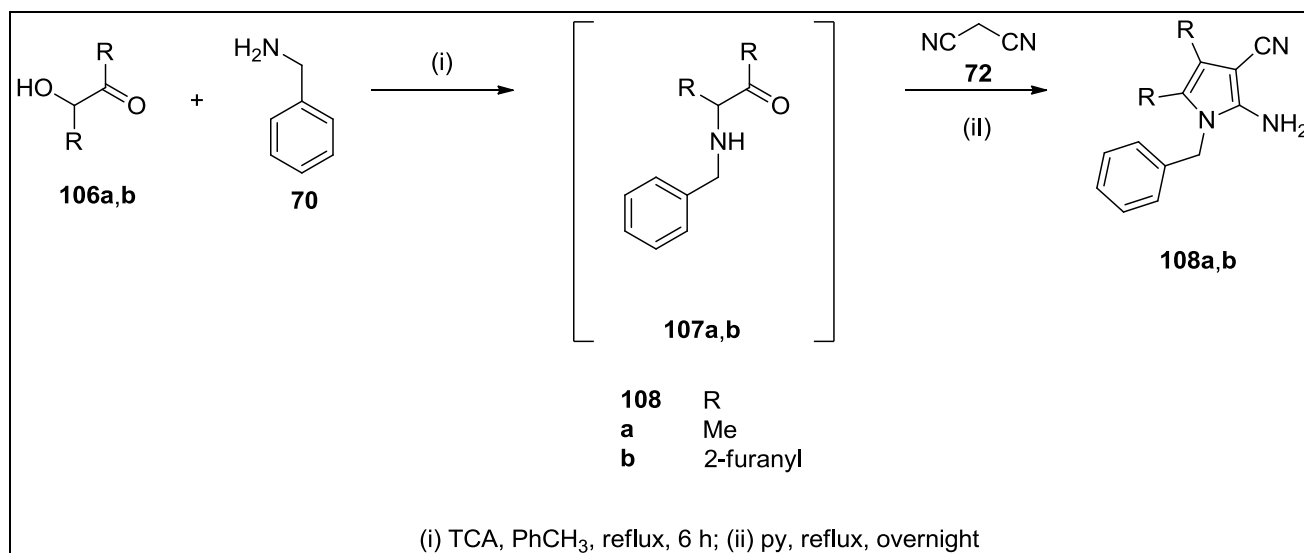


Figure 3.2: The MVD computational model of **105** docked into the active site of IMP-1. Atom colours: carbon on ligand in yellow, carbon on IMP-1 in grey, nitrogen in blue, oxygen in red and hydrogen in white. The Zn^{2+} ions are shown as red spheres. The dashed, green lines represent hydrogen bonds.

Table 3.1: Notable atom-atom interactions and distances between ligand **105** and the active site of IMP-1, as predicted by MVD.

Interaction	Type	Atom-atom distance (Å)
N-4-Zn1	ionic	2.03
N-5-Zn2	ionic	2.26
N-4-N (His79)	hydrogen	2.61 (N-N)
N-3-N (His79)	hydrogen	2.85 (N-N)
N-3-N (Asn167)	hydrogen	2.80 (N-N)
N-2-N (Asn167)	hydrogen	2.79 (N-N)

In addition, the vicinal 4,5-diphenyl side chains of the pyrrole **65** lead compound can also be substituted with methyl and 2-furanyl side chains, in order to study the extent of hydrophobic interaction between the phenyl rings of **65** with the mobile L3 loop (Section 1.9).⁴ The starting materials required for the syntheses of these derivatives, acetoin (**108a**) and furoin (**108b**) are both commercially available (Scheme 3.2).



Scheme 3.2: The proposed syntheses of 2-aminopyrrole-3-carbonitrile with vicinal dimethyl **108a** and di-2-furanyl **108b** side chains.

The MVD computational model of **108a** complexed with IMP-1 suggested that the ligand doesn't have any hydrogen bond or ionic interactions with the active site of the enzyme (Figure 3.3). Furthermore, the vicinal methyl side chains of **108a** were predicted not to have any hydrophobic contacts with Val25 (61) and Val31 (67), which are part of the mobile L3 loop (Section 2.2). The only plausible interaction between the ligand and the enzyme is a π - π stacking interaction between the pyrrole ring of **108a** and indole ring of Trp28 (64). Trp28 (64), which is positioned at the edge of the mobile loop, closes the active site of the enzyme upon substrate or inhibitor binding (Section 1.9).⁵ This prediction is reflected in the low MolDock score magnitude of the *in silico* model of **108a**-IMP-1 complex (Table 3.2). The Moldock score is a prediction of the binding affinity of the ligand with the enzyme. The larger the negative value of the Moldock score is, the higher the predicted binding affinity.

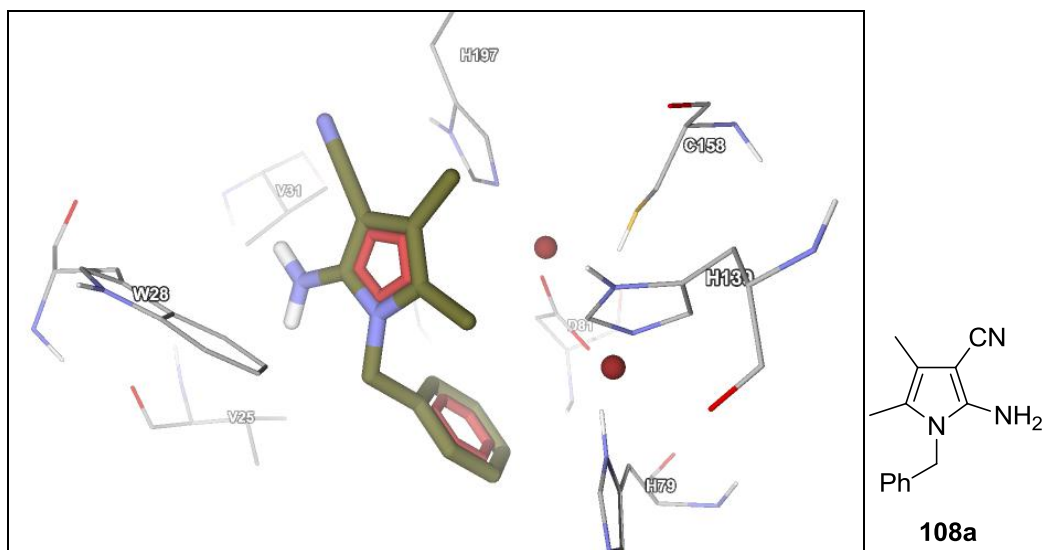
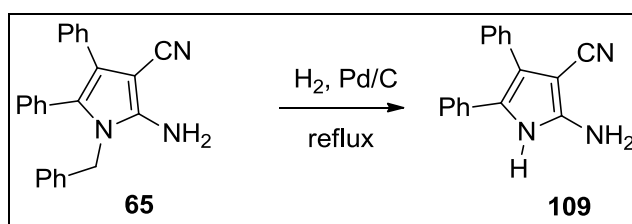
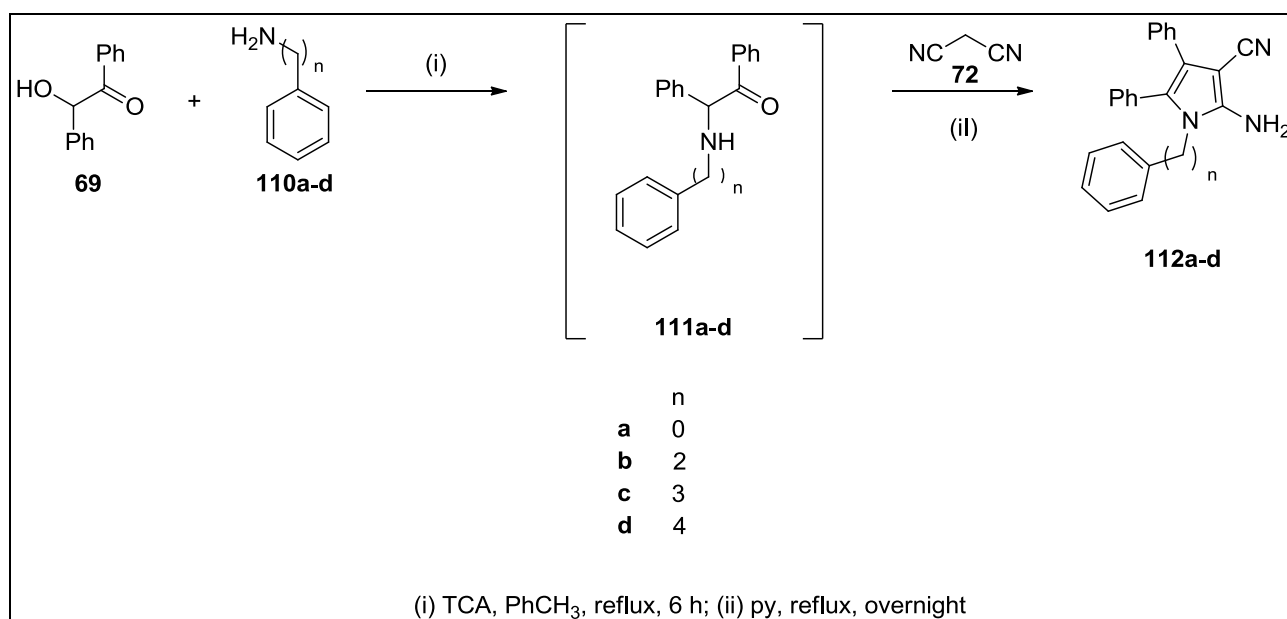


Figure 3.3: The *in silico* model of **108a** complexed with IMP-1, as predicted by MVD. Atom colours: carbon on ligand in olive green, carbon on IMP-1 in grey, nitrogen in blue, oxygen in red and hydrogen in white. The Zn²⁺ ions are shown as red spheres.

Finally, the *N*-benzyl side chain of pyrrole **65** can be removed by a catalytic hydrogenolysis reaction, in order to evaluate the importance of the *N*-benzyl moiety in inhibitor-enzyme binding (Scheme 3.3). Furthermore, the distance between the pyrrole ring nitrogen and the phenyl ring can also be varied to augment the IMP-1 inhibitory SAR study of this pharmacophore (Scheme 3.4).



Scheme 3.3: The proposed *N*-debenzylation of pyrrole **65** via a catalytic hydrogenolysis reaction.



Scheme 3.4: The proposed syntheses of pyrrole **65** derivatives with various chain lengths between the pyrrole ring nitrogen and phenyl ring.

MVD *in silico* modelling of **112a** bound in the active site of IMP-1 suggested only one hydrogen bond interaction between the 3-cyano group of the ligand with the terminal amino group of Lys161 (224) (Figure 3.4). The *in silico* model didn't predict any interactions between the ligand with the Zn²⁺ centres.

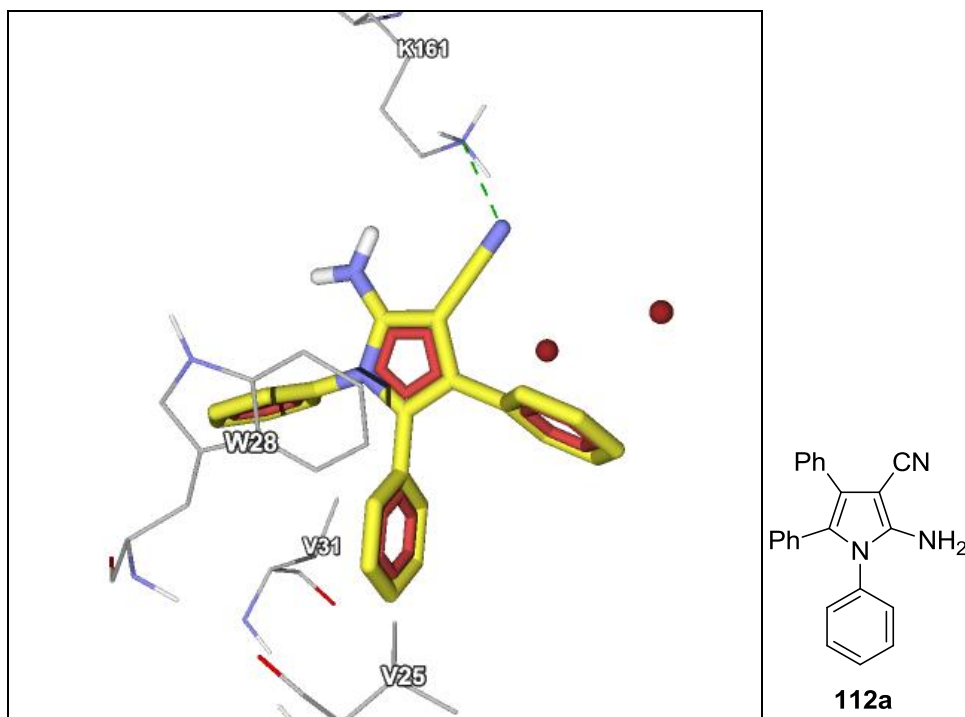


Figure 3.4: The MVD computational model of **112a** bound in the active site of IMP-1. Atom colours: carbon on ligand in yellow, carbon on IMP-1 in grey, nitrogen in blue, oxygen in red and hydrogen in white. The Zn^{2+} ions are shown as red spheres. The dashed, green line represents a hydrogen bond (N-N distance 3.10 Å).

On the other hand, the MVD computational docking of **112d** complexed with IMP-1 suggested that the carbon chain between the pyrrole nitrogen and phenyl ring has additional hydrophobic contacts with Val25 (61), Val30 (66), Val31 (67) and Phe51 (87) (Figure 3.5). Furthermore, the computational model also predicted hydrogen bond interactions between the 3-cyano nitrogen of the ligand and the terminal amino group of Lys161 (224) (N-N distance 2.79 Å), and N-H of the His139 (196) imidazole ring (N-N distance 2.61 Å).

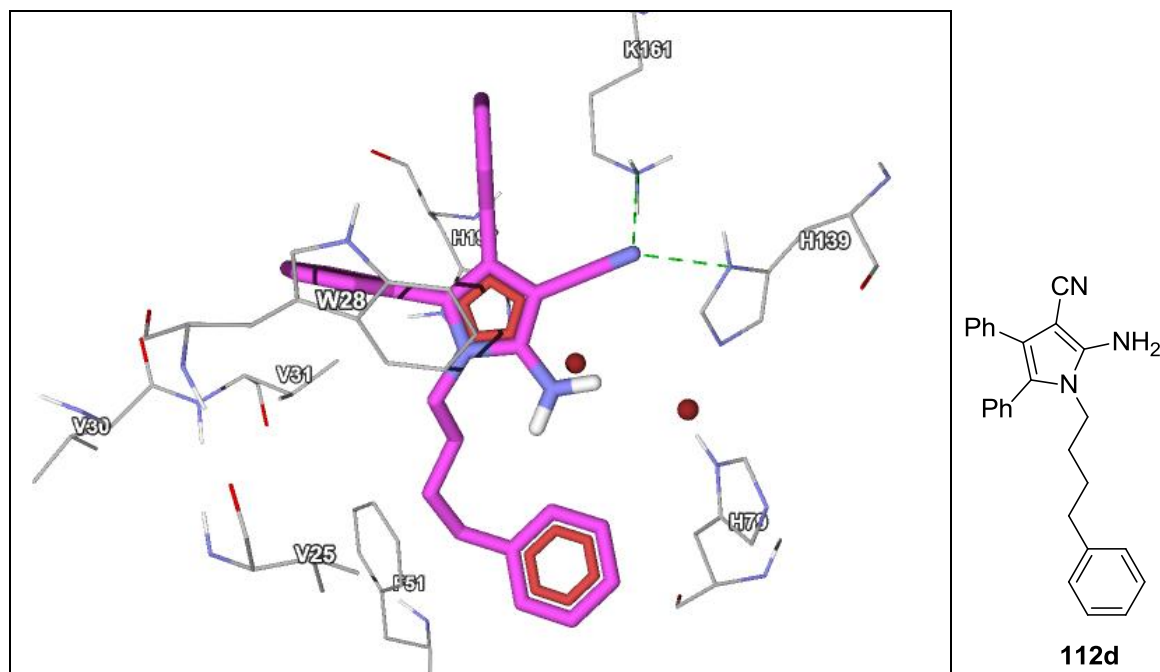


Figure 3.5: The *in silico* model of **112d** complexed with IMP-1, as proposed by MVD. Atom colours: carbon on ligand in magenta, carbon on IMP-1 in grey, nitrogen in blue, oxygen in red and hydrogen in white. The Zn²⁺ ions are shown as red spheres. The dashed, green lines represent hydrogen bonds.

The MVD Moldock score is derived from the docking scoring function, E_{score} which is in turn defined from the ligand-protein interaction energy, E_{inter} and the internal energy of the ligand, E_{intra} (Equation 3.1).⁶ Table 3.2 lists the Moldock scores obtained from the molecular docking of pyrrole derivatives **104**, **105**, **108a**, **108b**, **109** and **112a-d**, as well as pyrrole **65**.

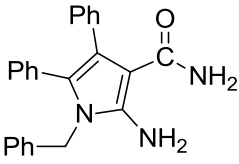
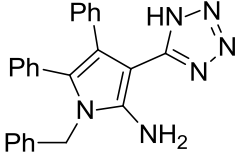
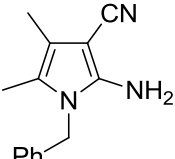
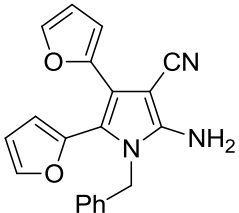
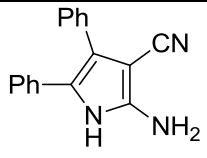
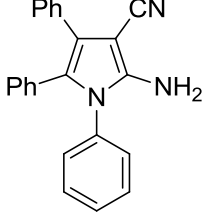
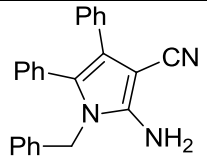
$$E_{score} = E_{inter} + E_{intra}$$

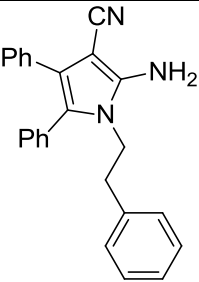
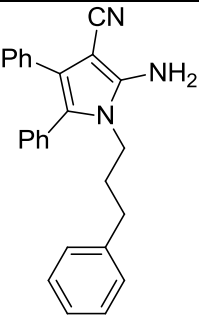
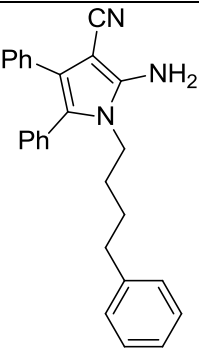
Equation 3.1: The definition of the docking scoring function, E_{score} .⁶

As previously mentioned, tetrazole **105** is the only pyrrole derivative predicted in this series of derivatives to have interactions between the ligand and the zinc ions. This is reflected in its MolDock score magnitude, which is the largest in this series of ligands. Conversely, derivative **108a** which was predicted to exhibit minimal binding interactions

with the enzyme was calculated to exhibit the lowest MolDock score magnitude in this series of ligands. In addition, a trend of increasing magnitude of the MolDock score is observed as the chain length between the pyrrole ring nitrogen and phenyl ring increases, with **112c** and **112d** predicted to have the same score.

Table 3.2: The MolDock scores (kcal mol⁻¹) of pyrroles **65**, **104**, **105**, **108a**, **108b**, **109** and **112a-d** bound with IMP-1, as predicted by MVD

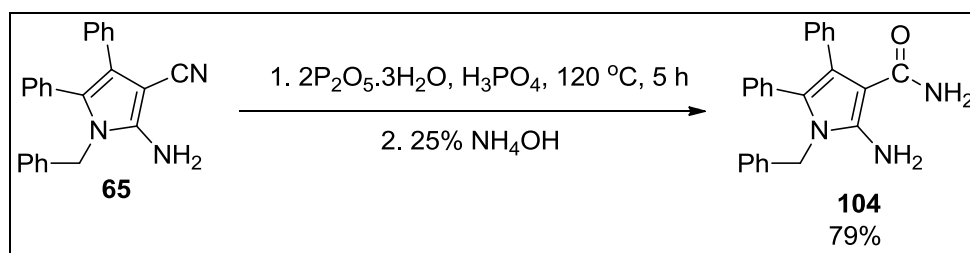
Ligand	Molecular structure	MolDock score (kcal mol ⁻¹)
104		-109.0
105		-204.7
108a		-85.4
108b		-125.0
109		-91.7
112a		-113.3
65^a		-116.2

112b		-125.2
112c		-142.1
112d		-142.6

3.3 Results and discussion

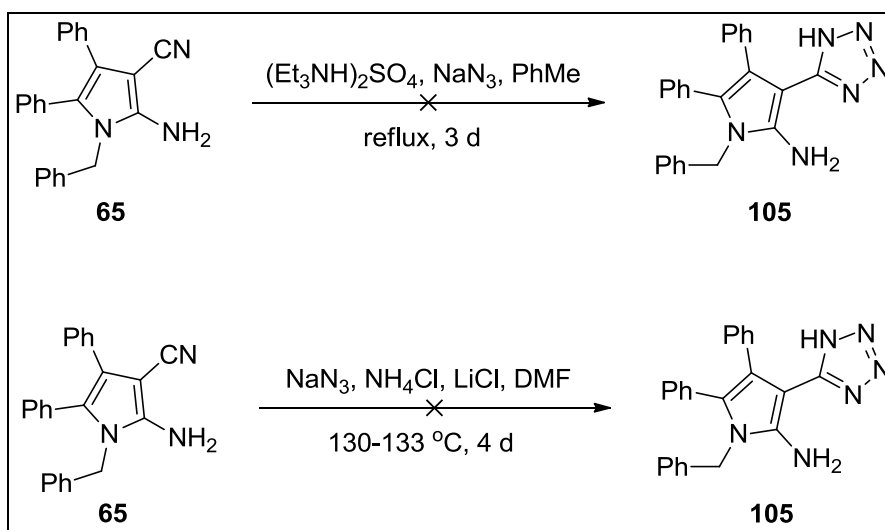
3.3 a) Synthetic work

The acid-catalysed hydrolysis of the 3-cyano group of pyrrole **65** to the carboxamide derivative, **104** was accomplished by using polyphosphoric acid and phosphoric acid, as reported by Eger and colleagues on another 2-amino-1*H*-pyrrole-3-carbonitrile analogue (Scheme 3.5).⁷



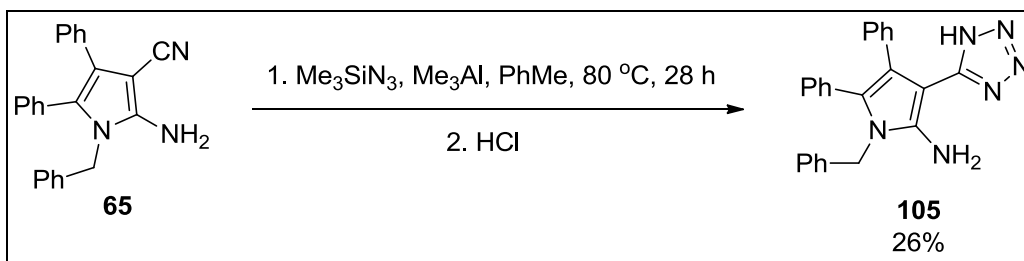
Scheme 3.5: The acid-catalysed hydrolysis of pyrrole-3-carbonitrile **65** to pyrrole-3-carboxamide **104**.

Hydrazoic acid (HN_3), which is formed *in situ* from sodium azide and an ammonium salt, is commonly used as the azide reagent in the tetrazolyl derivatisation of aromatic nitriles.⁸⁻¹³ However, the thermal 1,3-dipolar cycloaddition of the 3-cyano group of pyrrole **65** with sodium azide and ammonium salts, such as triethylammonium sulfate or ammonium chloride failed to give the tetrazole product **105** (Scheme 3.6).^{8,10} The percentage of starting material **65** recovered from both attempts was 80% and 83%, respectively. This implies that hydrazoic acid is not the appropriate azide reagent for the 1,3-dipolar cycloaddition of the 3-cyano group of pyrrole **65**.¹³



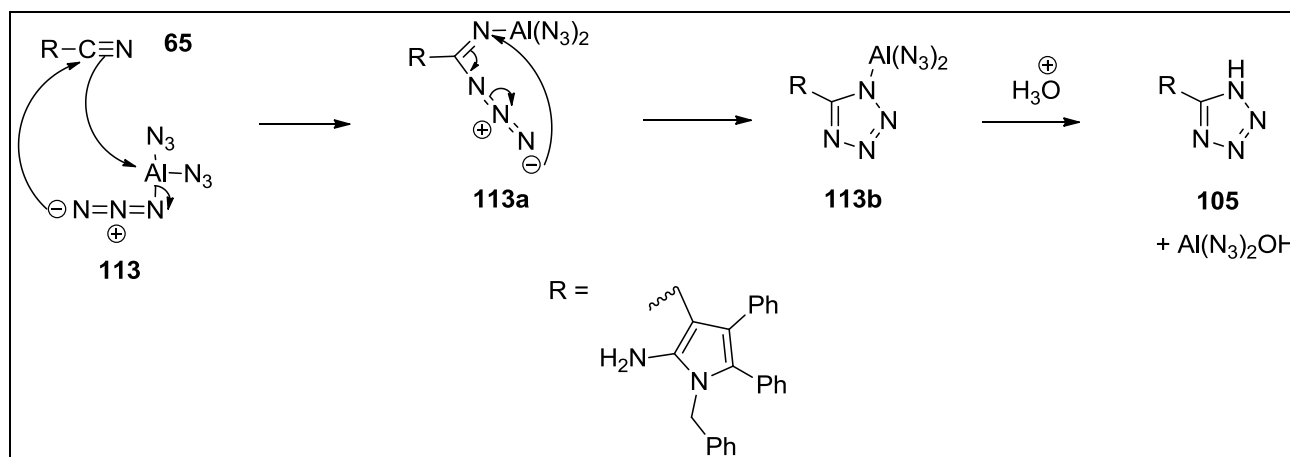
Scheme 3.6: The unsuccessful 1,3-dipolar cycloaddition of pyrrole-3-carbonitrile **65** with sodium azide and ammonium salts.

The tetrazolyl derivatisation of pyrrole-3-carbonitrile **65** was finally achieved using aluminium triazide (**113**) as the azide reagent (Scheme 3.7). The reagent is formed *in situ* from trimethylsilylazide, Me_3SiN_3 and trimethylaluminium, Me_3Al .¹³

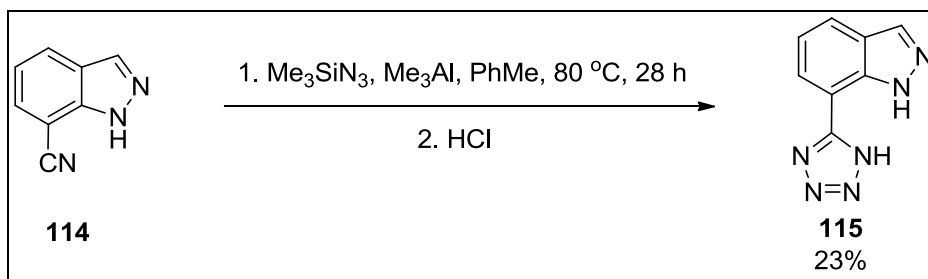


Scheme 3.7: The successful 1,3-dipolar cycloaddition of pyrrole-3-carbonitrile **65** with trimethylsilylazide, Me_3SiN_3 and trimethylaluminium, Me_3Al .

The low reaction yield may be due to the bulky vicinal diphenyl groups and the *N*-benzyl side chain of pyrrole **65**, which may hinder the access of aluminium triazide (**113**) to the 3-cyano group of **65** (Scheme 3.8).¹³ Another explanation for this observation is that the 2-amino group of pyrrole **65** may form a Lewis acid-base complex with trimethylaluminium.¹⁴ In addition, a low reaction yield was also reported by Cottyn and co-workers in their attempt to derivatise an aromatic indazole carbonitrile, **114** to a tetrazole derivative, **115** with the same azide reagent (Scheme 3.9).¹⁵



Scheme 3.8 The mechanism of the 1,3-dipolar cycloaddition of pyrrole **65** with aluminium triazide (**113**), as proposed by Huff and Staszak.¹³



Scheme 3.9: The tetrazolyl derivatisation of 1*H*-indazole-7-carbonitrile (**114**), as reported by Cottyn *et al.*¹⁵

The molecular structures of derivatives **104** and **105** were characterised by NMR (¹H and ¹³C), and IR spectroscopy, as well as low resolution mass spectrometry (LRMS) and high resolution mass spectrometry (HRMS).

The carbonyl carbon of carboxamide **104** was confirmed by the appearance of a downfield signal at δ 168.7 ppm, and the disappearance of the nitrile carbon (C≡N) at δ 117.5 ppm in its ¹³C NMR spectrum (Figure 3.6).¹⁶ In addition, the disappearance of the nitrile, C≡N stretch at around 2220 cm⁻¹, and the appearance of a carbonyl, C=O stretch at 1670.7 cm⁻¹ in the IR spectrum of **104** further confirmed the presence of the carbonyl group of the carboxamide (Figure 3.7).¹⁶

Lastly, the HRMS spectrum of **104** showed a key molecular ion peak, having a *m/z* ratio of 368.1758, which corresponds to the [M + H]⁺ ion of the hydrolysed carboxamide product (spectrum not shown). The experimental *m/z* ratio corresponds to a chemical formula of C₂₄H₂₂N₃O and has a mass measurement error of 0.10 mDa or 0.27 ppm from its calculated *m/z* value of 368.1757.¹⁷

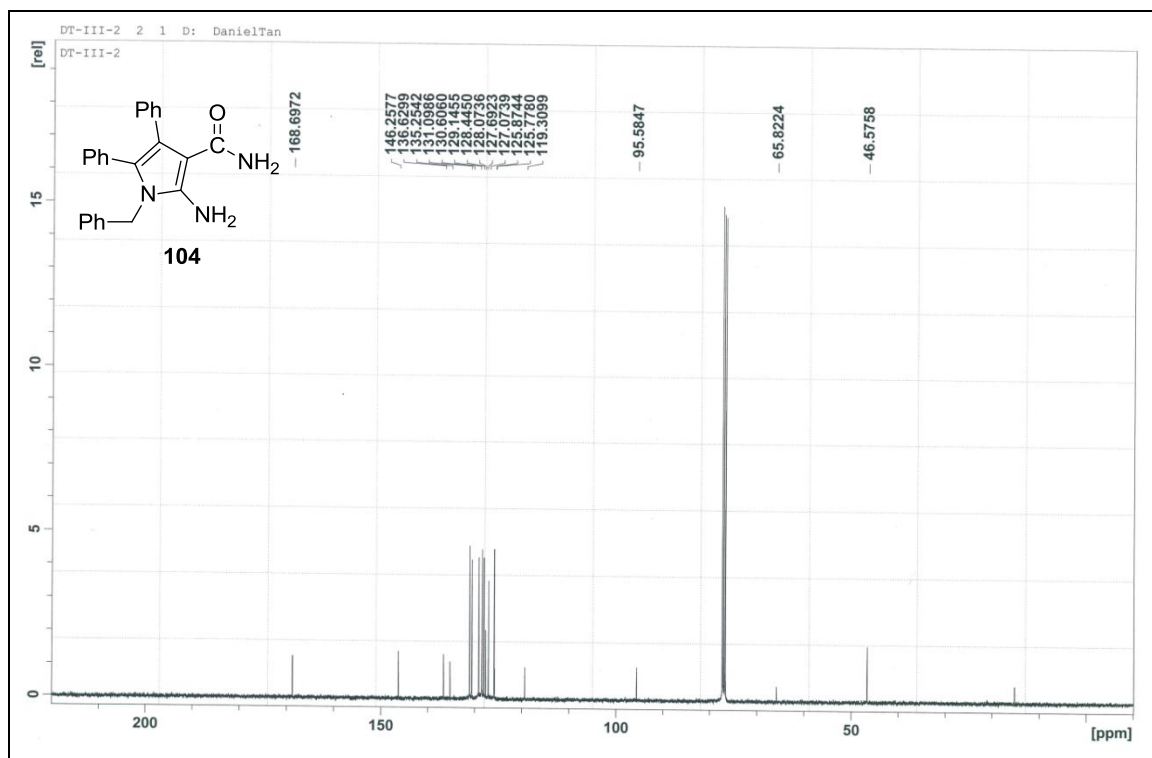


Figure 3.6: The ^{13}C NMR (100 MHz, CDCl_3) spectrum of carboxamide **104**. The triplet at δ 77.0 ppm is due to CDCl_3 . The peaks at δ 15.2 and δ 65.8 ppm are due to a diethyl ether impurity in the sample.

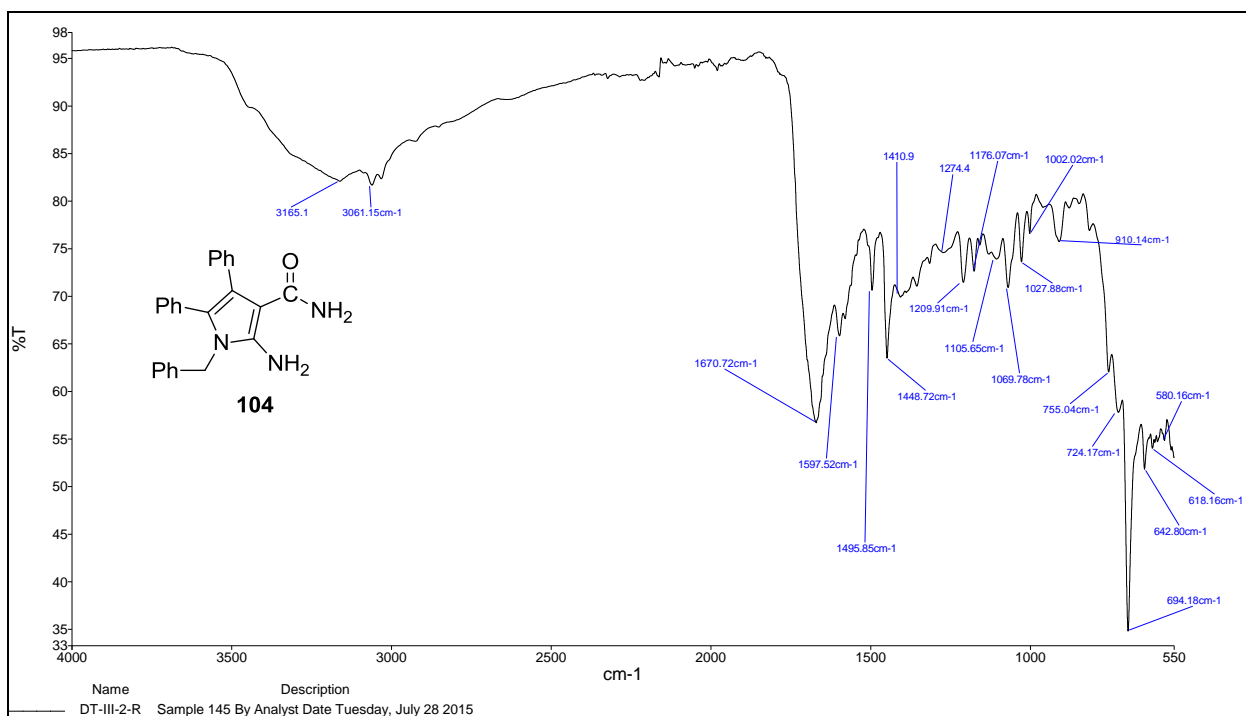


Figure 3.7: The IR spectrum of carboxamide **104**.

As for compound **105**, the presence of the tetrazole ring of the pyrrole derivative was confirmed by its ^1H and ^{13}C NMR spectra (Figure 3.8 and 3.9, respectively). The broad, downfield ^1H signal at δ 10.80 ppm is indicative of the tetrazolyl N-H proton; whereas the downfield ^{13}C signal at δ 151.3 ppm corresponds to the tetrazolyl, N-CH=N carbon.¹⁸

Furthermore, the chemical formula of **105** was confirmed by HRMS analysis as having a total number of six nitrogen atoms, as would be expected for the tetrazolyl product. The negative mode HRMS spectrum of the compound showed a molecular ion peak with a m/z value of 391.1685, that suggests a chemical formula of $\text{C}_{24}\text{H}_{19}\text{N}_6$ (spectrum not shown). This observed m/z ratio corresponds to the $[\text{M} - \text{H}]^-$ ion of the product and has a mass measurement error of 0.80 mDa or 2.0 ppm from its calculated m/z value of 391.1677.

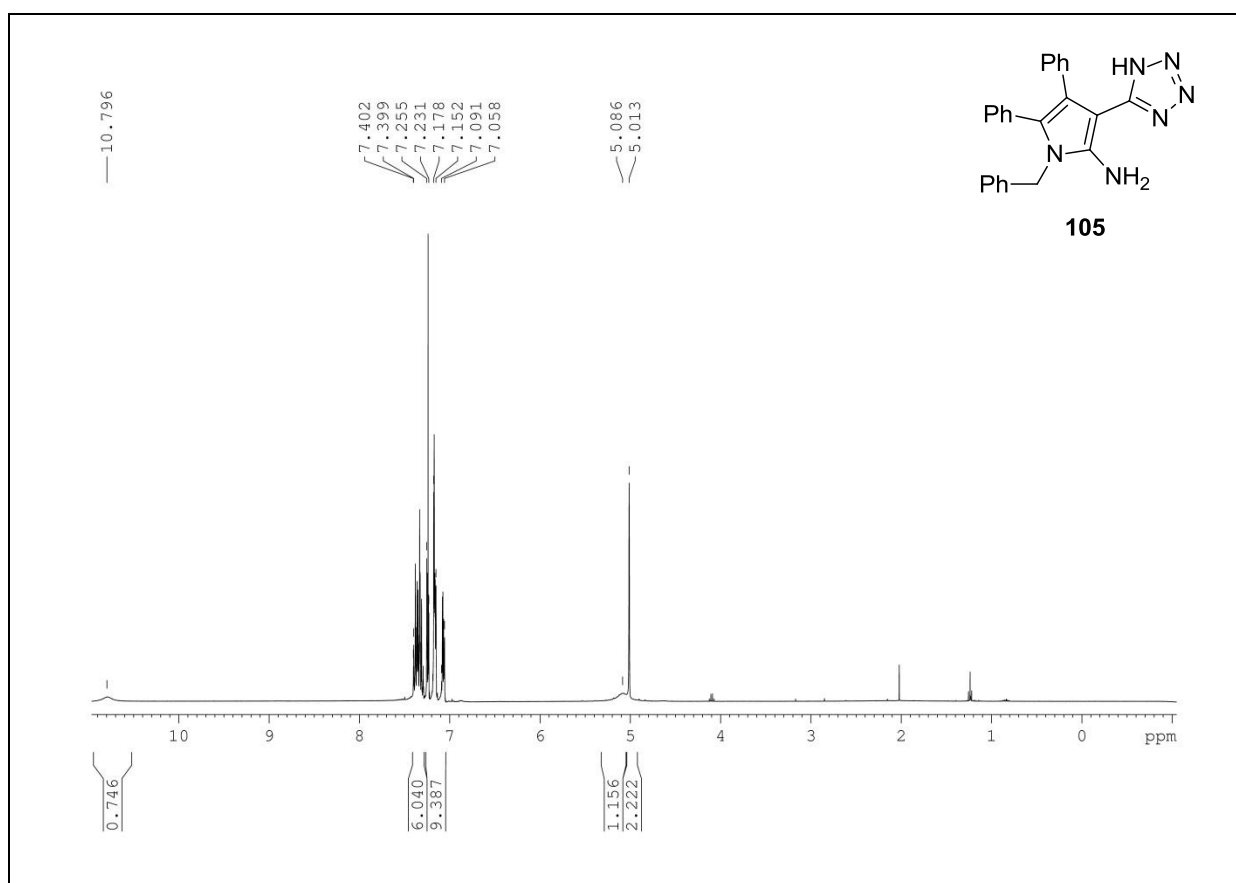


Figure 3.8: The ^1H NMR (400 MHz, CDCl_3) spectrum of tetrazole **105**. A triplet, singlet and quartet at δ 1.24 ppm, 2.02 ppm and 4.10 ppm, respectively is due to trace amounts of ethyl acetate in the sample. The broad singlet at δ 5.09 corresponds to the amino, NH_2 protons of **105**, which was expected to give an integration of two protons.

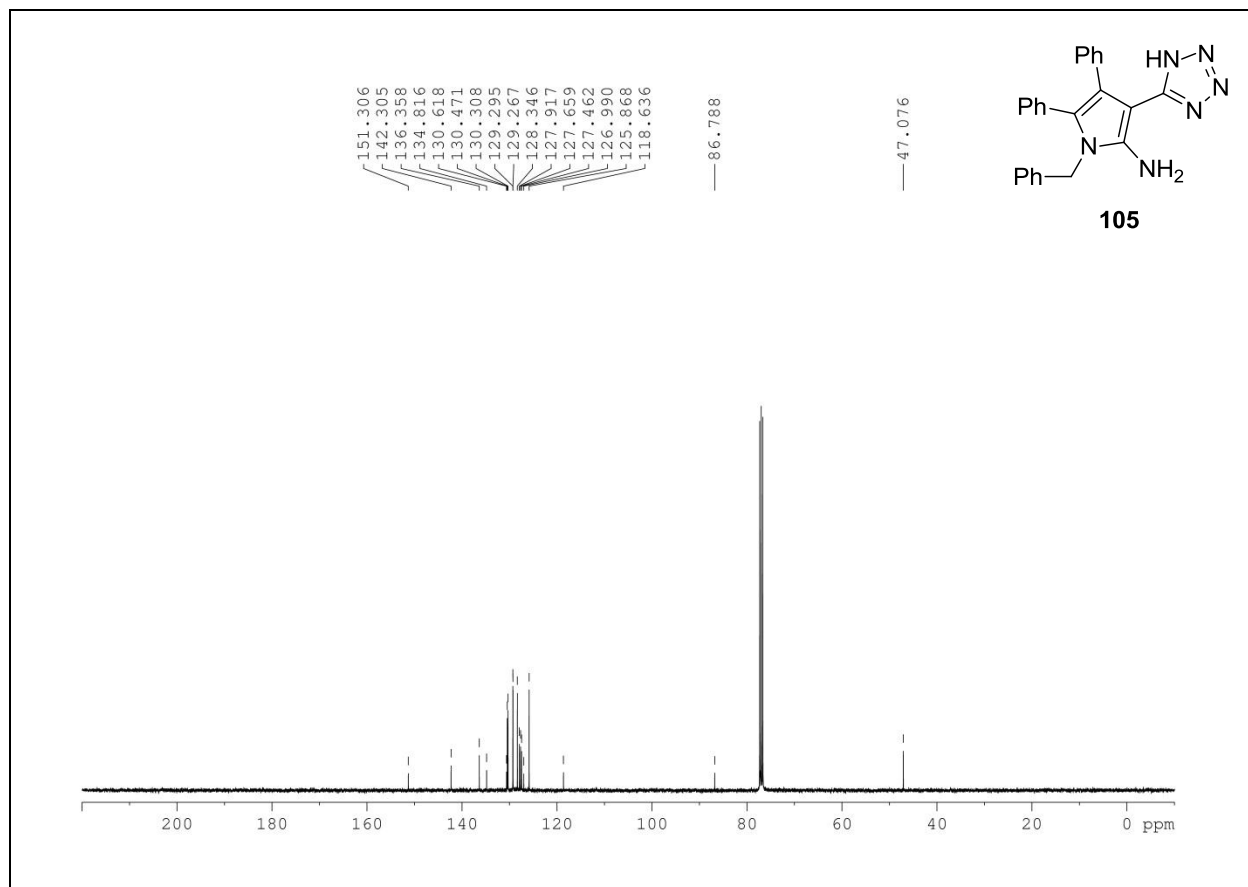
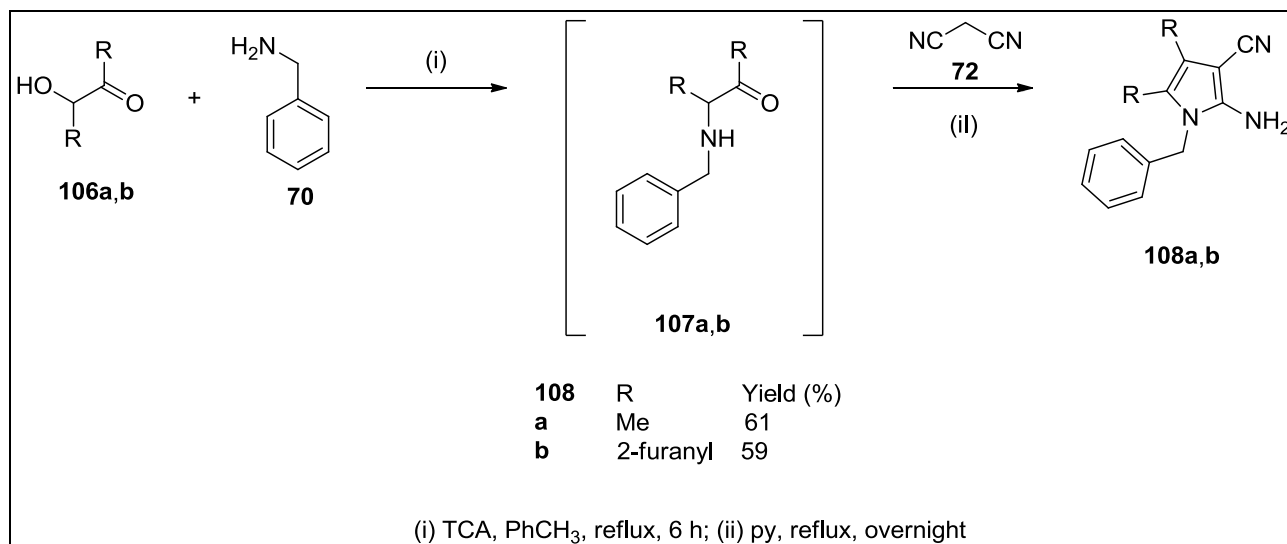


Figure 3.9: The ¹³C NMR (100 MHz, CDCl₃) spectrum of tetrazole **105**. The triplet at δ 77.0 ppm is due to CDCl₃.

The vicinal dimethyl **108a** and di-2-furanyl **108b** derivatives of pyrrole **65** were successfully synthesised in moderate yields of 61 and 59% *via* the condensation of benzylamine (**70**) and malononitrile (**72**) with acetoin (**106a**) and furoin (**106b**), respectively (Scheme 3.10).



Scheme 3.10: The syntheses of 2-aminopyrrole-3-carbonitrile with vicinal dimethyl **108a** and di-2-furanyl **108b** side chains.

The structural identities of derivatives **108a** and **b** were elucidated by ¹H and ¹³C NMR as well as IR spectroscopy. The ¹³C NMR spectra of both **108a** and **b** showed resonance signals at around δ 46-47 ppm and δ 117 ppm, corresponding to the *N*-benzylic and nitrile carbon, respectively (Section 2.3 a). The ¹³C NMR spectrum of **108a** is shown as a representative spectrum in Figure 3.10. In addition, the benzylic protons of **108a** and **b** were shown to resonate as a two-proton singlet at δ 4.9 ppm in the ¹H NMR spectra of the said compounds (Figure 3.11). Interestingly, upon closer inspection on the ¹H NMR spectrum of **108a**, the two vicinal methyl protons of **108a** were depicted to resonate as a pair of three-proton doublets with an average coupling constant of 0.6 Hz.¹⁹ This long-range ⁵*J* (CH₃-CH₃) coupling across four single bonds and one double bond is known as homoallylic coupling (Figure 3.12).²⁰

The IR spectra of the compounds also showed two broad peaks at around 3420-3450 and 3330 cm⁻¹, as well as a moderately-intense peak at around 2200 cm⁻¹. The first two peaks correspond to the two N-H stretching bands of the 2-amino group, whereas the other peak corresponds to the nitrile stretch of the 3-cyano group of the compounds (spectra not shown).

In addition, the molecular weight and chemical formula of derivatives **108a** and **b** were confirmed by HRMS analysis (spectra not shown). For example, the positive mode HRMS spectrum of **108a** showed a molecular ion peak with a *m/z* value of 226.1344,

suggesting a chemical formula of $C_{14}H_{16}N_3$. The observed m/z ratio corresponds to the $[M + H]^+$ ion of the compound and has a mass measurement error of 0.50 mDa or 2.2 ppm from its calculated m/z value of 226.1339.

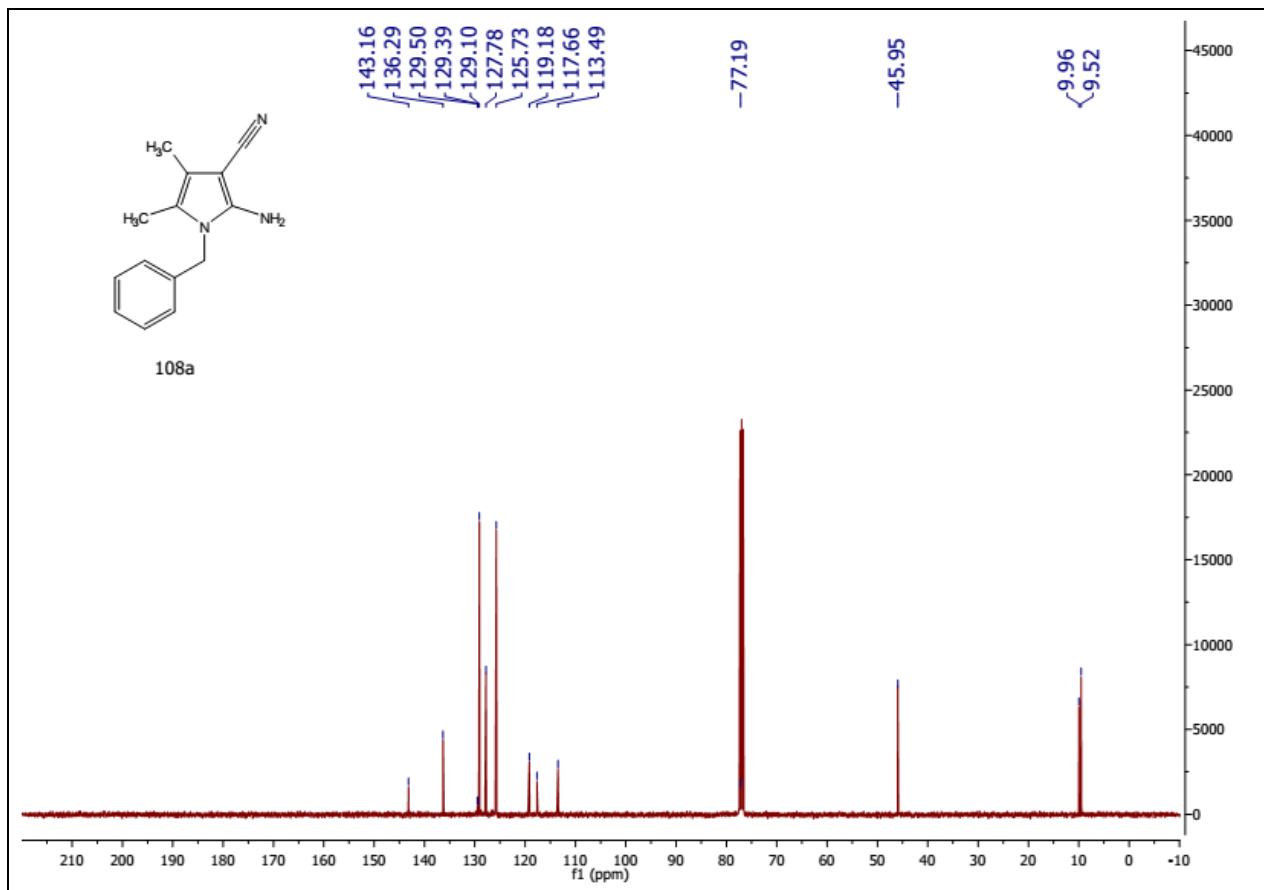


Figure 3.10: The ^{13}C NMR (100 MHz, $CDCl_3$) spectrum of **108a**. The residual solvent peak is a triplet at δ 77.0.

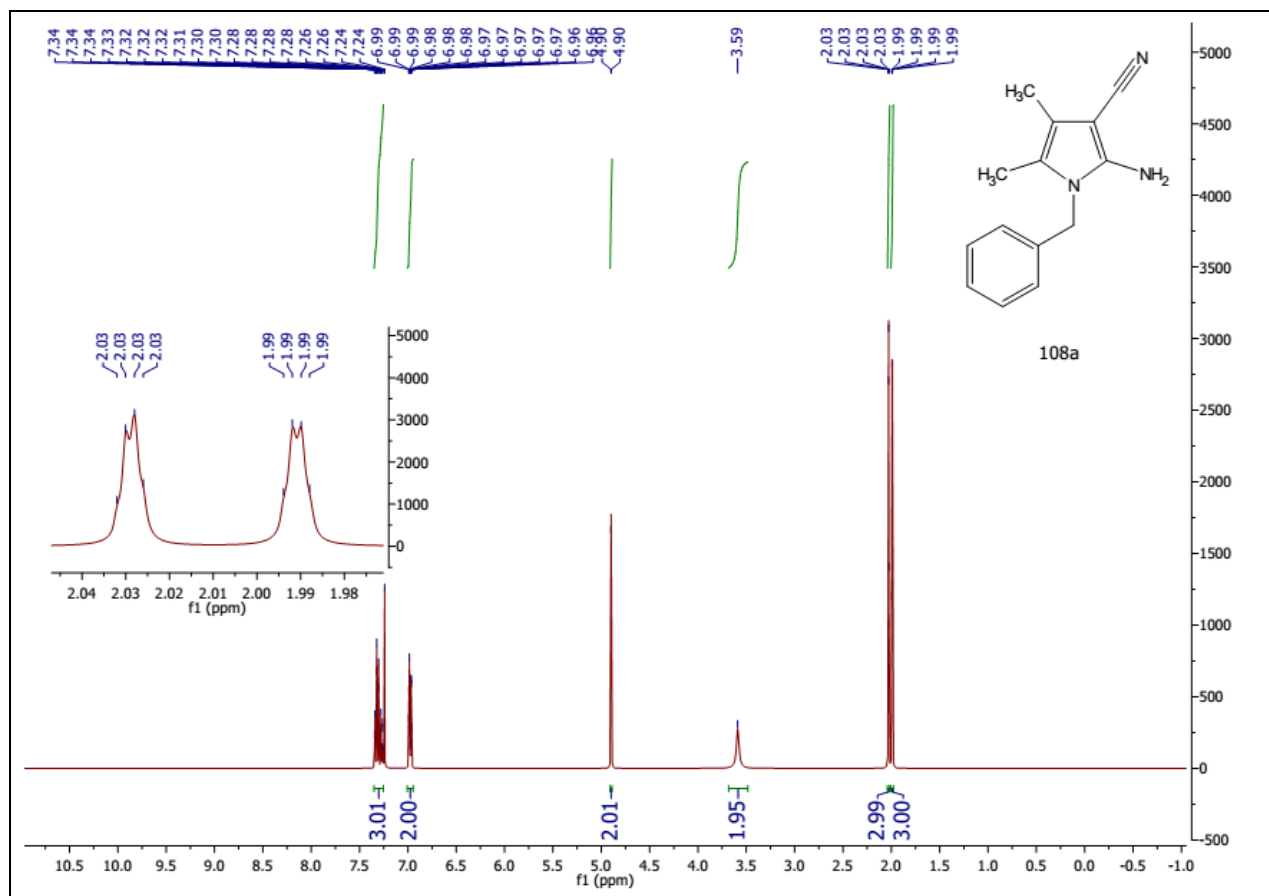


Figure 3.11: The ^1H NMR (400 MHz, CDCl_3) spectrum of **108a**.

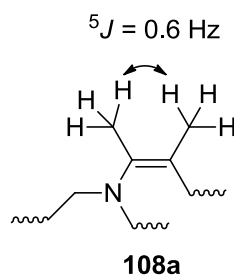
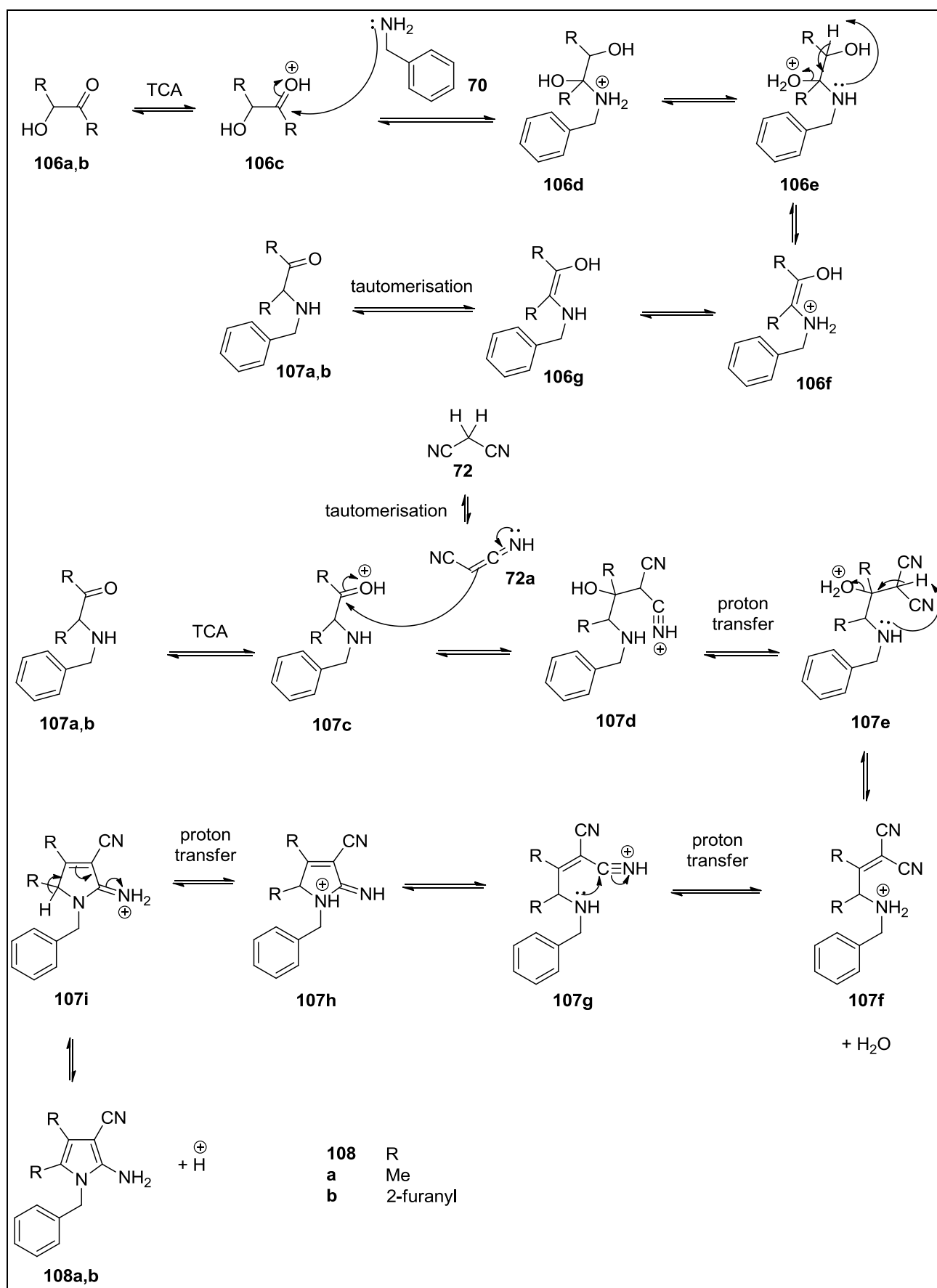


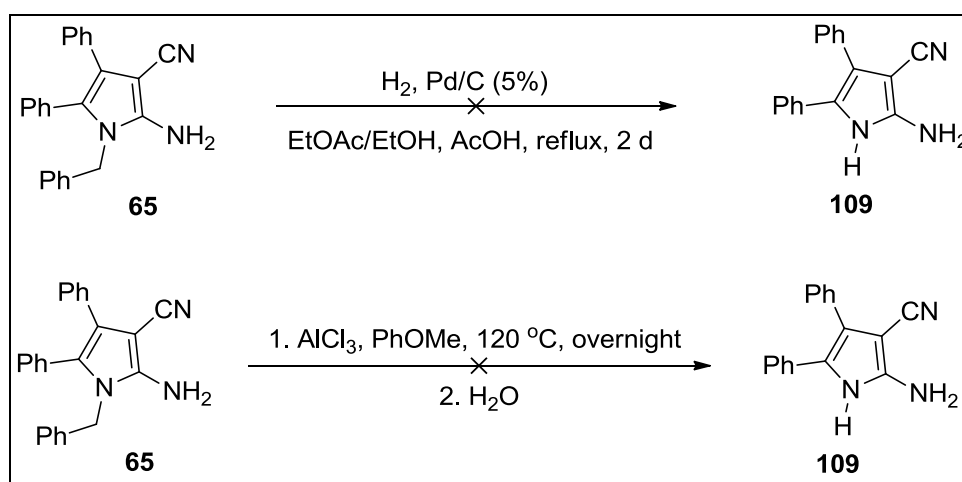
Figure 3.12: The 5J homoallylic coupling between the protons of the two vicinal methyl groups of **108a**.

The proposed mechanism for the syntheses of pyrrole derivatives **108a** and **b** are illustrated in Scheme 3.11. Initially, acetoin (**106a**) or furoin (**106b**) condenses with benzylamine (**70**) to give α -aminoketone **107a, b**, which then undergoes Knoevenagel condensation with malononitrile (**72**) to give **107f**.^{21,22} Further cyclisation and aromatisation of **107f** finally afford the pyrrole derivative **108a** or **b**.²¹ Both the aforementioned condensation reactions are catalysed by trichloroacetic acid, TCA.²²



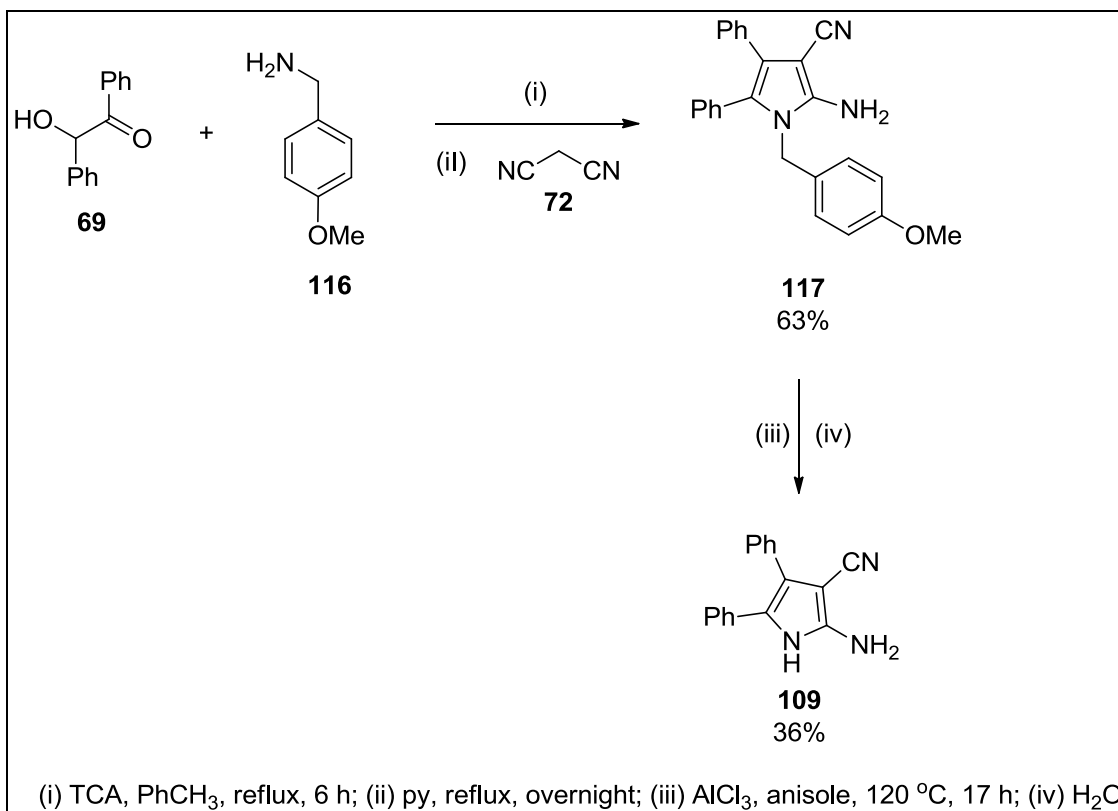
Scheme 3.11: The proposed mechanism for the syntheses of **108 a** and **b**.

As anticipated, the *N*-debenzylation of pyrrole **65** was a challenging task, as the *N*-benzyl groups of nitrogen-bearing aromatic heterocyclic rings, such as indoles, imidazoles and pyrroles are highly resistant against deprotection.^{23,24} The Pd/C-catalysed hydrogenolysis²⁵ and aluminium chloride-promoted debenzylation²⁴ were both unsuccessful in the removal of the *N*-benzyl group of pyrrole **65** (Scheme 3.12). The percentage of pyrrole **65** recovered from the catalytic hydrogenolysis and aluminium chloride-promoted debenzylation reaction was 70% and 92%, respectively.



Scheme 3.12: The unsuccessful *N*-debenzylation attempts of pyrrole **65**.

The aluminium chloride-promoted deprotection was finally accomplished on an *N*-4-methoxybenzyl derivative **117** of pyrrole **65**, as suggested by Greene (Scheme 3.13).^{24,26} Nevertheless, the reaction yield is low, and 27% of the starting material **117** was recovered from the reaction mixture. The low reaction yield could be due to the formation of an acid-base complex between the 2-amino group of pyrrole **117** and aluminium chloride, as previously described for tetrazole **105**.¹⁴ Nevertheless, another outcome of this synthetic exercise is that the *N*-4-methoxybenzyl derivative **117** can be assayed for its IMP-1 inhibitory activity.



Scheme 3.13: The de-*N*-methoxybenzylation of pyrrole **117** with aluminium chloride and anisole.

The molecular structures of the *N*-4-methoxybenzyl protected pyrrole **117** and deprotected pyrrole **109** were characterised by NMR (¹H and ¹³C), and IR spectroscopy, including spectrometric methods, such as LRMS and HRMS (the IR and HRMS spectra are not shown).

The ¹H and ¹³C NMR spectra of **117** showed characteristic signals for the *N*-4-methoxybenzyl moiety of the pyrrole (Figures 3.13 and 3.14, respectively). The three methoxy protons (OCH₃) and methoxy carbon (OCH₃) of **117** were depicted to resonate as a singlet at δ 3.79 ppm and a OCH₃ signal at δ 55.3 ppm in the ¹H and ¹³C NMR spectrum, respectively.¹⁶ The downfield ¹³C NMR signal at δ 159.3 corresponds to the *ipso* C-OCH₃ carbon, while the pair of doublets at δ 6.88 ppm and δ 6.99 ppm in the ¹H NMR spectrum of **117** is characteristic of a *para*-disubstituted phenyl ring pattern.^{16,27} Furthermore, the two benzylic protons (NCH₂) and benzylic carbon (NCH₂) of **117** were shown to resonate as a singlet at δ 4.84 ppm and a NCH₂ signal at δ 46.5 ppm in the ¹H and ¹³C NMR spectrum, respectively (Section 2.3 a).

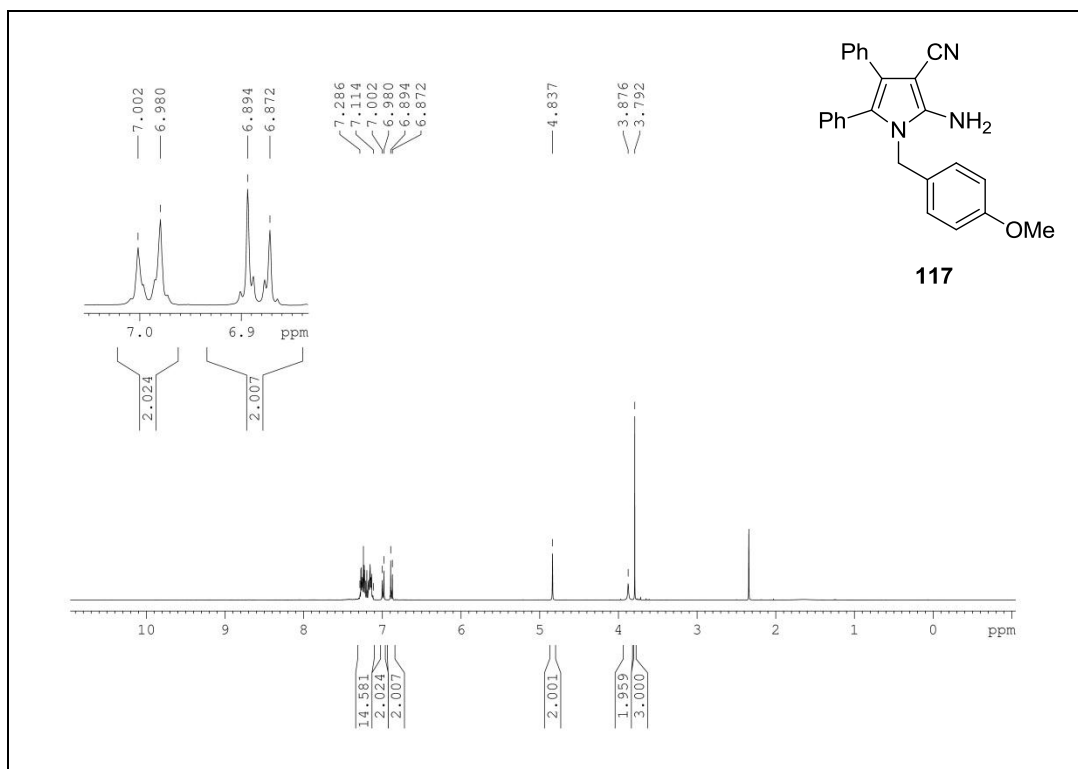


Figure 3.13: The ¹H NMR (400 MHz, CDCl₃) spectrum of **117**. A singlet at δ 2.34 ppm and an excess of five protons in the aromatic region of δ 7.11-7.29 are due to a toluene impurity in the sample.

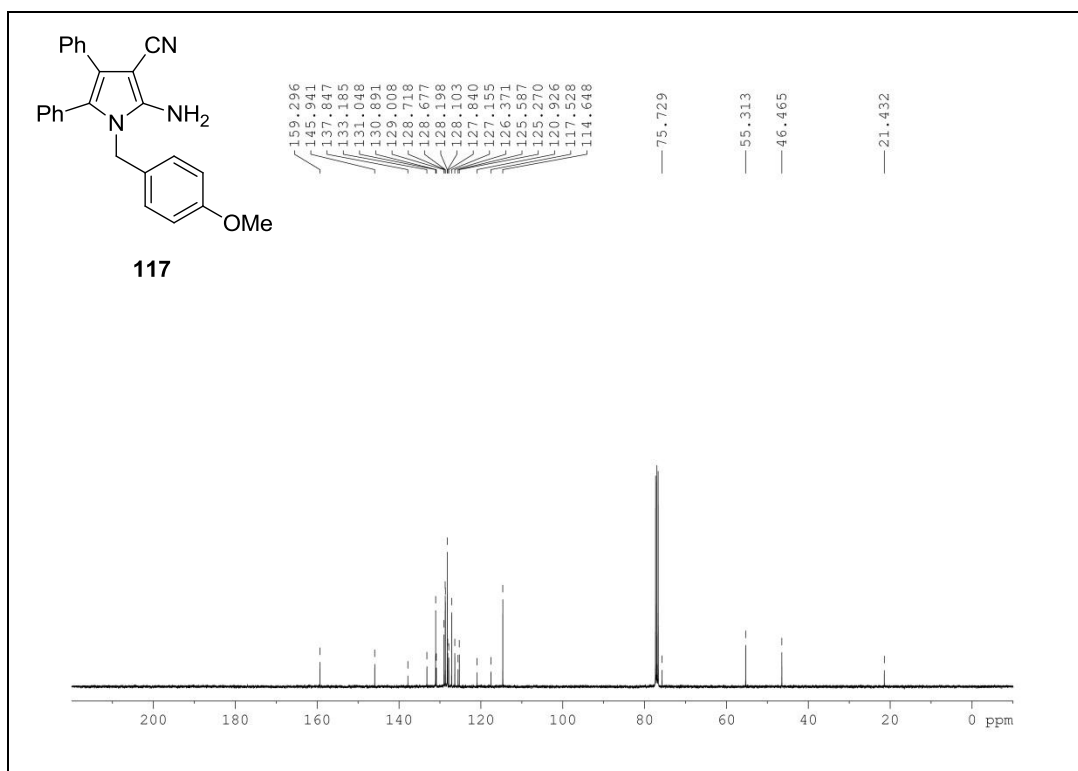


Figure 3.14: The ^{13}C NMR (100 MHz, CDCl_3) spectrum of **117**. ^{13}C signal at δ 21.4, 125.3, 128.2, 129.0 and 137.8 ppm are due to a toluene impurity in the sample, and the triplet at δ 77.0 ppm is due to CDCl_3 .

On the contrary, none of the aforementioned characteristic ^1H and ^{13}C NMR signals of **117** were present in the ^1H and ^{13}C NMR spectra of pyrrole **109** (Figures 3.15 and 3.16, respectively). Instead, a broad singlet at δ 10.81, which appears in the ^1H NMR spectrum of **109**, corresponds to the N-H proton of the deprotected pyrrole.¹⁶ In addition, the presence of an additional N-H stretching band at 3373.0 cm^{-1} in the IR spectrum of **109** suggests that it corresponds to the deprotected pyrrole N-H bond of the compound, therefore also confirming that the deprotection reaction of **117** did occur (Figure 3.17).²⁸

The structural identity of **109** in terms of its molecular weight was confirmed by its negative mode HRMS analysis (Figure 3.18). The most intense peak in the spectrum was found to have a m/z ratio of 258.1047, that corresponds to the $[\text{M} - \text{H}]^-$ ion of the deprotected pyrrole (Figure 3.18). This observed m/z value also suggests a chemical formula of $\text{C}_{17}\text{H}_{12}\text{N}_3$ and has a mass measurement error of 1.0 mDa or 3.9 ppm from its calculated m/z value of 258.1037.

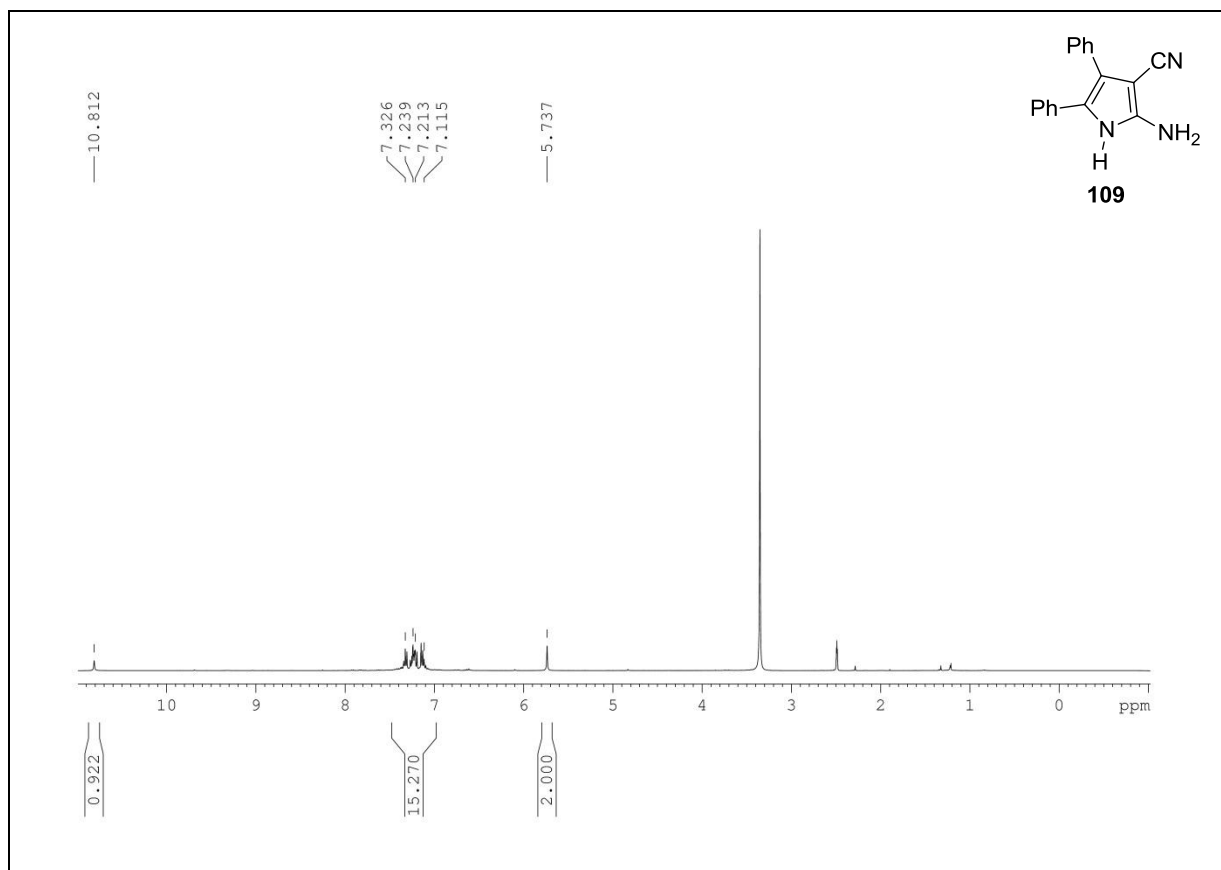


Figure 3.15: The ¹H NMR (400 MHz, DMSO-*d*₆) spectrum of **109**. A quintet at δ 2.49 is due to DMSO-*d*₆. An intense singlet at δ 3.35 ppm is due to water in the sample.

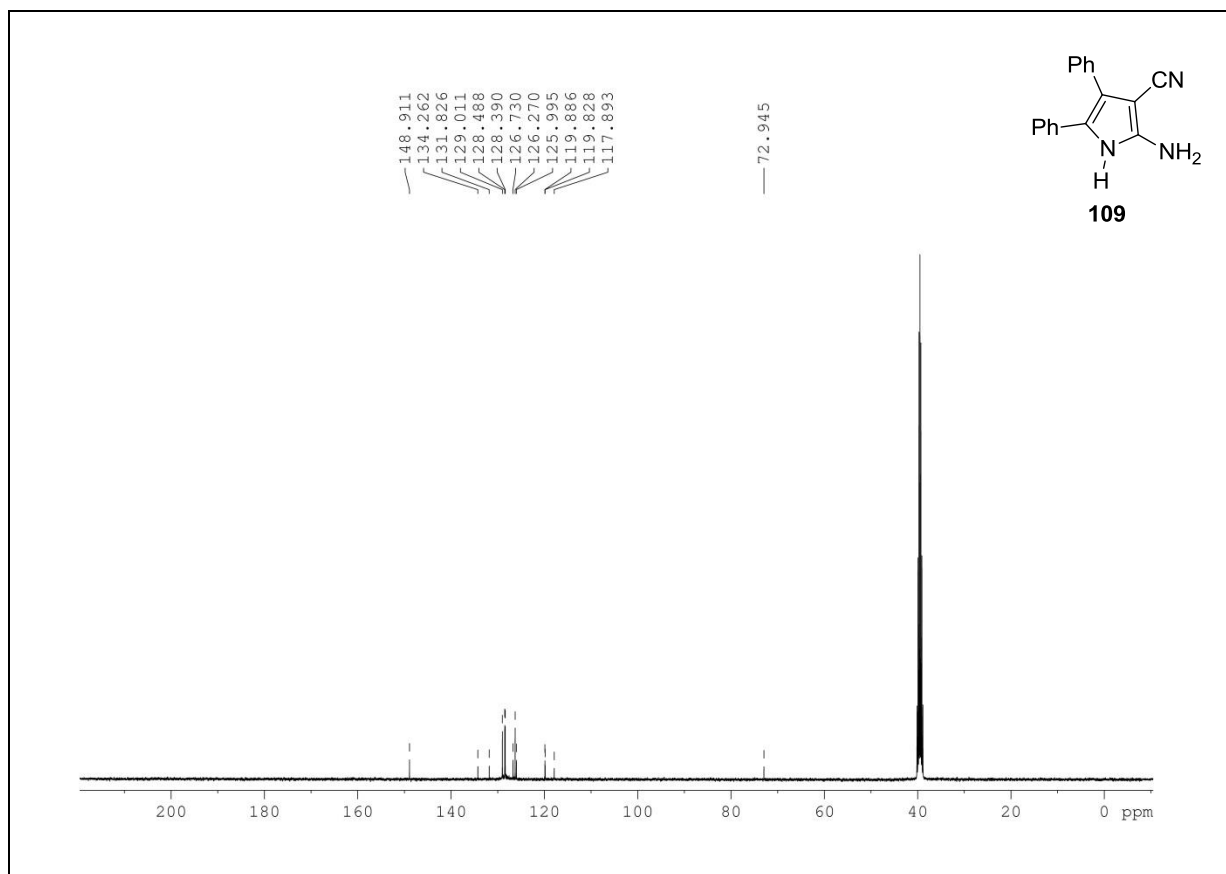


Figure 3.16: The ^{13}C NMR (100 MHz, $\text{DMSO-}d_6$) spectrum of **109**. A septet at 39.5 ppm is due to $\text{DMSO-}d_6$.

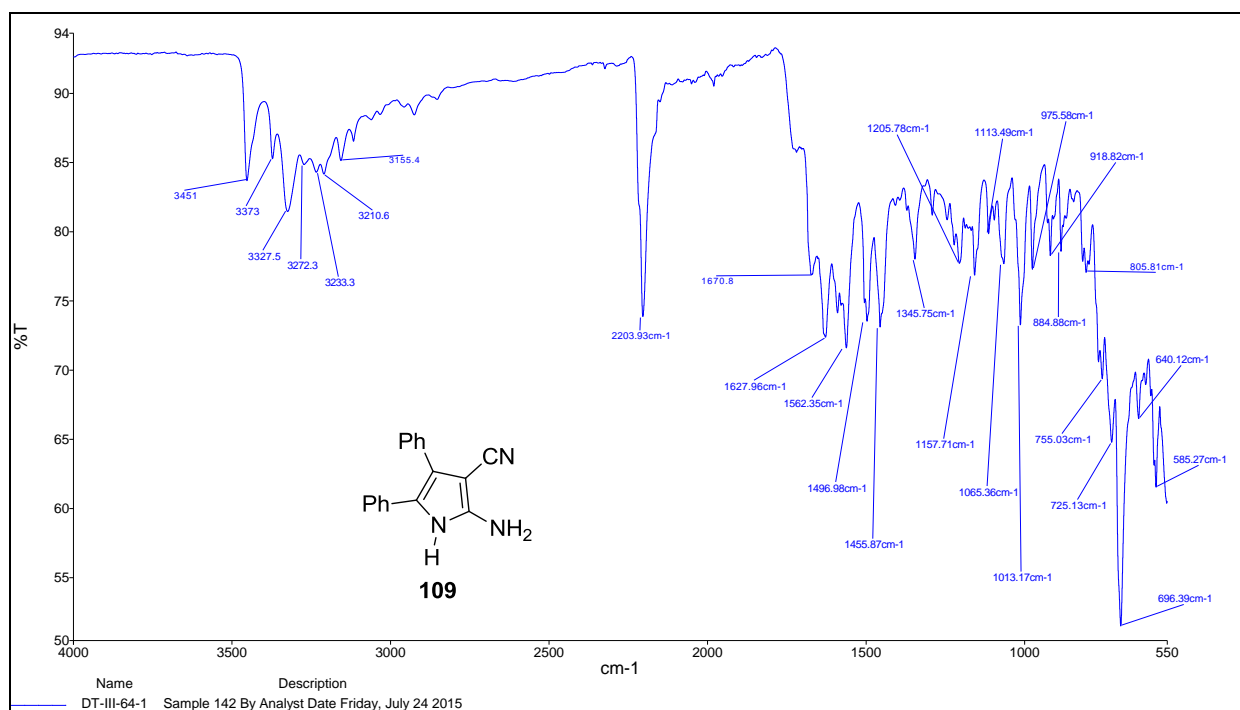


Figure 3.17: The IR spectrum of **109** (neat sample).

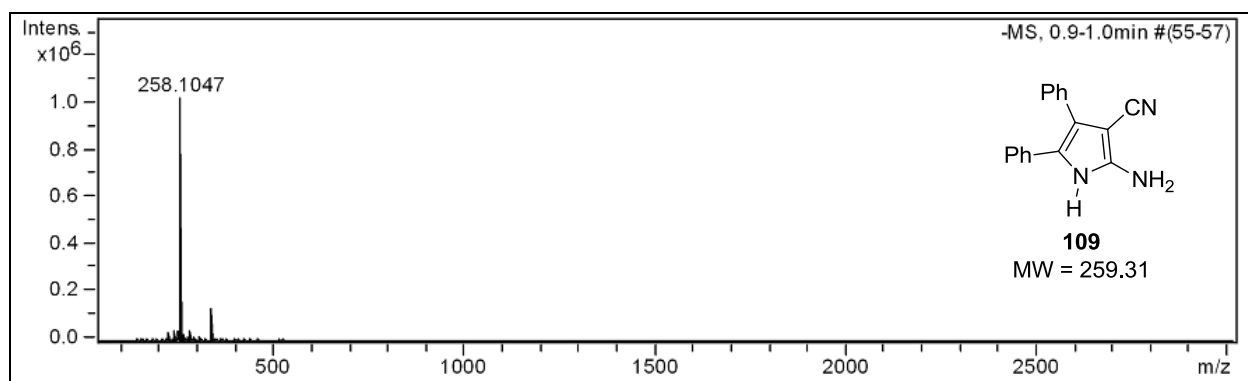
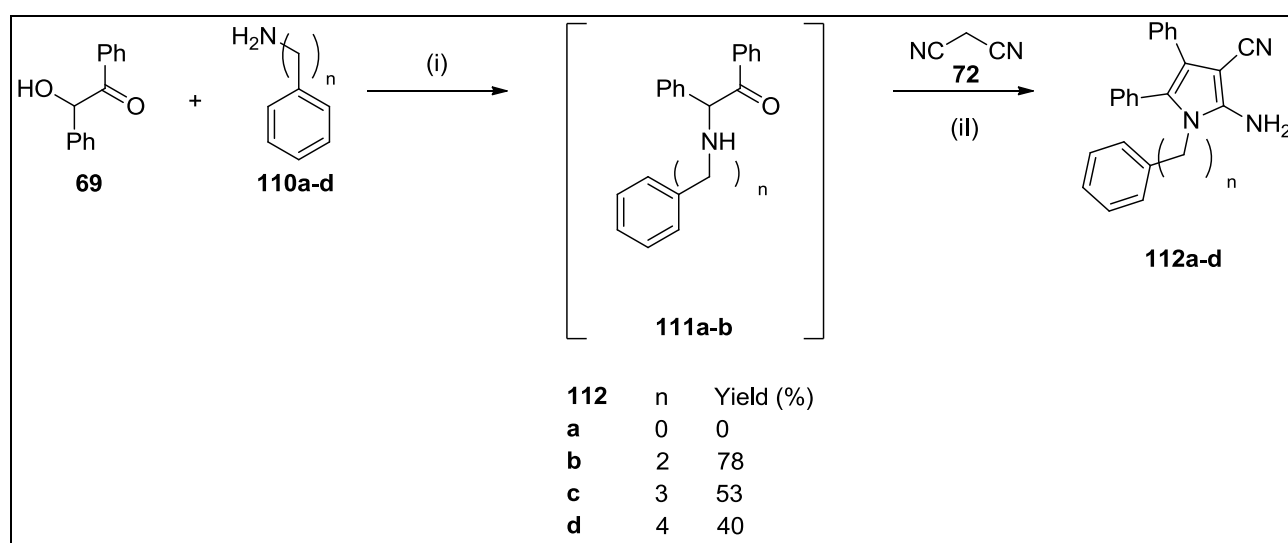
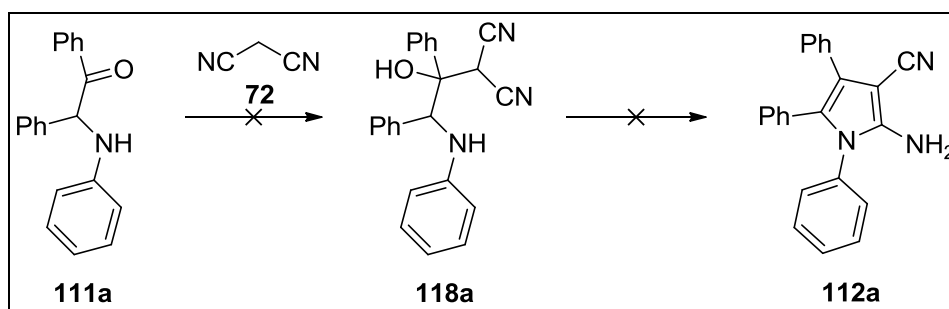


Figure 3.18: The negative mode HRMS spectrum of **109**.

All of the pyrrole derivatives with carbon chain lengths $n = 2, 3$ and 4 between the pyrrole ring nitrogen and the phenyl ring (**112b-d**), except derivative **112a** ($n = 0$) were successfully synthesised in good to moderate yields (Scheme 3.14). Instead, the corresponding α -aminoketone intermediate **111a** of derivative **112a** was fully recovered from the reaction mixture. This may be due to α -aminoketone **111a** not being nucleophilic and basic enough to facilitate further nucleophilic addition and elimination steps, that are both essential for the formation, cyclisation and aromatisation of pyrrole **112a** (Scheme 3.15).

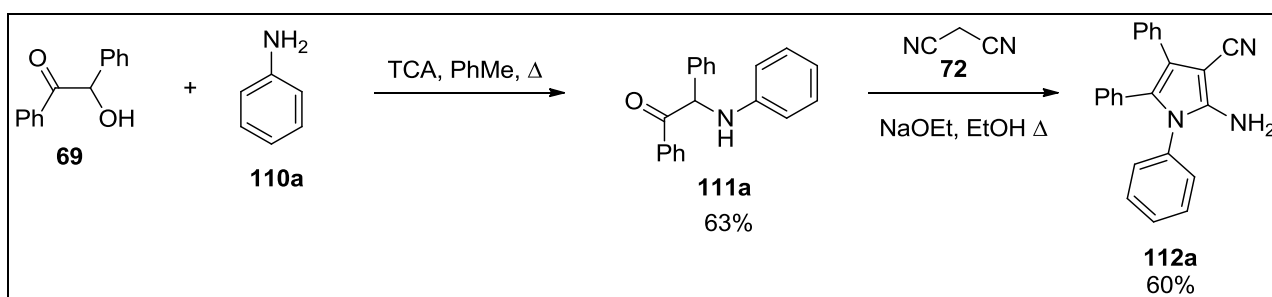


Scheme 3.14: The syntheses of pyrrole derivatives **112a-d**, with varying chain lengths between the pyrrole nitrogen and phenyl ring.

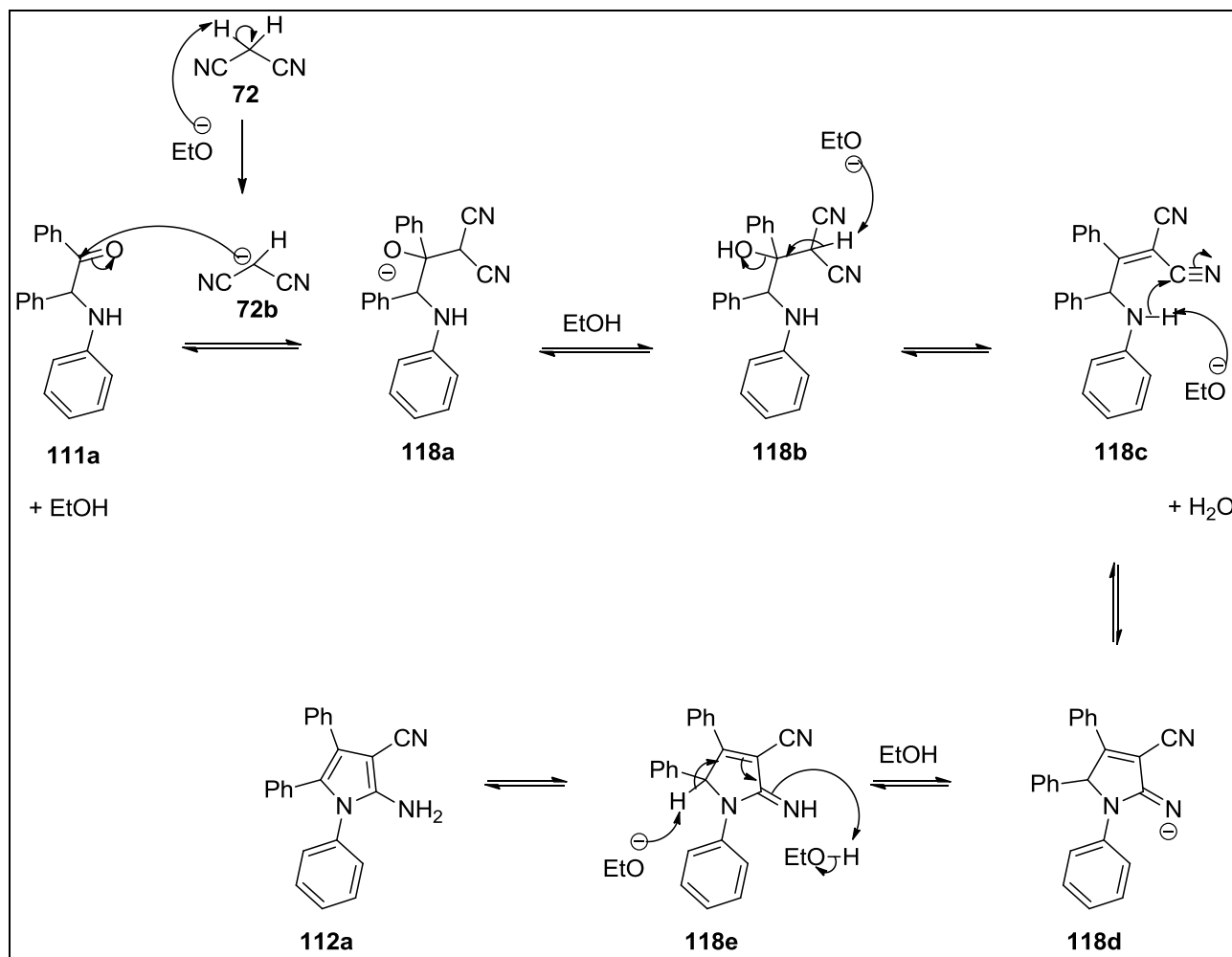


Scheme 3.15: The unsuccessful nucleophilic addition, cyclisation and aromatisation of α -aminoketone **111a** to pyrrole **112a**.

A strong base, such as sodium ethoxide is thus required to convert the α -aminoketone **111a** to the pyrrole product **112a**. The addition of sodium ethoxide into the reaction mixture, as suggested by Roth and Eger finally afforded pyrrole **112a** in a moderate yield of 60% (Scheme 3.16)²⁹. The role of sodium ethoxide in the conversion of α -aminoketone **111a** to pyrrole **112a** is illustrated in Scheme 3.17.



Scheme 3.16: The successful sodium ethoxide-catalysed synthesis of pyrrole **107a**, as suggested by Roth and Eger²⁹.



Scheme 3.17: The proposed mechanism for the conversion of α -aminoketone **111a** to pyrrole **112a**, with the utility of sodium ethoxide as the general base catalyst.

The presence of two N-H stretching bands at 3473.5 and 3384.4 cm^{-1} , as well as a cyano, C \equiv N stretching band at 2199.60 cm^{-1} in the IR spectrum of **112a** confirmed the amino and cyano functional groups of the compound (Figure 3.19). Moreover, the disappearance of the α -aminoketone carbonyl stretching peak at 1670.5 cm^{-1} also confirmed the successful conversion of **111a** to **112a** (the IR spectrum of **111a** is shown in Figure 3.20 as a comparison to that of **112a**).³⁰ In addition, the positive mode HRMS analysis of **112a** had detected a molecular ion peak with a m/z ratio of 358.1316, which corresponds to the $[\text{M} + \text{Na}]^+$ ion of the pyrrole (spectrum not shown). The experimental m/z value suggests a chemical formula of C₂₃H₁₇N₃Na and has a mass error measurement of 0.10 mDa or 0.28 ppm from its calculated m/z value of 358.1315.

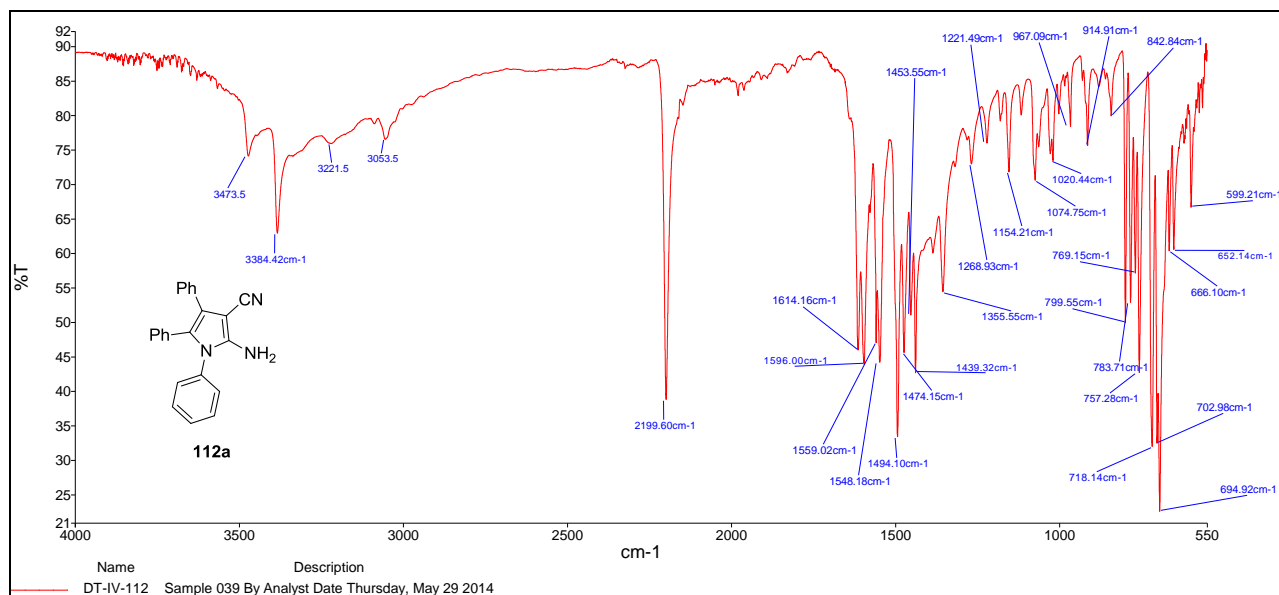


Figure 3.19: The IR spectrum of pyrrole **112a** (neat sample).

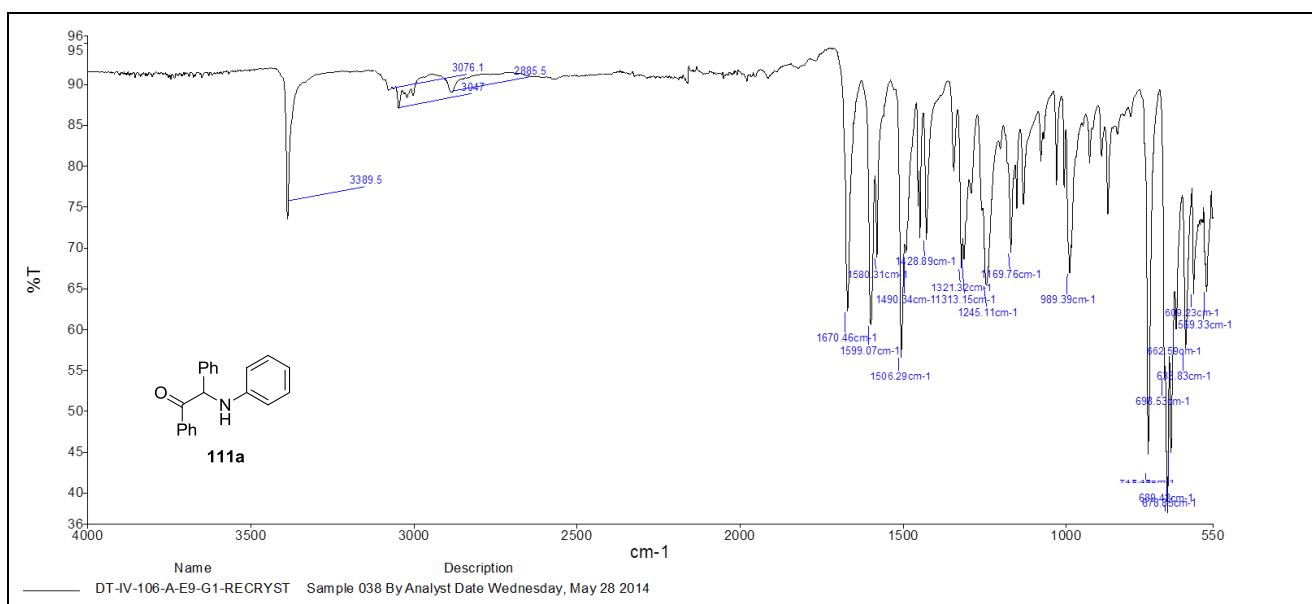


Figure 3.20: The IR spectrum of α -aminoketone **111a** (neat sample).

The structural identities of the rest of the pyrrole derivatives of this series, **112b-d** were confirmed by NMR (¹H and ¹³C) and IR spectroscopy, as well as LRMS and HRMS. The varying carbon chain lengths between the pyrrole ring nitrogen and phenyl ring of derivatives **112b-d** were observed in the aliphatic region of their ¹H and ¹³C NMR spectra. The ¹H and ¹³C NMR spectra of **112b** are shown as representative NMR spectra of the rest of the pyrrole series in Figure 3.21 and 3.22, respectively.

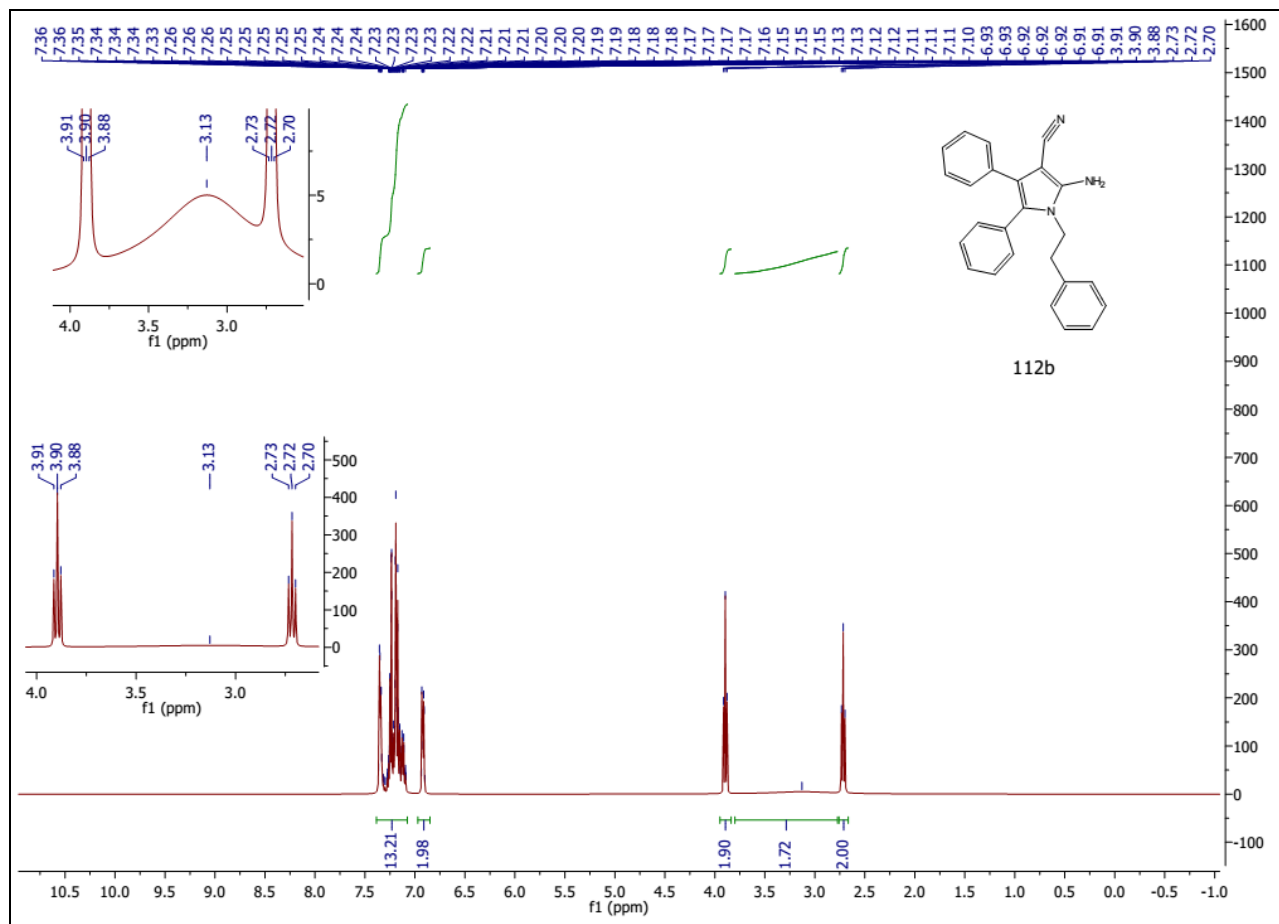


Figure 3.21: The ¹H NMR spectrum (400 MHz, CDCl₃) of **112b**. The protons of the *N*-phenethyl side chain of **112b** (NCH₂CH₂) are shown to resonate as a pair of two-proton triplets at δ 2.72 and 3.90 ppm.

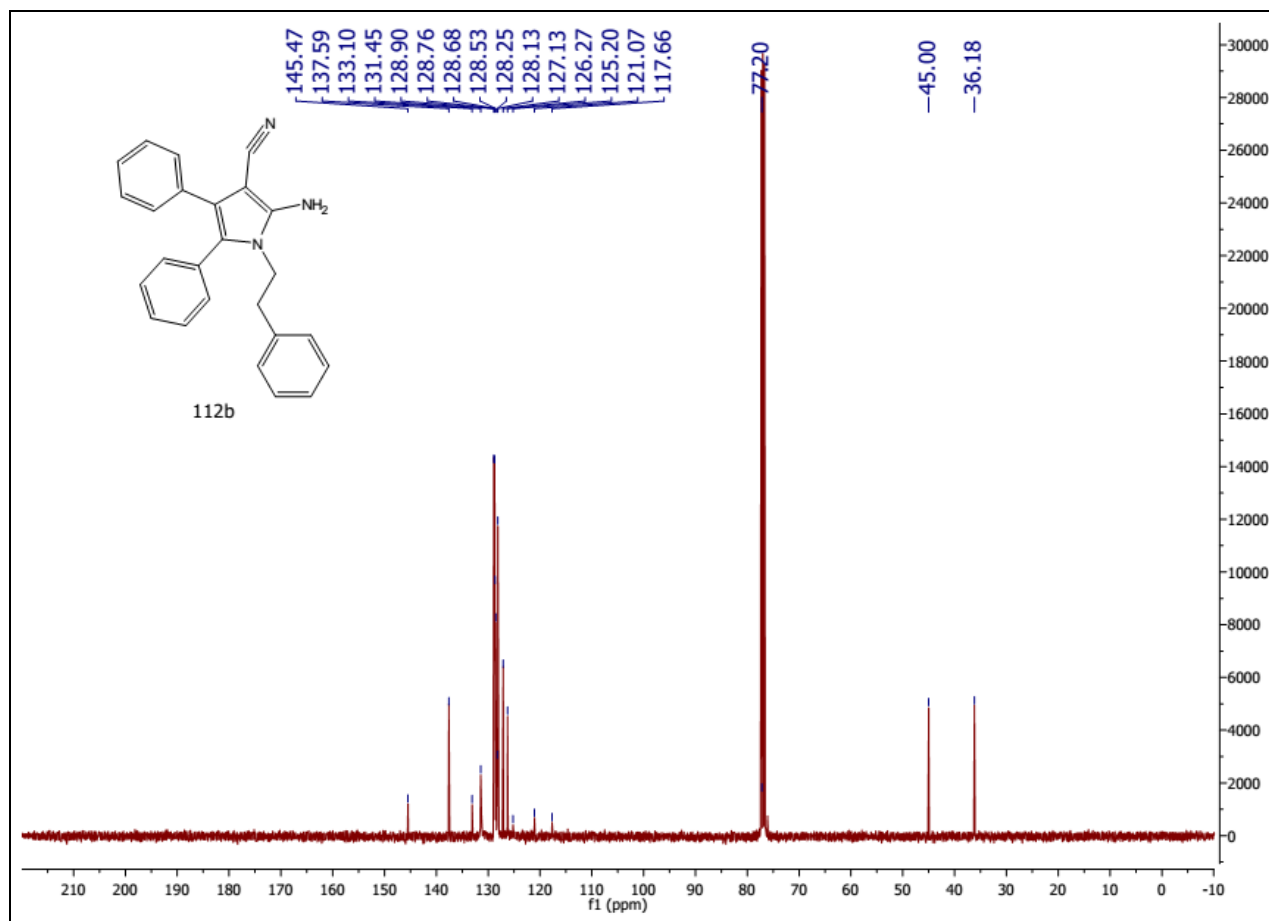
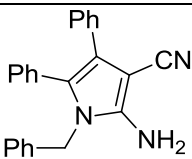
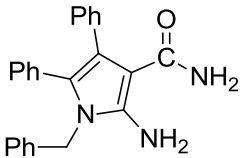
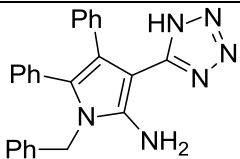
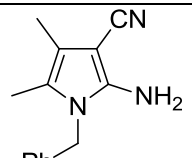
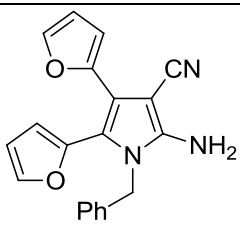
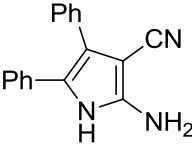
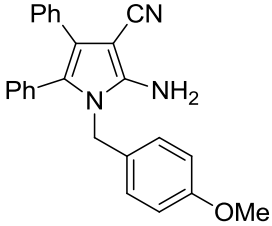


Figure 3.22: The ^{13}C NMR spectrum (100 MHz, CDCl_3) of **112b**. The 3-carbonitrile carbon ($\text{C}\equiv\text{N}$) and the two carbon atoms of the *N*-phenethyl side chain of **112b** (NCH_2CH_2) are shown to resonate at δ 117.7, 45.0 and 36.2 ppm, respectively. The triplet at δ 77.0 is due to CDCl_3 .

3.3 b) Enzymatic kinetic study

The synthetic pyrrole derivatives **104**, **105**, **108a** and **108b**, **109**, **112a-d** and **117** were screened against IMP-1, and the results are presented in Tables 3.3 and 3.4. The kinetic assay results showed that replacement of the 3-cyano group of pyrrole **65** with an amide group led to a total loss of inhibitory activity for carboxamide **104**. In addition, substitution of the cyano group with a tetrazole ring resulted in a 67-76% decrease in inhibitory potency across all inhibitor concentrations tested for **105**. These two observations demonstrate the crucial role of the 3-cyano group of pyrrole **65** in maintaining IMP-1 inhibitory activity of the pyrrole.

Table 3.3: The percentage inhibition of pyrrole derivatives **104**, **105**, **108a**, **b**, **109** and **117** against IMP-1 (10 nM, containing BSA at a final conc. of 20 $\mu\text{g mL}^{-1}$), at pH 7.0 and 25 $^{\circ}\text{C}$, with CENTA (20 μM) as the substrate.

Inhibitor	Molecular structure	Percentage inhibition (%)		
		Inhibitor concentration		
		5 μM	10 μM	20 μM
65^a		23.2 \pm 4.8	26.0 \pm 2.7	54.7 \pm 2.8
104		0	0	1.0 \pm 3.4 ^b
105		7.3 \pm 2.3	8.7 \pm 1.3	13.1 \pm 1.2
108a		3.0 \pm 1.4	2.3 \pm 3.3	2.8 \pm 1.5
108b		35.6 \pm 2.7	23.2 \pm 3.9	44.2 \pm 2.0
109		3.2 \pm 2.1	12.0 \pm 2.6	7.9 \pm 2.6
117		7.7 \pm 2.9	20.1 \pm 4.3	39.3 \pm 2.2

^aPyrrole **65** is shown for comparison. ^bThe inhibitor concentration was 25 μM .

Direct ligand-metal ion interactions observed in 3D structures of inhibitor-enzyme complexes are associated with potent, competitive inhibitors of MBLs (Section 1.11).³¹⁻³⁴ However, the MVD computational model of tetrazole **105** bound to IMP-1, which predicted plausible ionic interactions between the negatively charged tetrazole ring and the Zn²⁺ ions (Figure 3.2), does not reflect the observed inhibitory activity of the ligand.

Conversely, the Glide *in silico* model of **105** complexed with IMP-1 proposed that the tetrazole ring doesn't bind in the vicinity of the metal centres. Instead, it interacts with Lys161 (224) *via* a π -cation interaction (average distance atom-atom 6.1 Å) (Figure 3.23)*. The model also predicted a hydrogen bond interaction between N-3 of the tetrazole ring and the terminal hydroxyl group of Ser198 (N-O distance 3.34 Å). This demonstrates the inconsistency in molecular docking results obtained from different programs and the possibility of low correlation between the docking results and experimental kinetic assay results.³⁵ Therefore, an X-ray crystal structure of pyrrole **65** bound with IMP-1 is needed to determine the actual binding mode of the 3-cyano group with the enzyme.

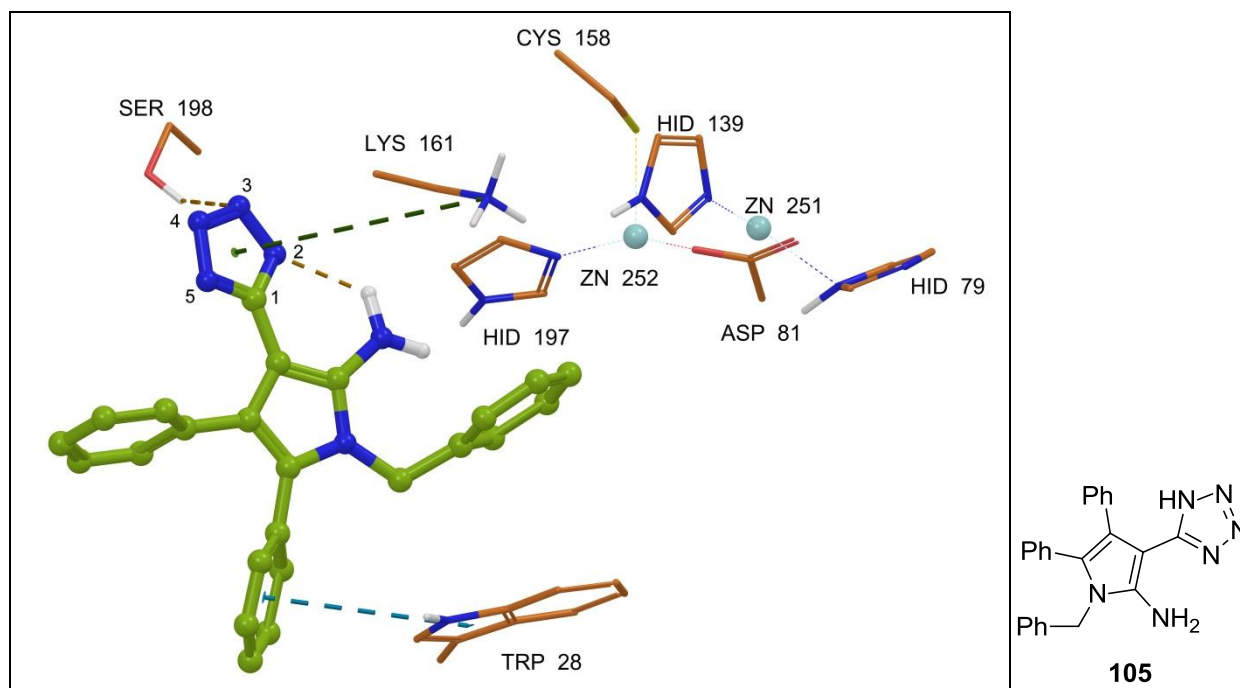


Figure 3.23: The Glide computational model of **105** complexed with IMP-1. Atom colours: carbon on ligand in green, carbon on IMP-1 in orange, nitrogen in blue, oxygen in red and hydrogen in white. The Zn²⁺ ions are shown as turquoise spheres, with Zn251 and Zn252 denoting Zn1 and Zn2, respectively. The dashed, orange, green and blue lines represent hydrogen bond, π -cation and π - π stacking interactions, respectively.

Replacement of the vicinal 4,5-diphenyl side chains of pyrrole **65** with dimethyl side chains resulted in a significant loss in IMP-1 inhibitory activity for example **108a**. This observation is in agreement with the MVD *in silico* model and MolDock score of **108a** bound with IMP-1 (Figure 3.3 and Table 3.2), which suggested that the ligand has fewer hydrophobic contacts with the L3 loop, and no interactions with the enzyme active site. On the contrary, substitution of the vicinal 4,5-diphenyl side chains of pyrrole **65** with di-2-furanyl side chains, which is a bioisostere of the phenyl ring, led to maintenance of inhibitory activity of **108b**.³⁶ The observed inhibitory activity agrees well with the MolDock score of **108b**-IMP1, which is comparable in magnitude with that of pyrrole **65** (Table 3.2). These observations highlight the importance of the 4,5-diphenyl side chains in maintaining IMP-1 inhibitory activity of pyrrole **65**.

Removal of the *N*-benzyl side chain also led to a significant loss of IMP-1 inhibitory activity, as observed for the deprotected pyrrole **109**. On the contrary, the *N*-4-methoxybenzyl derivative, **117** exhibited relatively similar inhibitory activity as pyrrole **65**, particularly at an inhibitor concentration of 10 μ M. These observations imply that the *N*-benzyl side chain is also required in retaining IMP-1 inhibitory activity of pyrrole **65**. In addition, Glide computational modelling of **117** bound in the enzyme active site suggested that the 4-methoxy moiety of the ligand binds in the vicinity of the Zn2 site, with O-Zn distance of 2.00 Å (Figure 3.24)*.

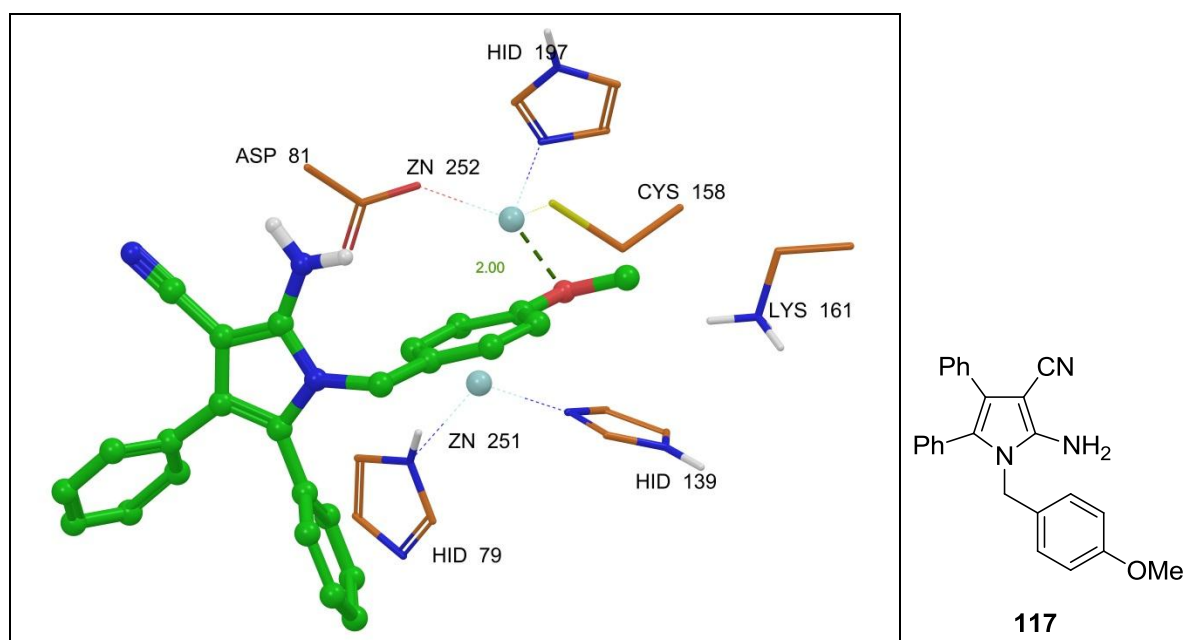
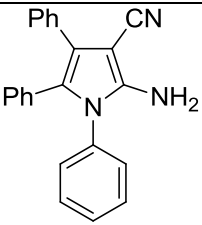
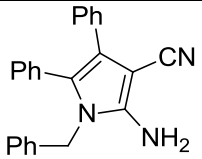


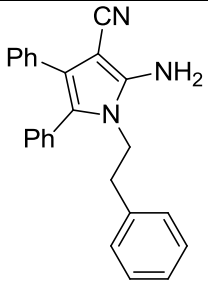
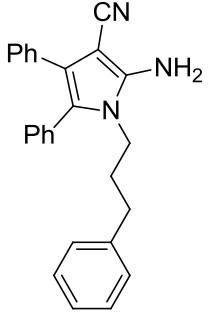
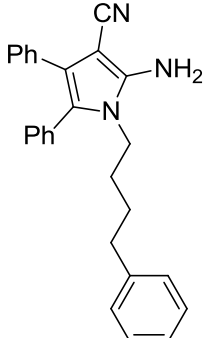
Figure 3.24: The Glide *in silico* model of **117** bound in the active site of IMP-1. Atom colours: carbon on ligand in green, carbon on IMP-1 in orange, nitrogen in blue, oxygen in red and hydrogen in white. The Zn²⁺ ions are shown as turquoise spheres, with Zn251 and Zn252 denoting Zn1 and Zn2, respectively.

*Glide work was carried out by Ajit Kandale, a PhD student with the McGeary group.

Based on the kinetic assay results shown in Table 3.3, the introduction of spacers of various lengths between the pyrrole ring nitrogen and phenyl ring didn't result in any enhancement of IMP-1 inhibitory activity for examples **107b-d**. Furthermore, omission of the benzylic carbon between the pyrrole ring nitrogen and phenyl ring led to a significant loss in inhibitory activity, as observed for example **107a**. These observations further substantiate the earlier finding that the *N*-benzyl side chain is essential for maintenance of IMP-1 inhibitory activity of pyrrole **65**.

Table 3.4: The percentage inhibition of pyrrole derivatives **112a-d** and **65** against IMP-1 (0.1 nM, containing BSA at a final conc. of 20 µg mL⁻¹), at pH 7.0 and 25 °C, with CENTA (70 µM) as the substrate.

Inhibitor	Molecular structure	Percentage inhibition (%)		
		Inhibitor concentration		
		5 µM	10 µM	20 µM
112a		0	0	6.6±2.7
65^a		6.4±1.3	17±1.0	27±1.9

112b		0	4.8±0.77	16±1.5
112c		3.5±1.9	4.1±0.81	10±1.3
112d		4.2±0.86	8.7±1.1	18±1.4

^aPyrrole **65** is shown for comparison.

3.4 Conclusion

The 3-carbonitrile functional group of pyrrole **65** was successfully hydrolysed to a carboxamide group, **104**, and derivatised to a tetrazole ring, **105**, using aluminium triazide (**113**) as the azide reagent.

All *N*-debenzylation attempts of pyrrole **65** were unsuccessful. The derivatisation of the *N*-benzyl moiety to a more labile group, such as an *N*-4-methoxybenzyl group, was thus necessary to facilitate deprotection of the pyrrole.

Kinetic assay results of **104** and **105** against IMP-1 showed that the 3-cyano group of pyrrole **65** is crucial in maintaining IMP-1 inhibitory potency of the pyrrole. An X-ray structure of pyrrole **65** co-crystallised with the enzyme is therefore needed to ascertain the actual binding mode of the 3-cyano group with the enzyme.

The vicinal 4,5-diphenyl side chains of pyrrole **65** are also important for retaining IMP-1 inhibitory potency of the inhibitor, as modification of the side chains from diphenyl to dimethyl side chains resulted in complete loss of activity. Hydrophobic contacts between the mobile L3 loop of the enzyme with pyrrole **65** via the diphenyl side chains is thus vital for the observed inhibitory potency of the compound.

The *N*-benzyl side chain of pyrrole **65** is also another essential pharmacophore of the inhibitor, as kinetic assay results revealed that removal of the chain or omission of the benzylic carbon led to significant decrease in IMP-1 inhibitory activity. This was further substantiated by the finding that the introduction of spacers of various lengths between the pyrrole ring nitrogen and phenyl ring didn't result in enhancement of IMP-1 inhibitory activity.

The only two pyrrole derivatives in this series which demonstrated comparable IMP-1 inhibitory activity with pyrrole **65** are derivatives **108b** and **117**. Glide computational modelling predicted that the 4-methoxy group of **117** binds in the vicinity of the metal ions. Various substituents, such as halides or a nitro group on the *N*-benzyl ring could be explored for future SAR study of pyrrole **65**. Furthermore, the vicinal 4,5-diphenyl rings could also be substituted with bulky groups, such as a methoxy or a *t*-butyl group to increase hydrophobic contacts with the enzyme.

3.5 Experimental

3.5 a) General synthetic, spectroscopic and spectrometric experimental

Refer to Section 2.5 a.

3.5 b) Preparation of 2-Amino-1-benzyl-4,5-diphenyl-1*H*-pyrrole-3-carbonitrile (65**)**

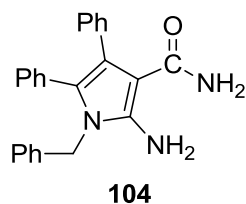
Refer to Section 2.5 b.

3.5 c) General procedure for the syntheses of 2-aminopyrrole-3-carbonitrile derivatives **108a,b**, **117** and **112b-d**.^{21,37}

A mixture of the appropriate α -hydroxyketone (10 mmol), the appropriate benzylamine (10 mmol) and trichloroacetic acid (0.08 g, 0.5 mmol) in dry toluene (15 ml) was refluxed using a Dean-Stark apparatus for 2-4 h under Ar, after which it was cooled to room temperature. The reaction mixture turned yellow as the reaction progressed. Malononitrile (0.66 g, 10 mmol), followed by pyridine (81 μ l, 0.080 g, 1.0 mmol) was added to the cooled mixture and reflux was resumed overnight under Ar. The mixture was cooled to room temperature, and filtered. The solid product obtained was washed successively with cold toluene (5 x 25 ml), followed by cold petroleum ether (5 x 25 ml), and purified by either recrystallisation or silica gel column chromatography.

3.5 d) Experimental data of synthesised compounds

2-Amino-1-benzyl-4,5-diphenyl-1*H*-pyrrole-3-carboxamide (**104**)⁷

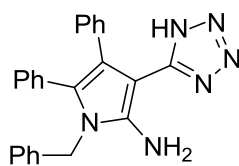


Pyrrole **65** (0.31 g, 0.90 mmol) was added to a mixture of polyphosphoric acid (6.4 g phosphoric oxide and 4.5 ml phosphoric acid) and phosphoric acid (3.6 g, 1.9 ml). The reaction mixture was heated at 120 °C for 5 h, after which it was quenched with a mixture of ice and 25% ammonia (20 ml). The addition of ammonia to the mixture was continued until a pH of 7 was achieved. The precipitate obtained was then filtered off and recrystallised from EtOAc to afford the title compound as a black semi-solid (0.26 g, 79%). R_f : 0.24 (30% EtOAc in PE). ^1H NMR (400 MHz, CDCl_3) δ (ppm): 4.91 (br s, 2H, NCH_2Ph), 5.06 (br s, 2H, D_2O exchangeable protons), 6.98-7.38 (m, 15H, Ar-H). ^{13}C (100 MHz, CDCl_3) δ (ppm): 46.6 (NCH_2Ph), 95.6 (CCONH_2), 119.3 (Ar-C), 125.8 (Ar-C), 125.9 (Ar-CH), 127.1 (Ar-CH), 127.7 (Ar-CH), 128.1 (Ar-CH), 128.4 (Ar-CH), 129.1 (Ar-CH), 130.6 (Ar-CH), 131.1 (Ar-CH), 135.3 (Ar-C), 136.6 (Ar-C), 146.3 (C-NH₂), 168.7 (C=O). LRMS: m/z 368.1 [$\text{M} + \text{H}$]⁺. HRMS, found: m/z 368.1758, $\text{C}_{24}\text{H}_{22}\text{N}_3\text{O}$ requires 368.1757. IR ν_{max} (cm^{-1}): 3165.1 (N-H stretch), 3061.2, 1670.7 (C=O stretch), 1597.5, 1495.9, 1448.7, 1410.9, 1274.4, 1209.9, 1176.1, 1105.7, 1069.8, 1027.9, 1002.0.

Preparation of polyphosphoric acid³⁸

A 1.8 parts by weight of phosphoric oxide (6.4 g) was dissolved in a 2.0 part by weight of phosphoric acid (7.6 g, 4.5 ml) at 160 °C.

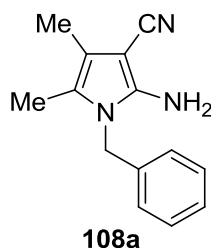
1-Benzyl-4,5-diphenyl-3-(1*H*-tetrazol-5-yl)-1*H*-pyrrol-2-amine (**105**)¹³



105

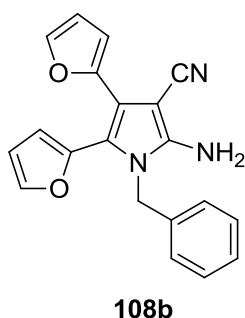
Trimethylsilyl azide (0.23 ml, 0.20 g, 1.7 mmol) was cautiously added to trimethylaluminium (2.0 M in toluene, 0.85 ml, 1.7 mmol) at 0 °C. A solution of pyrrole **65** (0.45 g, 1.3 mmol) in toluene (7 ml) was added dropwise to the resulting clear solution at 0 °C. The reaction mixture was stirred at rt for 30 min and then overnight at 80 °C. The reaction mixture was cooled to 0 °C and subsequently poured into a biphasic mixture of 6 ml of EtOAc and 6 ml of 6 M HCl. The aqueous layer was extracted with EtOAc (2 x 40 ml) and the organic layers were combined, washed with brine, dried over anhydrous Na₂SO₄ and concentrated *in vacuo* to afford a golden-coloured solid (0.59 g). The crude product was finally subjected to silica gel column chromatography [EtOAc/PE (3:17) → EtOAc/PE (7:13)] to afford the title compound as a light brown solid (0.13 g, 26%), m.p.: 143.5-145.6 °C (with degradation). *R*_f: 0.52 (30% EtOAc in PE). ¹H NMR (400 MHz, CDCl₃) δ (ppm): 5.01 (s, 2H, NCH₂Ph), 5.09 (br s, 2H, NH₂, D₂O exchangeable), 7.06-7.08 (m, 2H, Ar-H), 7.15-7.18 (m, 5H, Ar-H), 7.23-7.26 (m, 2H, Ar-H), 7.29-7.40 (m, 6H, Ar-H), 10.79 (br s, 1H, tetrazole NH, D₂O exchangeable). ¹³C NMR (100 MHz, CDCl₃) δ (ppm): 47.1 (NCH₂Ph), 86.8 (C-CH=N), 118.6 (Ar-C), 125.9 (Ar-CH), 127.0 (Ar-C), 127.5 (Ar-CH), 127.7 (Ar-CH), 127.9 (Ar-CH), 128.3 (Ar-CH), 129.27 (Ar-CH), 129.29 (Ar-CH), 130.3 (Ar-CH), 130.5 (Ar-CH), 130.6 (Ar-C), 134.8 (Ar-C), 136.4 (Ar-C), 142.3 (C-NH₂), 151.3 (NH-CH=N); LRMS: *m/z* 391.1 [M - H]⁻. HRMS, found: *m/z* 391.1685, C₂₄H₁₉N₆ requires 391.1677. IR ν_{max} (cm⁻¹): 3421.8 (N-H stretch), 3304.8 (N-H stretch), 3217.0, 3165.1, 3061.2, 3032.0, 1683.8, 1573.8, 1497.0, 1481.1, 1453.4, 1443.9, 1357.7, 1270.6, 1170.5, 1070.7, 1001.0.

2-Amino-1-benzyl-4,5-dimethyl-1*H*-pyrrole-3-carbonitrile (**108a**)



Acetoin (0.88 g, 10 mmol) and benzylamine (1.1 ml, 1.1 g, 10 mmol) were used for the synthesis of the title compound, which was obtained as a dark brown solid from silica gel column chromatography of the crude product [EtOAc/PE (1:4) → EtOAc/PE (3:7)] (2.3 g, 61%), m.p.: 72.3-74.9 °C. R_f : 0.52 (30% EtOAc in PE, visible as a blue spot under 254 nm). ^1H NMR (400 MHz, CDCl_3) δ (ppm): 1.99 (d, 3H, $J = 0.5$ Hz, CH_3), 2.03 (d, 3H, $J = 0.6$ Hz, CH_3), 3.59 (br s, 2H, NH_2 , exchangeable with D_2O), 4.90 (s, 2H, NCH_2Ph), 6.96-6.99 (m, 2H, Ar-H), 7.26-7.34 (m, 3H, Ar-H). ^{13}C NMR (100 MHz, CDCl_3) δ (ppm): 9.5 (CCH_3), 10.0 (CCH_3), 45.9 (NCH_2Ph), 77.2 (C-CN), 113.5 (C), 117.7 ($\text{C}\equiv\text{N}$), 119.2 (C), 125.7 (Ar-CH), 127.8 (Ar-CH), 129.1 (Ar-CH), 136.3 (Ar-C) 143.2 (C-NH_2); LRMS: m/z 226.1 [$\text{M} + \text{H}$] $^+$. HRMS, found: m/z 226.1344, $\text{C}_{14}\text{H}_{16}\text{N}_3$ requires 226.1339. IR ν_{max} (cm^{-1}): 3418.5 (N-H stretch), 3330.8 (N-H stretch), 3233.3, 2202.1 ($\text{C}\equiv\text{N}$ stretch), 1650.9, 1603.3, 1564.2, 1509.2, 1496.2, 1455.0, 1441.9, 1354.6, 1303.7, 1244.4, 1176.6, 1146.9, 1016.4.

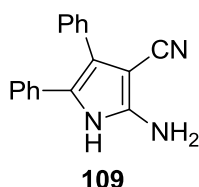
2-Amino-1-benzyl-4,5-di(furan-2-yl)-1*H*-pyrrole-3-carbonitrile (**108b**)



Furoin (1.92 g, 10.0 mmol) and benzylamine (1.1 ml, 1.1 g, 10 mmol) were used for the synthesis of the title compound, which was obtained as a dark brown solid from silica gel column chromatography of the crude product [EtOAc/PE (1:4) → EtOAc/PE (3:7)] (1.9 g, 59%), m.p.: 162.0-165.4 °C. R_f : 0.54 (30% EtOAc in PE, visible as a blue spot under UV). ^1H NMR (400 MHz, CDCl_3) δ (ppm): 3.91 (br s, 2H, NH_2 , D_2O exchangeable), 4.88 (s, 2H, NCH_2Ph), 6.34 (d, 2H, $J = 1.2$ Hz, furanyl-H), 6.43-6.46 (m, 2H, furanyl-H), 7.09-7.11 (m,

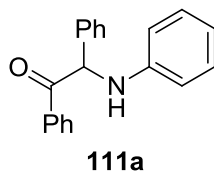
2H, Ar-H), 7.35-7.36 (m, 4H, Ar-H), 7.47 (dd, 1H, $J_1 = 0.8$ Hz, $J_2 = 1.8$ Hz, Ar-H). ^{13}C NMR (100 MHz, CDCl_3) δ (ppm): 47.4 (NCH₂Ph), 74.1 (C-CN), 106.6 (Ar-CH), 111.0 (Ar-CH), 111.1 (C), 113.1 (Ar-CH), 114.2 (Ar-C), 115.2 (C), 116.7 (C≡N), 126.3 (Ar-CH), 128.2 (Ar-CH), 129.2 (Ar-CH), 135.5 (C) 141.4 (Ar-CH), 143.3 (Ar-CH), 143.5 (C), 146.4 (C-NH₂), 147.3 (C); LRMS: m/z 352.1 [M + Na]⁺. HRMS, found: m/z 352.1055, C₂₀H₁₅N₃NaO₂ requires 352.1056. IR ν_{max} (cm⁻¹): 3454.2 (N-H stretch), 3327.5 (N-H stretch), 3269.0, 3236.6, 3210.6, 3152.1, 3116.4, 2200.1 (C≡N stretch), 1673.7, 1633.9, 1562.7, 1497.0, 1456.0, 1346.0, 1203.0, 1156.9, 1013.0.

2-Amino-4,5-diphenyl-1H-pyrrole-3-carbonitrile (**109**)²⁴



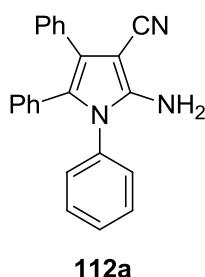
A solution of pyrrole **117** (0.30 g, 0.79 mmol) in anisole (5 ml) was added to a stirred suspension of aluminium chloride (0.53 g, 4.0 mmol) in anisole (5 ml) at 0°C for 5 mins. The reaction mixture was then heated at 120 °C for 17 h. Next, the reaction mixture was cooled to rt and poured into water (20 ml) and extracted with EtOAc (3 x 10 ml). The organic layers were collected and washed successively with saturated NaHCO₃ (10 ml), water (10 ml) and brine (10 ml), and dried over anhydrous Na₂SO₄. The excess EtOAc solvent was removed *in vacuo* and the resulting crude product (brown oil) was purified by silica gel column chromatography [EtOAc/PE (1:19) → EtOAc/PE (3:7)] to give the title compound as a black solid (0.075 g, 36%), m.p.: 98.5-99.0 °C. R_f : 0.21 (30% EtOAc in PE). ^1H NMR (400 MHz, DMSO-*d*₆) δ (ppm): 5.74 (br s, 2H, NH₂, D₂O exchangeable), 7.11-7.33 (m, 10H, Ar-H), 10.81 (br s, 1H, NH, D₂O exchangeable). ^{13}C NMR (100 MHz, DMSO-*d*₆) δ (ppm): 72.9 (C-CN), 117.9 (C≡N), 119.8 (Ar-C), 119.9 (Ar-C), 126.0 (Ar-CH), 126.3 (Ar-CH), 126.7 (Ar-CH), 128.4 (Ar-CH), 128.5 (Ar-CH), 129.0 (Ar-CH), 131.8 (Ar-C) 134.3 (Ar-C), 148.9 (C-NH₂); LRMS: m/z 258.1 [M - H]⁻. HRMS, found: m/z 258.1047, C₁₇H₁₂N₃ requires 258.1037. IR ν_{max} (cm⁻¹): 3451.0 (N-H stretch), 3373.0 (N-H stretch), 3327.5 (N-H stretch), 3272.3, 3233.3, 3210.6, 3155.4, 2203.9 (C≡N stretch), 1670.8, 1628.0, 1562.4, 1497.0, 1455.9, 1345.8, 1205.8, 1157.7, 1113.5, 1065.4, 1013.2.

1,2-Diphenyl-2-(phenylamino)ethanone (**111a**)



A mixture of benzoin (2.12 g, 10.0 mmol), aniline (0.90 ml, 0.93 g, 10 mmol) and trichloroacetic acid (0.08 g, 0.5 mmol) in dry toluene (20 ml) was refluxed using a Dean-Stark apparatus for 3 h (LRMS monitoring). The yellow solution was evaporated *in vacuo* to give a brown solid residue (3.3 g). Silica gel column chromatography [EtOAc/PE (1:19) → EtOAc/PE (7:93)] afforded the title compound as a brown solid (1.81 g, 63%), m.p.: 93.8-95.7 °C (lit. m.p. 98-99 °C).⁴⁰ *R*_f: 0.58 (30% EtOAc in PE). ¹H NMR (300 MHz, CDCl₃) δ (ppm): 6.03 (s, 1H, CHNH), 6.68-6.71 (m, 3H, Ar-H), 7.09-7.29 (m, 5H, Ar-H), 7.39-7.44 (m, 4H, Ar-H), 7.52 (tt, 1H, *J*₁ = 2.4 Hz, *J*₂ = 7.5 Hz), 7.95-7.98 (m, 2H, Ar-H). ¹³C NMR (75 MHz, CDCl₃) δ (ppm): 63.3 (CHNH), 114.3 (Ar-CH), 118.6 (Ar-C), 128.2 (Ar-CH), 128.3 (Ar-CH), 128.7 (Ar-CH), 128.9 (Ar-CH), 129.1 (Ar-CH), 129.2 (Ar-CH), 133.5 (Ar-CH), 134.9 (Ar-CH), 137.1 (Ar-C), 145.2 (Ar-C), 196.7 (C=O); LRMS: *m/z* 288.0 [M + H]⁺. IR *v*_{max} (cm⁻¹): 3389.5 (N-H stretch), 1670.5 (C=O stretch), 1599.1, 1580.3, 1506.3, 1490.3, 1428.9, 1321.3, 1313.2, 1245.1, 1169.8.

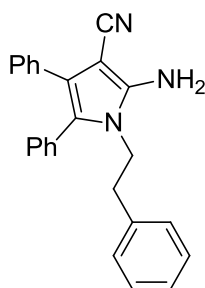
2-Amino-1,4,5-triphenyl-1*H*-pyrrole-3-carbonitrile (**112a**)²⁹



Malononitrile (0.18 g, 2.7 mmol) was added to a hot solution of α-aminoketone **111a** (0.78 g, 2.7 mmol) in absolute EtOH (6 ml). A solution of sodium (72 mg, 3.1 mmol) in absolute EtOH (3 ml) was then added dropwise to the mixture, and the mixture was heated under reflux for 18 h. The orange solid which had formed was filtered off and washed with EtOH (2 x 10 ml). Recrystallisation of the orange precipitate from MeOH afforded the title compound as an orange solid (0.55 g, 60%), m.p.: 242.4-246.6°C (literature 248-250°C).⁴¹ *R*_f: 0.27 (30% EtOAc in PE, visible as a blue spot under UV). ¹H NMR (400 MHz, CDCl₃) δ

(ppm): 4.15 (br s, 2H, NH₂), 6.87-6.90 (m, 2H, Ar-H), 7.02-7.08 (m, 3H, Ar-H), 7.13-7.29 (m, 7H, Ar-H), 7.33-7.39 (m, 3H, Ar-H). ¹³C NMR (100 MHz, CDCl₃) δ (ppm): 74.2 (C-CN), 117.4 (C≡N), 121.3 (Ar-C), 124.7 (Ar-C), 126.6 (Ar-CH), 127.0 (Ar-CH), 128.0 (Ar-CH), 128.2 (Ar-CH), 128.3 (Ar-CH), 128.8 (Ar-CH), 129.0 (Ar-CH), 129.7 (Ar-C), 130.6 (Ar-C), 130.7 (Ar-CH), 133.1 (Ar-C), 135.3 (Ar-C), 146.5 (C-NH₂); LRMS: *m/z* 358.0 [M + Na]⁺. HRMS, found: *m/z* 358.1316, C₂₃H₁₇N₃Na requires 358.1315. IR (ν_{max}, cm⁻¹): 3473.5 (N-H stretch), 3384.4 (N-H stretch), 3221.5, 3053.5, 2199.6 (C≡N stretch), 1614.2, 1596.0, 1559.0, 1548.2, 1494.1, 1474.2, 1453.6, 1439.3, 1355.6, 1268.9, 1221.5, 1154.2.

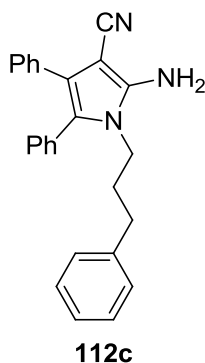
2-Amino-1-phenethyl-4,5-diphenyl-1*H*-pyrrole-3-carbonitrile (**112b**)



112b

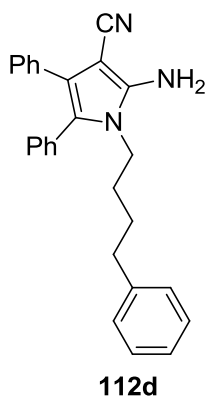
Benzoin (2.12 g, 10.0 mmol) and phenethylamine (1.3 ml, 1.2 g, 10 mmol) were used for the synthesis of the title compound. Silica gel column chromatography [EtOAc/PE (1:9) → EtOAc/PE (23:77)] of the crude product afforded the title compound as a brown solid (2.8 g, 78%), m.p.: 186.9-190.7 °C. *R_f*: 0.33 (30% EtOAc in PE, visible as a blue spot under UV). ¹H NMR (400 MHz, CDCl₃) δ (ppm): 2.71 (t, 2H, *J* = 7.0 Hz, CH₂Ph), 3.46 (br s, 2H, NH₂, D₂O exchangeable), 3.90 (t, 2H, *J* = 7.0 Hz, NCH₂), 6.91-6.93 (m, 2H, Ar-H), 7.11-7.25 (m, 10H, Ar-H), 7.34-7.36 (m, 3H, Ar-H). ¹³C NMR (100 MHz, CDCl₃) δ (ppm): 36.2 (CH₂), 45.0 (N-CH₂), 76.1 (C-CN), 117.7 (C≡N), 121.1 (Ar-C), 125.2 (Ar-C), 126.3 (Ar-CH), 127.1 (Ar-CH), 128.1 (Ar-CH), 128.3 (Ar-CH), 128.5 (Ar-CH), 128.7 (Ar-CH), 128.8 (Ar-CH), 128.9 (Ar-CH), 131.5 (Ar-CH), 133.1 (Ar-C), 137.6 (Ar-C), 145.5 (Ar-C); LRMS: *m/z* 362.0 [M - H]⁻. HRMS, found: *m/z* 362.1663, C₂₅H₂₀N₃ requires 362.1663. IR ν_{max} (cm⁻¹): 3428.2 (N-H stretch), 3349.0 (N-H stretch), 3059.0, 3025.8, 2937.0, 2194.5 (C≡N stretch), 1624.0, 1601.2, 1545.9, 1496.9, 1481.7, 1453.8, 1442.1, 1350.8, 1224.0, 1141.2, 1029.5, 1013.7.

2-Amino-4,5-diphenyl-1-(3-phenylpropyl)-1H-pyrrole-3-carbonitrile (**112c**)



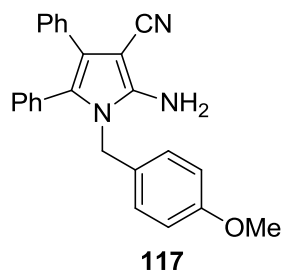
Benzoin (2.12 g, 10.0 mmol) and 3-phenyl-1-propylamine (1.4 ml, 1.4 g, 10 mmol) were used for the synthesis of the title compound. Filtration of the reaction mixture and washing of the precipitate with cold toluene (2 x 30 ml) afforded the title compound as a light brown solid (2.0 g, 53%), m.p.: 161.0-165.3 °C. *R_f*: 0.38 (30% EtOAc in PE, visible as a blue spot under UV). ¹H NMR (400 MHz, CDCl₃) δ (ppm): 1.85 (quin, 2H, *J* = 7.6 Hz, CH₂CH₂Ph), 2.46 (t, 2H, *J* = 7.4 Hz, CH₂Ph), 3.65 (t, 2H, *J* = 7.8 Hz, NCH₂), 7.00-7.02 (m, 2H, Ar-H), 7.09-7.26 (m, 10H, Ar-H), 7.30-7.39 (m, 3H, Ar-H). ¹³C NMR (100 MHz, CDCl₃) δ (ppm): 30.7 (CH₂), 32.5 (CH₂), 42.6 (N-CH₂), 75.7 (C-CN), 117.7 (C≡N), 120.9 (Ar-C), 125.3 (Ar-C), 126.3 (Ar-CH), 128.09 (Ar-CH), 128.13 (Ar-CH), 128.56 (Ar-CH), 128.59 (Ar-CH), 128.7 (Ar-CH), 128.91 (Ar-CH), 128.94 (Ar-CH), 131.2 (Ar-CH), 133.1 (Ar-C), 140.2 (Ar-C), 145.2 (Ar-C); LRMS: *m/z* 376.1 [M - H]⁻. HRMS, found: *m/z* 376.1815, C₂₆H₂₂N₃ requires 376.1819. IR *v*_{max} (cm⁻¹): 3420.0 (N-H stretch), 3338.3 (N-H stretch), 3243.6, 3059.3, 3024.3, 2934.1, 2856.0, 2191.5 (C≡N stretch), 1947.4, 1632.5, 1601.3, 1558.4, 1505.4, 1495.3, 1462.9, 1453.1, 1444.1, 1372.4, 1356.8, 1320.3, 1227.9, 1211.7, 1179.3, 1151.3, 1110.2, 1079.8, 1029.4.

2-Amino-4,5-diphenyl-1-(4-phenylbutyl)-1H-pyrrole-3-carbonitrile (**112d**)



Benzoin (2.12 g, 10.0 mmol) and 4-phenylbutylamine (1.6 ml, 1.5 g, 10 mmol) were used for the synthesis of the title compound. Silica gel column chromatography [EtOAc/PE (1:4) → EtOAc/PE (23:77)] of the crude product afforded the title compound as a brown solid (2.8 g, 78%), m.p.: 150.3-153.1°C. *R_f*: 0.40 (30% EtOAc in PE, visible as a blue spot under UV). ¹H NMR (400 MHz, CDCl₃) δ (ppm): 1.42-1.57 (m, 4H 2 x CH₂), 2.47 (t, 2H, *J* = 7.3 Hz, CH₂Ph), 3.64 (t, 2H, *J* = 7.0 Hz, NCH₂), 7.02-7.05 (m, 2H, Ar-H), 7.16-7.26 (m, 10H, Ar-H), 7.30-7.31 (m, 3H, Ar-H). ¹³C NMR (100 MHz, CDCl₃) δ (ppm): 27.8 (CH₂), 28.9 (CH₂), 34.9 (CH₂), 43.2 (N-CH₂), 75.8 (C-CN), 117.7 (C≡N), 120.9 (Ar-C), 125.2 (Ar-C), 126.0 (Ar-CH), 126.2 (Ar-CH), 128.08 (Ar-CH), 128.12 (Ar-CH), 128.3 (Ar-CH), 128.4 (Ar-CH), 128.59 (Ar-CH), 128.64 (Ar-CH), 131.3 (Ar-CH), 133.2 (Ar-C), 141.3 (Ar-C), 145.1 (Ar-C); LRMS: *m/z* 390.1 [M - H]. HRMS, found: *m/z* 390.1970, C₂₇H₂₄N₃ requires 390.1976. IR *v*_{max} (cm⁻¹): 3418.6 (N-H stretch), 3341.1 (N-H stretch), 3243.8, 3061.6, 3024.6, 2934.2, 2857.4, 2191.2 (C≡N stretch), 1947.6, 1631.6, 1601.0, 1558.2, 1495.4, 1462.7, 1453.2, 1443.5, 1357.3, 1319.7, 1225.9, 1212.0, 1179.6, 1150.0, 1110.5, 1074.7, 1029.3, 733.5.

2-amino-1-(4-methoxybenzyl)-4,5-diphenyl-1*H*-pyrrole-3-carbonitrile (**117**)



Benzoin (2.12 g, 10.0 mmol) and 4-methoxybenzylamine (1.3 ml, 1.4 g, 10 mmol) were used for the synthesis of the title compound, which was obtained as a golden solid (2.4 g, 63%), m.p.: 148.0-150.6 °C. *R_f*: 0.40 (30% EtOAc in PE, visible as a blue spot under UV). ¹H NMR (400 MHz, CDCl₃) δ (ppm): 3.79 (s, 3H, OCH₃), 3.88 (br s, 2H, NH₂, D₂O exchangeable), 4.84 (s, 2H, NCH₂PhOCH₃), 6.88 (d, 2H, *J* = 8.8 Hz, Ar-H), 6.99 (d, 2H, *J* = 8.8 Hz, Ar-H), 7.14-7.27 (m, 10H, Ar-H). ¹³C NMR (100 MHz, CDCl₃) δ (ppm): 46.5 (NCH₂PhOCH₃), 55.3 (OCH₃), 75.7 (C-CN), 114.7 (Ar-CH), 117.5 (C≡N), 120.9 (Ar-C), 125.6 (Ar-C), 126.4 (Ar-CH), 127.2 (Ar-CH), 127.8 (Ar-C), 128.1 (Ar-CH), 128.68 (Ar-CH), 128.72 (Ar-CH), 130.9 (Ar-C) 131.0 (Ar-CH), 133.2 (Ar-C), 145.9 (Ar-C), 159.3 (Ar-C); LRMS: *m/z* 378.2 [M - H]. HRMS, found: *m/z* 378.1599, C₂₅H₂₀N₃O requires 378.1612. IR

v_{\max} (cm^{-1}): 3416.3 (N-H stretch), 3328.3 (N-H stretch), 3233.7, 2202.9 (C≡N stretch), 1651.5, 1603.3, 1564.4, 1508.8, 1495.9, 1455.4, 1441.9, 1354.6, 1244.0, 1176.6, 1016.5.

3.5 e) Expression and purification of IMP-1

Refer to Appendix 1.

3.5 f) Preparation of CENTA (73)

Refer to Appendix 2.

3.5 g) IMP-1 screening assay of the derivatives⁴¹⁻⁴⁴

The screening assays was performed in triplicates, with CENTA as the substrate and HEPES X (50 mM HEPES, 0.1 M NaCl, 100 μM ZnCl_2 , pH 7.0) as the buffer, at 25 °C. The final concentration of IMP-1 and CENTA was 0.1, 10 nM and 20, 70 μM , respectively. Bovine serum albumin (final concentration of 20 $\mu\text{g ml}^{-1}$) was added to the enzyme solution for enzyme stability. The synthetic derivatives of pyrrole **65** were assayed at final concentrations of 5, 10 and 20 μM , except for **104**, which was assayed at 5, 10 and 25 μM . The rate of CENTA hydrolysis was monitored at 405 nm ($\epsilon = 6400 \text{ M}^{-1} \text{ cm}^{-1}$) (Scheme 2.4). The percentage inhibition of an inhibitor was calculated based on the residual activity of the enzyme in the presence of the inhibitor (Equation 2.1).

3.5 h) Computational modelling

Refer to Appendix 3.

References

- (1) Toney, J. H.; Fitzgerald, P. M. D.; Grover-Sharma, N.; Olson, S. H.; May, W. J.; Sundelof, J. G.; Vanderwall, D. E.; Cleary, K. A.; Grant, S. K.; Wu, J. K.; Kozarich, J. W.; Pompliano, D. L.; Hammond, G. G. *Chemistry & Biology* **1998**, 5, 185.

- (2) Bebrone, C.; Delbrück, H.; Kupper, M. B.; Schlömer, P.; Willmann, C.; Frère, J.-M.; Fischer, R.; Galleni, M.; Hoffmann, K. M. V. *Antimicrobial agents and chemotherapy* **2009**, *53*, 4464.
- (3) Spencer, J.; Read, J.; Sessions, R. B.; Howell, S.; Blackburn, G. M.; Gamblin, S. J. *Journal of the American Chemical Society* **2005**, *127*, 14439.
- (4) Zhang, H.; Hao, Q. *The Federation of American Societies for Experimental Biology Journal* **2011**, *25*, 2574.
- (5) Palzkill, T. *Annals of the New York Academy of Sciences* **2013**, *1277*, 91.
- (6) Thomsen, R.; Christensen, M. H. *Journal of Medicinal Chemistry* **2006**, *49*, 3315.
- (7) Eger, K.; Pfahl, J. G.; Folkers, G.; Roth, H. J. *Journal of Heterocyclic Chemistry* **1987**, *24*, 425.
- (8) Ek, F.; Wistrand, L.-G.; Frejd, T. *The Journal of Organic Chemistry* **2003**, *68*, 1911.
- (9) Mita, Y.; Noguchi-Yachide, T.; Ishikawa, M.; Hashimoto, Y. *Bioorganic and Medicinal Chemistry* **2013**, *21*, 608.
- (10) Nakamura, T.; Sato, M.; Kakinuma, H.; Miyata, N.; Taniguchi, K.; Bando, K.; Koda, A.; Kameo, K. *Journal of Medicinal Chemistry* **2003**, *46*, 5416.
- (11) Gawande, S. D.; Raihan, M. J.; Zanwar, M. R.; Kavala, V.; Janreddy, D.; Kuo, C.-W.; Chen, M.-L.; Kuo, T.-S.; Yao, C.-F. *Tetrahedron* **2013**, *69*, 1841.
- (12) Jeong, S.; Song, X.; Jeong, S.; Oh, M.; Liu, X.; Kim, D.; Moon, D.; Lah, M. S. *Inorganic Chemistry* **2011**, *50*, 12133.
- (13) Huff, B. E.; Staszak, M. A. *Tetrahedron Letters* **1993**, *34*, 8011.
- (14) Németh, B.; Guégan, J.-P.; Veszprémi, T.; Guillemin, J.-C. *Inorganic Chemistry* **2013**, *52*, 346.
- (15) Cottyn, B.; Acher, F.; Ramassamy, B.; Alvey, L.; Lepoivre, M.; Frapart, Y.; Stuehr, D.; Mansuy, D.; Boucher, J.-L.; Vichard, D. *Bioorganic and Medicinal Chemistry* **2008**, *16*, 5962.
- (16) Dudley Williams; Fleming, I.; sixth ed.; McGraw-Hill Education: Berkshire, UK, 2008.
- (17) Brenton, A. G.; Godfrey, A. R. *Journal of the American Society for Mass Spectrometry* **2010**, *21*, 1821.
- (18) Habibi, D.; Nasrollahzadeh, M.; Faraji, A. R.; Bayat, Y. *Tetrahedron* **2010**, *66*, 3866.
- (19) Kamieńska-Trela, K.; Kania, L.; Bednarek, E. *Magnetic Resonance in Chemistry* **1993**, *31*, 268.
- (20) Pinhey, J. T.; Sternhell, S. *Tetrahedron Letters* **1963**, *4*, 275.
- (21) Vorob'ev, E. V.; Kurbatov, E. S.; Krasnikov, V. V.; Mezheritskii, V. V.; Usova, E. V. *Russian Chemical Bulletin, International Edition* **2006**, *55*, 1492.

- (22) Raymond K. Mackie; Smith, D. M. *Guidebook to Organic Synthesis*; Longman, 1982.
- (23) Haddach, A. A.; Kelleman, A.; Deaton-Rewolinski, M. V. *Tetrahedron Letters* **2002**, 43, 399.
- (24) Watanabe, T.; Kobayashi, A.; Nishiura, M.; Takahashi, H.; Usui, T.; Kamiyama, I.; Mochizuki, N.; Noritake, K.; Yokoyama, Y.; Murakami, Y. *Chemical and Pharmaceutical Bulletin* **1991**, 39, 1152.
- (25) Ross, B. P.; DeCruz, S. E.; Lynch, T. B.; Davis-Goff, K.; Toth, I. *Journal of Medicinal Chemistry* **2004**, 47, 1251.
- (26) Wuts, P. G. M.; Greene, T. W.; *Greene's Protective Groups in Organic Synthesis*; John Wiley & Sons, Inc.: 2014, p 895.
- (27) Field, L. D.; Sternhell, S.; Kalman, J. R. *Organic Structures from Spectra*; John Wiley and Sons: Chichester, UK, 2002.
- (28) Jones, R. *Australian Journal of Chemistry* **1963**, 16, 93.
- (29) Roth, H. J.; Eger, K. *Archiv der Pharmazie* **1975**, 308, 179.
- (30) Alcaide, B.; Escobar, G.; Pérez-Ossorio, R.; Plumet, J. *Organic Preparations and Procedures International* **1982**, 14, 220.
- (31) Toney, J. H.; Hammond, G. G.; Fitzgerald, P. M. D.; Sharma, N.; Balkovec, J. M.; Rouen, G. P.; Olson, S. H.; Hammond, M. L.; Greenlee, M. L.; Gao, Y.-D. *Journal of Biological Chemistry* **2001**, 276, 31913.
- (32) Concha, N. O.; Janson, C. A.; Rowling, P.; Pearson, S.; Cheever, C. A.; Clarke, B. P.; Lewis, C.; Galleni, M.; Frère, J.-M.; Payne, D. J.; Bateson, J. H.; Abdel-Meguid, S. S. *Biochemistry* **2000**, 39, 4288.
- (33) Lienard, B. M. R.; Garau, G.; Horsfall, L.; Karsisiotis, A. I.; Damblon, C.; Lassaux, P.; Papamicael, C.; Roberts, G. C. K.; Galleni, M.; Dideberg, O.; Frere, J.-M.; Schofield, C. J. *Organic and Biomolecular Chemistry* **2008**, 6, 2282.
- (34) Lassaux, P.; Hamel, M.; Gulea, M.; Delbrück, H.; Mercuri, P. S.; Horsfall, L.; Dehareng, D.; Kupper, M.; Frère, J.-M.; Hoffmann, K.; Galleni, M.; Bebrone, C. *Journal of Medicinal Chemistry* **2010**, 53, 4862.
- (35) Olsen, L.; Pettersson, I.; Hemmingsen, L.; Adolph, H.-W.; Jørgensen, F. *Journal of Computational Aided Molecular Design* **2004**, 18, 287.
- (36) Urbano, M.; Guerrero, M.; Zhao, J.; Velaparthi, S.; Schaeffer, M.-T.; Brown, S.; Rosen, H.; Roberts, E. *Bioorganic and Medicinal Chemistry Letters* **2011**, 21, 5470.

- (37) Coumar, M. S.; Tsai, M.-T.; Chu, C.-Y.; Uang, B.-J.; Lin, W.-H.; Chang, C.-Y.; Chang, T.-Y.; Leou, J.-S.; Teng, C.-H.; Wu, J.-S.; Fang, M.-Y.; Chen, C.-H.; Hsu, J. T. A.; Wu, S.-Y.; Chao, Y.-S.; Hsieh, H.-P. *ChemMedChem* **2010**, *5*, 255.
- (38) B.S. Furniss; A.J. Hannaford; V. Rogers; P.W.G Smith; Tatchell, A. R. *Vogel's Textbook of Practical Organic Chemistry*, fourth ed.; Longman Scientific and Technical: Essex, 1978.
- (39) McEwen, W. E.; Grossi, A. V.; MacDonald, R. J.; Stamegna, A. P. *The Journal of Organic Chemistry* **1980**, *45*, 1301.
- (40) Mohamed, M.; El-Domany, R.; Abd El-Hameed, R. In *Acta Pharmaceutica* 2009; Vol. 59, p 145.
- (41) Hussein, W. M.; Fatahala, S. S.; Mohamed, Z. M.; McGeary, R. P.; Schenk, G.; Ollis, D. L.; Mohamed, M. S. *Chemical Biology and Drug Design* **2012**, *80*, 500.
- (42) Mohamed, M. S.; Hussein, W. M.; McGeary, R. P.; Vella, P.; Schenk, G.; Abd El-hameed, R. H. *European Journal of Medicinal Chemistry* **2011**, *46*, 6075.
- (43) Vella, P., *The Development of New Drug Leads to Combat Bacterial Resistance towards Antibiotics*, PhD, The University of Queensland, 2012.
- (44) Vella, P.; Hussein, W. M.; Leung, E. W. W.; Clayton, D.; Ollis, D. L.; Mitić, N.; Schenk, G.; McGeary, R. P. *Bioorganic and Medicinal Chemistry Letters* **2011**, *21*, 3282.

CHAPTER 4: OPTIMISATION OF (2*RS*, 4*R*)-3-(2-MERCAPTOACETYL)-2-PHENYLTHIAZOLIDINE-4-CARBOXYLIC ACID AS POTENT INHIBITORS OF IMP-1

4.1 General introduction

MBL inhibitor design based on the β -lactam molecular scaffold is a propitious approach for the search of more potent, broad-spectrum MBL inhibitors.¹ Thus far, this approach has been fruitful in the identification of two highly potent IMP-1 inhibitors, **59** (Section 1.11 f) and **119**, which exhibit inhibitory potencies in the submicro- to nanomolar range (Figure 4.1).^{2,3} Both of the mercaptocarboxylate-type inhibitors, **59** and **119** were originally designed to structurally mimic the β -lactam substrate, in order to facilitate the study of the 3D active site architecture of B1 MBLs and the flexibility of the mobile L3 loop, respectively.²⁻⁴

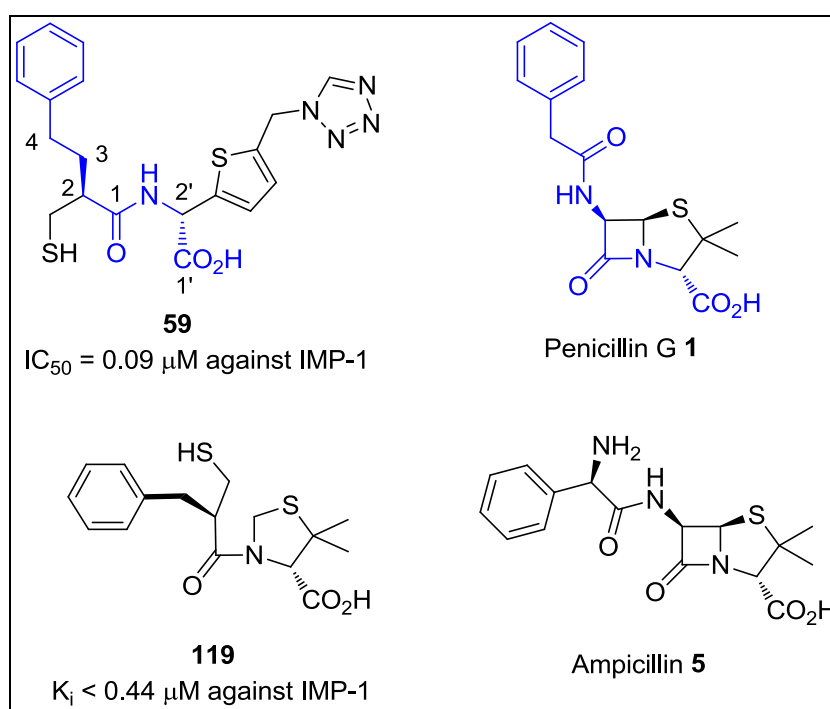


Figure 4.1: The potent mercaptocarboxylate-type IMP-1 inhibitors, **59** and **119**, (left) which structurally resemble penicillins **1** and **5** (right).²⁻⁴ Part of the structure of **59** which is similar to penicillin G (**1**) is highlighted in blue, whereas **119** has an open mercapto chain *in lieu* of a β -lactam ring.

The 3D structure of **59** co-crystallised with IMP-1 revealed that the inhibitor binds tightly in the active site of the enzyme through three key interactions (Figure 4.2):

- ionic interactions between the thiolate group of **59** and the Zn²⁺ centres (S-Zn1 distance 2.2 Å and S-Zn2 distance 2.4 Å);
- interactions involving the C1'-carboxylate oxygens of **59** and the enzyme, such as a salt bridge interaction between the terminal amino group of Lys161 (224) and the C1'-carboxylate oxygen (N-O distance 2.7 Å), as well as a hydrogen bond interaction between the amide backbone N-H of Asn167 (233) and the C1'-carbonyl oxygen (N-O distance 2.9 Å);
- hydrophobic contacts between the 4-phenyl ring of **59** and the hydrophobic pocket of the enzyme, which comprises of Glu23, Val25 (61), Val31 (67) and Phe51 (87), as well as π - π stacking interaction between the thiophene ring of **59** and Trp28 (64) indole ring.²

Furthermore, the *S* absolute configuration at both C-2 and C-2' is essential for the observed, noteworthy IC₅₀ potency of the inhibitor.²

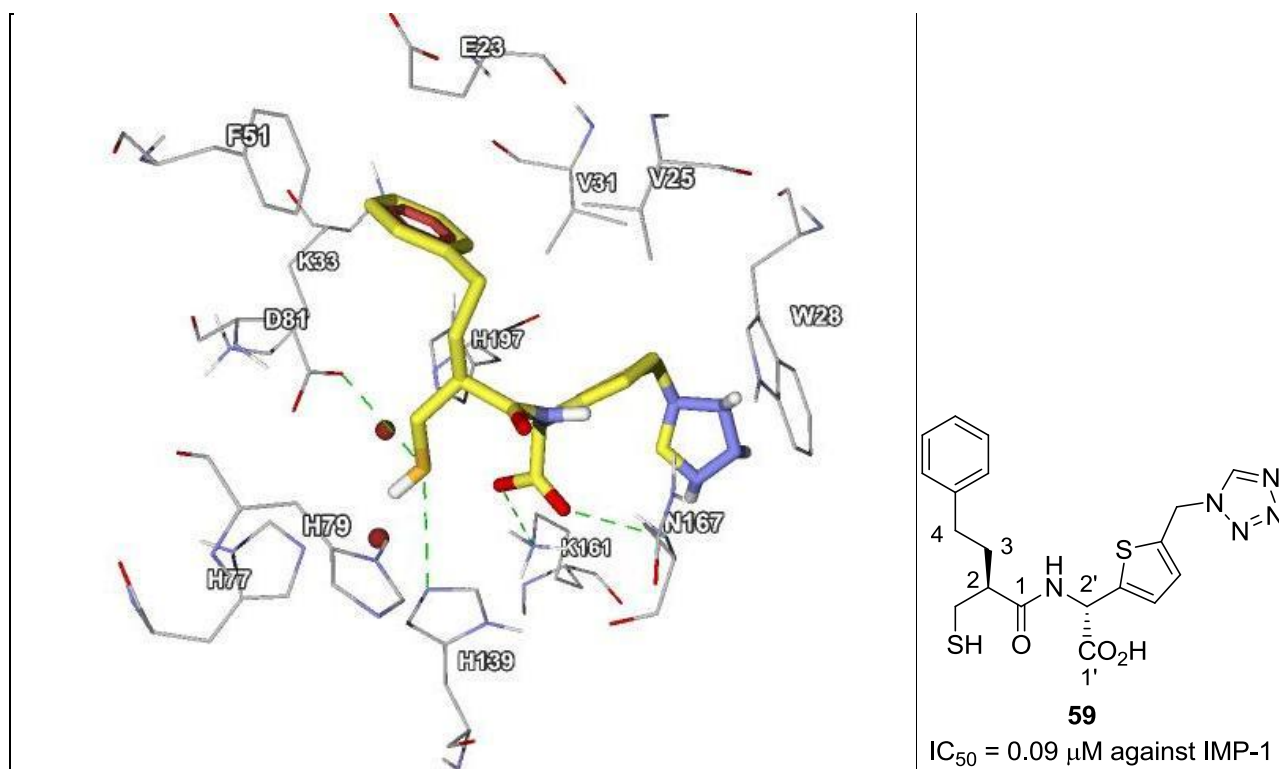


Figure 4.2: The active site view of the crystal structure of **59** bound with IMP-1 (PDB No.: 1DD6).² Atom colours: carbon on inhibitor in yellow, carbon on IMP-1 in grey, nitrogen in

blue, oxygen in red and sulfur in gold. The red spheres represent the Zn²⁺ ions and the green dotted lines represent ionic and hydrogen bonds (figure drawn with MVD).¹⁷

Comparably, NMR studies of inhibitor **119** bound with the CcrA B1 MBL revealed that the flexibility of the L3 β -hairpin loop decreased upon inhibitor binding, particularly Trp64 (28), which is located at the edge of the loop.⁴ This implies that the loop is involved in the binding of a broad-range of β -lactam substrates, with various hydrophobic side chains, which are readily accommodated by a flexible hydrophobic pocket, adjacent to the enzyme active site.⁴ In addition, the loop also functions in shielding the enzyme active site from solvent exposure.⁴

The five-membered thiazolidine ring, which is part of the bicyclic ring structure of penicillins, is an interesting scaffold for the design of MBL inhibitors.⁵ Thiazolidines **120a** and **60b** (Section 1.11 f) were identified by Chen *et al.*⁶ and Feng *et al.*,⁷ respectively, to exhibit moderate to potent inhibitory activity against B1 MBLs (Figure 4.3).

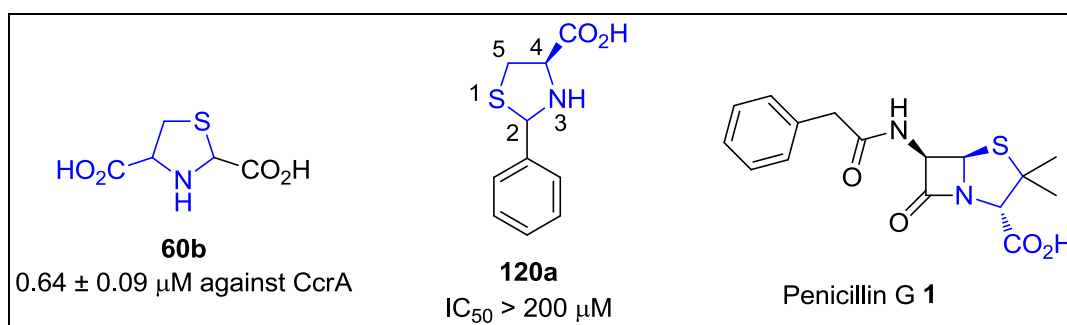


Figure 4.3: Reported MBL inhibitors, **60b** and **120a** bearing the thiazolidine ring, which is highlighted in blue.

(2*RS*, 4*R*)-2-Phenylthiazolidine-4-carboxylic acid (**120a**), which has a modest inhibitory activity against IMP-1, is an advantageous starting point for the design of more potent IMP-1 inhibitors. Preliminary Glide computational modelling of the 2*S*, 4*R* isomer of **120a** in complex with IMP-1 suggested that both of the carboxylate oxygens of **120a** bind to the metal centres, with O-Zn distances of 1.99-2.81 Å (Figure 4.4). In addition, the 2-phenyl ring of **120a** was predicted to fit into the hydrophobic pocket, which comprises of Val25 (61) and Val31 (67), as well as a favourable hydrophobic contact with Trp28 (64).

However, the *in silico* model didn't predict any significant interactions between the ligand and the conserved amino acid residues Lys161 (224), or Asn167 (233).

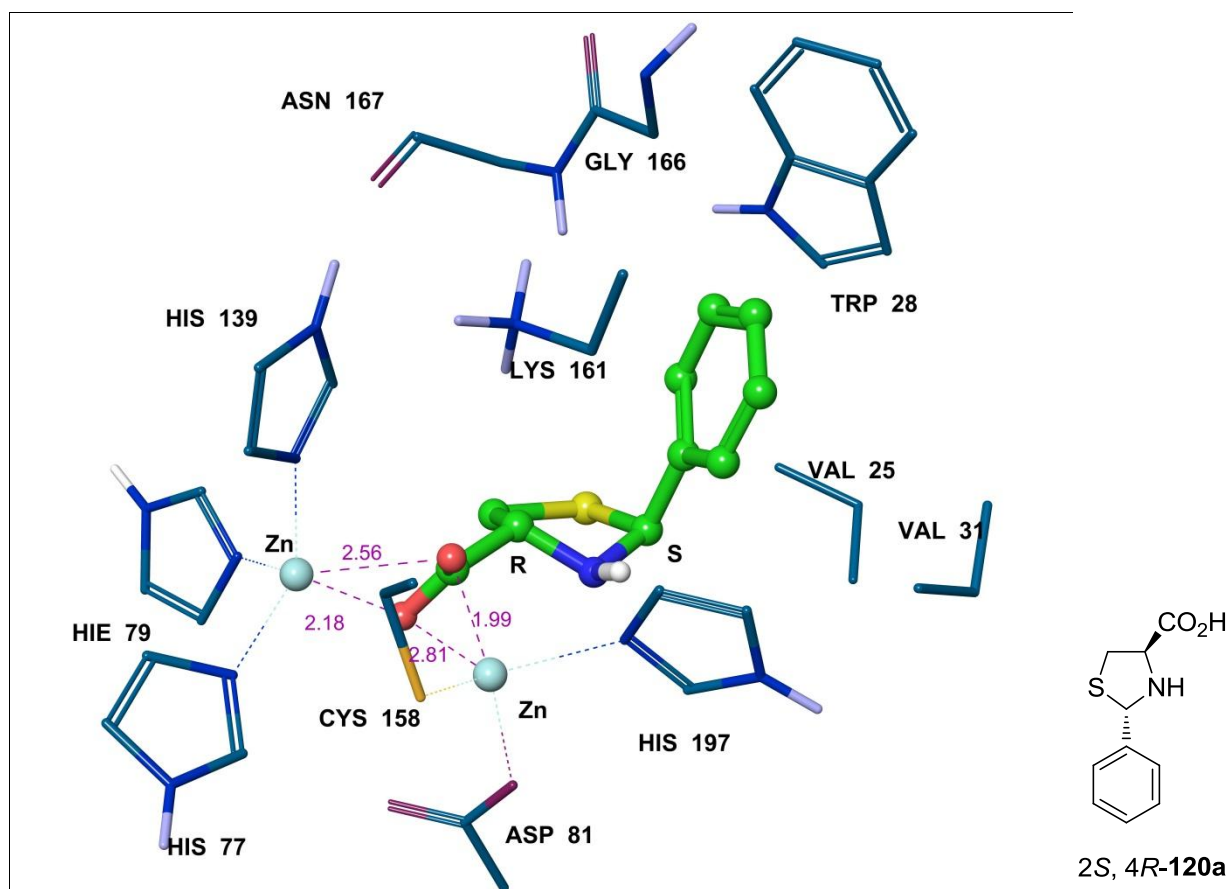
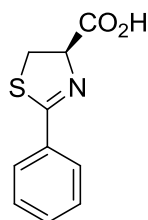


Figure 4.4: The active site view of the *in silico* model of 2S, 4R-120a bound with IMP-1, as predicted by Glide. Atom colours: carbon on ligand in green, carbon on IMP-1 in light blue, hydrogen in white, nitrogen in navy blue, oxygen in purple and sulfur in yellow. The zinc ions are represented as cyan spheres. The purple dotted lines represent ionic interactions between the ligand and zinc ions.

Chen and colleagues also reported a similar Glide *in silico* model of a structurally related inhibitor, **121** in complex with IMP-1 (model not shown).⁶ The computational model of **121**-IMP-1 suggested ionic interactions between the carboxylate group of the ligand with both of the zinc ions, but no interactions between the ligand and Lys161 (224) or Asn167 (233) amino acid residue.⁶

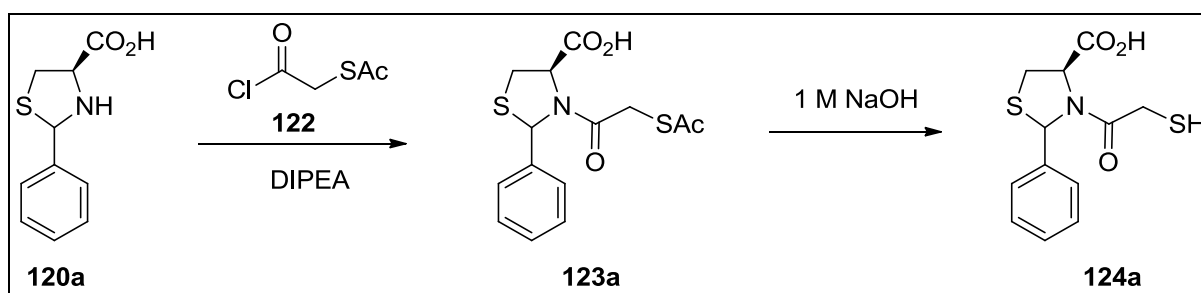


121

IC₅₀ = 5.5 μM against IMP-1

It is therefore envisaged that linkage of the thiazolidine ring nitrogen of **120a** with a potent zinc chelator, such as a thiol group, would allow the 4-carboxylate group of the inhibitor to bind with Lys161 (224) *via* a salt bridge interaction, and simultaneously preserve direct ligand-Zn interaction.

The secondary thiazolidine ring nitrogen of **120a** can be linked with mercaptoacetic acid (**30**), which has a K_i potency of 0.23 μM against IMP-1 (Section 1.11 a).⁸ This can be achieved by acylating **120a** with *S*-(2-chloro-2-oxoethyl) ethanethioate (**122**), which is the thioacetate-protected, acyl chloride derivative of **30** (Scheme 4.1). Removal of the thioacetate protecting group from intermediate **123a** by base-promoted hydrolysis will finally afford the mercapto-amide-linked thiazolidine compound, **124a**.



Scheme 4.1: The acylation of thiazolidine **120a** with acyl chloride **122** to afford the mercapto-amide-linked thiazolidine compound, **124a**.

Glide molecular modelling of the 2*S*, 4*R* diastereomer of **124a** bound with IMP-1 predicted that the ligand binds to both Zn²⁺ ions through its thiol group (S-Zn1 distance 3.8 Å and S-Zn2 distance 4.1 Å) (Figure 4.5). Furthermore, one of the carboxylate oxygens of the ligand binds to the terminal amino group of Lys161 (224) *via* an ionic bond interaction

(O-N distance 2.5 Å), while the other oxygen interacts with the N-H amide backbone of Asn167 (233) through another hydrogen bond interaction (O-N distance 2.7 Å).

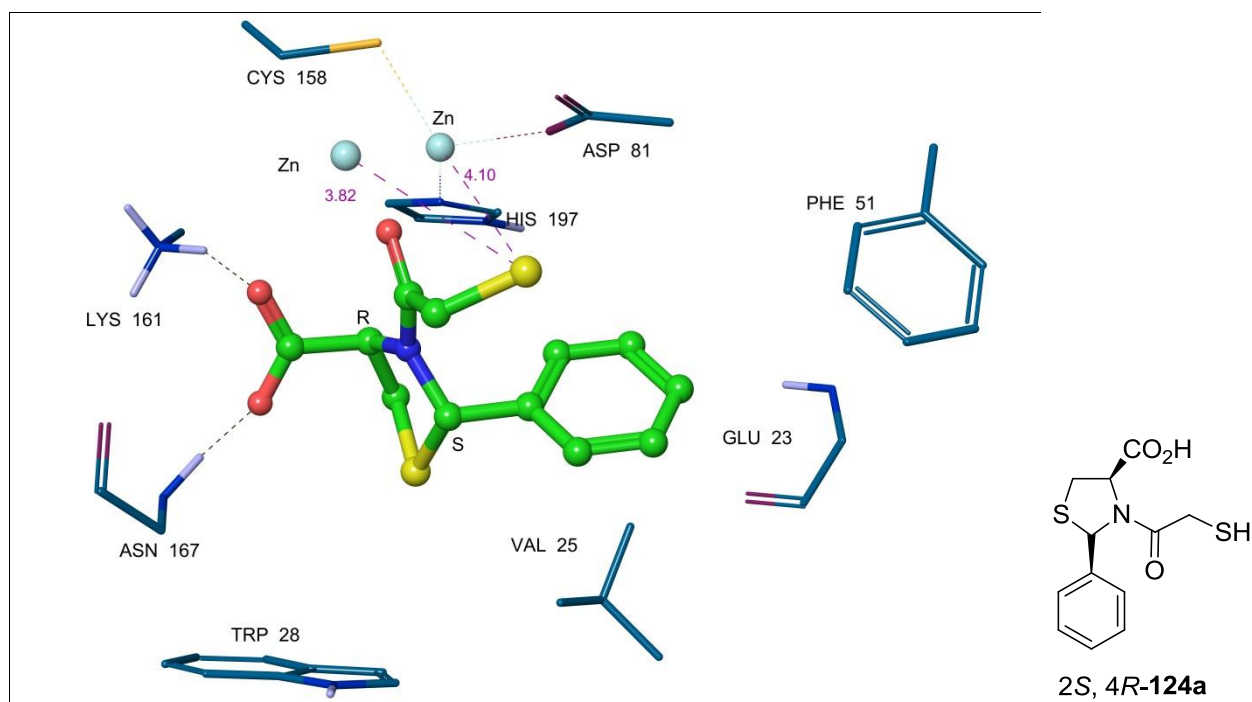


Figure 4.5: The active site view of the computational model of 2S, 4R-**124a** in complex with IMP-1, as predicted by Glide. Atom colours: carbon on ligand in green, carbon on IMP-1 in light blue, hydrogen in white, nitrogen in navy blue, oxygen in purple and sulfur in yellow. The zinc ions are represented as cyan spheres. The dotted purple and green lines represent ionic and hydrogen bond interactions, respectively.

On the other hand, the Glide *in silico* model of the 2R, 4R diastereomer of **124a** in complex with IMP-1 suggested a different binding mode between the ligand and the enzyme (Figure 4.6). In this model, both of the carboxylate oxygens of the ligand were predicted to bind to both of the Zn²⁺ ions, with an O-Zn distance of 1.9 Å for each bond. In addition, the thiolate group of the ligand was suggested to have an ionic interaction with the Lys161 (224) terminal amino group (S-N distance 4.1 Å), as well as a hydrogen bond interaction with the N-H backbone of Asn167 (233) (S-N distance 3.3 Å).

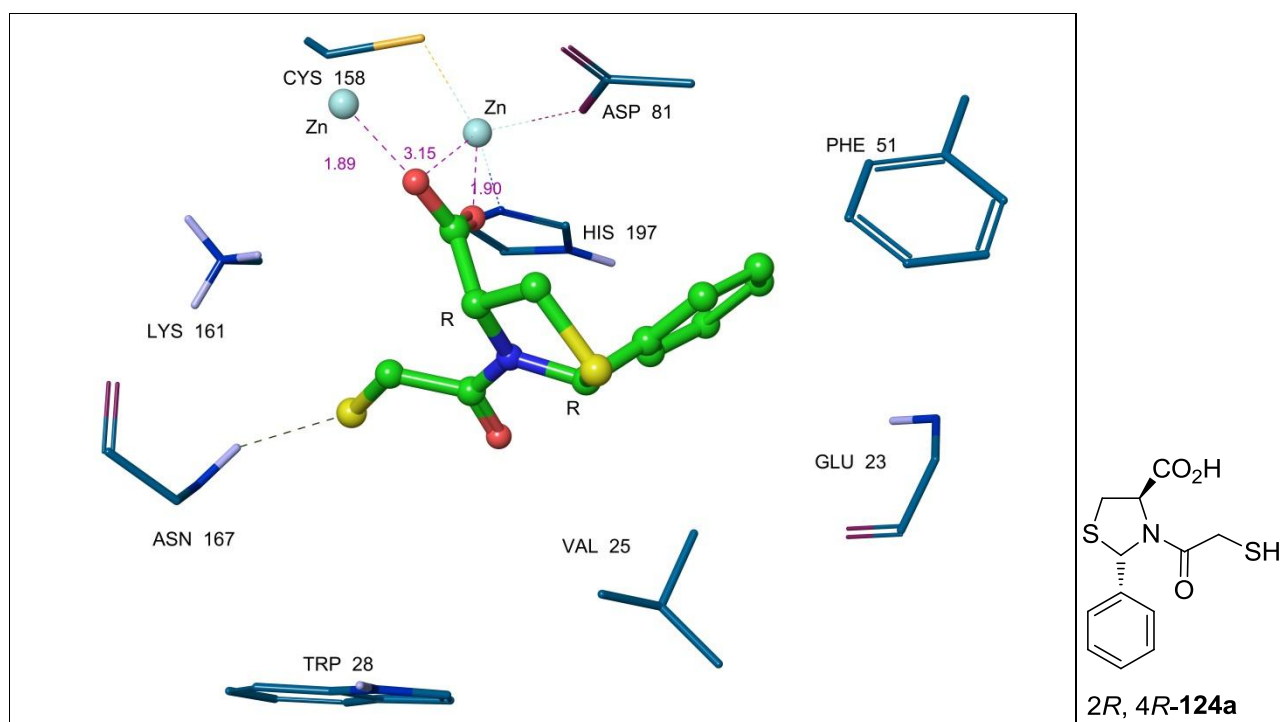


Figure 4.6: The active site view of the *in silico* model of **2R, 4R-124a** bound with IMP-1, as predicted by Glide. Atom colours: carbon on ligand in green, carbon on IMP-1 in light blue, hydrogen in white, nitrogen in navy blue, oxygen in purple and sulfur in yellow. The zinc ions are represented as cyan spheres. The dotted purple and green lines represent ionic and hydrogen bond interactions, respectively.

This chapter focuses on the SAR of various derivatives of (2*RS*, 4*R*)-3-(2-mercaptoacetyl)-2-phenylthiazolidine-4-carboxylic acid (**124a**) as IMP-1 inhibitors.

4.2 Research plan

The synthetic work was completed by Dr Sara Mustaddiq, then an occupational trainee with the McGeary group (2013-2014), who synthesised a range of mercapto-amide-linked thiazolidines **124a-o**, with various aromatic rings and substituents on the phenyl ring (Figure 4.7).⁹ My contribution to this project included inhibitor design and enzymatic inhibition study, whereas the computational modelling of the inhibitors was carried out by Ajit Kandale, a PhD student with the McGeary group.

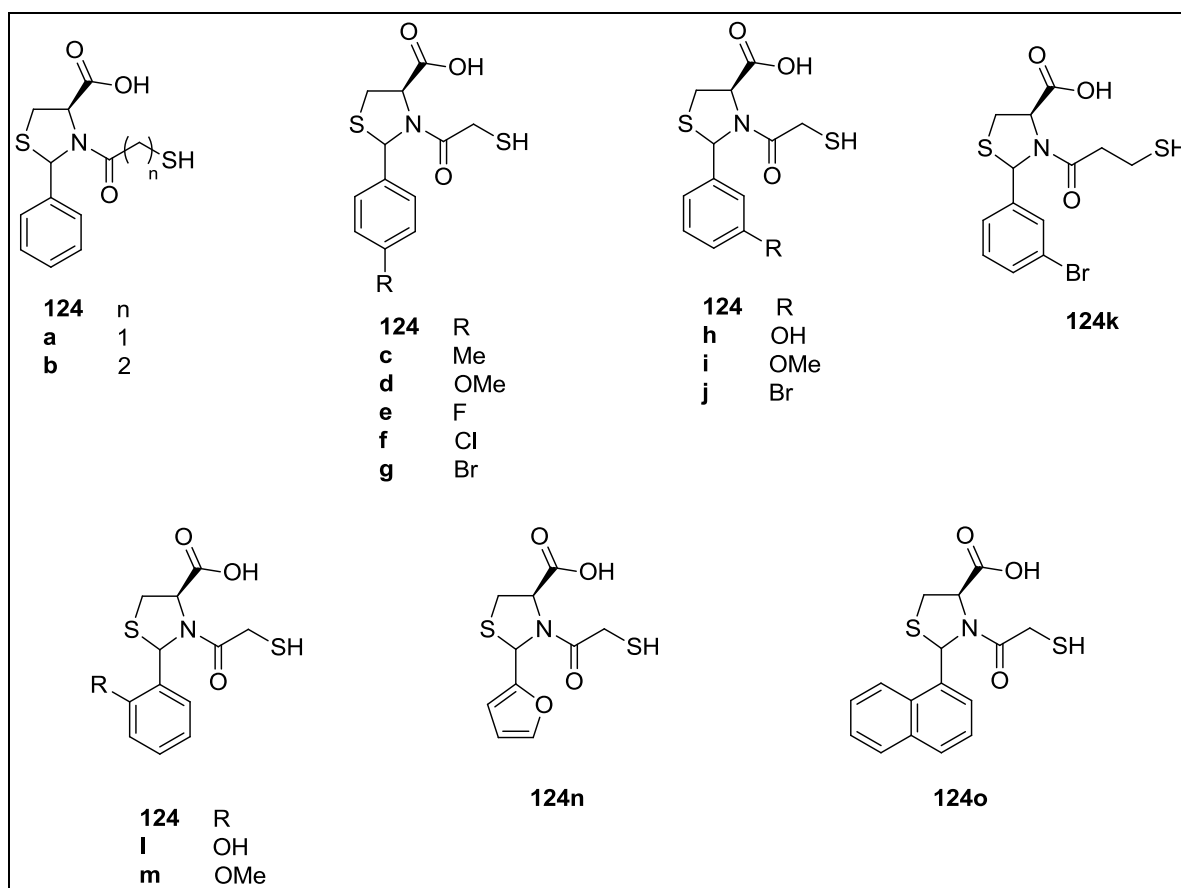
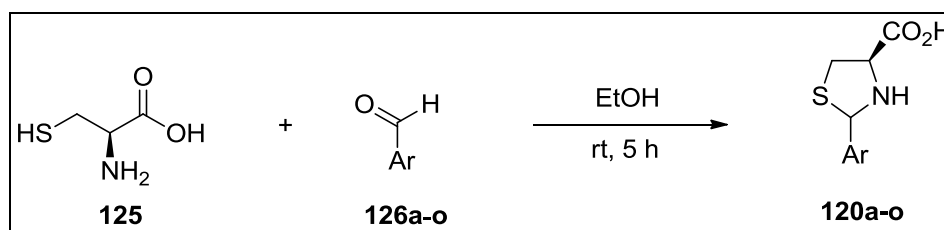


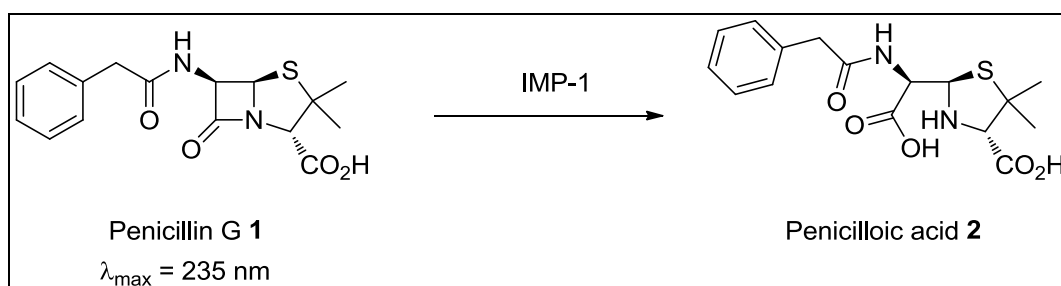
Figure 4.7: The various mercapto-amide-linked thiazolidines **124a-o**, which were synthesised by Dr Sara Mustaddiq.⁹

The (2*RS*, 4*R*)-2-arylthiazolidine-4-carboxylic acids, **120a-o** which are the starting materials for the syntheses of the mercapto-amide-linked thiazolidines **124a-o**, were prepared from the condensation of L-cysteine (**125**) with various aromatic aldehydes, **126a-o** (Scheme 4.2).^{9,10}



Scheme 4.2: The preparation of the (2*RS*, 4*R*)-2-arylthiazolidine-4-carboxylic acid starting materials, **120a-o**.^{9,10}

The β -lactam substrate for the IMP-1 kinetic assays of thiazolidines **124a-o** would have to be penicillin G (**1**), as CETA (**73**) has the propensity to react with the thiol group of the inhibitors.¹¹ The enzyme activity in the presence and absence of the inhibitors can be measured as the rate of penicillin G (**1**) consumption, which can be monitored spectrophotometrically at 235 nm ($\epsilon = 936 \text{ M}^{-1} \text{ cm}^{-1}$) (Scheme 4.3). The K_m and k_{cat} parameter for the hydrolysis of penicillin G (**1**) by IMP-1 is 520 μM and 320 s^{-1} , respectively.¹²



Scheme 4.3: Hydrolysis of penicillin G (**1**) by IMP-1 as a measurement of enzyme activity.

The crystal structure of mercaptocarboxylate **59** bound with IMP-1 (PDB no.: 1DD6) can be used for computational docking of the mercapto-amide-linked thiazolidine derivatives with the active site of the enzyme.² Both of the 2*R*, 4*R* and 2*S*, 4*R* diastereomer of the synthetic derivatives can be docked separately by using the Glide program, as suggested by Chen *et al.*⁶

4.3 Results and discussion

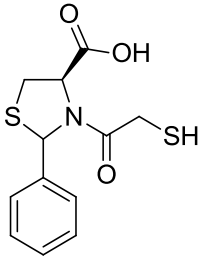
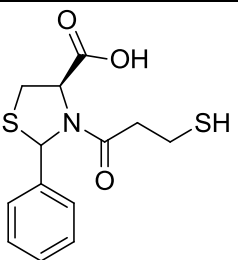
4.3 a) Enzymatic kinetic studies

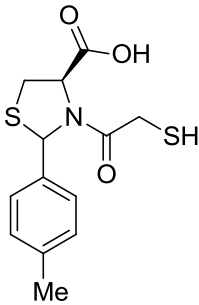
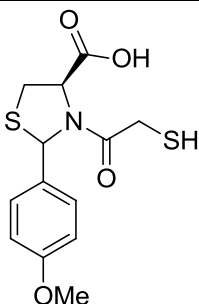
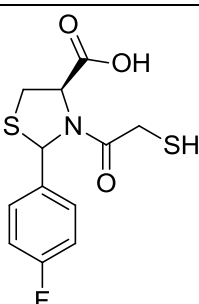
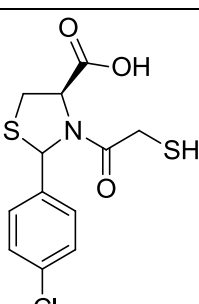
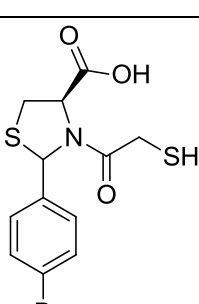
The mercapto-amide-linked thiazolidines **124a-o** were screened against IMP-1 (5 nM) at four different inhibitor concentrations: 0.1, 1, 10 and 100 μM , and the results are presented in Table 4.1. The majority of the thiazolidines, except **124c** and **124o** showed inhibitory activity close to, or above 50% at an inhibitor concentration of 10 μM . This is an appreciable, 20-fold improvement for this series of inhibitors, as thiazolidine **120a** was originally reported to have an IC_{50} value greater than 200 μM against IMP-1.⁶

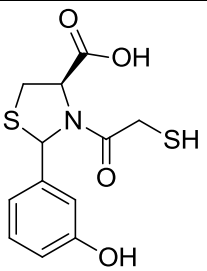
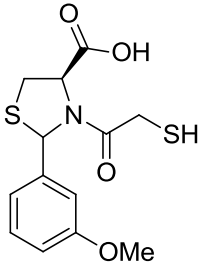
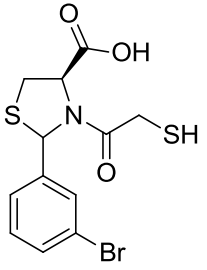
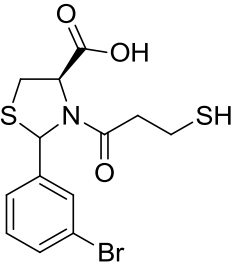
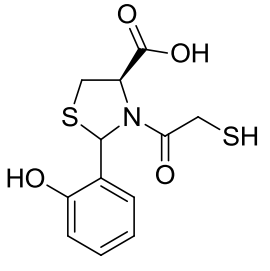
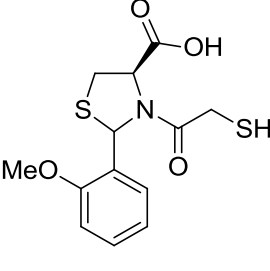
Thiazolidine **124a**, which has an unsubstituted phenyl ring, was selected as the reference compound for the selection of other thiazolidine derivatives for further inhibition constant, K_i study against IMP-1. The reference compound demonstrated a percentage inhibition of 87.3% at an inhibitor concentration of 10 μM against the enzyme. Therefore, thiazolidine derivatives exhibiting a percentage inhibition close to (13-19%) or greater than 87.3% at 10 μM inhibitor concentration were selected for the study (Table 4.2).

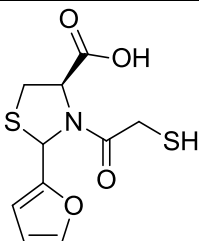
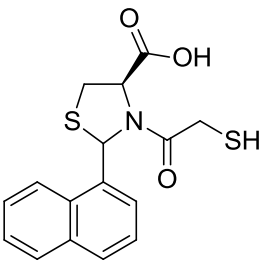
According to the screening results, thiazolidine derivatives with electron donating groups on the phenyl ring, such as methyl, methoxy or hydroxyl groups displayed decreased inhibitory activity as compared to the reference compound **124a**. These derivatives, except for the *p*-methoxy substituted thiazolidine **124d**, which has comparable activity with **124a**, were not selected for the K_i study. On the contrary, thiazolidine derivatives bearing a halide group on the phenyl ring demonstrated comparable or greater inhibitory activity than the reference compound. These observations suggest that the inhibitory potencies of the thiazolidine derivatives are influenced by the electronic nature of the substituent on the phenyl ring.

Table 4.1: The percentage inhibition of thiazolidine derivatives **124a-o** screened against IMP-1 (5 nM, containing BSA at a final conc. of 20 $\mu\text{g mL}^{-1}$) at pH 7.0 and 25 $^\circ\text{C}$, with penicillin G (1 mM) as the substrate.

Inhibitor 124	Molecular structure	Percentage Inhibition (%)			
		0.1 μM	1 μM	10 μM	100 μM
a		5.6 \pm 2.2	11.3 \pm 3.31	87.3\pm3.49	100
b		0 \pm 17	19.5 \pm 6.70	95\pm2.7	100

c		9.5±0.8	18.6±2.89	38.6±1.61	100
d		11.2±2.97	20.3±2.66	84.6±10.8	97.4±5.56
e		0±1.5	11.0±1.47	76.4±1.83	99.5±2.60
f		13.9±3.57	55.0±1.64	100	100
g		25.6±4.19	41.9±7.93	100	100

h		10.9±4.21	8.92±3.38	57.9±3.55	87.1±2.52
i		8.50±5.25	20.6±3.02	63.4±1.10	100
j		0±5	18.4±1.95	70.5±3.78	100
k		10.8±2.35	89.2±2.04	100	100
l		21.7±6.02	15.4±3.55	50.4±4.15	100
m		21.1±3.99	11.3±2.28	47.8±4.92	100

n		35.4±8.92	40.3±11.3	75.0±6.95	100
o		27.2±8.02	17.9±2.82	29.2±3.80	78.3±4.16

Inhibition percentages of derivatives which are comparable to or higher than that of the reference compound **124a** at 10 μ M inhibitor concentration are highlighted in red.

The K_i study of the selected thiazolidine derivatives suggested that all of the derivatives assayed exhibit competitive inhibition mode against IMP-1, with similar potencies (Table 4.2). The only exception to this is the *p*-bromo derivative, **124g** which is the most potent derivative in this series, with a K_{ic} potency of 0.57 μ M against the enzyme.

On the contrary, the least potent thiazolidine derivative in this series is the *p*-methoxy derivative, **124d**. This observation is consistent with an earlier view that electron donating substituents on the phenyl ring have a diminishing effect on the inhibitory potencies of the thiazolidine derivatives.

Moreover, there is an increasing trend in inhibitory potency as the *p*-halide substituent on the phenyl ring of the derivatives is replaced with a larger halide group in the following order: Br > Cl > F. This *p*-halogen effect in IMP-1 inhibitory activity was also observed by Siemann *et al.* in their SAR study of *N*-arylsulfonyl hydrazones **127-130, a-c** as IMP-1 inhibitors (Table 4.3).¹³ These observations suggest that halogen bonding between the *p*-halide group and the backbone carbonyl oxygen of certain amino acids, such as Val and Phe may come into play.¹⁴ Halogen bonds, which is shown by quantum mechanics/molecular mechanics (QM/MM) calculations to be comparable in strength with hydrogen bonds increase in strength in the following order: I > Br > Cl.¹⁴

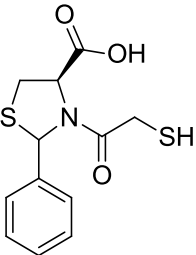
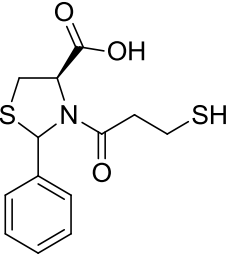
Interestingly, switching the position of the *p*-bromo substituent of **124g** to a *meta* position as in **124j**, led to a marked, 17-fold decrease in IMP-1 inhibitory potency. This

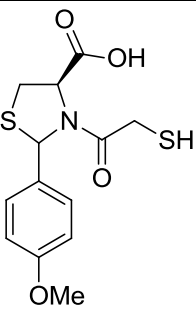
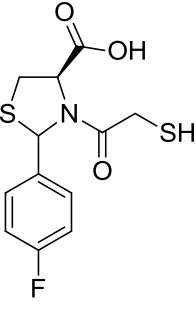
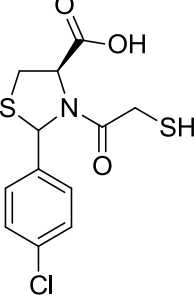
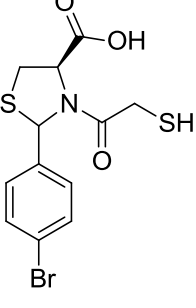
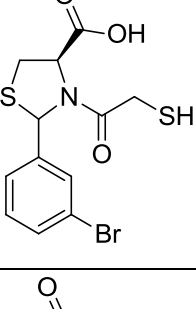
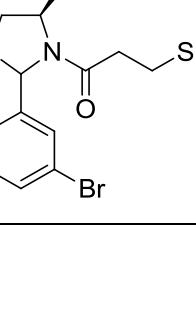
observation demonstrates that the *p*-halide position is crucial for the observed IMP-1 inhibitory potencies of the thiazolidine derivatives **124e**, **124f** and **124g**.

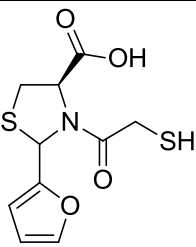
Furthermore, the addition of an extra methylene group between the thiol group and the amide group of **124a** didn't result in any significant effects on the IMP-1 inhibitory potency for **124b**. This effect was moderately observed for the *meta*-bromo derivative, **124k** which has a two-fold enhancement in inhibitory potency as compared to **124j**. The addition of methylene groups between the thiol group and the amide group only affects the inhibitory potency of the thiazolidines to a small extent.

Substitution of the 2-phenyl ring with a furan ring also didn't result in any significant changes in inhibitory potency for **124n**. As mentioned previously, the furan ring is a bioisostere of the phenyl ring (Section 3.3b).¹⁵

Table 4.2: The competitive (K_{ic}) and uncompetitive (K_{iuc}) inhibition constants (μM) of selected thiazolidine derivatives against IMP-1 (10 nM, containing BSA at a final conc. of $20 \mu\text{g mL}^{-1}$) at pH 7.0 and 25 °C, with varying concentrations of the penicillin G substrate (0.4-1.2 mM).

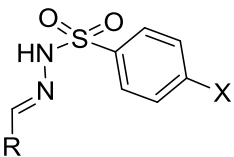
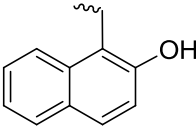
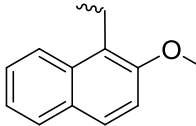
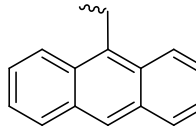
Inhibitor 124	Structure	K_{ic} (μM)	K_{iuc} (μM)
a		7.16 ± 3.12	-
b		8.78 ± 2.45	-

d		14.7 ± 7.3	-
e		4.20 ± 0.98	-
f		1.37 ± 0.41	-
g		0.57 ± 0.47	-
j		9.54 ± 3.17	-
k		4.03 ± 0.94	-

n		10.4 ± 3.1	-
----------	---	------------	---

“-“ Denotes a large value (10^1 - 10^2 mM range).

Table 4.3: The IC_{50} (μ M) data of *N*-arylsulfonyl hydrazones **127-130**, **a-c** against IMP-1 (4 nM, with a final BSA conc. of 1μ g ml⁻¹), with nitrocefin (20 μ M) as the substrate at pH 7.3, and 30 °C.¹³

Inhibitor 	X	IC_{50} (μ M)*		
		R		
		 (a)	 (b)	 (c)
127	I	17.5	6.3	3.0
128	Br	25	13	4.6
129	Cl	55	19	7.0
130	F	150	55	13.5

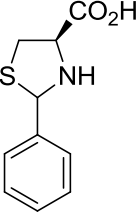
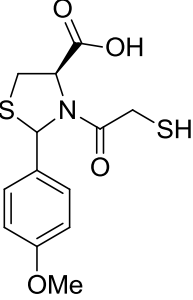
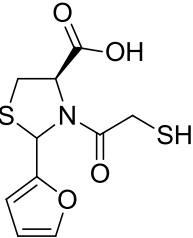
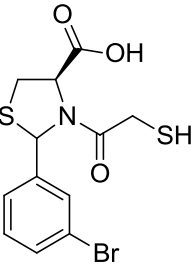
*The margin of error for the measurements were within 10%.

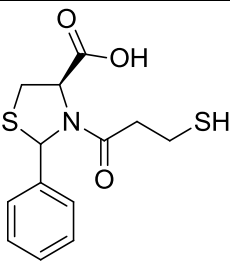
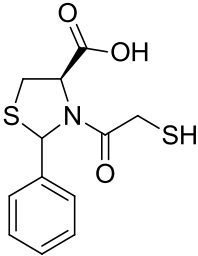
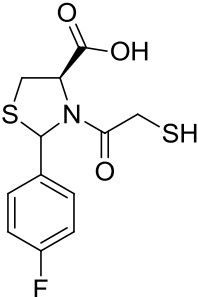
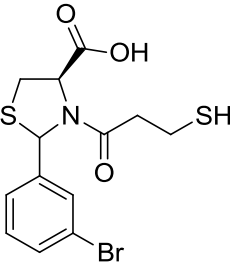
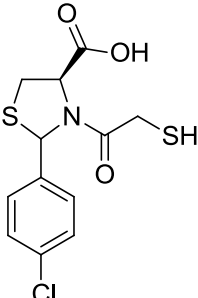
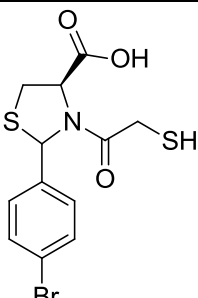
4.3 b) Computational modelling study

Both of the *2R*, *4R* and *2S*, *4R* diastereomer of the selected thiazolidine derivatives were docked separately into the active site of IMP-1 by using the Glide program. The docking scores of the *in silico* models, together with the binding affinities of the docked ligands are shown in Table 4.4. Like the Moldock score, the GlideScore is also a prediction of the binding affinity of the ligand with the enzyme.¹⁶ The bigger the magnitude of the GlideScore is, the greater the predicted binding affinity (Section 3.2).¹⁶ The docking results showed little variation in the GlideScore of the docked ligands. This observation is reflective of the K_i values of the inhibitors, which also exhibited a lack of distribution.

Nevertheless, the *2R*, *4R* and *2S*, *4R* diastereomer of the docked thiazolidine derivatives exhibit different binding modes, as previously described for those of **124a** (Section 4.1). The *2R*, *4R* diastereomers were predicted to bind to the zinc ions *via* the 4-carboxylate groups, whereas the *2S*, *4R* diastereomers were predicted to bind to the zinc ions through the thiolate groups.

Table 4.4: The GlideScore values (kcal mol^{-1}) and binding affinities (μM) of selected thiazolidine derivatives, including **120a** and the original co-crystallised ligand, **59** for comparison.

Ligand	Molecular structure	GlideScore (kcal mol^{-1})		Binding affinity (μM)
		<i>2R</i>	<i>2S</i>	
120a		-5.74	-7.50	>200*
124d		-7.59	-9.76	14.7 ± 7.3
124n		-7.82	-8.42	10.4 ± 3.1
124j		-7.47	-9.12	9.54 ± 3.17

124b		-7.78	-9.62	8.78 ± 2.45
124a		-8.53	-8.77	7.16 ± 3.12
124e		-8.39	-8.68	4.2 ± 0.98
124k		-7.64	-7.78	4.03 ± 0.94
124f		-8.34	-9.37	1.37 ± 0.41
124g		-8.56	-9.55	0.57 ± 0.47

59		-12.2	0.09*
-----------	--	-------	-------

*IC₅₀ values.

4.4 Conclusion

The SAR study of the mercapto-amide-linked thiazolidine derivatives **124a-o** demonstrated that the electronic nature of the substituent on the phenyl ring affects the IMP-1 inhibitory activity of the derivatives, with electron donating substituents having a diminishing effect on the inhibitory activity of the derivatives. Substitution of the phenyl ring with various electron withdrawing substituents such as a nitro or a trifluoromethyl group may be helpful in further examining this effect.

In addition, the IMP-1 inhibitory potency of the *p*-halide derivatives increases as the size of the halide substituent increases in the following order: Br > Cl > F. The position of the *p*-halide substituent on the phenyl ring is also essential for the observed high inhibitory potency of the *p*-halide derivatives.

Introduction of an additional methylene group between the thiol group and the amide group, or replacement of the phenyl ring with a furan ring, both have an insignificant effect on the IMP-1 inhibitory potency of the thiazolidine derivatives.

Computational modelling of the thiazolidine derivatives suggested the possibility of two distinct binding modes for each diastereomer.

4.5 Experimental

4.5 a) IMP-1 screening assay of the inhibitors

The screening assay was performed in triplicates, with penicillin G as the substrate and HEPES X (50 mM HEPES, 0.1 M NaCl, 100 μM ZnCl₂, pH 7.0) as the buffer at 25 °C. The final concentration of IMP-1 and penicillin G was 5 nM and 1 mM, respectively. Bovine serum albumin (final concentration of 20 μg ml⁻¹) was added to the enzyme solution for

enzyme stability. The inhibitors were assayed at final concentrations of 0.1, 1, 10 and 100 μM . The rate of penicillin G hydrolysis was monitored at 235 nm ($\epsilon = 936 \text{ M}^{-1} \text{ cm}^{-1}$) (Scheme 4.3). The percentage inhibition of an inhibitor was calculated based on the residual activity of the enzyme in the presence of the inhibitor (Equation 2.1).

4.5 b) IMP-1 K_i assay of the inhibitors

The K_i assay conditions are the same as the screening assay conditions, except that various inhibitor concentrations were assayed against different substrate concentrations. The final inhibitor concentrations assayed were: 0.2-50 μM , while the final substrate concentrations used were: 0.4, 0.5, 0.6, 0.8, 1.0, and 1.2 mM. The raw kinetic data were analysed by non-linear regression method, based on Equation 2.1, with the aid of WinCurveFit program (Kevin Raner Software). According to the Equation 2.2, it is assumed that the inhibitor is either competitive, uncompetitive or a mixed-mode inhibitor. The K_i plot of **124f** is shown in Figure 4.8 as a representative K_i plot of all the inhibitors assayed in this series.

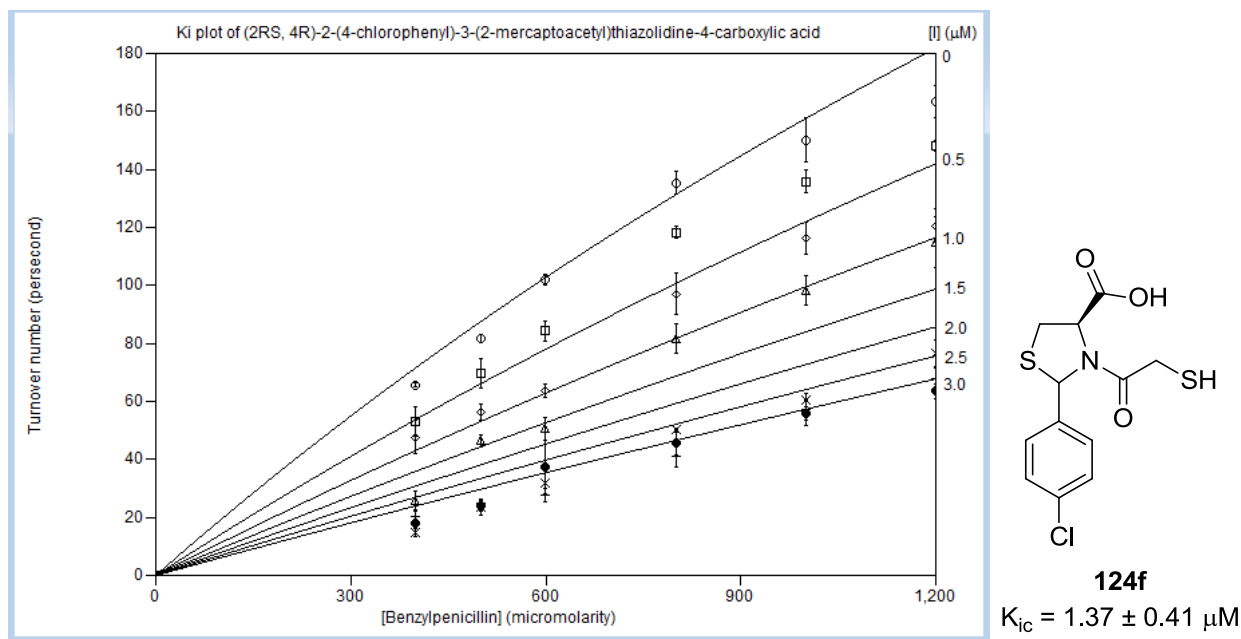


Figure 4.8: The K_i plot of thiazolidine **124f** ($r^2 = 0.98$).

References

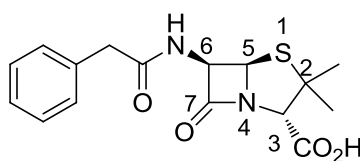
- (1) King, D. T.; Strynadka, N. C. J. *Future Medicinal Chemistry* **2013**, *5*, 1243.
- (2) Concha, N. O.; Janson, C. A.; Rowling, P.; Pearson, S.; Cheever, C. A.; Clarke, B. P.; Lewis, C.; Galleni, M.; Frère, J.-M.; Payne, D. J.; Bateson, J. H.; Abdel-Meguid, S. S. *Biochemistry* **2000**, *39*, 4288.
- (3) Moali, C.; Anne, C.; Lamotte-Brasseur, J.; Gros Lambert, S.; Devreese, B.; Van Beeumen, J.; Galleni, M.; Frère, J.-M. *Chemistry and Biology* **2003**, *10*, 319.
- (4) Scrofani, S. D. B.; Chung, J.; Huntley, J. J. A.; Benkovic, S. J.; Wright, P. E.; Dyson, H. J. *Biochemistry* **1999**, *38*, 14507.
- (5) Fast, W.; Sutton, L. D. *Biochimica et Biophysica Acta (BBA) - Proteins and Proteomics* **2013**, *1834*, 1648.
- (6) Chen, P.; Horton, L. B.; Mikulski, R. L.; Deng, L.; Sundriyal, S.; Palzkill, T.; Song, Y. *Bioorganic and Medicinal Chemistry Letters* **2012**, *22*, 6229.
- (7) Feng, L.; Yang, K.-W.; Zhou, L.-S.; Xiao, J.-M.; Yang, X.; Zhai, L.; Zhang, Y.-L.; Crowder, M. W. *Bioorganic and Medicinal Chemistry Letters* **2012**, *22*, 5185.
- (8) Goto, M.; Takahashi, T.; Yamashita, F.; Koreeda, A.; Mori, H.; Ohta, M.; Arakawa, Y. *Biological and Pharmaceutical Bulletin* **1997**, *20*, 1136.
- (9) Mustaddiq, S.; *Unpublished work*, University of Queensland: 2014.
- (10) Gududuru, V.; Hurh, E.; Dalton, J. T.; Miller, D. D. *Journal of Medicinal Chemistry* **2005**, *48*, 2584.
- (11) Arjomandi, O. K., *Synthesis of Inhibitors of Metallo- β -lactamase (IMP-1)*, PhD, University of Queensland, 2015.
- (12) Laraki, N.; Franceschini, N.; Rossolini, G. M.; Santucci, P.; Meunier, C.; de Pauw, E.; Amicosante, G.; Frère, J. M.; Galleni, M. *Antimicrobial Agents and Chemotherapy* **1999**, *43*, 902.
- (13) Siemann, S.; Evanoff, D. P.; Marrone, L.; Clarke, A. J.; Viswanatha, T.; Dmitrienko, G. I. *Antimicrobial Agents and Chemotherapy* **2002**, *46*, 2450.
- (14) Lu, Y.; Shi, T.; Wang, Y.; Yang, H.; Yan, X.; Luo, X.; Jiang, H.; Zhu, W. *Journal of Medicinal Chemistry* **2009**, *52*, 2854.
- (15) Urbano, M.; Guerrero, M.; Zhao, J.; Velaparthi, S.; Schaeffer, M.-T.; Brown, S.; Rosen, H.; Roberts, E. *Bioorganic and Medicinal Chemistry Letters* **2011**, *21*, 5470.
- (16) Friesner, R. A.; Murphy, R. B.; Repasky, M. P.; Frye, L. L.; Greenwood, J. R.; Halgren, T. A.; Sanschagrin, P. C.; Mainz, D. T. *Journal of Medicinal Chemistry* **2006**, *49*, 6177.

(17) Molegro Virtual Docker, version 6.0.1, CLC bio, 2014.

CHAPTER 5: CONCLUSIONS AND FUTURE STUDIES

5.1 Conclusions

The naturally-occurring β -lactam ring is a unique molecular structure that mimics part of the structure of the bacterial cell wall,¹ that consists of a complex structure of polymeric glycan strands, which are cross-linked by peptide bonds, with the involvement of the transpeptidase enzyme.² As such, β -lactam bearing compounds, such as penicillin G (1) have the propensity to be mistakenly recognised as the actual bacterial cell wall material, and thus form stable acyl-enzyme complexes with bacterial transpeptidase.¹ This interference leads to the disruption of the bacterial cell wall biosynthesis, which ultimately leads to bacterial cell death.¹ β -Lactams are thus classified as antibiotic chemical, an agent that has an adverse effect on the bacterial cell and not on the eukaryotic host.³ Since its administration in the 1940's, β -lactam antibiotics have been the cornerstone of chemotherapy for bacterial infections, with over 50% of all antibiotics currently in use bearing the β -lactam ring.^{1,4}



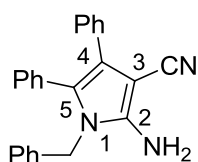
Penicillin G 1

One of the bacterial responses to the widespread use of β -lactam antibiotics is in the form of biochemical resistance, *i.e.* the expression of β -lactam degrading enzymes, or β -lactamases.¹ The zinc-dependent metallo- β -lactamases, MBLs is one of the classes of the β -lactamase enzymes.^{1,5} Currently, of major concern is the rapid, global distribution of MBLs, particularly the plasmid-mediated B1 MBLs, which are transferable on mobile genetic elements among related and unrelated bacterial species.⁶ Furthermore, the B1 MBLs exhibit a broad-spectrum β -lactam substrate profile.⁶ Thus far, there are no clinical inhibitors available for the inhibition of MBLs.^{7,8} In light of these findings, the B1 MBLs, such as the Imipenemase 1 (IMP-1) enzyme present as an attractive biological target for medicinal chemistry study.

The active site architecture of IMP-1 is characterised by the presence of two zinc ions in the active site, Zn1 and Zn2, as well as a mobile β -hairpin L3 loop adjacent to the active site (Figures 1.16 and 1.17, Section 1.9).⁹⁻¹¹ The zinc ions are bridged by a hydroxide ion that is proposed to be the attacking nucleophile on the β -lactam carbonyl group (Figure 1.17).⁹ Studies have shown that the L3 loop is stabilised upon inhibitor or substrate binding.^{8,9} In addition, the active site also consists of two conserved amino acid residues-Lys161 (224), which binds to the 3-carboxylate group of penicillins *via* a salt bridge interaction and Asn167 (233), that is part of the oxyanion hole that stabilises the C-7 carbonyl oxygen of penicillins upon nucleophilic attack (Figure 4.2, Section 4.1).⁹

Thus far, MBL inhibitor design has been centred around the zinc ions, hydrogen donor region, such as Lys161 (224) and mobile L3 loop.¹² This approach has led to the successful design of mercaptocarboxylate- and dicarboxylate-type inhibitors with binding affinities in the submicro- to nanomolar range.¹²

In 2012, the McGeary and Schenk group were the first to identify 2-amino-1-benzyl-4,5-diphenyl-1*H*-pyrrole-3-carbonitrile (**65**) as a competitive IMP-1 inhibitor.¹³ Preliminary MVD computational modelling of this structurally unique inhibitor bound with IMP-1 suggested hydrophobic contacts between the mobile loop and the vicinal diphenyl side chains of **65**, a hydrogen bond interaction between the 3-carbonitrile nitrogen and the Lys161 (224) terminal amino group, and another hydrogen bond interaction between one of the 2-amino hydrogens and His139 (196), which is a Zn1 chelator (Figure 2.1, Section 2.2). Nonetheless, the *in silico* model did not predict any interactions between **65** and the zinc ions. A structure-activity relationship (SAR) study of **65** was therefore initiated to examine these *in silico* predictions.



65

$$K_{ic} = 21 \pm 10 \mu\text{M}$$

Chapter 2 described the SAR study of the 2-amino group of **65**, whereby a series of *N*-acyl derivatives were synthesised and assayed against IMP-1 (Figure 5.1). The corresponding synthetic *N,N*-diacyl imide intermediates were isolated and evaluated for their inhibitory potency.

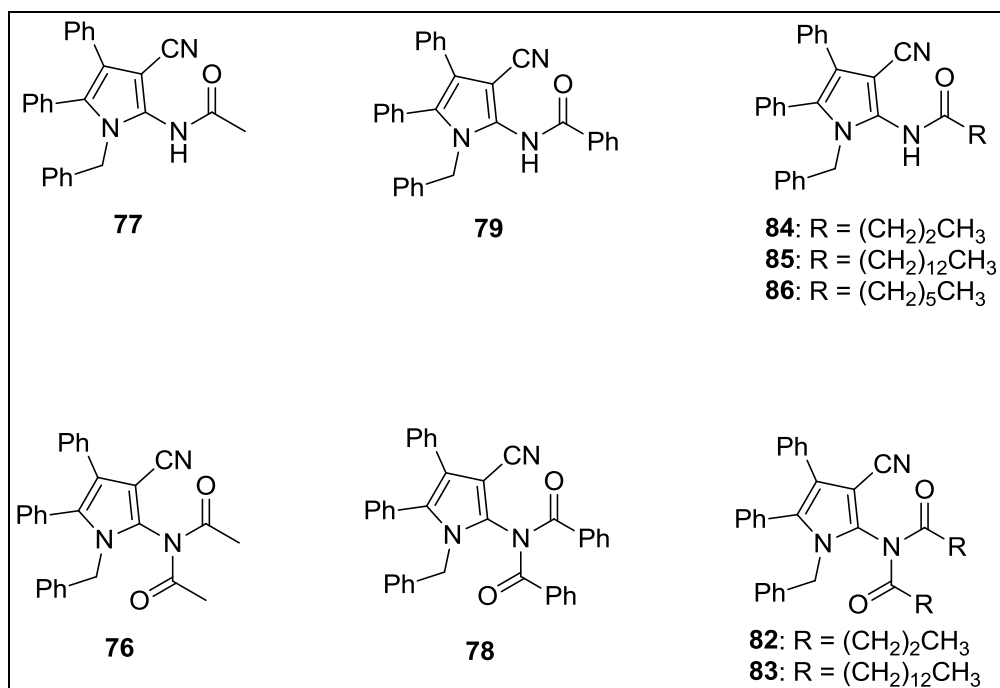


Figure 5.1: The first series of *N*-substituted derivatives of pyrrole **65**.

The IMP-1 screening results of the first series of *N*-substituted pyrrole **65** derivatives showed that introduction of an *N*-arylamide group enhances the inhibitory potency of the pyrrole moderately. This finding led to the design of a second series of *N*-substituted pyrrole derivatives (Figure 5.2). In addition, a stability test of the imide derivatives in the presence of IMP-1 revealed that the imides resist the hydrolytic activity of the enzyme.

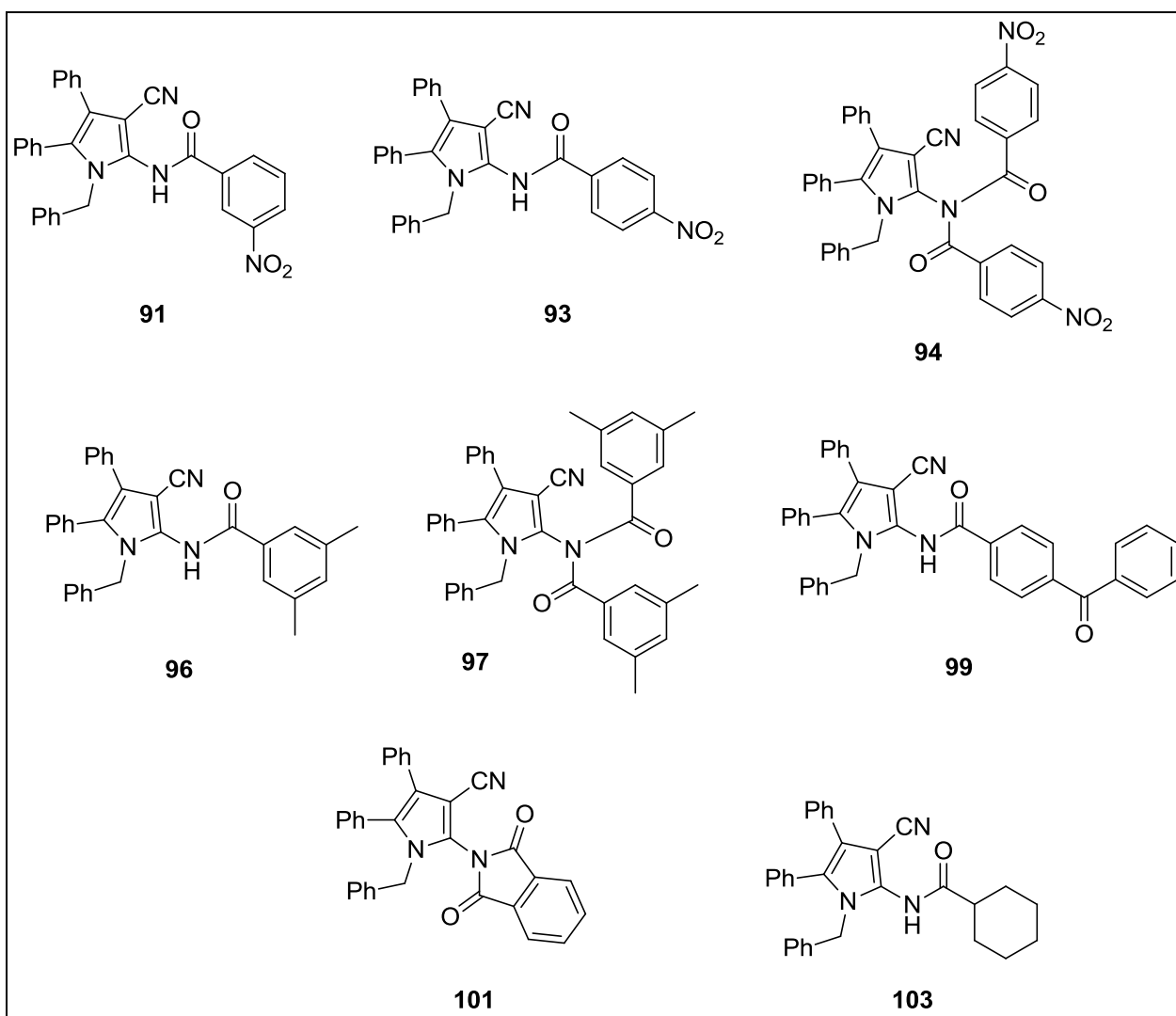


Figure 5.2: The second series of *N*-substituted derivatives of pyrrole **65**.

N-4-Nitrobenzamide **93** and 4-benzoyl-*N*-benzamide **99** were subsequently identified as the two most potent IMP-1 inhibitors for this class of compounds, with a 14- to 17-fold enhancement in IMP-1 inhibitory potency compared to the pyrrole lead compound **65** (Figure 5.3). The kinetic assay results suggested that **93** is a purely competitive inhibitor, whereas **99** is a solely uncompetitive inhibitor. Glide computational modelling of **93** in complex with IMP-1 suggested that one of the 4-nitro oxygens has direct coordination with both of the zinc ions, which may explain its purely competitive inhibition mode (Figure 2.7). Nevertheless, an X-ray crystal structure is still needed to ascertain the actual binding mode of the inhibitor with the enzyme. On the contrary, the *in silico* model of **99** bound with IMP-1 suggested that the active site of the enzyme may not be big enough to accommodate the inhibitor (Figure 2.9). Inhibitor **99** may probably bind to an enzyme site distinct from the active site.

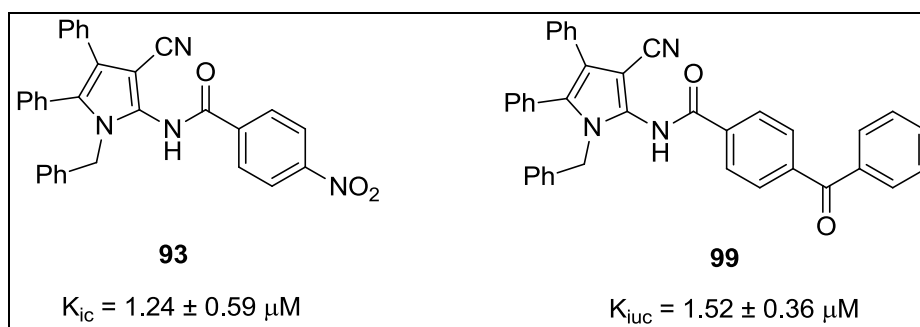


Figure 5.3: The two most potent *N*-arylamide derivatives of pyrrole **65**.

In addition, the position of the nitro group on the phenyl ring of the *N*-nitrobenzamide derivatives **91** and **93** influences both the IMP-1 inhibitory potency and binding modes of the derivatives.

The SAR of the 3-cyano group, vicinal 4,5-diphenyl and *N*-benzyl side chains of pyrrole **65** were described in Chapter 3. Figure 5.4 shows the modified synthetic pyrrole **65** derivatives which were used for this study.

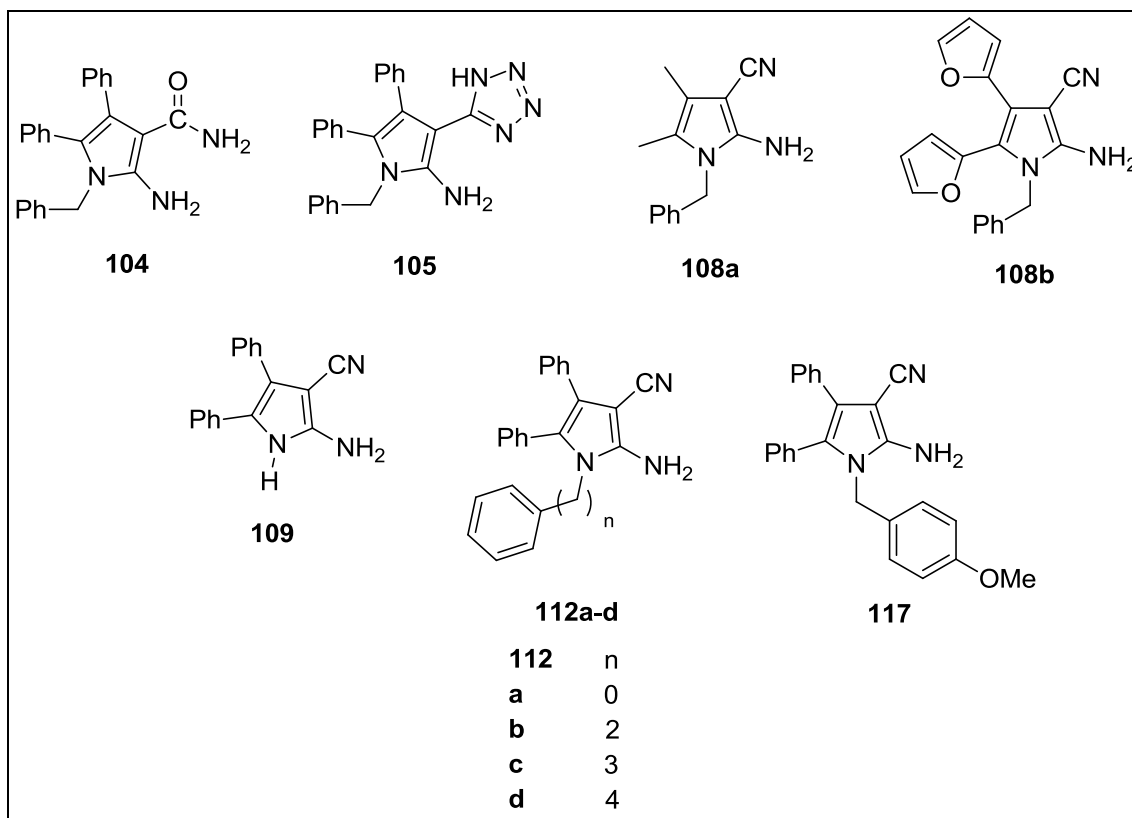


Figure 5.4: The synthetic derivatives which were used in the SAR study of the 3-cyano group, vicinal 4,5-diphenyl and *N*-benzyl side chains of pyrrole **65**.

The design of tetrazole **105** was based on a preliminary MVD docking simulation of deprotonated tetrazole **105** in complex with IMP-1 (Figure 3.3). The *in silico* model predicted ligand-Zn interactions *via* the tetrazolyl nitrogens, and a high binding affinity for **105**. An attempt at derivatising pyrrole **65** into tetrazole **105** was only successful by using aluminium triazide as the azide reagent.

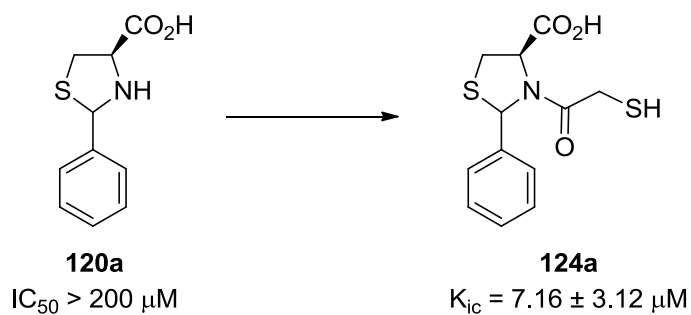
Contrary to the docking result, tetrazole **105** exhibited a significant decrease in IMP-1 inhibitory activity, while carboxamide **104** didn't show any inhibitory activity against the enzyme. Therefore, retention of the 3-cyano group is crucial for maintenance of IMP-1 inhibitory activity for pyrrole **65**.

The significant loss in IMP-1 inhibitory activity for **108a**, but retention of IMP-1 inhibitory activity for **108b** highlights the importance of the vicinal 4,5-diphenyl side chains in making favourable hydrophobic contacts with the L3 mobile loop.

All attempts at deprotecting pyrrole **65** were unsuccessful. Deprotection of the pyrrole was only successful on the *N*-4-methoxybenzyl derivative **117**, by using aluminium chloride as the deprotection agent.

Removal of the *N*-4-methoxybenzyl side chain as in **109**, or omission of the benzylic carbon as in **107a** led to a significant loss of IMP-1 inhibitory activity. Furthermore, chain lengthening between the pyrrole ring nitrogen and phenyl ring didn't result in improvement of IMP-1 inhibitory activity. Therefore, the *N*-benzyl chain is vital for the observed IMP-1 inhibitory activity of pyrrole **65**.

Chapter 4 described the optimisation of (2*RS*, 4*R*)-2-phenylthiazolidine-4-carboxylic acid (**120a**), as an IMP-1 inhibitor by linking the ring nitrogen of **120a** with a highly-affinitive zinc chelator, such as mercaptoacetic acid (Scheme 5.1).



Scheme 5.1: The optimisation of thiazolidine **120a** as a potent IMP-1 inhibitor, **124a**.

The work was later expanded to include a range of mercapto-amide-linked thiazolidines **124a-o** (Figure 5.5).

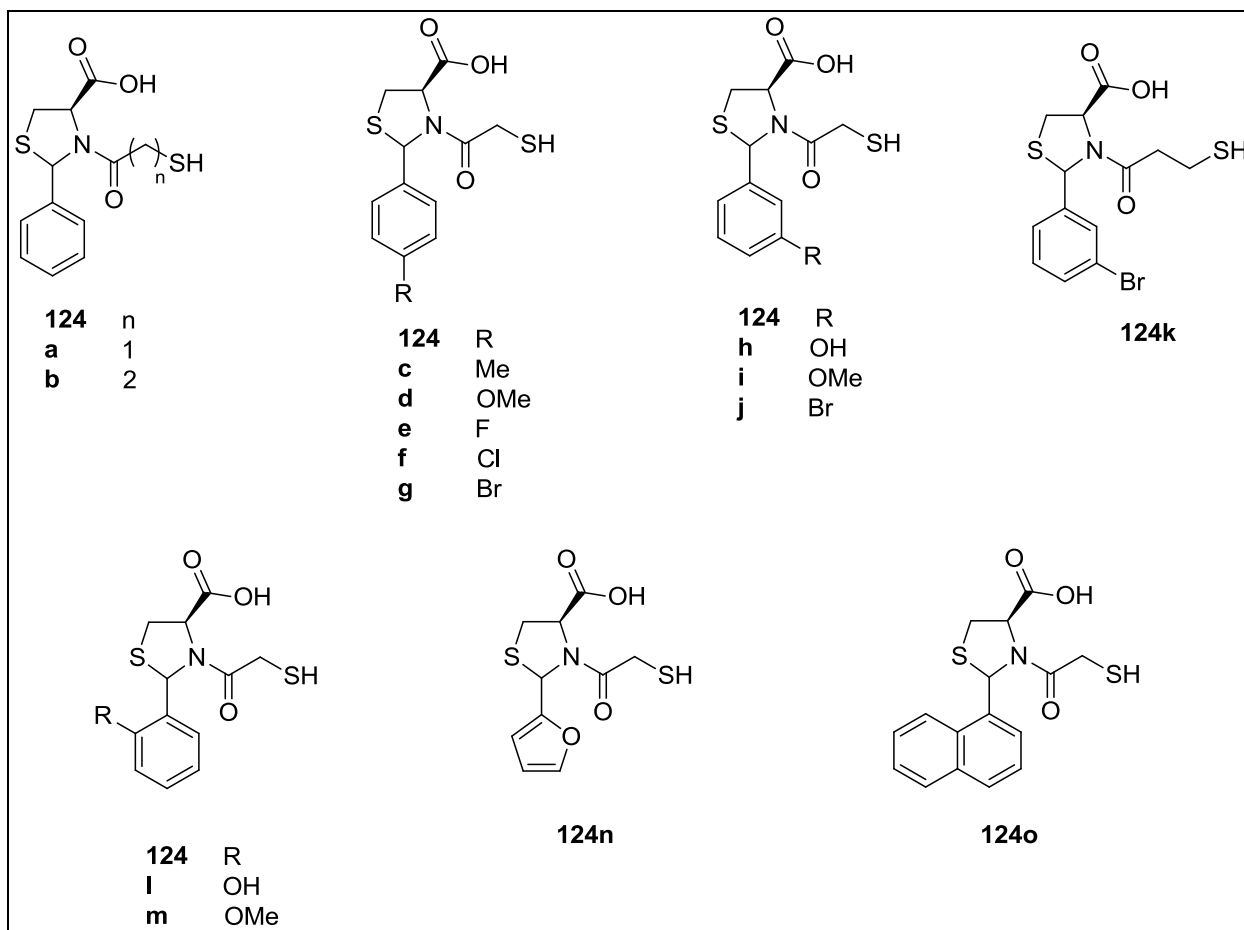


Figure 5.5: The mercapto-amide-linked thiazolidines **124a-o**, which were studied.

The SAR of thiazolidines **124a-o** demonstrated that the electronic nature of the substituent has a significant effect on the IMP-1 inhibitory potency of the derivatives. In addition, the IMP-1 inhibitory potency of the *p*-halide derivatives increases as the size of the halide group increases, suggesting the involvement of halogen bonding in inhibitor-enzyme interaction.¹⁴ Furthermore, the addition of a methylene group between the thiol group and amide group has no significant effect on the IMP-1 inhibitory potency of the thiazolidines.

Glide computational modelling of the thiazolidines suggested different binding modes for each diastereomer. The *2R*, *4R* diastereomers were predicted to bind to the zinc ions *via* the carboxylate groups, while the *2S*, *4R* diastereomers were predicted to bind in an S-Zn fashion.

5.2 Future studies

Computational modelling by either MVD or Glide program remains inconclusive in predicting the actual binding modes of pyrrole **65** or its synthetic derivatives with IMP-1. An X-ray crystal structure of either pyrrole **65**, or its most potent derivative, *N*-4-nitrobenzamide **93** bound with the enzyme is therefore needed to ascertain the actual binding modes of the inhibitor with the enzyme. This will set the direction for future SAR studies involving pyrrole **65**. Work in obtaining an X-ray crystal structure of **93** in complex with the B3 AIM-1 enzyme is currently underway in the Schenk group.

Nevertheless, there are a few suggestions for future SAR studies of pyrrole **65** (Figure 5.6). *N*-2-nitrobenzamide **131** can be introduced to study the effect of the nitro group position in IMP-1 inhibitory activity for the *N*-nitrobenzamide series. In addition, bulky groups, such as a methoxy or a *t*-butyl group can be introduced on the vicinal 4,5-diphenyl rings to study their effect in hydrophobic contacts with the enzyme (**132**). Various electron withdrawing groups and halide substituents can also be introduced on the *N*-benzyl ring to study the substituent effect on IMP-1 inhibitory (**133**).

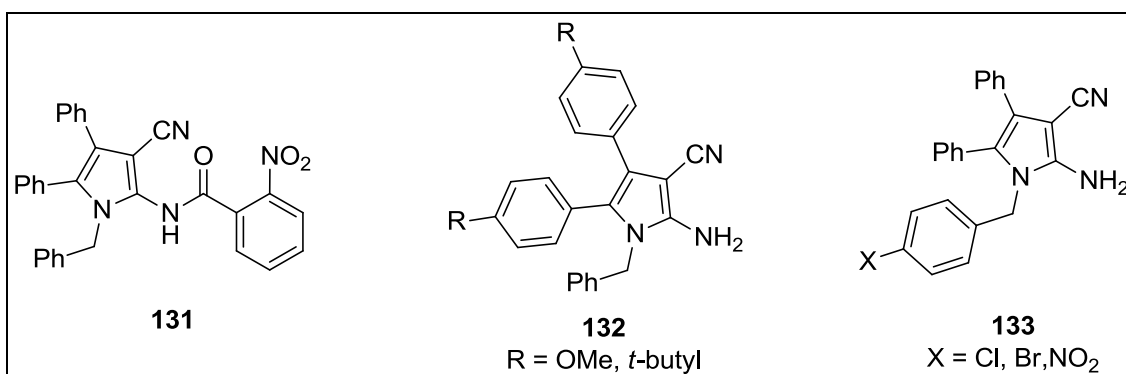


Figure 5.6: Suggestions for the future SAR study of pyrrole **65**.

Pyrrole **65** and its potent synthetic derivatives can also be assayed against another B1 MBL, such as NDM-1, which has a pronounced L3 loop that may make favourable hydrophobic contacts with the vicinal 4,5-diphenyl side chains of the pyrrole.⁸ This work is currently in progress in the Schenk group.

As for the mercapto-amide-linked thiazolidine series, a few more examples are needed to complete the SAR study of this class of inhibitors (Figure 5.7). One of the suggested examples is the *p*-iodo derivative **124p**, which is needed to further reinforce the view that the IMP-1 inhibitory potency increases as the *p*-halide size increases. Furthermore, electron withdrawing groups, such as a trifluoromethyl group or a nitro group can be introduced on the phenyl ring to study the effect of these substituents on IMP-1 inhibitory potency. A methylene group can also be introduced between the phenyl ring and thiazolidine ring to study the effect of increased ring flexibility in IMP-1 inhibitory activity.

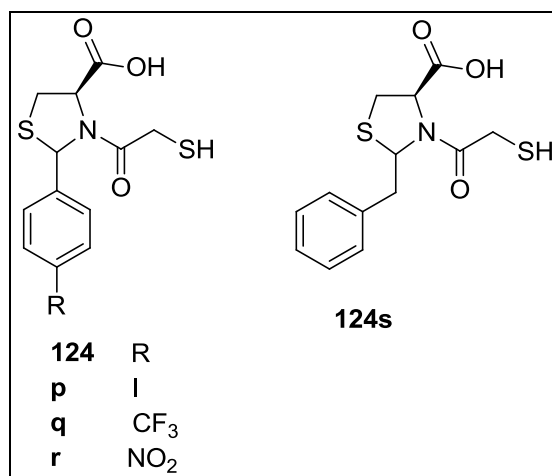


Figure 5.7: Suggested examples for the future SAR study of thiazolidines.

References

- (1) Fisher, J. F.; Meroueh, S. O.; Mobashery, S. *Chemical Reviews* **2005**, *105*, 395.
- (2) Lee, W.; McDonough, M. A.; Kotra, L. P.; Li, Z.-H.; Silvaggi, N. R.; Takeda, Y.; Kelly, J. A.; Mobashery, S. *Proceedings of the National Academy of Sciences* **2001**, *98*, 1427.
- (3) Walsh, C. *Nature* **2000**, *406*, 775.
- (4) Bush, K. *Annals of the New York Academy of Sciences* **2010**, *1213*, 1.
- (5) Drawz, S. M.; Bonomo, R. A. *Clinical Microbiology Reviews* **2010**, *23*, 160.
- (6) Bebrone, C. *Biochemical Pharmacology* **2007**, *74*, 1686.
- (7) McGeary, R. P.; Schenk, G.; Guddat, L. W. *European Journal of Medicinal Chemistry* **2014**, *76*, 132.
- (8) Zhang, H.; Hao, Q. *The Federation of American Societies for Experimental Biology Journal* **2011**, *25*, 2574.
- (9) Palzkill, T. *Annals of the New York Academy of Sciences* **2013**, *1277*, 91.
- (10) Toney, J. H.; Hammond, G. G.; Fitzgerald, P. M. D.; Sharma, N.; Balkovec, J. M.; Rouen, G. P.; Olson, S. H.; Hammond, M. L.; Greenlee, M. L.; Gao, Y.-D. *Journal of Biological Chemistry* **2001**, *276*, 31913.
- (11) Concha, N. O.; Janson, C. A.; Rowling, P.; Pearson, S.; Cheever, C. A.; Clarke, B. P.; Lewis, C.; Galleni, M.; Frère, J.-M.; Payne, D. J.; Bateson, J. H.; Abdel-Meguid, S. S. *Biochemistry* **2000**, *39*, 4288.
- (12) Fast, W.; Sutton, L. D. *Biochimica et Biophysica Acta (BBA) - Proteins and Proteomics* **2013**, *1834*, 1648.
- (13) Hussein, W. M.; Fatahala, S. S.; Mohamed, Z. M.; McGeary, R. P.; Schenk, G.; Ollis, D. L.; Mohamed, M. S. *Chemical Biology and Drug Design* **2012**, *80*, 500.
- (14) Lu, Y.; Shi, T.; Wang, Y.; Yang, H.; Yan, X.; Luo, X.; Jiang, H.; Zhu, W. *Journal of Medicinal Chemistry* **2009**, *52*, 2854.

APPENDIX 1: THE EXPRESSION AND PURIFICATION OF IMP-1

Expression of IMP-1^{1,2}

Competent BL21 (DE3) *E. coli* cells were transformed by pET47b-IMP-1 plasmid *via* the heat-shock method at 42 °C. The transformed cells were then cultured in LB broth (4 x 20 mL) supplemented with kanamycin (50 µg ml⁻¹) at 30 °C for 14 h. The starter culture was subsequently grown at 37 °C in Terrific Broth (4 x 500 mL) supplemented with kanamycin (50 µg ml⁻¹) and ZnCl₂ (25 µM) to an optical density at 600 nm (OD₆₀₀) of 0.4-0.6, before induction with IPTG (1 mM).* The cells were then incubated for 24 h at 25 °C, for enzyme expression to take place. The cells were finally harvested by centrifugation at a speed of 5000 rpm for 20 min at 4 °C. The cell pellet obtained (the average mass from two preparations was 25.059 g) was stored at -20 °C until ready to be extracted and purified.

*Care must be taken to ensure that the OD₆₀₀ doesn't exceed 0.6, for optimum enzyme induction. An OD₆₀₀ of 0.4 and 0.58 was achieved within 30 and 45 minutes of culture growth at 37 °C, respectively.

Extraction of IMP-1 from the cell pellet^{1,2}

The frozen cell pellet was re-suspended in 18 mL of HEPES A (50 mM HEPES, 500 µM ZnCl₂, pH 7.0) and lysed (breaking up of the cell wall) by the addition of lysozyme (0.2 mg ml⁻¹) and one tablet of Roche EDTA-free protease inhibitor cocktail (25 mg), followed by sonication. MgCl₂ (10 mM) and Roche DNase I (1 µg per 1 mL mixture) was added to the lysate mixture. The lysate was left for 20 mins (in order for the DNase I to take effect) at 0 °C prior to centrifugation at 12500 rpm for 32 min at 4 °C.

Purification of crude IMP-1^{1,2}

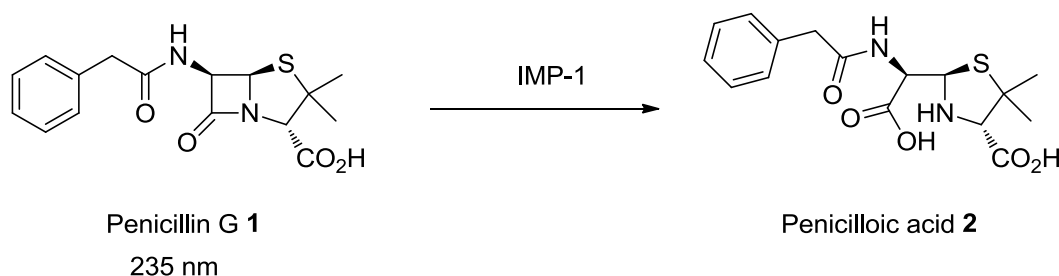
The supernatant obtained from the previous centrifugation (13 mL) was filtered through a 0.22 µm Milipore membrane filter before being loaded on a SP-sepharose cation exchange column (GE Healthcare).* The enzyme was eluted with HEPES A over a gradient of 0–1.0 M NaCl. The eluted fractions were assayed for IMP-1 activity with penicillin G (0.5 mM) as the substrate. The fractions containing IMP-1 were pooled together and concentrated to 5 ml prior to being loaded on a Sephacyl S-200 gel filtration size exclusion column (GE Healthcare).* The enzyme was eluted with HEPES A. Fractions

that were active against penicillin G were pooled and stored at -20 °C, with 15% glycerol added to the enzyme solution as a cryoprotectant.

*Purification by the SP-sepharose and S-200 column was necessary to remove plasmid DNA and high-molecular weight impurities, respectively.³

Enzymatic kinetic assay²

The fractions obtained from each step of fast protein liquid column chromatography (FPLC) were assayed for IMP-1 enzyme activity by using penicillin G as the substrate (500 μM final conc.) and HEPES X as the buffer (50 mM HEPES, 0.1 M NaCl, 100 μM ZnCl₂, pH 7.0). The activity of IMP-1 was measured as by monitoring the rate of penicillin G consumption at 235 nm ($\epsilon = 936 \text{ M}^{-1} \text{ cm}^{-1}$), pH 7.0 and 25 °C (Scheme A.1.1).



Scheme A.1.1: The rate of penicillin G consumption at 235 nm as the measurement of IMP-1 activity.

Enzyme quantification^{1,2}

Enzyme quantification was carried out by measuring the absorbance of the enzyme at 280 nm ($\epsilon = 44620 \text{ M}^{-1} \text{ cm}^{-1}$).

Results and discussion

The chromatogram of the elution profile of IMP-1 from the SP-sepharose column is shown in Figure A1.1. Based on the chromatogram, fractions 5, 10, 11, 12, 13, 14, 20, 25, 32, 34, 39, 45, 46, 48 and 49 were selected and assayed for IMP-1 activity (Table A.1.1). Fractions exhibiting IMP-1 enzyme activity greater than $0.001 \mu\text{mol min}^{-1}$, *i.e.* fractions 12-48 were pooled, concentrated and purified by the S-200 column.

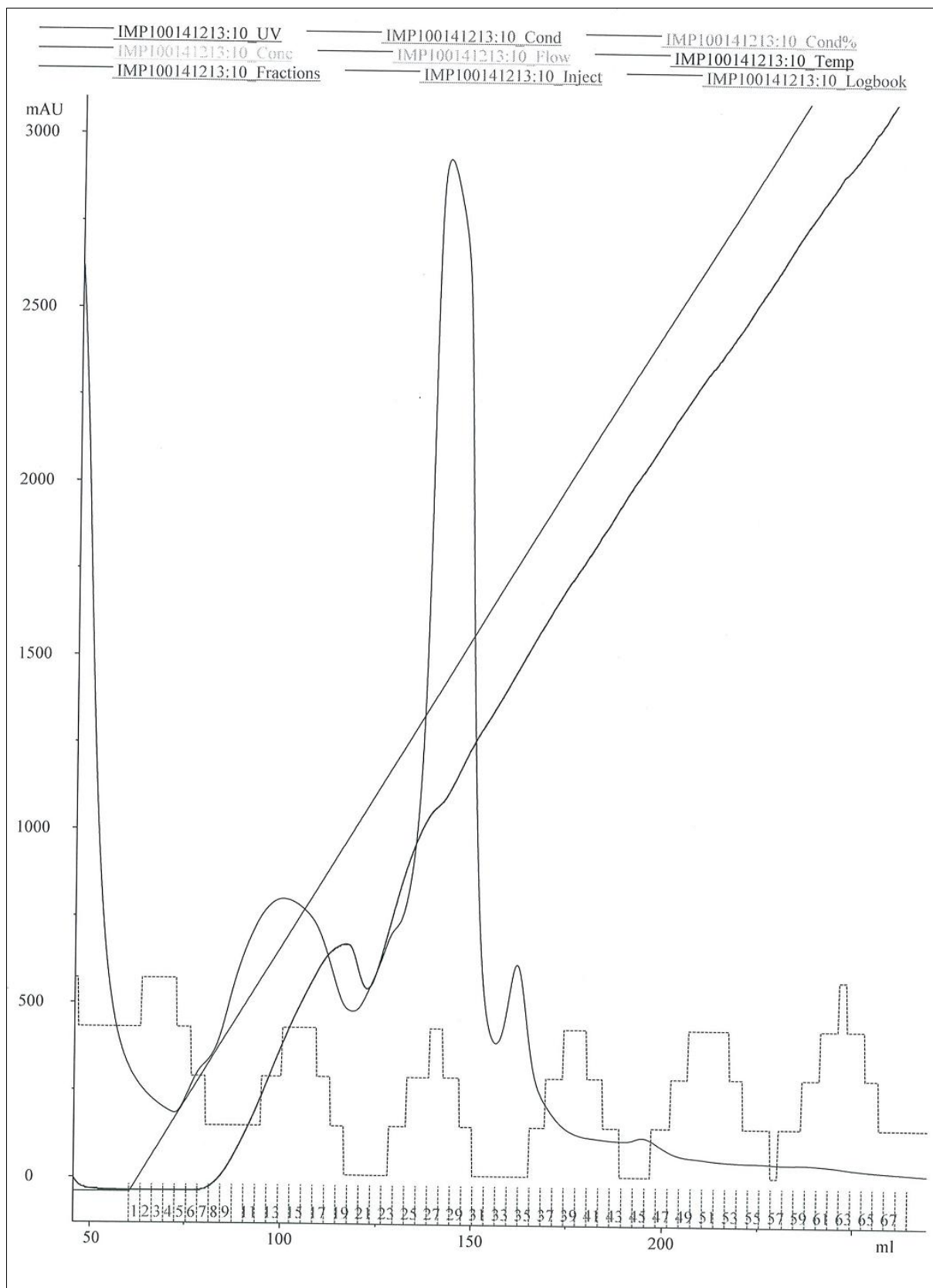


Figure A.1.1: The chromatogram of the elution profile of IMP-1 from the SP-sepharose column, eluted with HEPES A over a gradient of 0–1.0 M NaCl, pH 7.0 at a flow rate of 4.0 ml min⁻¹.

Table A.1.1: The IMP-1 enzyme activity ($\mu\text{mol min}^{-1}$) of fractions eluted from the SP-sepharose column with penicillin G (500 μM) as the substrate, at pH 7.0, 25 °C.

Fractions	IMP-1 enzyme activity ($\mu\text{mol min}^{-1}$)
5	-0.001
10	-0.002
11	0.001
12	0.016
13	0.010
14	0.020
20	0.125
25	0.322
32	0.242
34	0.116
39	0.045
45	0.023
46	0.023
48	0.019
49	0.001

The chromatogram of the elution profile of IMP-1 from the S-200 column is shown in Figure A.1.2. Based on the chromatogram, fractions 12, 18, 23, 30, 33, 40 and 57 were selected, assayed for IMP-1 enzyme activity and quantified (Table A.1.2). Fractions 10-14, 15-19, 20-22, 23-29, 30-32 and 33-40 were finally pooled and stored at -20 °C with 15% glycerol added to the enzyme solution as a cryoprotectant.

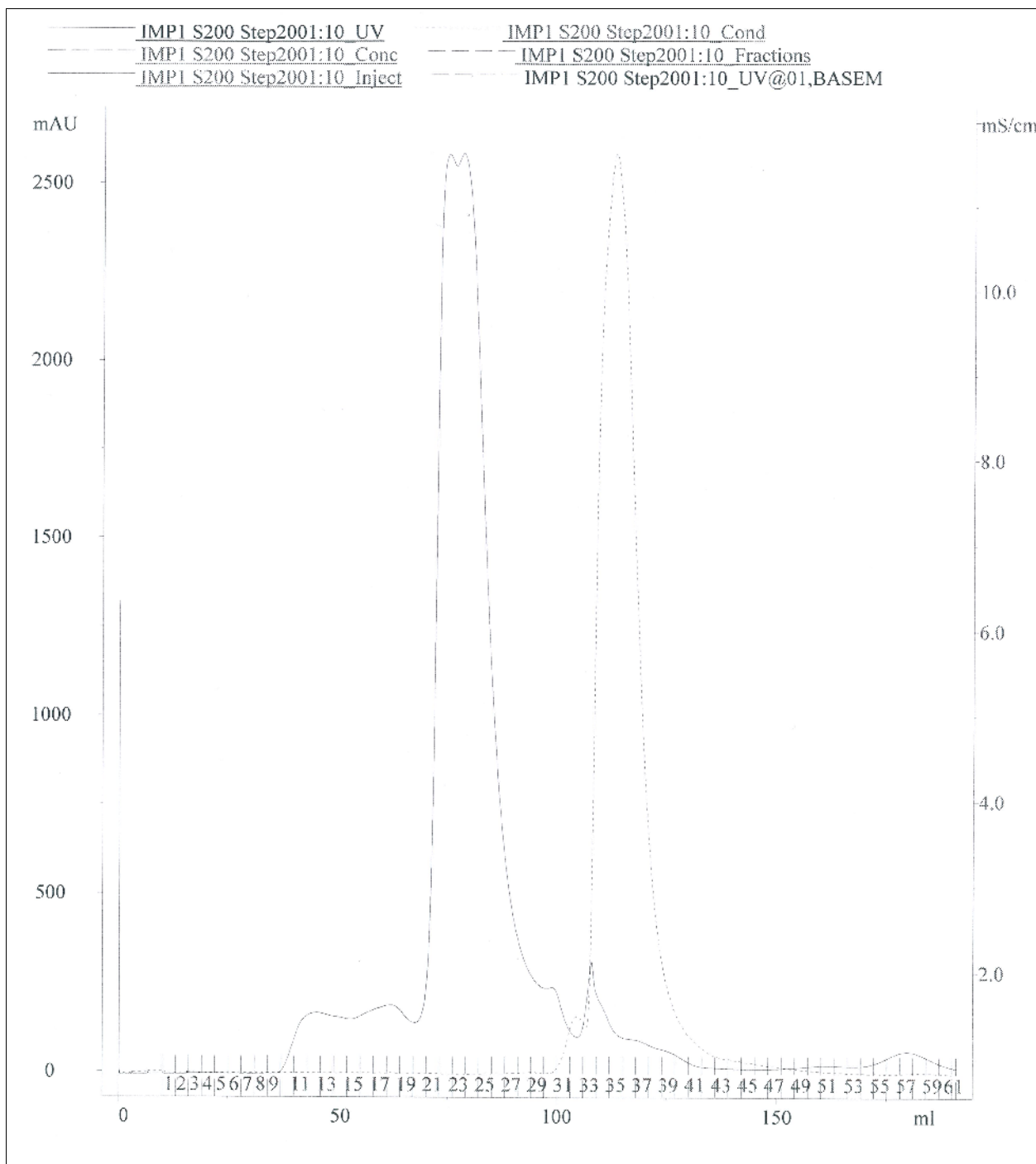


Figure A.1.2: The chromatogram of the elution profile of IMP-1 from the S-200 column, eluted with HEPES A, pH 7.0 at a flow rate of 0.5 ml min^{-1} .

Table A.1.2: The IMP-1 specific activity ($\mu\text{mol min}^{-1}$), enzyme amount (mg), and turnover number, k_{cat} (s^{-1}) of fractions eluted from the S-200 column, with penicillin G (500 μM) as the substrate, at pH 7.0, 25 °C.

Fraction	Enzyme activity ($\mu\text{mol min}^{-1}$)	Enzyme conc. (μM)	Enzyme amount (mg)	Specific activity ($\mu\text{mol mg}^{-1} \text{min}^{-1}$)	k_{cat} (s^{-1})
12	0.039	25.4	0.007	5.68	2.56
18	0.104	35.6	0.010	10.9	4.89
23	0.032	108	0.003	11.1	5.00
30	0.090	47.5	0.013	7.05	3.17
33	0.172	9.41	0.003	67.8	30.5
40	0.018	9.41	0.003	6.94	3.12
57	0.015	ND	ND	ND	ND

“ND” denotes not determined.

The overall yield of IMP-1 obtained from two litres of culture was 12 mg. To evaluate the purity of the IMP-1 enzyme obtained, an SDS-PAGE analysis was run on a sample of the purified enzyme (Figure A.1.3). The analysis showed a single band, corresponding to 25 kDa, which is close to the expected molecular weight of IMP-1, which is 27 kDa.² Therefore, IMP-1 was successfully expressed and purified from known protocol.

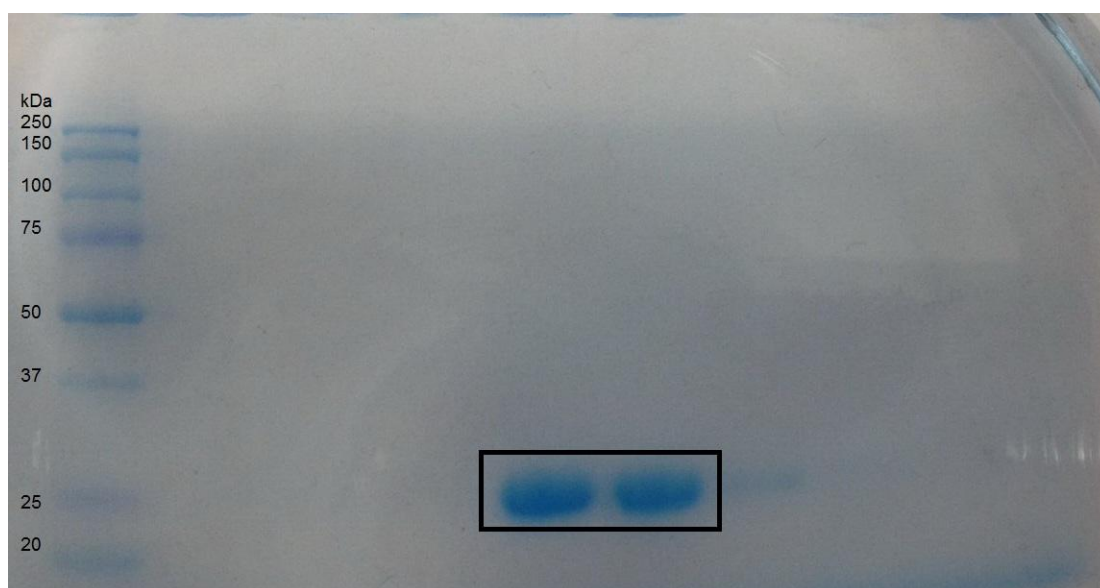


Figure A.1.3: The SDS-PAGE of purified IMP-1, stained with Bio-Safe Coomassie G-250. The band from two enzyme samples (in the black box) corresponds to 25kDa of the marker protein on the left.

References

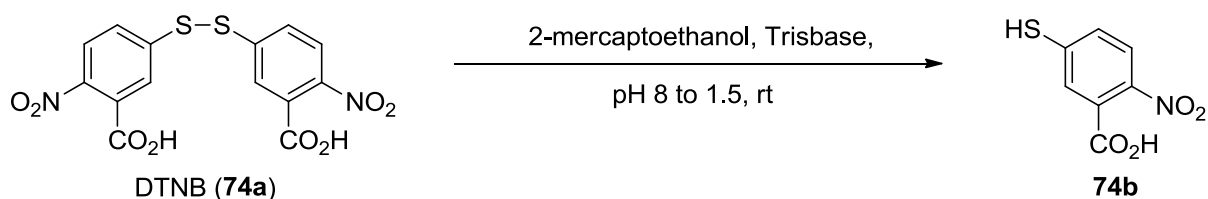
- (1) Leung, E. W. W., *Structure-function Relationships in Metal Dependent Enzymes*, PhD, The University of Queensland, 2010.
- (2) Vella, P. *The Development of New Drug Leads to Combat Bacterial Resistance towards Antibiotics*, PhD, The University of Queensland, 2012.
- (3) Scrofani, S. D. B.; Chung, J.; Huntley, J. J. A.; Benkovic, S. J.; Wright, P. E.; Dyson, H. J. *Biochemistry* **1999**, 38, 14507.

APPENDIX 2: PREPARATION OF CENTA

a) General synthetic, spectroscopic and spectrometric experimental

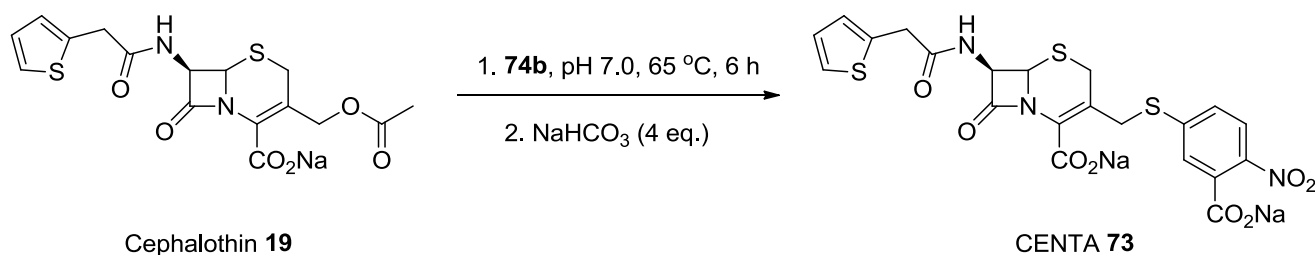
The chemicals and reagents were used without prior purification. NMR spectra were recorded on Bruker AVANCE 400 or 300 MHz spectrometers. Chemical shifts are reported in parts per million (ppm) on a scale relative to the solvent peak CD₃OD (¹H, 3.30 ppm). Coupling constants (*J*) are reported in Hz and peak multiplicities described as singlet (s), doublet (d), doublet of doublets (dd), and multiplet (m). Low-resolution ESI-MS measurements were carried out on a Bruker Esquire HCT (High Capacity 3D ion trap) instrument with a Bruker ESI source.

b) 5-Mercapto-2-nitrobenzoic acid (74b)¹



2-Mercaptoethanol (4.95 mL, 5.55 g, 71.0 mmol) was added to a solution of DTNB (1.01 g, 2.50 mmol) in 50 mL of Trisbase (0.5 M, pH 8.0). The mixture was stirred at rt for 5 mins, after which it was acidified to pH 1.5 by 6 M HCl. The mixture was then left to cool in an ice bath for 5 h and subsequently kept at 4-5 °C overnight. The orange crystals that formed were filtered and washed with cold 5% HCl solution (50 mL) to give the title compound as a bright orange crystal (0.70 g, 70%). ¹H NMR (400 MHz, CD₃OD) δ (ppm): 7.56 (dd, 1H, *J*₁ = 2.1 Hz, *J*₂ = 8.5 Hz), 7.64 (d, 1H, *J* = 2.0 Hz), 7.86 (d, 1H, *J* = 8.5 Hz). ESI-MS: *m/z* 197.8 [M - H]⁻. ESI-MS datum is in agreement with the literature.²

c) CENTA (73)^{2,3}



5-Mercapto-2-nitrobenzoic acid (**74b**) (0.48 g, 2.4 mmol) was added to a solution of cephalothin sodium salt (1.00 g, 2.4 mmol) in Milli-Q water (20 mL). The pH of the mixture was adjusted to pH 7.0 with NaOH (1M) and the mixture was stirred at 65 °C for 6 h. The mixture was cooled to rt and extracted with EtOAc (2 x 10 mL) to remove unreacted starting material. The aqueous layer was acidified to pH 2.0 with HCl (1 M). The insoluble red oil which formed was extracted with EtOAc (3 x 15 mL), and the organic layers were combined, dried over anhydrous Na₂SO₄ and evaporated *in vacuo* to give an orange solid. The solid residue was dissolved in one equivalent of NaHCO₃ (25 mL, 0.096 M, 2.4 mmol). Another three equivalents of NaHCO₃ (75 mL, 0.096 M, 7.2 mmol) was added to dissolve the remaining undissolved solid material. The mixture was filtered and the orange solution obtained was freeze-dried to afford the title compound as an orange solid (0.71 g, 50%). *R*_f: 0.84 in C18 reverse-phase TLC (50% MeOH in CHCl₃, observed as a single yellow spot). ¹H NMR (300 MHz, CD₃OD) δ (ppm): 3.37-3.65 (m, 2H), 3.78 (d, 2H, *J* = 2.7 Hz), 4.10-4.44 (m, 2H), 4.96 (d, 1H, *J* = 4.7 Hz), 5.60 (d, 1H, *J* = 4.7 Hz), 6.91-6.96 (m, 2H), 7.25 (dd, 1H, *J*₁ = 1.5 Hz, *J*₂ = 5.0 Hz), 7.58 (dd, 1H, *J*₁ = 2.2 Hz, *J*₂ = 8.6 Hz), 7.66 (d, 1H, *J* = 2.2 Hz), 7.88 (d, 1H, *J* = 8.9 Hz). ¹H NMR data are in agreement with the literature.²

Determination of kinetic parameters of IMP-1 with CENTA as the substrate

IMP-1 (5 nM) was assayed with CENTA as the substrate at concentrations ranging from 2-300 μM, at pH 7.0, 25 °C, and the kinetic profile is shown in Figure A.2.1. The kinetic assay results satisfy the Michaelis-Menten equation (Equation A.2.1), with an R² value of 0.98, and

the kinetic parameters are presented in Table A.2.1, together with literature values.^{2,3} The observed experimental parameters, particularly the Michaelis constant, K_m and turnover number, k_{cat} are vastly different from those reported in the literature.^{2,3} This may probably be due to differences in protein expression and purification conditions, amount of Zn^{2+} ions added and kinetic assay conditions. Nonetheless, the specificity constant, k_{cat}/K_m obtained ($2.66 \mu M^{-1} s^{-1}$) is closer in magnitude to that reported by Bebrone and colleagues ($2 \mu M^{-1} s^{-1}$).³

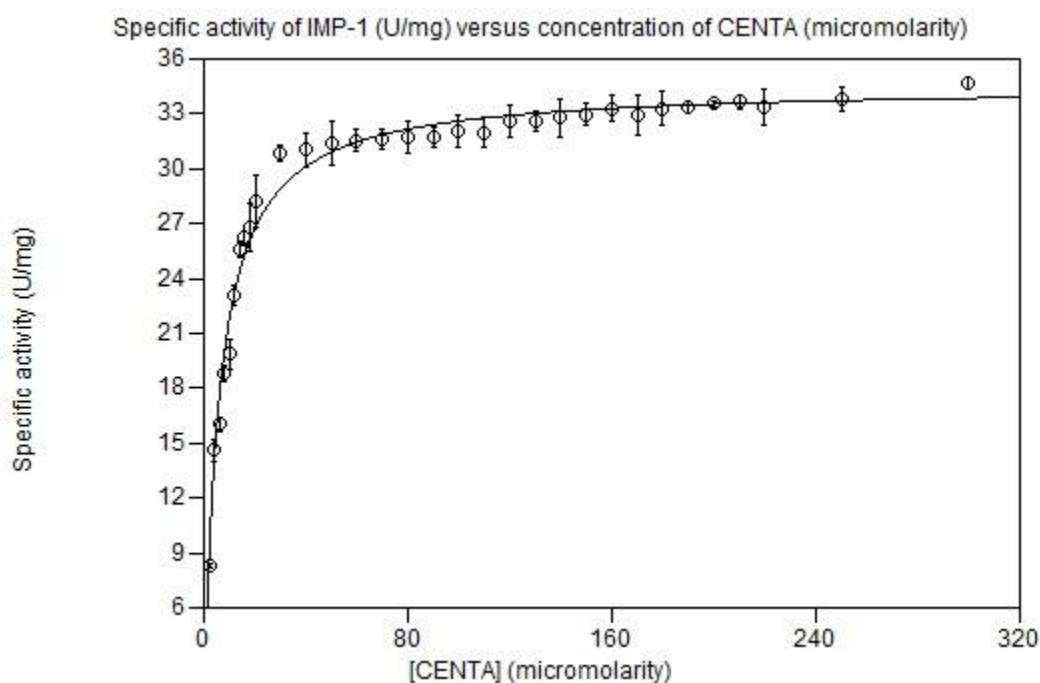


Figure A.2.1: The kinetic profile of IMP-1 (5 nM) with CENTA as the substrate at pH 7.0, 25 °C. The plot is typical of that of an enzyme obeying the Michaelis-Menten relationship.

$$v = \frac{V_{max}[S]}{K_m + [S]}$$

Equation A.2.1: The Michaelis-Menten equation, with v , V_{max} , $[S]$ and K_m denoting the reaction rate, limiting velocity, substrate concentration, and Michaelis constant, respectively.⁴

Table A.2.1: The experimental and literature kinetic parameters of IMP-1 with CENTA as the substrate.

Source	K_m (μM)	k_{cat} (s^{-1})	k_{cat}/K_m ($\mu\text{M}^{-1} \text{s}^{-1}$)
Experimental ^a	5.84 ± 0.25	15.5 ± 0.1	2.66 ± 0.12
Literature 1 ^b	400	200	2
Literature 2 ^c	17.1 ± 2.0	431.9	25.3

^aExperimental conditions were pH 7.0 and 25 °C, with HEPES X (50 mM HEPES, 0.1 M NaCl, 100 μM ZnCl_2) as the buffer and [IMP-1] of 5nM (containing BSA at a final conc. of 20 $\mu\text{g mL}^{-1}$).

^bValues taken from Bebrone *et al.*³ Standard deviation values did not exceed 10%. Assay conditions were pH 7.0 and 30 °C, with sodium phosphate (50 mM, 100 μM ZnSO_4) as the buffer and [IMP-1] of 1 nM.

^cValues taken from van Berkel *et al.*² Assay conditions were pH 7.2 and 24-25 °C, with HEPES (50 mM, 1 μM ZnSO_4 , 0.01% Triton X-100) and [IMP-1] of 1 nM (containing BSA at final conc. of 1 $\mu\text{g mL}^{-1}$).

References

- (1) Patchornik, A.; Degani, Y. *The Journal of Organic Chemistry* **1971**, *36*, 2727.
- (2) van Berkel, S. S.; Brem, J.; Rydzik, A. M.; Salimraj, R.; Cain, R.; Verma, A.; Owens, R. J.; Fishwick, C. W. G.; Spencer, J.; Schofield, C. J. *Journal of Medicinal Chemistry* **2013**, *56*, 6945.
- (3) Bebrone, C.; Moali, C.; Mahy, F.; Rival, S.; Docquier, J. D.; Rossolini, G. M.; Fastrez, J.; Pratt, R. F.; Frère, J. M.; Galleni, M. *Antimicrobial Agents and Chemotherapy* **2001**, *45*, 1868.
- (4) Nicholas C. Price; Raymond A. Dwek; R. George Ratcliffe; Wormald, M. R. *Principals and Problems in Physical Chemistry for Biochemists*; Oxford University Press: Oxford, 2008.

APPENDIX 3: COMPUTATIONAL MODELLING

Docking program

Preliminary *in silico* docking was performed on Molegro Virtual Docker (MVD), which has a potential binding site (cavity) prediction logarithm and piecewise linear potential (PLP) scoring function embedded in its program.¹ The PLP scoring function is useful as it takes hydrogen bond directionality into consideration.¹ In addition, the Glide program was also used to predict possible inhibitor-enzyme interactions. A unique feature of the Glide program is the extra precision (XP) scoring function, which estimates protein-ligand binding affinities based on water desolvation effects and protein-ligand structural motifs.²

Docking template

The 1JJT crystal structure (Figure 1.33) was used as the docking template for Chapters 2 and 3. As mentioned in Chapter 2, the 1JJT crystal structure was selected as the docking template as it has the highest resolution (1.3 Å) among all the IMP-1 3D crystal structures surveyed, with a very potent co-crystallised inhibitor bound in the active site (IC₅₀ of 9 nM).³ On the other hand, the 1DD6 crystal structure was used as the docking template for the thiazolidine series in Chapter 4 (Figure 4.2). The 1DD6 crystal structure was selected as the docking template as both the co-crystallised ligand and the docked ligands are mercaptocarboxylate-type inhibitors.⁴

Docking validation

The validation of the docking programs was carried out to evaluate the predictive power of the programs, by removing the original co-crystallised ligand from the docking template and re-docking the ligand into the template, in the absence of co-crystallised water molecules. The docking template used for this validation exercise is the 1JJT crystal structure.

The root mean square deviation (RMSD) of the docked pose superimposed over the original co-crystallised ligand was found to be 1.56 Å and 0.62 Å for the MVD (Figure A.3.1) and Glide (Figure A.3.2) program, respectively. The RMSD value obtained for the MVD program is significantly larger than that for the Glide program. Nevertheless, the RMSD value is not far from the average, expected value for the MVD program, *i.e.* 1.38 Å.¹ In view of this observation, docking poses obtained from the Glide program were used to rationalise inhibitor-enzyme interactions whenever MVD docking results were deemed unsatisfactory.

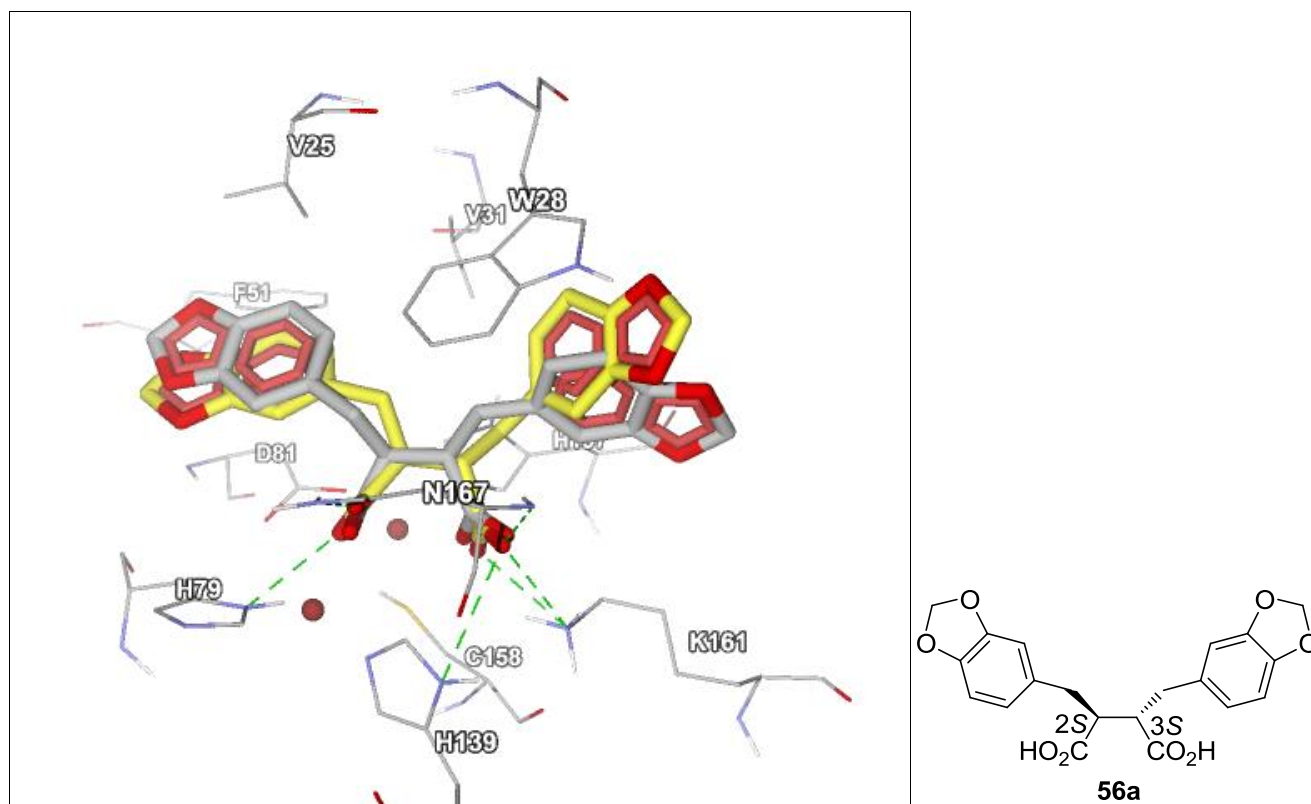


Figure A.3.1: The docking pose of **56a** superimposed over the original position of the co-crystallised ligand in the 1JJT crystal structure, with the use of MVD as the docking program. The docked pose is in yellow, whereas the original co-crystallised ligand is in grey. Atom colours on amino acid residues: carbon in grey, hydrogen in white, nitrogen in blue, oxygen in red and sulfur in gold. The zinc ions are represented as red spheres.

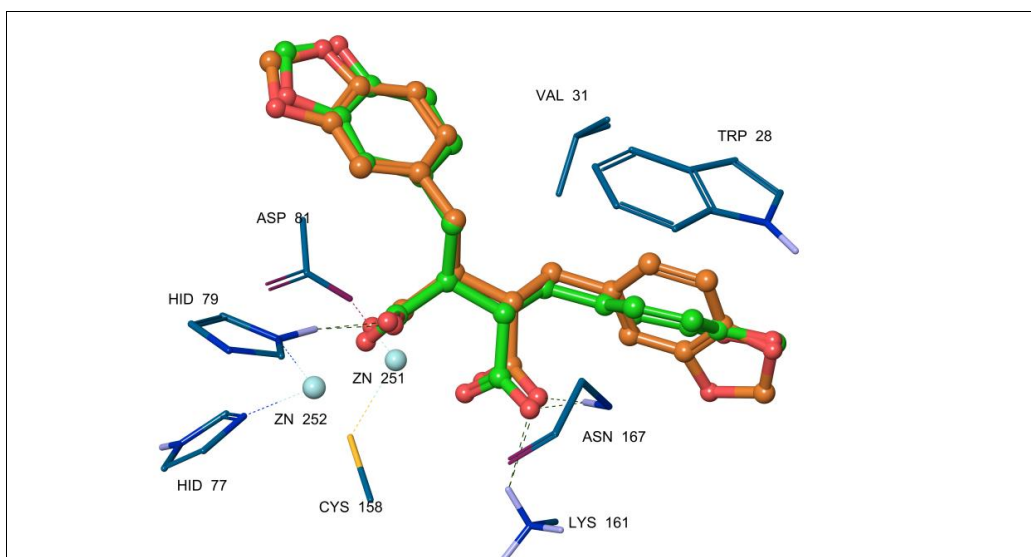


Figure A.3.2: The docking pose of **56a** superimposed over the original position of the co-crystallised ligand in the 1JJT crystal structure, with the use of Glide XP as the docking program. The docked pose is in green, whereas the original co-crystallised ligand is in orange. Atom colours on amino acid residues: carbon in teal, hydrogen in white, nitrogen in blue, oxygen in burgundy and sulfur in gold. The zinc ions are represented as cyan spheres.

Ligand preparation

The molecular structures of the ligands were drawn with ChemBio3D Ultra for MVD program and Maestro for Glide docking. The structures were energy minimized before docking. Ligands to be docked with the Glide program were energy minimised by the OPLS* 2005 force field, embedded in the MacroModel module of the Schrödinger suite. Thiol groups were prepared as thiolate ions (S^-)⁵, in addition, carboxyl and tetrazolyl groups were docked as in the deprotonated form.

MVD docking with 1JJT as the docking template

Co-factors other than the zinc metal centres (Zn251 and Zn252), water molecules and the bound ligand were removed prior to docking. Amino acid residues Val25 (61), Trp28 (64) and Val31 (67) were set as the flexible flap. A number of three cavities, with a grid resolution of 0.8 Å were detected, and the biggest cavity (71.1-66.0 Å³) was selected for docking.¹

Glide docking

The entire protein molecule was energy minimised by using the OPLS* 2005 force field. The minimised protein structure was used to generate a search grid by selecting the reported co-crystal ligand in 1JJT or 1DD6 and extending the docking search grid to 8 Å surrounding this ligand. Flexible docking was performed for all molecules by allowing the side chain hydroxyl groups of protein to rotate around their bond axes. An extra precision (XP) docking was performed for all the ligands.² Docking poses were visualised with Maestro.

*OPLS is the acronym for optimised potentials for liquid simulations.⁶ The parameters of the force field were optimised to fit experimental thermodynamic and structural properties of liquids.⁶

References

- (1) Thomsen, R.; Christensen, M. H. *Journal of Medicinal Chemistry* **2006**, *49*, 3315.
- (2) Friesner, R. A.; Murphy, R. B.; Repasky, M. P.; Frye, L. L.; Greenwood, J. R.; Halgren, T. A.; Sanschagrin, P. C.; Mainz, D. T. *Journal of Medicinal Chemistry* **2006**, *49*, 6177.
- (3) Toney, J. H.; Hammond, G. G.; Fitzgerald, P. M. D.; Sharma, N.; Balkovec, J. M.; Rouen, G. P.; Olson, S. H.; Hammond, M. L.; Greenlee, M. L.; Gao, Y.-D. *Journal of Biological Chemistry* **2001**, *276*, 31913.
- (4) Concha, N. O.; Janson, C. A.; Rowling, P.; Pearson, S.; Cheever, C. A.; Clarke, B. P.; Lewis, C.; Galleni, M.; Frère, J.-M.; Payne, D. J.; Bateson, J. H.; Abdel-Meguid, S. S. *Biochemistry* **2000**, *39*, 4288.
- (5) Olsen, L.; Jost, S.; Adolph, H.-W.; Pettersson, I.; Hemmingsen, L.; Jørgensen, F. S. *Bioorganic and Medicinal Chemistry* **2006**, *14*, 2627.
- (6) Jorgensen, W. L.; Tirado-Rives, J. *Journal of the American Chemical Society* **1988**, *110*, 1657.